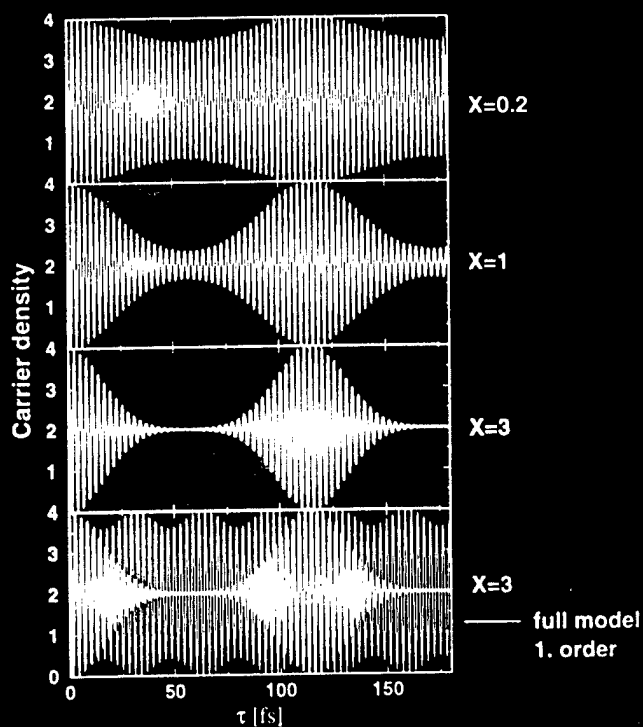


Walter Pötz and W. Andreas Schroeder (Eds.)

Coherent Control in Atoms, Molecules, and Semiconductors

Proceedings of an International Workshop
held in Chicago, USA, 19-22 May 1998



Kluwer Academic Publishers

FINAL REPORT

1. ONR PROPOSAL NUMBER: 98PR04900-00
3. TITLE OF PROPOSAL: *International Workshop on Coherent Control of Charge Carrier Dynamics in Semiconductors*
4. CONTRACT OR GRANT NUMBER: N00014-98-1-0513
5. NAME OF INSTITUTION: University of Illinois at Chicago
6. AUTHORS OF REPORT: Walter Poetz

PROJECT SUMMARY

The *International Workshop on Coherent Control of Charge Carrier Dynamics in Semiconductors* was held May 18-22, 1998 at the University of Illinois at Chicago. An international and multi-disciplinary group of scientists presented recent results on coherent control phenomena in atoms, molecules, and semiconductors. Pertinent open physical questions, as well as potential technological applications and the future of the field were discussed. Referreed proceedings were published under the title *Coherent Control in Atoms, Molecules, and Semiconductors*, by Kluwer in spring of 1999 (ISBN 0-7923-5649-7).

19990610 008

DTIC QUALITY INSPECTED 4

*International Workshop on Coherent Control of
Charge Carrier Dynamics in Semiconductors*

TABLE OF CONTENTS

PROJECT SUMMARY	1
I. WORKSHOP SCHEDULE	2
II. ADDRESSES OF PARTICIPANTS	6

Workshop Schedule

Tuesday, May 19, 1998

6:00 to 9:00 pm: Reception, Registration, Manuscript Drop-Off, SES 2214 (Physics Department)

Wednesday, May 20, 1998

Lecture Center C1:

8:00 to 10:30: Late Registration, Manuscript Drop-Off and Pickup for Review

8:15 - 8:30: Welcome and Opening Remarks

Chair: P. Lambropoulos

8:30-9:00: H. Rabitz, (Princeton University, USA), "**Controlling Quantum Dynamics Phenomena**"

9:00-9:30: D. Elliott (University of Purdue, USA), "**Laser-Phase-Insensitive Coherent Control of Photoion Product States in 2-Photon vs 2-Photon Ionization of Atomic Barium**"

9:30-10:00: P. Brumer (University of Toronto, Canada), "**Scenarios and Successes in Molecular Coherent Control**"

10:00-10:30: Coffee Break and Late Registration, Manuscript Drop-Off and Pickup for Review

Chair: H. Rabitz

10:30-11:00: R. Gordon (University of Illinois at Chicago, USA) , "**The Role of the Molecular Phase in the Coherent Control of Photodissociation and Photoionization of Gas Phase Molecules**"

11:00-11:30: Dimitrios Charalambidis (University of Crete, Greece), "**Recent Experiments of Quantum Coherent Control in Atomic Systems**"

11:30-12:00: T. Seideman (National Research Council, Canada) , "**Gas Phase Coherent Control as a Route to Nanoscale Surface Processing**"

12:00-2:00pm: Manuscript Pickup for Review, Lunch Break

Chair: P. Brumer

2:00-2:30: H. van Driel (University of Toronto, Canada), **"Coherent Control of Free Carriers in Bulk Semiconductors"**

2:30-3:00: P. Lambropoulos (Max Planck Institute fuer Quantenoptik, Garching, Germany), **"Coherent Control of Localized States Interacting with Continua"**

3:00-3:30: M. Holthaus (University of Marburg, Germany), **"Coherent Control of Quantum Localization"**

3:30-4:00: Coffee Break

Chair: M. O. Scully

4:00-4:30: J. Sipe (University of Toronto, Canada), **"Coherent Carrier and Current Control in Bulk Semiconductors: The Link to the Susceptibilities of Nonlinear Optics"**

4:30-5:00: T. Kuhn (University of Muenster, Germany), **"Coherent Control of Heavy-Light Hole and Phonon Quantum Beats"**

Thursday, May 21, 1998

Lecture Center C1:

Chair: T. Norris

8:30-9:00: F. Loeser (Institut fuer Angewandte Photophysik, Dresden, Germany), **"Optical Control of Bloch Oscillation Amplitudes in Semiconductor Superlattices"**

9:00-9:30: S.-L. Chuang (University of Illinois at Urbana-Champaign, USA) , **"Quantum Beat in a Wannier-Stark Ladder"**

9:30-10:00: M. O. Scully (Texas A&M, USA) , **"Quantum Coherence and Tunneling-Induced Transparency in Semiconductor Quantum Wells"**

10:00-10:30: Coffee Break

Chair: S. Datta

10:30-11:00: Thierry Amand (INSA, France), "**Coherent Control of 2D Excitons Probed by Time-Resolved Secondary Emission**"

11:00-11:30: Xuedong Hu, (University of Illinois at Chicago, USA), "**Coherent Control Schemes in Semiconductor Double Wells**"

11:30-12:00: M. Ivanov (National Research Council, Canada), "**Tunneling in Driven Double-Well Potentials: Control, Exploitation, and Relaxation**"

12:00-2:00: Lunch Break

Chair: W. A. Schroeder

2:00-2:30: K. Kawase (Tohoku Gakuin University, Sendai, Japan), "**Generation of Widely Tunable THz-Wave Using Nonlinear Optics**"

2:30-3:00: D. Citrin (Washington State University, USA), "**Coherent Control of Optical Excitations in Semiconductors: Optical Switches and Terahertz Emitters**"

3:00-3:30: A.M. Weiner (Purdue University, West Lafayette, USA), "**Control of Terahertz Radiation Through Femtosecond Pulse Shaping**"

3:30-4:00: Jacob B. Khurgin (Johns Hopkins University, USA), "**Heterodyning FIR Using Coherent Photovoltaic Effect**"

4:00-4:30: Coffee Break

4:30-6:00: Panel Discussion: (H. van Driel, K. Kawase, W. Pötz, H. Rabitz, M. O. Scully, A.M. Weiner) open questions, "crazy" ideas, etc.

7:30: Workshop Banquet (Greek Islands)

Friday, May 22, 1998

Lecture Center C1:

8:45-9:00 Announcements, **Review Reports Back to Organizers**

Chair: S.-L. Chuang

9:00-9:30: T. Norris (Center for Ultrafast Optical Science, University of Michigan, USA), "**Coherent Control of Normal Modes in Strongly Coupled Microcavities**"

9:30-10:00: Hui Cao (Northwestern University, USA), "**Exciton-Polaritons in Semiconductor Microcavities**"

10:00-10:30: Coffee Break, Review Reports Back to Organizers

Chair: T. Kuhn

10:30-11:00: R. Binder (Optical Sciences Center, University of Arizona, Tucson, USA), "**Ultrafast Adiabatic Population transfer in p-Doped Semiconductor Quantum Wells**"

11:00-11:30: M. Wagner (Cavendish Lab, Cambridge, UK), "**Tunneling of Low-Energetic Electrons in the Presence of Intense Laser Fields: The Formation of Dynamical Barrier States**"

11:30: Closing Remarks, Manuscripts Back to Authors

Lunch

Addresses of Participants

Thierry Amand
Laboratoire de Physique de la Matiere Condensee, CNRS-UMR 5830
Institut National des Sciences Appliquees
Departement de Genie Physique
Complexe Scientifique de Rangueil
31077 Toulouse cedex 4, FRANCE
Tel.:+33 (0)5 61 55 96 34
Fax.:+33 (0)5 62 17 18 50
e-mail: amand@insa-tlse.fr

M. K. Balakirev
Institute of Semiconductor Physics
Russian Academy of Sciences
Siberian Branch
Prosp. Lavrentyeva, 13
Novosibirsk, 630090
RUSSIA
E-mail:Balak@isp.nsc.ru

Rudolf H Binder
Optic Sci Ctr
Univ of Arizona
Tucson AZ 85721
Phone (520) 621-2892
Fax (520) 621-6778
Email binder@argonaut.opt-sci.arizona.edu

Paul W Brumer
Dept of Chem
Univ of Toronto
Toronto ON M5S 3H6 Canada
Phone 416 975 3569
Email pbrumer@tikva.chem.utoronto.ca

Hui Cao, Ph.D.
Assistant Professor
Dept. of Physics & Astronomy, Northwestern University
2145 Sheridan Road, Evanston, IL 60208
Tel: (847) 467-5452 Fax: (847) 491-9982
Email: h-cao@nwu.edu

Dimitrios Charalambidis
University of Crete, Physics Department
and
FO.R.T.H.-I.E.S.L.
P.O. Box 1527, 711 10 Heraklio, Crete, Greece

Tel.: +30-81-391464
Fax: +30-81-391318
e-mail: chara@iesl.forth.gr

Shun Lien Chuang
Dept of Elec & Comp Engr
UIUC
1406 W Green St
Urbana IL 61801
Phone (217) 333-3359
Fax 217 333 5701
Email s-chuang@uiuc.edu

David Scott Citrin
Dept of Phys
Washington State Univ
Pullman WA 99164-2814
Phone (509) 335-3698
Fax (509) 335-7816
Email citrin@wsu.edu

P. B. Corkum,
Steacie Institute for Molecular Sciences
National Research Council of Canada
Ottawa, Ontario, Canada K1A 0R6.
e-mail: paul.corkum@nrc.ca

Supriyo Datta
Sch of Elec Engr
Purdue Univ
West Lafayette IN 47907-1285
Phone (317) 494-3511
Fax 317 494 6440
Email DATTA@ECN.PURDUE.EDU

Daniel Elliott
1285 Elec Engr
Purdue Univ
West Lafayette IN 47907
Phone (765) 494-3442
Fax (765) 494-6951
Email ELLIOTTD@ECN.PURDUE.EDU

Matvey Vul'fovich Entin Institute of Semiconductor Physics
Siberian Branch
Russian Academy of Sciences
Novosibirsk 630090, Russia.
Fax:007-383-2-332-771,

e-mail: entin@isp.nsc.ru

Robert J Gordon
Dept of Chem MC 111
Univ of Illinois
845 W Taylor St
Chicago, IL 60607-7061
Phone (312) 996-3280
Fax (312) 996-0431
Email rjgordon@uic.edu

Martin Holthaus
Universitaet Marburg
FB Physik
D-35032 Marburg
fx: 01106421284511

Xuedong Hu
432 S Clinton #B2
Oak Park, IL 60302
Phone (312) 996-3407
Fax (312) 996-9016
Email xuh@uic.edu

Misha Ivanov
Femtosecond Program,
Steacie Institute for Molecular Sciences
NRC of Canada, 100 Sussex Drive, room 2069,
Ottawa, Ontario K1A 0R6, Canada
phone: (613)-993-9973
NEW (!!) fax: (613)-991-3437
e-mail: ivanov@ned1.sims.nrc.ca,
misha.ivanov@nrc.ca

Kodo Kawase
Applied Physics
Tohoku Gakuin University
Katahira
Sendai 980-77
Japan
kawase@tjxx.tohoku-gakuin.ac.jp

Peter Kocevar
Inst. Theoretische Physik
Universitaet Graz
Universitaetsplatz 5
A-8010 Graz
Austria

Tilmann Kuhn
Inst. f. Theor. Physik
Universitaet Muenster
D-48149 Muenster
Germany
kuhnti@nwz.uni-muenster.de

Jacob B. Khurgin
Department of Electrical and Computer Engineering
Johns Hopkins University
Baltimore MD 21218
(410) 516 7518
(410) 516 8380
Fax (410) 516 5566
jbk@doomsday.ece.jhu.edu

P P Lambropoulos
Max-Planck Inst for Quantenoptik
Hans-Kopfermann Str 1
D-85748 Garching, Germany
Email labro@mpq.mpg.de
Homepage www.mpq.mpg.de

Falk Loeser
Institut fuer Angewandte Photophysik
Technische Universitaet Dresden
D-01062 Dresden
Ph: +49-351-463-4389, Fax: +49-351-463-7065

Dmitri E. Nikonov
Assistant Research Engineer
Department of Electrical and Computer Engineering
University of California
Santa Barbara, CA 93106-9560
phone (805) 893-7682
fax (805) 893-3262
dmitri@quantum.ece.ucsb.edu

Ted Norris
Center for Ultrafast Optical Science
University of Michigan
2200 Bonisteel Blvd.
Ann Arbor, MI 48109-2099
734-764-9269
tnorris@eecs.umich.edu

Wolfgang Porod
Dept of Elec Engr

Univ of Notre Dame
Notre Dame IN 46556
Phone (219) 631-6376
Fax 219 631 4393
Email wolfgang.porod@nd.edu

Herschel A Rabitz
Dept of Chem
Princeton Univ
129 Frick Lab
Princeton NJ 08544-1009
Phone (609) 258-3917
Fax (609) 258-6746
Email hrabitz@chembax.princeton.edu

F. Rossi
Univ. di Modena
Dipartimento di Fisica
I-41100 Modena
FX: 0113959367488

Marlan O Scully
Phys Dept
Texas A&M Univ
College Station TX 77843-4242
Phone (409) 862-2333
Fax 409 845 2590

Tamar Seideman
National Research Council of Canada
100 Sussex Drive
Ottawa, Ontario K1A 0R6
(613) 990-0945
(613) 947-2838
tamar.seideman@nrc.ca

John Edward Sipe
Dept of Phys
Univ of Toronto
Toronto ON M5S 1A7 Canada
Phone 416 978 4517
Fax 416 978 2537
Email sipe@physics.utoronto.ca

Arthur L Smirl
Photonics Lab
Univ of Iowa
100 IATL

Iowa City IA 52242-1000
Phone (319) 335-4580

Henry M van Driel
Dept of Phys
Univ of Toronto
Huron and Russell
Toronto ON M5S 1A1 Canada
Phone (416) 978 4200
Fax 416 978-5848
Email vandriel@physics.utoronto.ca

Mathias Wagner
Cavendish Lab
Hitachi Cambridge Lab
Madingley Rd
Cambridge C83 0HE
England
Phone 865 272338
Fax 865 272400

A. M. Weiner
School of Elec Engr
Purdue Univ
1285 Elec Engr Bldg
West Lafayette IN 47907-1285
Phone (765) 494-5574
Fax (765) 494-6951
Email amw@ecn.purdue.edu

Coherent Control in Atoms, Molecules, and Semiconductors

Coherent Control in Atoms, Molecules, and Semiconductors

Proceedings of an International Workshop held in Chicago,
U.S.A., 19–22 May 1998

Edited by

Walter Pötz

*Department of Physics,
University of Illinois at Chicago,
U.S.A.*

and

W. Andreas Schroeder

*Department of Physics,
University of Illinois at Chicago,
U.S.A.*



Kluwer Academic Publishers

Dordrecht / Boston / London

A C.I.P. Catalogue record for this book is available from the Library of Congress.

ISBN 0-7923-5649-7

Published by Kluwer Academic Publishers,
P.O. Box 17, 3300 AA Dordrecht, The Netherlands.

Sold and distributed in North, Central and South America
by Kluwer Academic Publishers,
101 Philip Drive, Norwell, MA 02061, U.S.A.

In all other countries, sold and distributed
by Kluwer Academic Publishers,
P.O. Box 322, 3300 AH Dordrecht, The Netherlands.

Printed on acid-free paper

All Rights Reserved
©1999 Kluwer Academic Publishers
No part of the material protected by this copyright notice may be reproduced or
utilized in any form or by any means, electronic or mechanical,
including photocopying, recording or by any information storage and
retrieval system, without written permission from the copyright owner

Printed in the Netherlands.

LIST OF SPONSORS

U.S. Office of Naval Research
U.S. Army Research Office

Vice-Chancellor's Office for Research, University of Illinois at Chicago
College of Liberal Arts and Sciences, University of Illinois at Chicago
Department of Physics, University of Illinois at Chicago

TABLE OF CONTENTS

LIST OF SPONSORS	v
PREFACE	xi
PART I: ATOMIC AND MOLECULAR SYSTEMS	1
P. Brumer and M. Shapiro Scenarios in Coherent Control	3
D. Charalambidis, N. E. Karapanagioti, D. Xenakis, E. Papastathopoulos, C. Fotakis, O. Faucher, E. Hertz, S. Cavalieri, R. Eramo, L. Fini, and M. Materazzi Quantum Control in Atomic Systems	15
F. Wang, J. Huang, and D. S. Elliott Laser-phase-sensitive Coherent Control of Photoion Product States in 2-Photon vs. 2-Photon Ionization of Atomic Barium	27
R. J. Gordon, J. A. Fiss, L. Zhu, and T. Seideman Coherent Phase control of Photoionization and Photodissociation	39
P. Lambropoulos and T. Nakajima Coherent Control of Atomic Photoionization and Autoionization	51
M. O. Scully, M. Fleischhauer, E. S. Fry, A. Imamoglu, M. D. Lukin, D. Nikonov, Th. Walther, and S. F. Yelin Lasing Without Inversion via Interference of Double-Dark Resonances in Atomic and Quantum Well Systems	63

PART II: COHERENT CONTROL IN SEMICONDUCTORS	73
H. M. van Driel, J. E. Sipe, A. Haché, and J. M. Fraser Coherence Control of Free Carriers in Bulk Semiconductors	75
X. Marie, T. Amand, P. Le Jeune, M. Brousseau, and J. Barrau Coherent Control of 2D Excitons Probed by Time-Resolved Secondary Emission	87
R. Binder and M. Lindberg Many-Body Effects in the Ultrafast Population Transfer in p-Doped Semiconductor Quantum Wells	103
T. Kuhn, V. M. Axt, M. Herbst, and E. Binder Coherent Control of Heavy-Light Hole and Phonon Quantum Beats	113
X. Hu and W. Pötz Coherent Control Schemes in Semiconductor Double Wells	127
S. Hughes and D. S. Citrin Terahertz-Control of Charge-Carrier Wavepackets in Semiconductor Quantum Wells	147
H. Cao Microcavity Exciton-Polariton	157

PART III: COHERENT PHENOMENA AND RELATED TOPICS 169

M. Holthaus	
Coherent Control of Quantum Localization	171
M. Wagner	
Tunneling of Low-Energetic Electrons in the Presence of Intense Laser Fields: The Formation of Dynamical Barrier States	183
E. M. Baskin and M. V. Entin	
Hopping Mechanism of Coherent Photovoltaic Effect and Photoinduced Polar Anisotropy in Glass	191
J. B. Khurgin, B. Saif, and B. Seery	
Heterodyning Scheme Employing Quantum Interference	203
K. Kawase and H. Ito	
Generation of Widely Tunable THz-Wave Using Nonlinear Optics	213
LIST OF PARTICIPANTS	221

PREFACE

The *International Workshop on Coherent Control of Carrier Dynamics in Semiconductors* was held May 19 to 22, 1998 at the University of Illinois at Chicago. Its intent was to bring together an international and interdisciplinary group of scientists to discuss recent progress, pertinent problems, and open questions in the field of coherent control in atoms, molecules, and semiconductors, in particular. Twenty-seven scientists from the physical chemistry, quantum optics, semiconductor, electrical engineering, and laser communities accepted our invitation and made this event a meeting of exciting presentations and vivid discussions.

This volume contains the proceedings of this workshop. Most speakers accepted our invitation to provide a manuscript either on specific aspects of their work or a brief review of their area of research. All manuscripts were reviewed. It is hoped that they provide not merely an overview of most of the issues covered during the workshop, but also represent an account of the current state of coherent control in general. Hence, it is hoped that they are also of interest to a large number of scientists active in one of the areas listed above.

The organizers of this workshop would like to thank all the participants for making this meeting a complete success. We are particularly indebted to Dr. Larry R. Cooper at the U.S. Office of Naval Research and Dr. Michael A. Stroscio at the U.S. Army Research Office for external financial support. We also wish to thank the Vice-Chancellor's Office for Research, the College of Liberal Arts and Sciences, the Department of Physics at the University of Illinois at Chicago for internal financial support. Finally, we wish to thank Dr. Xuedong Hu, Dr. Manjusha Mehendale, Tatiana Krivocheeva, and Nathan W. Rimington for help with the organization of this workshop.

Walter Pötz, Chair
W. Andreas Schroeder, Co-Chair

October, 1998

PART I: Atomic and Molecular Systems

SCENARIOS IN COHERENT CONTROL

PAUL BRUMER

*Chemical Physics Theory Group and
Photonics Research Ontario
University of Toronto
Toronto M5S 3H6 Canada*

AND

MOSHE SHAPIRO

*Chemical Physics Department,
Weizmann Institute of Science
Rehovot, Israel 76100*

Abstract. Coherent control of molecular processes provides a means of controlling the dynamics of molecules, and of molecular processes, via laser induced quantum interference. We briefly review this approach, with a focus on scenarios useful for controlled currents in semiconductors and on alternate new control scenarios.

1. Introduction

Since 1986, efforts to control molecular motion and molecular processes have turned to the use of quantum interference as a means of directing molecules towards desired goals. Below we provide a brief sketch of the ideas which underlay the coherent control approach and call attention to the two scenarios which have either been proposed or utilized to control photocurrents in semiconductors. In addition we mention recent new directions in this area. Both comprehensive (Shapiro & Brumer 1997) and elementary reviews (Brumer & Shapiro 1995) are available elsewhere. Alternate methods of addressing the molecular control problem have also been recently reviewed by Gordon and Rice (1997).

Many of the proposed coherent control scenarios rely upon a simple way of achieving active control over the prepared and final state of the system.

Specifically, active control over the final state is achieved by driving an initially pure molecular state through two or more independent coherent optical excitation routes. [Both the requirement for an initially pure molecular state and purely coherent excitation sources can be relaxed considerably. All that is really required is that some degree of molecular coherence be established in the molecular state prepared by the multiple excitation routes. See Shapiro & Brumer (1989); Jiang *et al.* (1996).] The final state of the system displays interference terms between these multiple routes, and its magnitude and sign depend upon laboratory parameters. As a consequence, final state characteristics can be manipulated directly in the laboratory.

This approach has a well-known analogy, the interference between paths as a beam of either particles or of light passes through a double slit. In that instance a source coherence leads to either constructive or destructive interference, manifest as patterns of enhanced or reduced probabilities on an observation screen. In the case of coherent control the overall coherence of a pure state plus laser source allows for the constructive or destructive manipulation of final state properties of molecules. The principles upon which this approach rests are similar to those relied upon in recent Quantum Optics developments including Electromagnetically Induced Transparency, Lasers Without Inversion, population trapping, etc. (Scully & Zubairy 1997). Interest in Chemical Physics, however, often focuses on complex multilevel multidimensional systems excited to coupled continua where molecular rearrangement can occur.

Recognition that the essential feature of coherent control is the generation of quantum interference through independent coherent excitation pathways allows for the development of numerous control scenarios based upon this principle. In the case of the control of photocurrents in semiconductors, an application particularly relevant to this workshop, two of these many (Shapiro & Brumer 1997) scenarios have been considered. We address these specifically below.

1.1. PHOTOIONIZATION OF A SUPERPOSITION STATE

Properties of a photocurrent generated in a semiconductor are usually controlled by a bias voltage (Seeger, 1973). The role of this voltage is to give *thermodynamic* preference to the flow of photoelectrons in one direction (the forward or backward direction in a $p - n$ junction.) In a p-type or n-type semiconductor the probability of carrier photoemission (from a single impurity) without an external voltage is anisotropic only inasmuch as the crystal possesses mass or dielectric constant anisotropies, but the probabilities of emission backward and forward along a given crystal axis are equal. Although photocurrents are commonly produced by laser illumination, the

laser coherence does not affect the process.

Here we review our coherent control scheme (Kurizki, Shapiro & Brumer), proposed originally in 1988, for generating and controlling photocurrents without bias voltage, relying instead on the coherence of the illuminating source. Specifically, a superposition of two bound donor (or exciton) states is photoionized by two mutually phase-locked lasers at slightly different frequencies with the same polarization axis. The result is a current along the direction of polarization. The realization of the scheme is discussed for shallow-level donors in semiconductors.

Consider a semiconductor doped with shallow-level donors. The bound state wavefunction of such a donor is successfully described by the hydrogenic effective-mass theory (Pantelides, 1978) with wavefunction:

$$\chi_n(\mathbf{r}) = \langle \mathbf{r} | \mathbf{n} \rangle = V^{-1/2} \int_{-\infty}^{\infty} B_{n,k} u_k(\mathbf{r}) e^{i\mathbf{k}\cdot\mathbf{r}} dk \quad (1)$$

Here $u_k(\mathbf{r})$ is the conduction band Bloch state correlated to the asymptotic free-electron momentum $\hbar\mathbf{k}$, V is the normalization volume and $B_{n,k}$ is the corresponding Fourier component of the hydrogenic wavefunction envelope χ_n . For semiconductors with effective-mass anisotropy, the χ_n are evaluated variationally (Faulkner, 1969; Kasami, 1968; Baldereschi & Diaz, 1970; Kohn & Luttinger 1955; Ridley, 1980). Although the theory described below holds for any superposition of bound donor states, a superposition of $|1s\rangle$ and $|2p_o\rangle$ states will be considered explicitly. For these cases a simple variational procedure (Kohn & Luttinger, 1955), whose results agree reasonably well with those of more refined procedures, yields

$$\begin{aligned} \chi_{1s} &= \pi^{1/3} \exp\{-(x^2 + y^2)/a^2 + z^2/b^2]^{1/2}\} \\ \chi_{2p_o} &= \sqrt{2}\pi^{3/4} b^{-1} z \exp\{-(x^2 + y^2)/a^2 + z^2/b^2]^{1/2}\}. \end{aligned} \quad (2)$$

Here the coordinates [normalized to the effective Bohr radius $a^* = \hbar^2/(m_{\perp}e^2)$] coincide with the main axes of the cubic crystal. Depending on the ratio $\gamma = m_{\perp}/m_{\parallel}$ (the parallel direction coinciding with z), the a and b parameters vary between $a = b = 1$ for nearly isotropic materials with $\gamma = 1$ (e.g. GaAs, GaSb, InAs) and $a \approx 4/3\pi$; $b \approx (1/3)(4/\pi)^{2/3}\gamma^{1/3}$ for highly anisotropic materials (e.g. Si or Ge) with $\gamma \ll 1$.

Let a superposition of the $|1s\rangle$ and $|2p_o\rangle$ states be prepared by some coherent process. As pointed out before, this can be achieved by a short coherent laser pulse or various other means. It is possible to discriminate against the excitation of the $|2p_{\pm 1}\rangle$ states either by frequency tuning, (e.g., the $2p_{\pm 1} - 2p_o$ splitting is $\sim 5\text{meV}$ in Si), or by linearly polarizing the laser along the z -axis. Consider now the simultaneous excitation of this

superposition state to a kinetic energy level E_k in the conduction band continuum by two z -polarized infrared or visible lasers with frequencies $\omega_{1s}, \omega_{2p_o}$; the former lifts the $|1s\rangle$ state to E_k and the latter lifts the $|2p_o\rangle$ state to E_k . These excitations involve the energy conservation relation:

$$E_k = \frac{\hbar^2 k_\perp^2}{2m_\perp} + \frac{\hbar^2 k_z^2}{2m_{||}} = \hbar\omega_n - |E_n| - \sum_p p\hbar\omega \quad (3)$$

Here the n -state energy is measured from the conduction-band edge and the last term accounts for the emission ($p > 0$) or absorption ($p < 0$) of p phonons of frequency ω . For the sake of simplicity, we shall use the zero phonon-frequency line; hence, $\hbar\omega_{1s} = E_k + |E_{1s}|$, $\hbar\omega_{2p_o} = E_k + |E_{2p_o}|$.

In what follows we consider only electric-dipole induced optical transitions with the electric field along the z axis. The electric dipole transition amplitudes from an impurity state $|\mathbf{n}\rangle$ to the asymptotic (far from impurity) plane wave $\langle \mathbf{r}|\mathbf{k}\rangle = V^{-1/2}e^{i\mathbf{k}\cdot\mathbf{r}}u_{\mathbf{k}}(\mathbf{r})$ is

$$\langle \mathbf{k}|\mu_z|\mathbf{n}\rangle = \frac{-ie\hbar}{m_{||}(E_k + |E_n|)} \langle \mathbf{k}|(-i\hbar\partial/\partial z)|\mathbf{n}\rangle \quad (4)$$

The last factor is, using Eq. (1), simply given as

$$\langle \mathbf{k}| -i\hbar\partial/\partial z|\mathbf{n}\rangle = \hbar\mathbf{k}_z \langle \mathbf{k}|\mathbf{n}\rangle = \hbar\mathbf{k}_z B_{n,k} \quad (5)$$

We now consider the photoionization of the superposition state,

$$|\psi\rangle = c_1|1\rangle + c_2|2\rangle \quad (6)$$

where 1 denotes the $1s$ state and 2 the $2p_o$ state. We let a z -polarized two-color source, whose electric field is given as,

$$\epsilon_z(t) = \epsilon_1 \cos(\omega_1 t + \phi_1) + \epsilon_2 \cos(\omega_2 t + \phi_2) \quad (7)$$

act on this superposition state. The rate (probability per unit time and unit solid angle) of photoemission to a conduction state with momentum $\hbar\mathbf{k}$ resulting from this action is,

$$P(\cos\theta) = (2\pi/\hbar)\rho(k) \left| \sum_{n=1,2} e^{-i\phi_n} \epsilon_n c_n \langle \mathbf{k}|\mu_z|\mathbf{n}\rangle \right|^2 \quad (8)$$

Here,

$$\begin{aligned} \cos\theta &= k_z/k; \sin\theta = k_\perp/\gamma^{1/2}k, \\ k &= (2m_{||}E_k)^{1/2}/\hbar, \\ \rho(k) &= (m_\perp V/8\pi^3\hbar^2)k \end{aligned} \quad (9)$$

and $\rho(k)$ is the density of final states. The Franck-Condon factor for the zero phonon line has been set here to unity.

Denoting $c_n = |c_n| \exp(i\alpha_n)$ and using Eqs. (4) and (5) in Eq. (8) gives the form:

$$P(\cos \theta) = [A_1|B_{1s,\mathbf{k}}|^2 + A_2|B_{2p_o,\mathbf{k}}|^2 + A_{12} \cos(\alpha_1 - \alpha_2 - \phi_1 + \phi_2 + \alpha_{12})|B_{1s,\mathbf{k}}B_{2p_o,\mathbf{k}}|] \cos^2 \theta \quad (10)$$

where

$$\begin{aligned} A_n &= \frac{2\pi e^2 \hbar^3 k^2 \rho(k) |\epsilon_n c_n|^2}{m_{||}^2 (E_k + E_n)^2} \quad (n = 1, 2) \\ A_{12} &= \frac{4\pi e^2 \hbar^3 k^2 \rho(k) |\epsilon_1 \epsilon_2 c_1 c_2|}{m_{||}^2 (E_k + E_1)(E_k + E_2)} \end{aligned} \quad (11)$$

Here α_{12} is defined by $B_{1s,\mathbf{k}}B_{2p_o,\mathbf{k}}^* = |B_{1s,\mathbf{k}}B_{2p_o,\mathbf{k}}| \exp(i\alpha_{12})$ and $E_1 = |E_{1s}|$, $E_2 = |E_{2p_o}|$.

The evaluation of $P(\cos \theta)$ requires the Fourier components $B_{\mathbf{n},\mathbf{k}}$. For the present choice of impurity states and z axis these components are obtained from Eq. (2) as

$$\begin{aligned} B_{1s,\mathbf{k}} &= 8\pi^{4/3} a^2 b V^{-1/2} / G^2 \\ B_{2p_o,\mathbf{k}} &= -i\sqrt{2}(32) a^2 b^2 \pi^{7/4} V^{-1/2} a^* k_z / G^3 \end{aligned} \quad (12)$$

with

$$G = G(\cos^2 \theta) = [1 + \gamma(a^* a k)^2 + (b^2 - a^2 \gamma)(a^* k)^2 \cos^2 \theta] \quad (13)$$

It is clear from Eq. (12) that $\alpha_{12} = \pi/2$.

Given the above expression, the net current flowing in the z -direction is given as

$$\begin{aligned} I_z^+ &= (e N V \hbar / m_{||}) \tau \times F \int_0^{2\pi} \int_0^\pi d\Omega P(\cos \theta) k \cos \theta \\ &= 256 (e N V \hbar^4 k^5 / m_{||}^3) \tau \times F a^4 b^3 \pi^{25/12} \frac{|\epsilon_1 \epsilon_2 c_1 c_2|}{(E_k + E_1)(E_k + E_2)} \\ &\quad \cos(\alpha_1 - \alpha_2 - \phi_1 + \phi_2 + \frac{\pi}{2}) \int_{-1}^{+1} dx \frac{x^4}{[G(x^2)]^5}, \end{aligned} \quad (14)$$

where τ is the free electron collisional relaxation time, N is the donor concentration in cm^{-3} , and F is the x-y cross-sectional area of the sample.

We note that contributions from the diagonal A_1 and A_2 terms are odd in $\cos \theta$ and have vanished, whereas the interference term induces a directional current flow! Thus coherent interference contributions result in a controlled directional current flow.

Several additional remarks are in order: First, the phases ϕ_1 and ϕ_2 of Eq. (7) contain the spatial phase factors $\exp[i\mathbf{k} \cdot \mathbf{R}]$, where \mathbf{k} is the light

wave vector. The difference in the spatial phases can be exactly offset by the phase difference $\alpha_1 - \alpha_2$ in the preparation step (e.g., in a Raman preparation of $|\psi\rangle$), or eliminated by phase matching. Second, there are substantial experimental simplifications associated with applying the photodissociating lasers at the same time as initiating the preparation of the superposition state. Third, two colour light also causes excitation (via ω_{2p_o}) of the $|1s\rangle$ level to the state at $[E_k + |E_{2p_o}| - |E_{1s}|]$ and of the $|2p_o\rangle$ level (via ω_{1s}) to the state at $[E_k + |E_{1s}| - |E_{po}|]$, i.e. the uncontrolled satellite contributions discussed above. In this case, however, these terms contribute to the A_1 and A_2 terms in Eq. (10) and hence do not contribute to degrade the controlled current I_z^+ .

The magnitude and sign of the current is controllable for a given host material and superposition state parameters via (a) the optical phase difference $\phi_1 - \phi_2$, (b) the donor number N , and/or (c) the ionizing field strengths ϵ_1 and ϵ_2 and their frequencies ω_1 and ω_2 . To estimate a typical current, consider the I_z resulting from the following parameters: $\epsilon_1 = \epsilon_2 = 0.1$ Volts/cm, $k = 5 \times 10^7 \text{ cm}^{-1}$, $|c_1 c_2| = 0.25$, and $\tau = 10^{-14}$ to 10^{-13} sec. The latter corresponds to a mean free path ($\hbar k \tau / m$) of 100 to 1000 Angstroms, a typical value for the ballistic electrons at the cited k value. Further $N(Si)V = 10^{18} \text{ cm}^{-3} V$ where V is the effective interaction volume. For a sample of 0.1 micron \times 10 micron \times 10 micron, $V = 10^{-11} \text{ cm}^3$. Utilizing Eq. (14), and these parameter values, we obtain a current $I_z = 10$ to 100 mA. Thus, sizeable currents may be readily produced, due to the high quantum efficiency of the silicon photoionization.

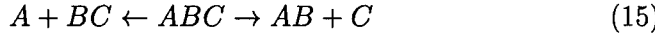
Equations (11)-(14) apply, evidently, to photoionization of other $|ns\rangle - |n'p_o\rangle$ superpositions, where $|n - n'| = 1$, upon substituting the appropriate Fourier coefficients $B_{ns,k}$ and $B_{n'p_o,k}$. It may turn out to be more practical to use other states than those discussed above.

1.2. N VS. M PHOTON ABSORPTION

The above procedure relies upon coherence established in a superposition state and interference generated by simultaneous irradiation with two sources. In the alternate scenario described below interference is established by excitation via two different operators, in particular operators inducing N-photon and M-photon absorption. Here we explicitly consider the case of M=3, N=1 (Shapiro, Hepburn & Brumer, 1988) and describe it in terms of molecular excitation, but the generality of the approach, to e.g. the semiconductor case should be clear. Indeed, this approach was subsequently applied experimentally, for the case of M=2, N=1 to the control of photocurrents in semiconductors (Dupont *et al.* 1995; Hache *et al.* 1997).

Consider a molecule which, when excited to total energy E , dissoci-

ates to a number of distinct products. The total Hamiltonian is denoted $H = H_q^0 + V_q$, where H_q^0 is the Hamiltonian of the separated products in the arrangement channel labeled by q , ($q = 1, 2, \dots$) and V_q is the interaction between products in arrangement q . For example, $q = 1, 2$ may be the A+BC and AB+C products, respectively, of the photon induced dissociation of a molecule denoted ABC:



We denote eigenvalues of H_0^q by $|E, n, q^0\rangle$, where n denotes the scattering angles and all quantum numbers other than E . Eigenfunctions of H , which correlate with $|E, n, q^0\rangle$ at large product separation, are labeled $|E, n, q^-\rangle$. By the definition (see, e.g. Taylor 1972) of $|E, n, q^-\rangle$, a state prepared experimentally as a superposition $|\Psi(t=0)\rangle = \sum_{n,q} c_{n,q} |E, n, q^-\rangle$ has probability $|c_{n,q}|^2$ of forming product in channel q , with quantum numbers n . As a consequence, the probability of forming a product in any asymptotic state is equal to the probability of initially forming the appropriate minus state which correlates with the desired product. The essence of control lies, therefore, in forming the desired linear combination at the time of preparation. The essence of the coherent control is to utilize phase and intensity properties of laser excitation to alter the character of the prepared state so as to enhance production of the desired product.

As a specific example of coherent control, consider unimolecular photoexcitation (Shapiro, Hepburn & Brumer 1988; Chan, Brumer & Shapiro 1991) where a system, initially in pure state $|E_i\rangle$, is excited to energy E , by simultaneous application of a CW field and its third harmonic:

$$\epsilon(t) = \epsilon_3 \hat{\epsilon}_3 \cos[(\omega_3 + \theta_3)t] + \epsilon_1 \hat{\epsilon}_1 \cos[(\omega_1 + \theta_1)t], \quad (16)$$

($\omega_3 = 3\omega_1$), providing two independent optically driven routes from $|E_i\rangle$ to $|E, n, q^-\rangle$. Here $\hat{\epsilon}_i$ ($i = 1, 3$) denotes a unit vector in the i^{th} field direction.

Straightforward perturbation theory, valid for the weak fields under consideration, gives the probability $P(E, q; E_i)$ of forming product at energy E in arrangement q as:

$$P(E, q; E_i) = P_3(E, q; E_i) + P_1(E, q; E_i) + P_{13}(E, q; E_i). \quad (17)$$

Here $P_3(E, q; E_i)$ is the probability arising from the one photon route,

$$P_3(E, q; E_i) = \left(\frac{\pi}{\hbar}\right)^2 \epsilon_3^2 \sum_n |\langle E, n, q^- | (\hat{\epsilon}_3 \cdot \mu)_{e,g} | E_i \rangle|^2. \quad (18)$$

where μ is the electric dipole operator, and $(\hat{\epsilon}_3 \cdot \mu)_{e,g} = \langle e | \hat{\epsilon}_3 \cdot \mu | g \rangle$ where $|g\rangle$ and $|e\rangle$ are the ground and excited electronic state wavefunctions, respectively. The second term is the photodissociation contribution

from the three photon route given by:

$$P_1(E, q; E_i) = \left(\frac{\pi}{\hbar}\right)^2 \epsilon_1^6 \sum_n |\langle E, n, q^- | T | E_i \rangle|^2, \quad (19)$$

with

$$T = (\hat{\epsilon}_1 \cdot \mu)_{e,g} (E_i - H_g + 2\hbar\omega_1)^{-1} (\hat{\epsilon}_1 \cdot \mu)_{g,e} (E_i - H_e + \hbar\omega_1)^{-1} (\hat{\epsilon}_1 \cdot \mu)_{e,g}. \quad (20)$$

The final and most significant term $P_{13}(E, q; E_i)$ arises from one photon-three photon interference:

$$P_{13}(E, q; E_i) = -2(\pi/\hbar)^2 \epsilon_3 \epsilon_1^3 \cos(\theta_3 - 3\theta_1 + \delta_{13}^{(q)}) |F_{13}^{(q)}| \quad (21)$$

with the amplitude $|F_{13}^{(q)}|$ and phase $\delta_{13}^{(q)}$ defined by

$$|F_{13}^{(q)}| \exp(i\delta_{13}^{(q)}) = \sum_n \langle E_i | T | E, n, q^- \rangle \langle E, n, q^- | (\hat{\epsilon}_3 \cdot \mu)_{e,g} | E_i \rangle. \quad (22)$$

The branching ratio $R_{qq'}$ for channels q and q' , can then be written as

$$R_{qq'} = \frac{P(E, q; E_i)}{P(E, q'; E_i)} = \frac{F_3^{(q)} - 2x \cos(\theta_3 - 3\theta_1 + \delta_{13}^{(q)}) \epsilon_0^2 |F_{13}^{(q)}| + x^2 \epsilon_0^4 F_1^{(q)}}{F_3^{(q')} - 2x \cos(\theta_3 - 3\theta_1 + \delta_{13}^{(q')}) \epsilon_0^2 |F_{13}^{(q')}| + x^2 \epsilon_0^4 F_1^{(q')}}. \quad (23)$$

where

$$\begin{aligned} F_3^{(q)} &= (\hbar/\pi)^2 \frac{P_3(E, q; E_i)}{\epsilon_3^2}, \\ F_1^{(q)} &= (\hbar/\pi)^2 \frac{P_1(E, q; E_i)}{\epsilon_1^6}, \end{aligned} \quad (24)$$

with $F_3^{(q')}$ and $F_1^{(q')}$ defined similarly. Here $x = \bar{\epsilon}_1^3/\bar{\epsilon}_3$ with $\epsilon_l = \bar{\epsilon}_l \epsilon_0$; the quantity ϵ_0 essentially carries the unit for the electric field.

The numerator and denominator of Eq.(23) each display what we regard as the canonical form for coherent control: independent contributions from more than one route which are modulated by an interference term. Since the interference term is controllable through variation of laboratory parameters (here the relative intensity and relative phase of the two lasers), so too is the product ratio $R_{qq'}$.

This 1-photon vs. 3-photon scenario has been investigated both computationally (Chan, Brumer & Shapiro 1991) and experimentally (Chen, Yin & Elliott 1990; Chen & Elliott 1990; Park, Lu & Gordon 1991; Zhu *et al.* 1995). Both show that extensive control over product probabilities is possible.

In most cases, n above denotes a set of quantum numbers, e.g. rotational, vibrational, electronic as well as scattering angles of the dissociation product. By summing only over a subset of the set n one can control the probability of forming product in states defined by the remaining quantum numbers. For example, if the sum over n excludes the scattering angle then one can control the probability of scattering into a particular angle (Asaro, Brumer & Shapiro 1988) which, for example, allows for control over photocurrent directionality.

One further note is of interest in the context of this workshop. In the studies above, N-photon and M-photon excitation both lead to the same energy. This is done to ensure that the interference term is time independent so that it does not average to zero over a given time interval. However, it is worth noting that allowing excitation to two different energies E and E' , will result in an interference term that oscillates with frequency $\Omega = (E - E')/\hbar$. In the case of electron excitation, simultaneous excitation to $E \neq E'$ may well lead to a useful source of tunable radiation, e.g. in the Terahertz domain. That is, by varying either of the frequencies inducing the M or N photon absorption one can control Ω , and hence the frequency of the emitted radiation.

1.3. OTHER SCENARIOS

Once one appreciates the essence of coherent control, i.e. the simultaneous coherent excitation of the system by multiple routes, numerous scenarios can be devised (Shapiro & Brumer 1997), many of which have been computationally shown to provide highly successful control schemes. For example, quantum interference may be introduced and manipulated through the use of laser pulse sequences. In the simplest such scenario (Seideman, Shapiro & Brumer 1989) an initial transform limited laser pulse excites a superposition of bound molecular Hamiltonian eigenstates and a subsequent transform-limited pulse carries this superposition to the continuum. By varying the characteristics of the pulses, and the time delay between them, one introduces and alters the quantum interference between routes to the continuum. High quality computations on the two-photon dissociation of IBr (Levy *et al.* 1990) and Li₂ (Abrashkevich *et al.* 1998) show that extensive control over the ratio of photodissociation products is possible.

Controlling molecular dynamics by altering the shape and detailed characteristics of laser pulses and laser pulse sequences was pioneered by Tannor and Rice (1986) and subsequently cast as an optimal control problem by Rabitz and coworkers (Shi, Woody & Rabitz 1988). There is sufficient representation at this workshop of this pulsed laser approach to warrant our limiting our remarks to three general observations. They are: (a) in each

of these approaches the essential effect of varying the characteristics of the laser pulses is to control and alter the quantum interferences introduced optically into the molecule whose dynamics we wish to control. The tendency to utilize short pulses implies, however, a large frequency bandwidth and hence the participation of many molecular energy levels; (b) our experience continues to be that CW excitation, or very simple pulse shapes, suffice to give excellent control, at least over product distributions in chemical reactions. It is unclear to us under what circumstances complicated pulse shapes will be required; and (c) optimal control calculations tend to yield many different pulse shapes which all reach the desired goal. As a consequence it is very difficult to extract the physics of the problem from either the optimal control computation or the optimal control result (Paci, Shapiro & Brumer 1998).

Coherent control is a rapidly growing field and there have been numerous new scenarios proposed in the past five years which are worthy of note. We call attention here to two specific advances. First, we note the particularly exciting prospect (Chen, Shapiro & Brumer 1995) in which a bound state of a molecular system is excited to the continuum by a laser of frequency ω which is, in turn, coupled to another (initially empty) bound state by an intense laser of frequency ω' . Varying either ω or ω' can be shown to provide an effective means of controlling the ratio of photodissociation products. This approach, which we call Incoherent Interference Control, is conceptually related to Laser Induced Continuum Structure (Knight, Lauder & Dalton 1990), but the latter has only been used to control the total ionization cross sections in atoms. Clearly, the ability to use this scenario to differentiate between different dissociation products, and to control their relative probabilities, constitutes a huge increase in the utility of this approach. In addition, the method can be shown to be relatively insensitive to both molecular collisions and to the quality of the lasers used. Hence the approach is highly resistant to effects which would normally cause loss of coherence, and hence loss of quantum-interference based control.

Both experimental and theoretical studies of Incoherent Interference Control (Chen, Shapiro & Brumer 1995; Shnitman *et al.* 1996) show it to be a very effective means of controlling photodissociation dynamics. In particular, a recent study of the dissociation of Na_2 to produce different atomic products showed that one could significantly increase the production of $\text{Na}(3s) + \text{Na}(3p)$ while simultaneously reducing the production of $\text{Na}(3s) + \text{Na}(3d)$ by varying ω' over 3 cm^{-1} . Experiment and theory were found to be in excellent agreement. Most recently we have examined the possibility of improving control over cross sections in this scenario by varying pulse orderings, intensities and widths in a pulsed laser version of incoherent interference control. Our results showed that excellent control

over cross sections is possible for a wide range of laser pulse parameters (Shapiro, Chen & Brumer 1997). Further, complementary work on multi-level adiabatic passage techniques (Kobrak & Rice 1998) suggests a deeper qualitative picture of the origins of quantum interference in this incoherent interference control scenario.

Finally we note that most of the work in coherent control has focused on unimolecular processes, i.e., processes involving excitation of a single molecule, such as that in Eq. (1). However, the vast majority of chemical reactions of interest are bimolecular in nature, i.e., of the type:



In a recent series of papers (Shapiro & Brumer 1996; Holmes, Shapiro and Brumer 1996; Abrashkevich, Brumer and Shapiro 1998) we showed how coherent control could be extended to control such processes. In particular, what is required for coherent control of collision processes is that one prepares the desired initial superposition of *degenerate collisional* eigenstates. For example, if one prepares an initial state as a superposition of asymptotic states $|E, n, q^0\rangle$, e.g. as $\sum c_n |E, n, q^0\rangle$, then the overall scattering cross section will display traditional scattering contributions from each of the $|E, n, q^0\rangle$ states, plus additional interference terms dependent upon the amplitude and phases of the c_n . Thus, by controlling these coefficients, i.e. the constitution of the initial superposition state, one also gains control over the outcome of the scattering process.

In summary, numerous scenarios for achieving control have been studied both numerically as well as computationally for simple molecular processes. Of these, many would seem applicable to studies of control in device physics.

Acknowledgment: This work was supported by the US Office of Naval Research.

References

ABRASHKEVICH, A., SHAPIRO, M. & BRUMER, P., 1998 manuscript in preparation.
 ABRASHKEVICH, D. G., SHAPIRO, M. & BRUMER, P. 1998 *J. Chem. Phys.* **108** 3585.
 ASARO, C., BRUMER, P. & SHAPIRO, M. *Phys. Rev. Lett.* 1988 **60** 1634
 BALDERESCHI, A. & DIAZ, M.G., *Nuov. Cim.* 1970 **68B**, 217. (1970).
 BRUMER, P. & SHAPIRO, M. 1995 *Scientific American* **272**, 56.
 CHAN, C. K., BRUMER, P. & SHAPIRO, M., 1991 *J. Chem. Phys.* **94** 2688.
 CHEN C. & ELLIOTT D. S. 1990 *Phys. Rev. Lett.* **65** 1737.
 CHEN, C., YIN, Y.-Y. & ELLIOTT, D. S. 1990 *Phys. Rev. Lett.* **64** 507.
 CHEN, Z., SHAPIRO, M. & BRUMER, P. 1995 *Phys. Rev. A* **52** 2225.
 DUPONT E., CORKUM, P.B., LIU, H.C., BUCHANEN M. & WASILEWSKI, Z.R. 1995 *Phys. Rev. Lett.* **74**, 3596
 FAULKNER, R.A. *Phys. Rev.* 1969 **184**, 713.
 GORDON, R. J. & RICE, S. A. 1997 *Ann. Rev. Phys. Chem.* **48** 601.

HACHE, A., KOSTOULOS, Y., ATANASOV, R., HUGHES, J.L.P., SIPE, J.E. & VAN DRIEL 1997 *Phys. Rev. Lett.* **78** 306.

HOLMES, D., SHAPIRO, M. & BRUMER, P. 1996 *J. Chem. Phys.* **105** 9162;

HUANG, K. & RHYS, A., Proc. Roy. Soc. 1950 A**204**, 406. 3435

JIANG, X.-P., BRUMER, P. & SHAPIRO, M. 1996 *J. Chem. Phys.* **104** 607.

KASAMI, A., J. Phys. Soc. Japan 1968 **24**, 551.

KNIGHT, P. L., LAUDER, M. A. & DALTON, B. J. 1990 *Phys. Rep.* **190** 1.

KOBRAK, M. & RICE, S. A. 1998, in press.

KOHN, W. & LUTTINGER, J.M., Phys. Rev. 1955 **98**, 915.

KURIZKI, G., SHAPIRO, M. & BRUMER, P. 1989 *Phys. Rev. B* **39** 3435.

LEVY, I., SHAPIRO, M. & BRUMER, P. 1990 *J. Chem. Phys.* **93** 2493.

PACI, J., SHAPIRO, M. AND BRUMER, P. 1998 *J. Chem. Phys.* (submitted)

PANTELIDES, S.T. *Rev. Mod. Phys.* 1978 **50**, 797.

PARK, S. M., LU, S.-P. & GORDON, R. J. 1991 *J. Chem. Phys.* **94** 8622.

RIDLEY, B.K., J. Phys. 1980C**13**, 2015.

SCULLY, M. O. & ZUBAIRY, M. S. 1997 *Quantum Optics* (Cambridge Univ. Press, Cambridge), Chap. 7 provides a recent review.

SEEGER K., *Semiconductor Physics* (Springer Verlag, Berlin, 1973).

SEIDEMAN, T., SHAPIRO, M. & BRUMER, P. 1989 *J. Chem. Phys.* **90** 7132.

SHAPIRO, M. & BRUMER, P. 1989 *J. Chem. Phys.* **90** 6179.

SHAPIRO, M. & BRUMER, P. 1996 *Phys. Rev. Lett.* **77** 2574;

SHAPIRO, M. & BRUMER, P. 1997 *Trans. Farad. Soc.* **82** 177

SHAPIRO, M., HEPBURN, J. & BRUMER, P. 1988 *Chem. Phys. Lett.* **149** 451.

SHAPIRO, M., CHEN, Z. & BRUMER, P. 1997 *Chem. Phys.* **217** 325

SHI, S., WOODY, A. & RABITZ, H. 1988 *J. Chem. Phys.* **88** 6870.

SHNITMAN, A., SOFER, I., GOLUB, I., YOGEV, A., SHAPIRO, M., CHEN, Z. & BRUMER, P. 1996 *Phys. Rev. Lett.* **76** 2886.

TANNOR, D. J. & RICE, S. A. 1985 *J. Chem. Phys.* **83** 5013.

TAYLOR, J. R. 1972 *Scattering Theory*, (Wiley, New York)

ZHU, L., KLEIMAN, V., LI, X., LU, S.-P., TRENTELMAN, K. & GORDON, R., J. 1995 *Science* **270** 77.

QUANTUM CONTROL IN ATOMIC SYSTEMS

D. CHARALAMBIDIS[‡], N. E. KARAPANAGIOTI^{*}, D. XENAKIS,
E. PAPASTATHOPOULOS[‡] AND C. FOTAKIS[‡]

*Foundation for Research and Technology–Hellas, Institute of Electronic
Structure and Laser, PO Box 1527, GR-711 10 Heraklion, Greece.*

[‡]*Also: Physics Department, University of Crete,
GR-713 10 Heraklion, Greece.*

^{*}*Present Address: Max-Planck-Institut für Quantenoptik,
Hans-Kopfermannstr. 1, D-857 48 Garching, Germany*

O. FAUCHER AND E. HERTZ

*Laboratoire de Physique, Université de Bourgogne, Faculté des Sciences
Mirande, BP 138, FR-21004 Dijon, France.*

S. CAVALIERI, R. ERAMO, L. FINI AND M. MATERAZZI

*Dipartimento di Fisica and European Laboratory for Non-Linear
Spectroscopy (LENS), Università di Firenze, Largo E. Fermi 2,
I-50125 Firenze, Italy*

Abstract. We review a series of recent experiments demonstrating quantum control of atomic processes and products induced by the interaction of the atom with coherent bichromatic electromagnetic fields. Since the effects under consideration are electromagnetically induced, control is established through the field parameters i.e. frequency, amplitude and phase. The controlled processes include resonant and non resonant multiphoton ionization, autoionization, radiative decay in multiple continua (ionization branching ratios) and third harmonic generation.

1. Introduction

Excitations of atoms via multiple indistinguishable pathways may occur during the interaction of an atom with more than one laser field. The existence of multiple coherent excitation channels results into intra-atomic quantum interferences that govern excitation probabilities and populations. This follows from the nature of the time dependent Schrödinger equation that describes the temporal evolution of the interacting system, it being an amplitude equation. In a classical picture, constructive or destructive interferences can be viewed as the result of the addition of different dipole moments of the atomic system as induced by the different field combinations involved in the excitation scheme. In the simplest case of two interfering excitation channels the two dipole moments may have any amplitude and phase relation and thus result into any

degree of constructive or destructive interference. In some cases it proves more convenient to adopt an alternative equivalent quantum mechanical picture to that of interfering amplitudes. In this picture one of the electromagnetic fields ‘dresses’ the atom while the second field is used to probe the dressed system which now exhibits different structure and excitation dynamics than the bare atom does.

Excitation schemes underlying this type of quantum interferences posses properties that depend on, and thus may be controlled by, the interference parameters. Some of the latter may be controlled in the laboratory by the field parameters, such as wavelength, polarization, intensity and phase. Turning these ‘knobs’ in the control room of the laboratory one can modify excitation and decay rates but also quantities that are considered traditionally to be determined only by the atomic parameters, such as autoionization profiles and ionization branching ratios.

In the present work we review selected examples of recent experimental results in coherent quantum control of processes and products of laser atom interactions. These include control of ionization and autoionization rates and profiles, light induced continuum structure, ionization branching ratios and frequency up-conversion. Although all schemes investigated are based on quantum interference and thus control is based on a coherent process, not all of them are phase-dependent as in some the phase is eliminated e.g. through successive absorption and emission of a photon of the same field (Raman type processes). For these reason we will classify the experiments into two categories: Phase insensitive and phase sensitive.

2. Phase insensitive quantum coherent control through laser induced continuum structure

The phase insensitive coherent control examples presented in this section are based on what has been now established as laser induced continuum structure (LICS). The basic scheme of LICS consists of two discrete states $|1\rangle$ and $|2\rangle$ (of which only $|1\rangle$ is initially populated) that are coupled via two electromagnetic fields ω_1, ω_2 to a continuum state $|c\rangle$ (Fig. 1a). ω_2 , which will be referred to as the coupling laser, is usually strong in order to induce the continuum structure (embedding one of the discrete states in the continuum), while ω_1 can be a weak probe of the induced structure. The overall coupling schemes leads to quantum mechanical interference of different ionization channels which is commonly probed through ionization or polarization rotation as a function of one of the laser wavelengths. Whenever the coupling of state $|1\rangle$ with the continuum involves more than one photons the effect can be also probed through the non-linear scattering of this field. There are several equivalent ways through which LICS can be described:

On the one hand, it can be described as an interference of different excitation channels of the continuum of the bare atom (Fig. 1a). The two fields also couple the two discrete states to each other through two-photon Raman processes, thus opening different pathways to the continuum. State $|1\rangle$ can ionize directly absorbing one photon of frequency ω_1 , or via the state $|2\rangle$ due to the two Raman couplings. The process involves two discrete states coupled to each other and to the same continuum satisfying the energy balance condition $E_{|1\rangle} + \hbar\omega_1 = E_{|2\rangle} + \hbar\omega_2$ and as such is closely related to an autoionization process, even if different types of couplings underlie the two processes.

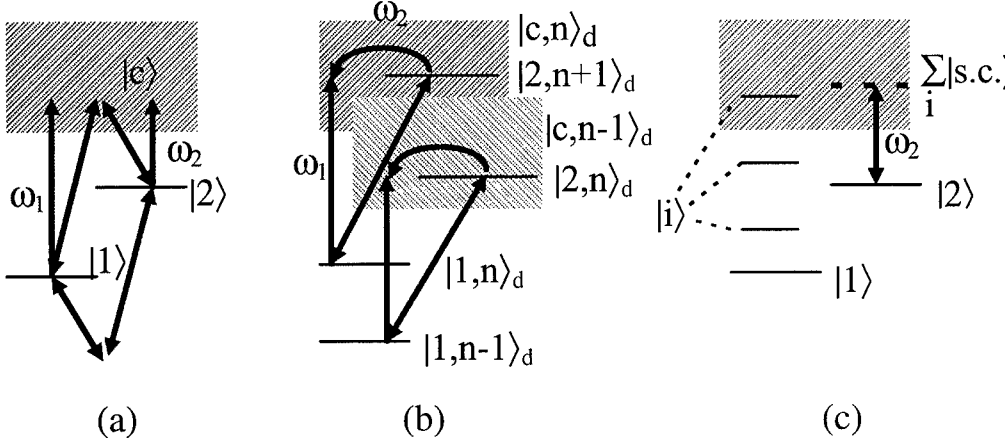


Figure 1. Three equivalent representations of LICS.

The full analogy between LICS and autoionization has been shown by Dai et al. (1). Consequently the interference process manifests itself as an asymmetric autoionizing-like resonance, the shape of which is determined, under low intensity and single rate approximation conditions by a q parameter equivalent to the Fano parameter in autoionization:

$$q = \frac{\text{Re } \Omega_{12}}{\text{Im } \Omega_{12}} = \frac{M_{12}}{\mu_{1c} \mu_{2c}}, M_{12} = \sum_l \frac{\mu_{1l} \mu_{l2}}{-\omega_2 + \omega_{1l}} d\omega_c + P \sum_l \frac{\mu_{1l} \mu_{l2}}{\omega_2 + \omega_{2l}} d\omega_c \quad (1)$$

where M_{12} is the two-photon transition moment between states $|1\rangle$ and $|2\rangle$, μ_{1c} , μ_{2c} are the bound-free transition moments, Ω_{12} is the two-photon Rabi frequency and \sum_l implies summation over the discrete and integration over the continuum part of the spectrum.

Due to incoherent channels involved, such as ionization of the system from state $|1\rangle$ via multiphoton absorption of the field ω_2 or ionization of state $|2\rangle$ via ω_1 , a practically constant ionization background will contribute to the ionization spectrum. Thus the ionization probability per unit time will be:

$$\frac{\partial P_{\text{ion}}}{\partial t} \sim [1 + kf(q, \delta)] \quad (2)$$

where P_{ion} is the ionization probability, k is a laser intensity dependent contrast parameter involving the widths of states $|1\rangle$, $|2\rangle$ and the laser bandwidths and δ is essentially the detuning $(E_1 + \hbar\omega_1) - (E_2 + \hbar\omega_2)$. If LICS is probed through ionization the degree of the asymmetry is given by the q parameter and the observability of the structure depends on the contrast parameter k . At higher laser intensities and conditions in which the single rate approximation breaks down, the shape of the LICS resonance depends on the laser intensity.

An equivalent way of describing the same effect is utilizing the dressed atom picture (Fig 1b). The strong field ω_2 dresses the system. The atom plus field, after introduction of the interaction with the field, exhibits a ladder of new eigenstates $|i, n\pm m\rangle_d$, n being the number of photons of the field ω_2 and m and integer. The $|2, n\pm m+1\rangle_d$ discrete states are now embedded in the $|c, n\pm m\rangle_d$ continua in which they can decay radiatively. ω_1 couples the $|1, n\pm m\rangle_d$ states with the $|2, n\pm m+1\rangle_d$ discrete and $|c, n\pm m\rangle_d$ continuum state, thus resulting in an autoionization like process.

Adopting a.c. Stark splitting terminology (Fig. 1c), it is worth noting that the dressed atom-photon states that are embedded in the continuum can be understood as the sum of the ac Stark split components $|s.c.\rangle$ resulting from the coupling of state $|2\rangle$ with all allowed states $|i\rangle$ of the system. This picture may be more convenient in describing LICS in structured continua, e.g. in the vicinity of autoionizing states. In the particular case in which one of these states is near resonant, its split component dominates and the sum may reduce to one term. If the detuning is less than the width of the states involved, the a.c. Stark splitting of the dressed autoionizing state may give rise to a window resonance in the spectrum due to the destructive interference of the two Autler-Townes components. In other words, the coherent superposition of the two states prepared by the coupling laser produces a dipole moment that has the same amplitude and is out of phase with the dipole moment induced by the probing laser.

Considering field phase sensitivity, LICS is immune to the relative phases of the two electromagnetic fields. The process involves absorption and emission of the frequency ω_2 the phase of the corresponding wave vanishes in the interaction.

The first observation of LICS in the smooth (unstructured) continuum of the Na atom was reported some years ago (2). The rate of ionization was controlled through the detuning δ , resulting into an asymmetric ionization structure that manifested the destructive and constructive interference at different detunings. In these early experiments laser intensity effects have also been studied. The interaction of the atom with the strong coherent electromagnetic field results into shifting of the energy levels of the atom. This a.c. Stark shifting may introduce an extra asymmetry in the profile of a spectral feature obtained as we tune the frequency of one field. Thus the overall measured profile of LICS will be the convolution of line shape resulting from the interference effect and the level shifting. The earlier experiments have been verified in an advanced version employing energy resolved photoelectron spectroscopy, and thus reducing background contributions from incoherent channels leading to different positions in the continuum, that has shown a clean asymmetric Fano type resonance (3).

Numerous experiments followed these first successful observations. LICS in three-photon excited structured continua has resulted into several interesting observations in atomic Ca. In these schemes LICS is in the vicinity of an autoionizing state (AIS). The virtual state of the Raman process that goes through the continuum is now lying near or is replaced by a third discrete state $|3\rangle$, the AIS. This third state adds oscillator strength, thus playing a dominating role and controlling the modification characteristics. Experiments have been performed in a Ca effusive beam as well as in Ca vapor in a heat pipe in a three-photon ionization scheme (4,5). The induced structure in the measured ionization rates can then be controlled through the detuning from the AIS resonance and the laser intensity. Since these two parameters lead to the same effect on the shape of the observed resonance, the intensity dependence of the measured profiles

has been interpreted to be due to the a.c. Stark shifting of the states and thus, effectively, to detuning. Furthermore the laser polarization proved to be a useful control 'knob' for switching 'on' and 'off' induced structures, as well as for turning them from peaks to dips and vice versa (5). The three-photon excitation of the continuum (or AIS) allowed the study of the effect also in third harmonic generation (THG) (6). THG could be controlled through the detuning and the dressing laser intensity. Enhancement or suppression of the harmonic by a factor of up to three could be observed. These experiments have also established the relation of LICS with a.c. Stark splitting (7), which due to the dominance of the near resonant AIS provided a convenient way for the interpretation of the results.

Very closely related to the experiments employing Λ -type coupling schemes of LICS are investigations on the resonant mixing of two Mg AIS ($3p^2 \ ^1S$ and $3p3d \ ^1P$) probed by a second electromagnetic field from the ground state of the atom. This excitation scheme is shown in figure 2(a). The experiments have been performed in a Mg effusive beam and have shown strong suppression of autoionization (see figure 2(b)) due to coherent population trapping in the ground state (8). Slight detuning of the resonant coupling of the two autoionizing states lead to the observation of asymmetric ionization profiles showing constructive and destructive interference features. In the spectra of the first column of figure 2(b), the probing wavelength is tuned, while in those of the second column ionization is shown as a function of the wavelength of the coupling laser.

When detuned far from resonant coupling, an induced structure in the continuum

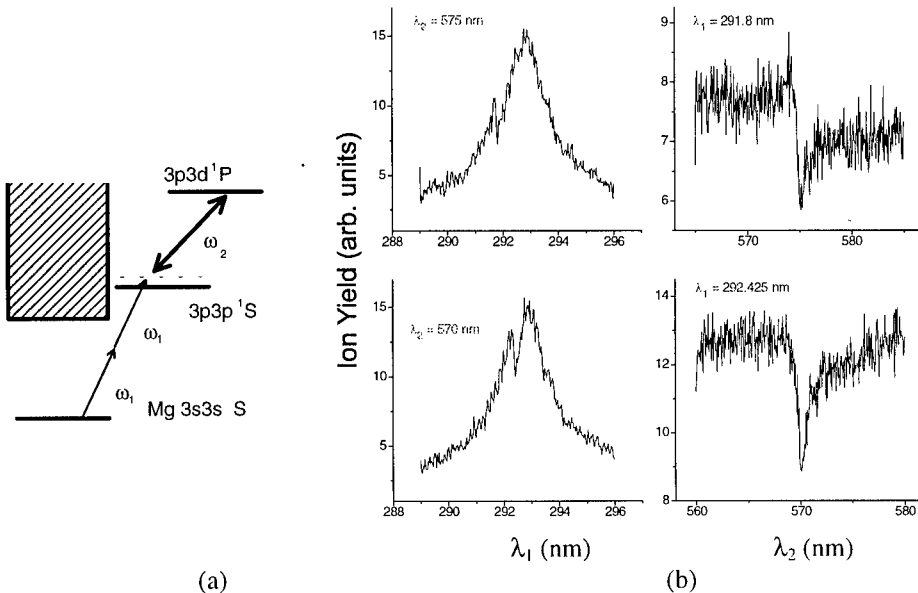


Figure 2. Mixing of two autoionizing states in Mg.
(a) The coupling scheme. (b) Coherent suppression and enhancement of autoionization.

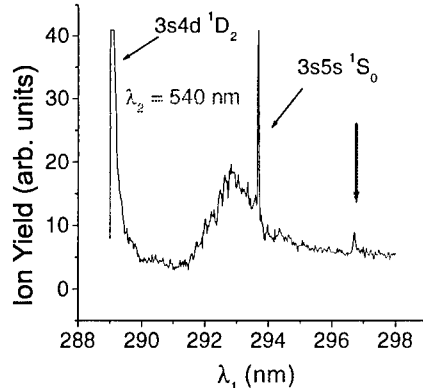


Figure 3. 'Above threshold' LICS. The structure shown with the vertical arrow is due to the 're-embedding' of the $3p3d\ ^1P$ AIS of Mg at a position in the continuum lower by the photon energy of the coupling laser. The other narrow structures are due to accidental one- or two-photon resonances.

has been observed and interpreted as being due to the 're-embedding' of the $3p3d\ ^1P$ AIS of Mg at a position in the continuum lower by the photon energy of the coupling laser (see fig. 3). High resolution photoelectron spectra have verified (9) that the observed structure in the total ionization spectrum is due to an 'above threshold' LICS and not to the autoionization decay of the resonant $3p3d\ ^1P$ state. This result has been further verified by theoretical calculations by Bachau et al. (10). In their work they have also demonstrated stabilization of ionization in the case of the resonant coupling due to the coherent population trapping. (9).

When the decay of the atomic system is in more than one continua, structure can be induced in all by dressing them with a strong laser field, the latter establishing a coupling between the continua and an atomic bound state. For the different continua there are different interfering channels causing ionization and thus LICS can be observed separately for each continuum by employing energy resolved photoelectron spectroscopy. Since the coupling of the ground and the excited bound state to each one of the continua is in general different, the LICS profiles are expected not to be the same for each continuum. Thus the ratio of the ionization products, namely electrons resulting from the decay into the different continua is expected to be modified through the LICS process and variable in the vicinity of the induced structure.

Recently (11) we have demonstrated control of ionization product ratios in atomic Xe. Ionization of the Xe ground state is in the two electronic continua, that correspond to the two fine structure levels of the ground state of the Xe^+ ion. Both continua are dressed through a second laser that couples the $5p^510p[1/2]_0$ state with each of them (see figure 4a). The dressed $^2P_{1/2}$ continuum, probed from the atomic ground state through three-photon absorption, exhibit a clear induced structure (window resonance), while the $^2P_{3/2}$ continuum possess no observable structure under the present experimental conditions, as manifested through high resolution photoelectron spectra. The normalized photoelectron yields for the decay into the two continua versus detuning $\Delta = E_{5p^6} + 3\hbar\omega_p - E_{5p^510p} - \hbar\omega_d$ are shown in figure 4(b) where E_{5p^6} is the ground

state energy and E_{5p^510p} is the energy of the $5p^510p[1/2]_0$ state. Hence the modified ionization ratio is controlled by the wavelength of the dressing field. In a similar coupling scheme control of the photofragmentation product ratio has been also demonstrated by LICS in dissociative continua (12). It should be noted that control of ionization branching ratios has been achieved in atomic Ba through a specific case of interference of two (one plus one) photon ionization channels, each of them being near resonant with two different excited states of the system. (13)

3. Phase sensitive quantum control

Interaction of an atomic system with a laser field and one of its harmonics may lead to the excitation of a bound or continuum state via two different channels with different degree of non-linearity, one of which involves a harmonic photon. Since the two fields are coherent with correlated phases, the excitation rate will be proportional to the square of the modulus of the sum of the two excitation amplitudes. The interference cross term and thus the excitation rate will modulate with the relative phase of the two fields.

We have recently demonstrated (14) control of the ionization rate in a four-photon resonant (with the $5p[5/2]_2$ state) five photon ionization of Kr. The $5p[5/2]_2$ state is excited via (i) four-photon absorption of the fundamental laser frequency ($4\omega_l + \omega_i$ ionization) and (ii) one third harmonic and one fundamental frequency photon absorption ($\omega_3 + \omega_l + \omega_i$ ionization), a particular aspect of the scheme being that interference occurs at a virtual level.

The excitation probability of the $5p[5/2]_2$ state is:

$$W \propto [\mu^{(4)} E_{10}^4]^2 + [\mu^{(2)} E_{10} E_{30}]^2 + 2\mu^{(4)} \mu^{(2)} E_{10}^5 E_{30} \cos(\vartheta_3 - 3\vartheta_l) \quad (3)$$

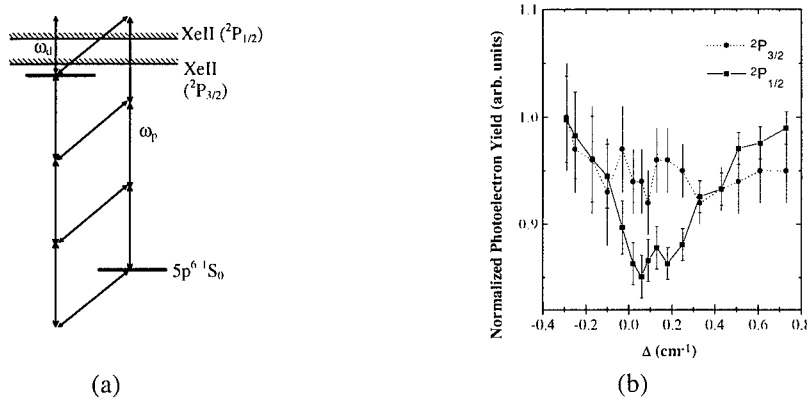


Figure 4. Control of ionization branching. (a) The coupling scheme, (b) normalized photoelectron yields versus detuning $\Delta = E_{5p^6} + 3\hbar\omega_p - E_{5p^510p} - \hbar\omega_l$

where $\mu^{(n)}$ is the effective n-photon (4 visible, and 1 visible + 1 VUV photon) electric dipole moment of the transition between the ground and the $5p[5/2]_2$ state, E_{10} electric field amplitude of the fundamental ($l=1$) and the third harmonic ($l=3$) and $\Delta\vartheta = \vartheta_3 - 3\vartheta_1$ where ϑ_1, ϑ_3 the phase of the fundamental and third harmonic waves. The excitation probability oscillates, as in the case of three-photon excitation, as $\cos(\Delta\vartheta)$. This is expected since the interference in the present scheme occurs at the three-photon level i.e. in the excitation of a virtual state and the absorption of the fourth fundamental photon does not affect the interference process as it adds the same phase and hence no phase difference in the two interfering channels and correspondingly for the harmonic.

By varying the relative phase of the two electromagnetic fields in a gas phase shifter a large modulation has been observed which is due to the chosen non-linear excitation scheme. The modulation depth, defined as $\frac{I_{\max} - I_{\min}}{1/2(I_{\max} + I_{\min})}$, where I_{\max} is

the maximum and I_{\min} the minimum ion signal of the modulation, has a maximum value close to 1.0 in the present experiment.

Non-resonant phase control of ionization has also been demonstrated from an excited Na state (16). In this experiment the interference process occurred between two bound-free atomic transitions with the initial state being the $3P_{1/2}$ excited state of Na and the final state in the continuum. The two bound-free transitions were three- and one-photon transitions employing the fundamental and the third harmonic of a Nd:YAG laser. The excited state was prepared through resonant absorption from the ground state. The observed modulation depth as defined above was 0.84.

In a similar scheme, phase control of harmonic generation has been demonstrated (15). The control of third harmonic generation in a Xe static cell (the ionization cell of the conventional phase control experimental set-up) was achieved through the presence of an additional, phase-correlated, third harmonic field created by the fundamental in the harmonic generation cell of the conventional phase control experimental set-up. The modulation of the third harmonic signal as a function of the pressure of the phase shifting cell was found to be in phase with the modulation of the ionization. The non-linear polarization $P_{3\omega}$ of the medium at 3ω in the second harmonic generating cell consists of three interfering terms

$$P_{3\omega} = \left[\left(\chi^{(3)}(\omega) \cdot E_{10}^3 + \chi^{(1)}(3\omega) \cdot E_{30} \right) e^{i3\vartheta_1} + \chi^{(1)}(3\omega) \cdot E_{30} e^{i\vartheta_3} \right] e^{i3\omega t} + c.c. \quad (4)$$

corresponding to the harmonic generation (non-linear scattering of the fundamental), while the two other terms are due to the scattering of the two third harmonic fields. All three terms are phase correlated and thus lead to a quantum interference in the third harmonic generation process.

Most of the phase sensitive control experiments in laser atom interactions involve photons of the fundamental frequency and its third harmonic. This is in most of the cases dictated by the selection rules of the excitation process resulting from angular momentum and parity conservation considerations, as a consequence of the spherical symmetry of the atomic potential. However, excitations involving absorption of an even

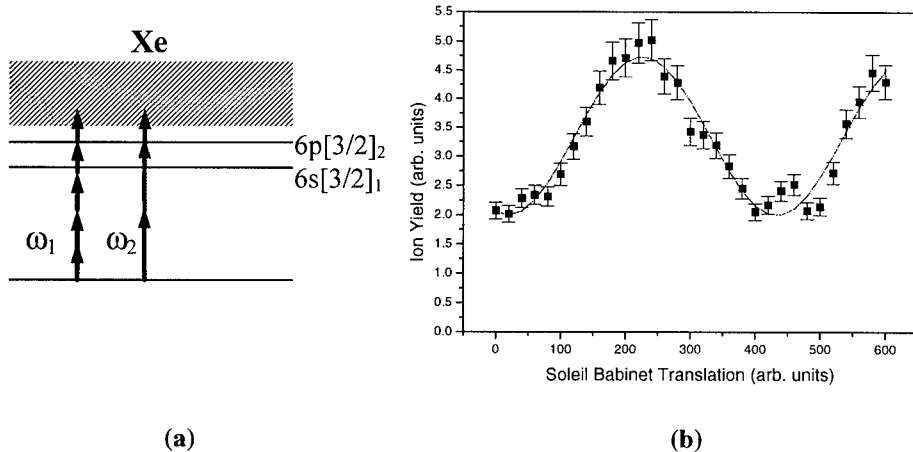


Figure 5. Phase control in Xe. (a) Excitation scheme. (b) Ionization measured as a function of the relative phase of the fields.

number of photons in all the interfering channels removes the requirement of using third harmonic generation. The excited state can be reached via two photons of the *second harmonic* of the laser beam, which is much more intense than the third harmonic, is in the UV region and hence more convenient to handle with.

For example, in the excitation of the $5p[5/2]_2$ state of Kr discussed above (14), the two excitation pathways could be four-photon (at the fundamental frequency) and two-photon (at the second harmonic frequency). The excitation probability of the bound state then becomes

$$W \propto [\mu^{(4)} E_{10}^4]^2 + [\mu^{(2)} E_{20}^2 + 2\mu^{(4)} \mu^{(2)} E_{10}^4 E_{20}^2 \cos[2(\vartheta_2 - 2\vartheta_1)] \quad (5)$$

where the indexes 1, 2 refer to the fundamental and the second harmonic field. Thus the probability depends on and is controlled through the phase difference $\Delta\vartheta = 2(\vartheta_2 - 2\vartheta_1)$.

Employing second instead of third harmonic has strong advantages with respect to the production process, the intensity, stability and visibility of the beam, as well as to the possibility of its propagation in several media and consequently the retardation of its phase relative to the phase of the fundamental. Experimental set-ups for this type of phase control experiments set less strict vacuum requirements and become simpler.

Recently we have performed an experiment in the ionization of Xe involving pathways including absorption of photons of the fundamental and the second harmonic.

The excitation scheme is shown in fig. 5(a). It is a four-photon resonant (with the $6p[3/2]_2$ state) 5-photon ionization of xenon. The $6p[3/2]_2$ state is excited via (i) four-photon absorption of the fundamental frequency and (ii) two-photon absorption of the second harmonic.

Figure 6 shows the experimental set-up. The second harmonic is produced in a type II BBO crystal. Its polarization is thus perpendicular to that of the fundamental. Both beams are propagated through a Soleil-Babinet retarder with its two propagation axes set parallel to the respective polarizations of the two fields. The retarder is thus used only in order to achieve variable phase relation in the two interfering excitation pathways and not in order to vary the ellipticity of the beams. A linear polarizer was used after the Soleil-Babinet retarder in order to select the appropriate field amplitudes in a common polarization plane, the polarization plane of the polarizer. Both beams were focused by means of an achromatic lens into the ionization cell, which was filled with the Xe gas and equipped with a charge collector. Similar results have been obtained in a Xe atomic beam.

The two excitation amplitudes can be made equal easily by rotating the polarizer so as to transmit the right polarization component of the two beams. Then, by tuning the relative phase of the two fields through the translational movement of one of the Soleil-Babinet wedges, strong modulation of the ionization signal could be observed as shown in the spectrum of figure 5(b).

The demonstrated interference at a virtual level is of importance for schemes that involve excitation of highly excited bound or continuum states, such as excitation of multiple continua aiming at the phase control of ionization branching ratios. Currently such an experiment is in progress in the above scheme by employing energy resolved photoelectron spectroscopy. It should be noted that phase control of molecular dissociation branching ratios has been achieved (17).

Recently we have been able to demonstrate field phase dependent autoionization in atomic Ca. Excitation is in the region of the $4p7s[\frac{1}{2}]^0$, doubly excited state autoionizing state and occurs from the atomic ground state through a three-photon channel ($3\hbar\omega$) and a single photon channel ($\hbar\omega_3$), ω_3 being the third harmonic of ω (Fig. 7(a)).

Due to the given excitation cross sections of the scheme, the energies of the fundamental and third harmonic, as well as the atomic number density available, a non conventional (14, 18) phase control experimental set-up (shown in fig. 8) had to be used. This employed an unfocused beam ionization geometry (by the two diverging fields) and an ion counting technique for the data acquisition procedure. The autoionization rate

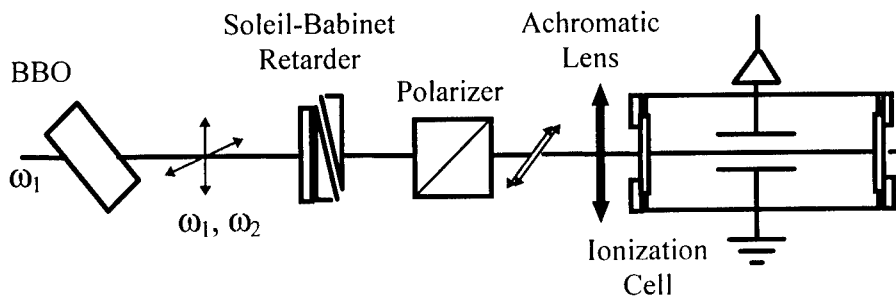


Figure 6. Experimental Set-up for schemes involving fundamental and second harmonic excitation channels

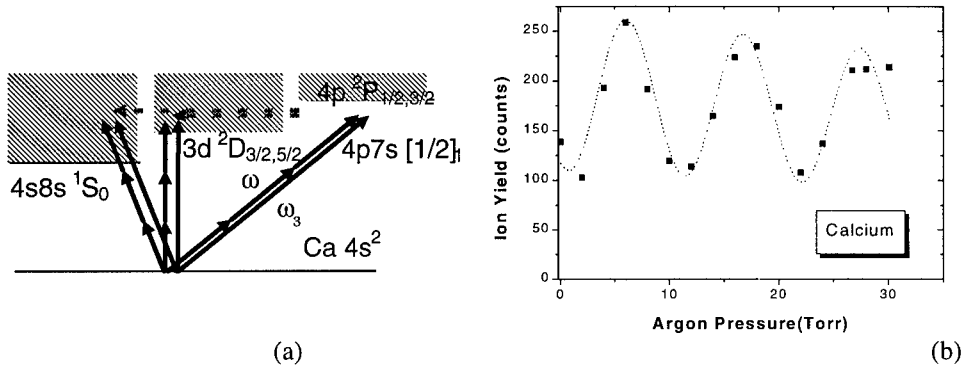


Figure 7. Phase control of autoionization rate. (a) Coupling scheme, (b) Ion yield vs relative phase

exhibits a sinusoidal modulation as a function of the relative phase of the two excitation fields, shown in figure 7(b).

This result is the initial step in the achievement of control of an autoionizing lineshape, which has been theoretically predicted (19) but has not been experimentally demonstrated so far. Furthermore, it demonstrates the feasibility of phase control in unfocused geometries with their corresponding advantages for applications of phase control in a large interaction volume and hence large number of species, e.g. for the control of chemical reactions.

4. Conclusions

Selected examples of recent experimental results in coherent quantum control of processes and products of laser atom interactions were reviewed. Control of ionization

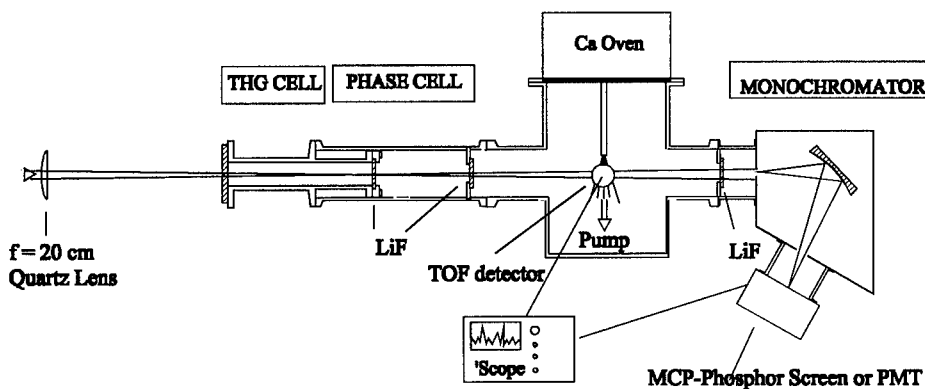


Figure 8. Experimental Set-up in the phase control experiment of autoionization in Ca

and autoionization rates, of light induced atomic structure, ionization branching ratios and frequency up-conversion were presented. Quantum interference of atomic transitions, induced by a bichromatic electromagnetic field, is underlying all the results of this work. Since the quantum interference is induced by the field, its parameters govern control of products and processes. Thus interaction dynamics and products may be controlled in the laboratory.

5. Acknowledgments

This work has been carried out in the Ultraviolet Laser Facility and the LENS facility. (TMR Program, contract number ERBFMECT950017).

6. References

1. Bo-nian Dai, and P. Lambropoulos, *Phys. Rev. A* **36**, 5205(1987)
2. Y.L. Shao, D. Charalambidis, C. Fotakis, J. Zhang, and P. Lambropoulos *Phys. Rev. Lett.* **67**, 3669 (1991); S. Cavalieri, F.S. Pavone, and C. Matera, *Phys. Rev. Lett.* **67**, 3673 (1991); S. Cavalieri, C. Matera, F.S. Pavone, J. Zhang, P. Lambropoulos, and T. Nakajima, *Phys. Rev. A* **47**, 4219 (1993)
3. S. Cavalieri, R., Eramo, and L. Fini, *J. Phys. B* **28**, 1793 (1995)
4. O.Faucher , D. Charalambidis, C. Fotakis, J. Zhang., and P. Lambropoulos, *Phys. Rev. Lett.* **70**, 3004 (1993)
5. O.Faucher, Y.L.Shao, D.Charalambidis, and C. Fotakis, *Phys. Rev. A* **50**, 641(1994)
6. O.Faucher, Y.L.Shao, and D. Charalambidis, *J. Phys. B* **26**, L309(1993)
7. Y.L. Shao, O. Faucher, J. Zhang and D. Charalambidis, *J. Phys. B* **28**, 755 (1995)
8. N.E.Karapanagioti, O.Faucher, Y.L.Shao, D.Charalambidis, H.Bachau, and E. Cormier, *Phys. Rev. Lett.* **74**, 2431 (1995)
9. N.E.Karapanagioti, D.Charalambidis, C.J.G.J.Uiterwaal, C.Fotakis, H.Bachau, I.Sánchez, and E.Cormier, *Phys. Rev. A* **53**, 2587 (1995)
10. H.Bachau, and I.Sánchez, *Z. Phys. D* **38**, 19 (1996)
11. S. Cavalieri, R. Eramo, L. Fini, M. Materazzi, O.Faucher and D. Charalambidis, *Phys. Rev. A* **57**, 2915 (1998)
12. A. Shnitman, I. Sofer, I. Golub, A. Yogeve M. Shapiro, Z. Chen, and P. Brumer, *Phys. Rev. Lett.* **76**, 2886 (1996)
13. Feng Wang, Ce Chen, and D.S. Elliott *Phys. Rev. Lett.* **77**, 2416 (1996)
14. N.E. Karapanagioti, D. Xenakis, D. Charalambidis and C. Fotakis *J. Phys. B* **29**, 3599 (1996)
15. D. Xenakis., N. E. Karapanagioti, C. Fotakis and D. Charalambidis, *Optics Commun.* **152**, 83 (1998)
16. S. Cavalieri, R. Eramo, L. Fini, *Phys. Rev. A* **55**, 2941 (1997)
17. Langchi Zhu, V. Kleiman, Xiaonong Li, Shao-Ping Lu, K. Trentelman, Yongjin Xie and R. J. Gordon, *Science* **270**, 77 (1995)
18. Chen Ce, Yi-Yian Yin and D. S. Elliott, *Phys. Rev. Lett.* **64**, 507 (1990); Chen Ce and D. S. Elliott, *Phys. Rev. Lett.* **65**, 1737 (1990)
19. T. Nakajima and P. Lambropoulos, *Phys. Rev. Lett.* **70** 1081 (1993); T. Nakajima and P. Lambropoulos, *Phys. Rev. A* **50** 595 (1994)

**LASER-PHASE-INSENSITIVE COHERENT CONTROL
OF PHOTOION PRODUCT STATES
IN 2-PHOTON VS. 2-PHOTON IONIZATION OF ATOMIC
BARIUM**

FENG WANG, JING HUANG AND D.S. ELLIOTT

*Purdue University
West Lafayette, IN*

1. Introduction

The use of coherent control techniques in atomic and molecular processes offers new possibilities for controlling the outcome of optical interactions, as well as new insights into fundamental interactions between laser fields and atomic and molecular systems. These processes are based on the explicit exploitation of the coherence properties of laser fields and the atomic and molecular interactions they induce. The advances we have witnessed over the past several years have been exciting indeed, and have continued the hope that laser phase might be the key necessary to open new doors of physics, chemistry, and applications based on these principles. Since the expertise of the participants of this workshop is so widely varied, we will start our discussion of coherent control with a brief review of the field and a general introduction to this new class of laser physics. We will include in this introduction a discussion of the fundamental principles of coherent control, and outline some of the experimental difficulties one might expect to encounter when observing coherent control processes in the laboratory. We will then describe in detail a series of investigations we have carried out in which we have observed the strong capability for controlling the photoionization products of atomic barium using the interference between two different two-photon ionization processes. The results we will describe are insensitive to the phase of the laser fields, and therefore offer a great simplification in the experimental techniques required to observe or use this interference.

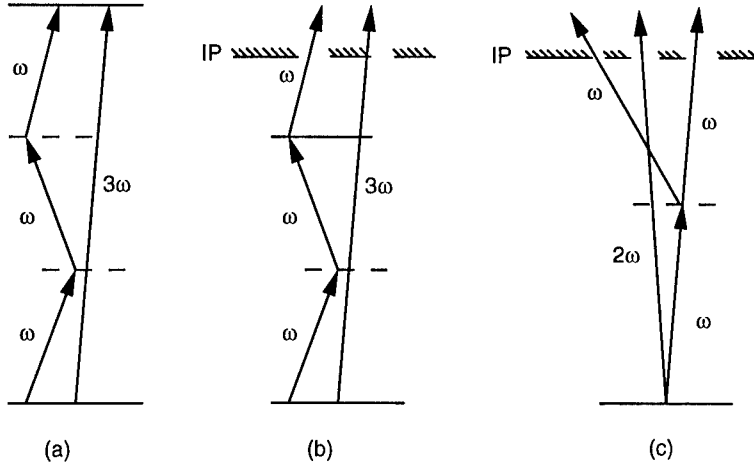


Figure 1. Examples of interfering interactions for two-pathway coherent control.

2. Two-Pathway Coherent Control

Most of the progress which falls under the umbrella known as coherent control can be categorized as either two-pathway control or short-pulse control. In two-pathway control processes, two (or more) optical interactions, both originating at the same initial state and terminating on a common final state, are driven concurrently by an optical field consisting of two or more discrete frequency components. By judicious choice of field properties and experimental geometry, we can adjust the relative phase and amplitude of the transition amplitudes of the different interactions in order to modify the net outcome of the process. Another form of coherent control involves the use of shaped pulses (optical fields in which the amplitude and phase are controlled so as to drive the quantum system towards a desired target state), or time-delayed short pulses in order to control the dynamics of the excitation. All of the work we have carried out in our laboratory, including the control of photoionization products we address in this chapter, are based on the two-pathway interference.

Brumer and Shapiro [1] have long been advocates of using two-pathway interference to control the outcome of optical interactions. Many recent experimental demonstrations of this type of interference, many of which will be mentioned here, have helped pave the way for application to control of complex systems. As an example of two-pathway interference, consider the two interactions represented schematically in figure 1a. This figure shows a linear interaction driven by a field of a frequency 3ω and a three-photon interaction using light at a frequency ω , which can each individually drive a transition between the ground state and the final (bound) state. These

two interactions can interfere, and the probability of inducing the transition depends on whether the interference is constructive or destructive, a condition which we can control experimentally by varying the phase between the field components. (Since the latter is a nonlinear interaction, a much higher intensity at the frequency ω is, of course, required to keep the two transition amplitudes of comparable magnitude.) We can illustrate the dependence of the transition rate on the relative phase for this process by considering the lowest-order perturbation expansion, of the form

$$W \propto |\mu^{(1)} E^{uv} e^{i\phi^{uv}} - \mu^{(3)} (E^{vis} e^{i\phi^{vis}})^3|^2 \quad (1)$$

In this expression, the first term is the linear transition amplitude driven by the field component at the frequency 3ω , whose amplitude and phase are E^{uv} and ϕ^{uv} , respectively. Similarly, the second term is the three-photon moment, proportional to the cube of the complex field component at frequency ω , whose amplitude and phase are E^{vis} and ϕ^{vis} , respectively. When we write the transition rate for noninterfering processes, we usually do not bother to explicitly include the optical phase of the field components, since it disappears upon taking the modulus squared of the transition amplitude. In equation 1, however, the cross term between the two amplitudes varies as the $\cos(\phi^{uv} - 3\phi^{vis})$, as seen when we expand the square,

$$W \propto |\mu^{(1)} E^{uv}|^2 + |\mu^{(3)} (E^{vis})^3|^2 + |\mu^{(1)} E^{uv}| |\mu^{(3)} (E^{vis})^3| \cos(\phi^{uv} - 3\phi^{vis}). \quad (2)$$

Phase control allows us an extra knob in the laboratory which we can turn to control the outcome of the optical interaction. This interference can be thought of in terms of an analogous interference in physical optics known as Young's double slit interference. In the latter, light from a point source passes through two slits in an otherwise opaque screen. The light transmitted by the double-slit pattern is observed on a viewing screen, where one can observe a set of bright and dark intensity fringes. We understand this pattern in terms of the interference between the optical field transmitted by each of the individual slits, which add together destructively or constructively, depending on the relative path length taken by each of the waves as they travel from the source, through one of the slits, and on to the viewing screen. It is important to remark that the interference leading to control of the optical interaction in atoms or molecules is *not* an interference between optical waves, but rather an interference between transition amplitudes. This interference on a bound-bound transition has been shown to allow control on the net rate of the transition in several atomic and molecular systems [2, 3, 4].

Interference has also been demonstrated on bound-free transitions, leading to control of branching ratios among final state products, as well as to

control of directional photo-currents. These interfering processes are illustrated schematically in figures 1b and 1c. In 1b, a three-photon versus one-photon scheme is again shown, similar to that shown in 1a, except that the final state is in the continuum. When the interfering processes lead to more than one continuum state, the amplitudes and phases of the transition amplitudes for the different continua will in general be different, and so the interference can be used to control the relative yield of the different products. Robert Gordon's group has used this scheme to control the relative yield of photoionization and photodissociation of molecular HI [5].

In figure 1c, the interference shown is between a one-photon and a two-photon interaction. Since these interactions lead to final states of different parity, an asymmetric continuum state is produced by this interference, and the asymmetry can be controlled by varying the phases between the amplitudes. This has been demonstrated in the photoionization of rubidium [6] and nitrous oxide [7], in HD dissociation products [8], and in control of conduction band currents in GaAs structures [9, 10].

A number of comments concerning experimental techniques, issues and difficulties in observing or exploiting these interferences are now in order. The requirement for the optical alignment of the beams can be quite stringent. For the case of three-photon vs. one-photon interference, for example, the phase difference $[\phi^{uv} - 3\phi^{vis}]$ must be uniform (i.e. variations in $[\phi^{uv} - 3\phi^{vis}] \ll 2\pi$) over the entire interaction region. One can easily show that the optical beams must propagate parallel to one another within an angle $\theta \ll \lambda^{uv}/w$, where w is the radius of the optical beam. Another factor which may cause the interference to vary throughout the interaction region is a difference in velocity of the optical waves. To avoid this, the refractive indices of the medium must be matched to within $(n^{uv} - n^{vis}) \ll \lambda^{uv}/\Delta z$, where Δz is the length of the interaction region (defined by the length of the absorbing medium or the length of the focal region of the laser beams).

It is also important to have good spatial overlap of the laser beams. In regions where one beam is present but the other beam is not, only one optical process can proceed, eliminating the possibility for interference and control. As this contributes to the noninterfering background, the depth of modulation observed by varying the relative phases of the fields is reduced. As we will see in the next section, the interference and control which is the main topic of this chapter is not subject to this difficulty.

Optical diffraction of the laser beams can also play an important role in coherent control [11]. This will be present whenever focussed laser beams in extended media are used. As a beam approaches the focal region, its intensity increases and the optical phase changes. Since the amplitude and phase of the visible and UV beams each vary through the focal region, and since one or both of the transition amplitudes depend on the fields nonlinearly,

the interference condition (relative amplitude as well as phase difference) will vary throughout the focal region. This effect can also decrease the effective depth of modulation of the interference.

In figure 1b we have shown an atomic resonance at the two-photon level for the three-photon ionization process. This can be a useful scheme for eliminating the $\Delta L = 3$ noninterfering channel, affording deeper modulation of the ion or dissociation products as we vary the phase. Use of intermediate resonances may, however, place tighter restrictions on the bandwidth of the laser used for these observations.

Extensive work has gone into determining the factors which have a significant effect on the net phase of the interference in the past few years. When using the interference to control the branching ratio into different photoionization or photodissociation channels, the ideal case would be that in which we could tune the optical phase difference to the value that would minimize the transition rate into one channel while simultaneously maximizing the transition rate leading to the other channel. Control is still evident under other conditions, even when the transition rates vary exactly in phase with each other, as long as the amplitudes are not perfectly matched to each other. Still, the question of what atomic and molecular factors affect the phase of the modulation signal is of great interest. One factor will be the detuning of the laser from intermediate resonances, as will be explored in detail in this chapter. Lee [12] and Gordon and Seideman, et. al. [13] have investigated a phase contribution which originates with coupled continua.

3. Laser-Phase Insensitive Coherent Control

We will now introduce a type of two-pathway coherent control we have used to control the branching ratio for different photoionization channels in atomic barium [14, 15]. This interference has many features in common with what we have already described, but we will also point out some notable differences, the most important of which is that this interference is independent of the laser phase. There has, to our knowledge, been only one other type of laser-phase-insensitive coherent control demonstrated, this based on laser-induced-continuum-structure in diatomic sodium [16] and atomic xenon [17]. The interference we use to control the photoionization channel for barium was first explored by Pratt in photoionization of molecular NO [18], and is based upon two different two-photon ionization processes. Figure 2 shows an energy schematic for this process. Each two-photon process is driven by a two-color laser field, with frequency components at ω_1 and ω_2 . Frequency ω_1 is tuned near the frequency of the transition from the ground state to an intermediate state $|i\rangle$, while ω_2 is

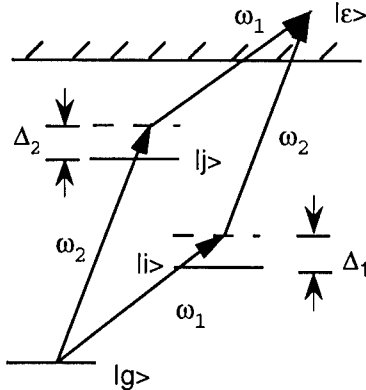


Figure 2. Energy diagram for laser-phase-insensitive two-photon versus two-photon interfering interactions.

nearly resonant with the transition from the ground state to a second intermediate state $|j\rangle$. Ionization results when the atom absorbs one photon at frequency ω_1 and one photon at frequency ω_2 . Since there are two pathways leading to the final continuum state, we should expect to observe interference. We can again illustrate this interference by examining the ionization rate in lowest-order terms.

$$W \propto |T_1 + T_2|^2 = \frac{e^4}{\hbar^2} \left| \frac{z_{\epsilon i} z_{ig}}{\Delta_1 + i\Gamma_i/2} + \frac{z_{\epsilon j} z_{jg}}{\Delta_2 + i\Gamma_j/2} \right|^2 |E_1 E_2|^2. \quad (3)$$

In this expression, ez_{mn} is the transition moment for the $|n\rangle \rightarrow |m\rangle$ transition, Γ_m is the linewidth of the level m , and $\Delta_{1(2)}$ is the detuning of the optical frequency $\omega_{1(2)}$ from the corresponding atomic transition frequency. Both transition amplitudes in equation 3 depend on the product $|E_1 E_2|^2$, so that the transition rate does not depend on the phase of either field. Thus we no longer observe the high sensitivity of the interfering interactions to wavefront misalignment and minor fluctuations, nor do we require matched refractive indices at the two optical frequencies. Of course, we need a new means of adjusting the relative phase of the transition amplitudes, but this is easily accomplished by tuning the frequency of one of the lasers from one side of resonance to the other. We exploit the frequency-dependent phase of the two-photon transition amplitude, as expressed in the frequency denominators given in equation 3. The critical necessity for beam overlap is also relaxed. Since both two-photon interactions depend on the local presence of both fields, there is no contribution to the background (noninterfering) signal at all from regions where the beams do not overlap. We should note the limitations of equation 3, which is valid only in the limit of lowest-order

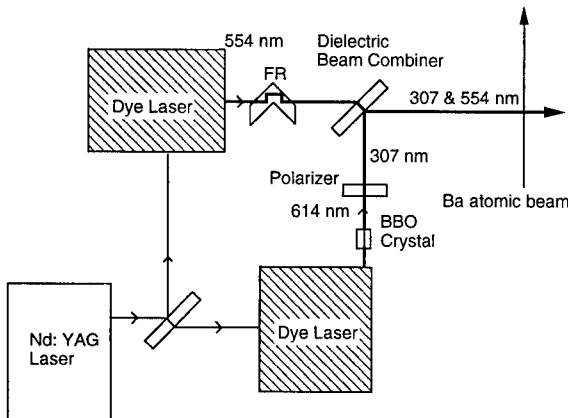


Figure 3. Experimental setup showing the two Nd:YAG laser pumped dye lasers, and optical components which align the polarizations of the 554 nm and 307 nm beams, and direct these beams toward the atomic barium beam. FR is a $\lambda/2$ Fresnel Rhomb.

perturbation theory. While we use this expression to illustrate the main idea of the interference, we recognize that this expression does not include many important features which are readily observed in experiments. For a more complete theoretical treatment, we refer the reader to the multi-channel density matrix approach of Nakajima, Zhang and Lambropoulos [19].

We carry out the measurements in a beam of atomic barium. As shown in figure 3, we use two pulsed dye lasers (~ 15 nsec pulse duration) at $\lambda_1 = 554$ nm and $2\lambda_2 = 614$ nm. The former is nearly resonant with the $6s^2 1S_0 \rightarrow 6s6p 1P_1$ transition. We frequency double the latter in a BBO crystal producing $\lambda_2 = 307$ nm, nearly resonant with the $6s^2 1S_0 \rightarrow 6s7p 1P_1$ transition. See figure 4 for an energy level diagram of barium [20]. We orient the linear polarization of both beams horizontally before they enter the interaction region. The control which we exert is over the branching ratio of the photoion core states. The ground state of the Ba^+ core is the $6s 2S_{1/2}$ state, but Ba^+ also has two low-lying excited states at 0.60 eV ($5d 2D_{3/2}$) and 0.70 eV ($5d 2D_{5/2}$). With our choice of laser wavelengths, we ionize to a continuum state about 1.06 eV above the ionization threshold, and we leave a fraction of the ions in each of these three continuum states. We distinguish these by time-of-flight measurements of the kinetic energy of the photoelectrons.

We have constructed a time-of-flight measurement apparatus which collects all electrons ejected into a 2π solid angle. This is necessary in order to decrease the sensitivity of our measurements to variations in the angular distribution of the ejected electrons. The time-of-flight collector consists of an ellipsoidal electron mirror which reflects the electrons ejected from the

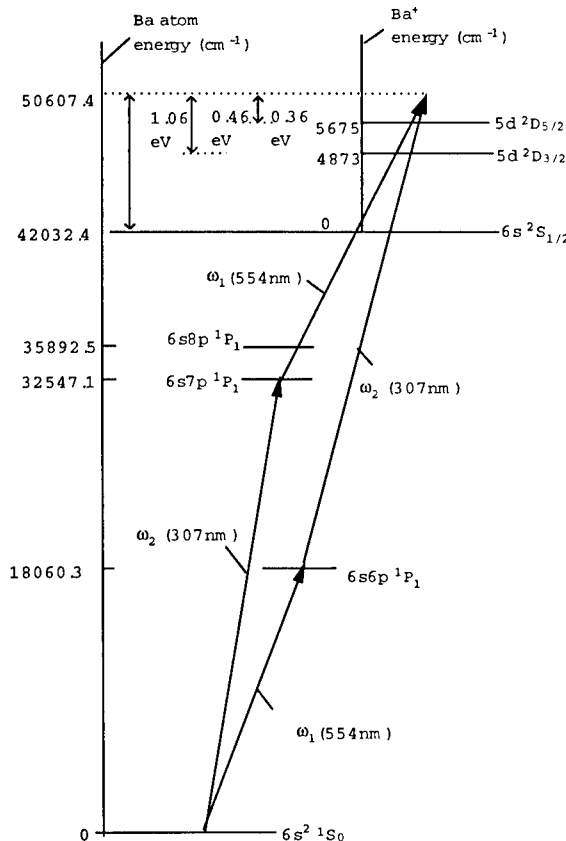


Figure 4. Energy level diagram of atomic barium.

interaction region at one focus of the ellipsoid toward the detector which is placed behind an aperture at the second focus of the ellipsoid. We shield the entire region to reduce electrostatic and magnetostatic fields which would otherwise perturb the trajectory of the photoelectrons in their flight. The detector is a 2-element microchannel plate multiplier (gain $\sim 10^6$) and a collection anode which is capacitively coupled to a digitizing oscilloscope. The trace of the oscilloscope shows three well-resolved peaks at energies of 1.06 eV, 0.46 eV and 0.36 eV, corresponding to the three internal states of the Ba⁺ ion. We measure the area under each peak as a function of Δ_1 to produce the series of spectra shown in figure 5. The detuning Δ_2 of the UV beam from the 6s² 1S₀ \rightarrow 6s7p¹P₁ resonance is shown in each panel. In figure 5a, Δ_2 is 18.7 cm⁻¹, large enough that the two-photon pathway via the 6s7p state is much weaker than that via the 6s6p. As the visible laser frequency is tuned through resonance, the spectra corresponding to

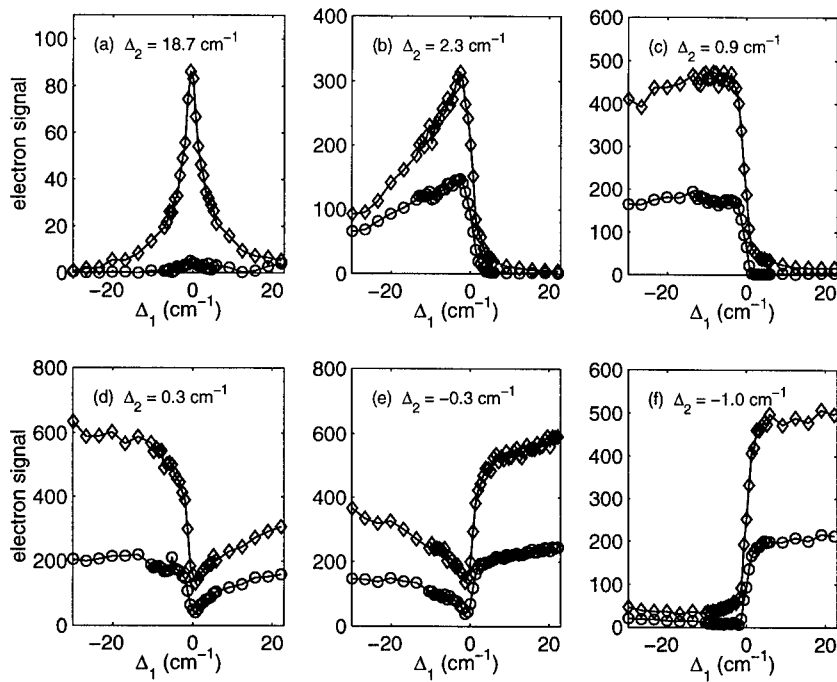


Figure 5. Asymmetric spectra showing the effect of the interference. The diamonds (circles) represent the two-photon ionization spectra where the final Ba^+ ionic state is the $6s\ ^2S_{1/2}$ ($5d\ ^2D_{3/2}$) state.

to the fast electrons (\diamond) and the slow electrons (\circ) are nearly symmetric. With the UV beam tuned closer to resonance, however, as in figure 5b where $\Delta_2 = 2.3$ cm $^{-1}$, the spectra recorded as the visible laser is tuned are very asymmetric. For $\Delta_1 < 0$, the transition amplitudes add constructively, while for $\Delta_1 > 0$, they add destructively. The frequency of the UV laser further approaches the resonance frequency in c and d, while in e and f, Δ_2 has become negative. Notice that the spectra in figures e and f are nearly the mirror image of those in figures d and c, a result of detuning the UV laser to the opposite side of the resonance. In figures c and f, we see very strong suppression of the slow electron peak to one side of resonance, with nearly all of the ionization under these conditions leaving the Ba^+ core in its ground state.

Over the past two years, we have measured the two-photon interference effects as a function of many experimental parameters, including the density of the atomic beam, the intensity of both lasers, the relative polarization of the lasers, and the choice of intermediate resonant states. In this chapter, we will limit our discussion to the dependence of the interference, and subsequent control of the photoion branching ratio, on the density of

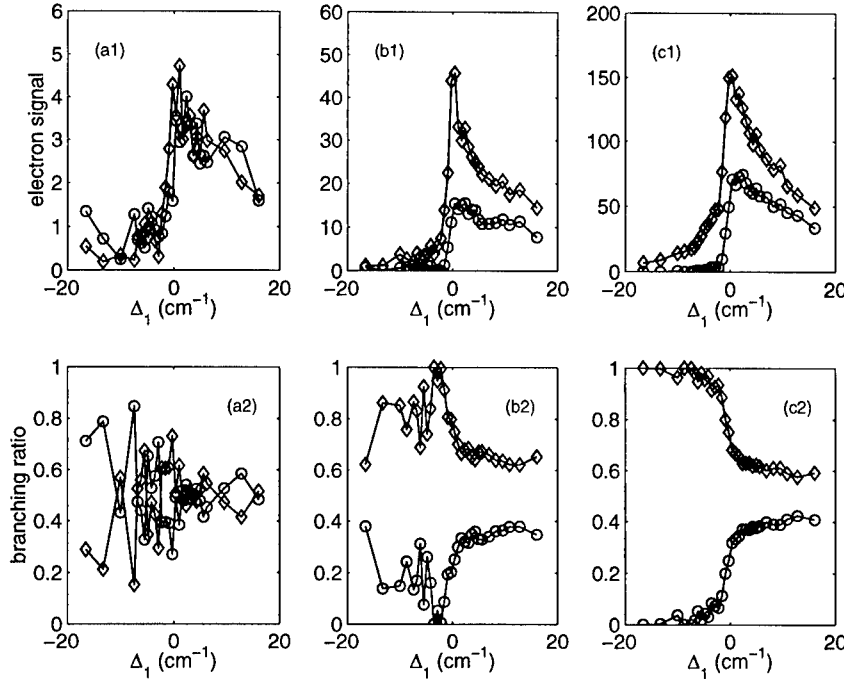


Figure 6. Density dependence of the coherent control process. The top row shows the spectra for 2-photon ionization, while the bottom row shows the branching ratios. The symbols are defined in the caption to figure 5. The atomic densities are (a) $0.33 \times 10^8 \text{ cm}^{-3}$, (b) $1.4 \times 10^8 \text{ cm}^{-3}$, and (c) $5.8 \times 10^8 \text{ cm}^{-3}$.

the atomic beam. In figure 6, we show the spectra (panels a1, b1, and c1) and corresponding branching ratios (panels a2, b2, and c2) for three different atomic beam densities, $0.33 \times 10^8 \text{ cm}^{-3}$, $1.4 \times 10^8 \text{ cm}^{-3}$, and $5.8 \times 10^8 \text{ cm}^{-3}$ for figures a, b and c, respectively. We observe asymmetric spectra in all three cases, since fast and slow peaks show destructive interference between the two ionization pathways for $\Delta_1 < 0$, and constructive interference for $\Delta_1 > 0$. For the lowest density data, shown in figure 6a, we cannot see any clear dependence of the branching ratio on Δ_1 . This implies that the ionization spectra associated with the different core states are all of the same shape, and the only difference is in the overall magnitude. The higher density data, however, show a clear control mechanism at work, especially in figure c2, where more than 95% of the ions find themselves in the $6s \ ^2S_{1/2}$ state for $\Delta_1 < 0$, but only 60% for $\Delta_1 > 0$. We are not able at this time to offer any firm explanations for this unusual behavior. In our original picture of individual atoms driven by the two-color laser field, there is no mechanism available to account for this. It would seem therefore that the atoms are acting back on the laser field in such a way as to

affect their relative intensities, allowing for strong cancellation of one of the products. This would likely be accompanied by leaving the atoms in one or the other of the intermediate states. It would be surprising, however, that the atoms could influence the field intensities so strongly at these atomic densities, where the atoms in the interaction region number only $\sim 10^5$. As an illustration of the scales involved here, the linear absorption length of the 554 nm line when tuned directly into resonance is 35 cm at the largest atomic density we used, yet our atomic beam is only 2 mm in diameter. We are working now to set up investigations to probe this paradoxical behavior. We are devising a scheme to monitor the intermediate state (6s6p and 6s7p) populations, using photoionization of the barium 6s5d 1D_2 and 6s7s 1S_0 states, populated by spontaneous decay of the 6s6p and 6s7p levels, respectively. This will help us to look for any redistributions of the atomic population as a function of density which may give us insight into the control process. We are also looking for redistribution of the energy in the laser beams, either among the different frequency components or by variation of the spatial and temporal profiles of the beams. With these new measurements, we hope to be able to understand this behavior better. Our lack of an explanation notwithstanding, our observation that the ability to control the photoionization branching ratios improves with increasing density is extremely encouraging. Useful application of coherent control to large scale photodissociation, for instance, requires a high density (maybe even a condensed phase) absorbing medium. With this new type of interference, coherent control of a high density medium becomes realizable.

4. Conclusion

We have described our observations of two-photon versus two-photon laser-phase-insensitive coherent control, which we have used to control the branching ratio for the various photoion states. We have demonstrated the capability to change the branching ratio leading to the ground state of the core from 60% to 95%, tuning the frequency of one of the lasers to do so. One outstanding feature of this interference is its insensitivity to the relative phase difference of the lasers. This allows for great experimental simplification when compared to most previous demonstrations of two-pathway coherent control, as well as the ability to work in high density media for which the refractive indices at the different optical wavelengths are not matched. The dependence of the control process on the density of the barium is perhaps the most intriguing feature of this interference. We have additional experimental studies underway to try to decipher the mechanism responsible for this control at high atomic densities.

This work was supported by the National Science Foundation under

Grant No. 9422597-PHY.

References

1. Paul Brumer and Moshe Shapiro, *Acc. Chem. Res.* **22**, 407 (1989); M. Shapiro, J.W. Hepburn and P. Brumer, *Chem. Phys. Lett.* **149**, 451 (1988); C.K. Chan, P. Brumer, and M. Shapiro, *J. Chem. Phys.* **94**, 2688 (1992).
2. Ce Chen, Yi-Yian Yin, and D.S. Elliott, *Phys. Rev. Lett.* **64**, 507 (1990).
3. S.M. Park, S.-P. Lu, and R.J. Gordon, *J. Chem. Phys.* **94**, 8622 (1992).
4. G. Xing, X. Wang, X. Huang, R. Bersohn, and B. Katz, *J. Chem. Phys.* **104**, 826 (1996); X. Wang, R. Bersohn, K. Takahashi, M. Kawasaki, and H. L. Kim, *J. Chem. Phys.* **105**, 2992 (1996).
5. L. Zhu, V. Kleinman, X. Li, S.P. Lu, K. Trentelman, and R.J. Gordon, *Science* **270**, 77 (1995).
6. Yi-Yian Yin, Ce Chen, D.S. Elliott, and A.V. Smith, *Phys. Rev. Lett.* **69**, 2353 (1992).
7. Yi-Yian Yin, D.S. Elliott, R. Shehadeh, and E.R. Grant, *Chem. Phys. Lett.* **241**, 591 (1995).
8. B. Sheehy, B. Walker, and L.F. DiMauro, *Phys. Rev. Lett.* **74**, 4799 (1995).
9. E. Dupont, P.B. Corkum, H.C. Liu, M. Buchanan, and Z.R. Wasilewski, *Phys. Rev. Lett.* **74**, 3596 (1995).
10. A. Haché, Y. Kostoulas, R. Atanasov, J.L.P. Hughes, J.E. Sipe, and H.M. van Driel, *Phys. Rev. Lett.* **78**, 306 (1997); and H.M. van Driel, J.E. Sipe, A. Haché, and R. Atanasov, *Phys. Stat. Sol. (b)* **204**, 3 (1997).
11. Ce Chen and D.S. Elliott, *Phys. Rev. Lett.* **65**, 1737 (1990).
12. Sungyul Lee, *J. Chem. Phys.* **107**, 2734 (1997).
13. L. Zhu, K. Suto, J.A. Fiss, R. Wada, T. Seideman and R.J. Gordon, *Phys. Rev. Lett.* **79**, 4108 (1997).
14. F. Wang, Ce Chen, and D.S. Elliott, *Phys. Rev. Lett.* **77**, 2416 (1996).
15. F. Wang and D.S. Elliott, *Phys. Rev. A* **56**, 3065 (1997).
16. A. Shnitman, I. Sofer, I. Golub, A. Yoge, M. Shapiro, Z. Chen, and P. Brumer, *Phys. Rev. Lett.* **76**, 2886 (1996).
17. S. Cavalieri, R. Eramo, L. Fini, M. Materazzi, O. Faucher and D. Charalambidis, *Phys. Rev. A* **57**, 2915 (1998).
18. S.T. Pratt, *J. Chem. Phys.* **104**, 5776 (1996).
19. T. Nakajima, J. Zhang and P. Lambropoulos, *Phys. Rev. Lett.* **79**, 3367 (1997).
20. C.E. Moore, *Atomic Energy Levels*, US Department of Commerce, NDRDS-NBS **35**, 1971.

COHERENT PHASE CONTROL OF PHOTOIONIZATION AND PHOTODISSOCIATION

ROBERT J. GORDON, JEANETTE A. FISS AND LANGCHI ZHU

University of Illinois at Chicago

*Department of Chemistry (m/c 111), 845 West Taylor Street,
Chicago, IL 60607-7061*

AND

TAMAR SEIDEMAN

National Research Council

Steacie Institute, 100 Sussex Drive, Ottawa K1AOR6, Canada

1. Introduction

A fundamental principle of quantum mechanics is that if a process can occur by more than one independent path, then the probability of that process occurring can be calculated by adding the probability amplitudes for each path and then squaring the sum. A well known example is the photoionization of an atom or a molecule. One route connecting the ground state $|g\rangle$ with the continuum $|E\hat{k}_1^-\rangle$ is direct ionization, with a probability amplitude that is proportional to

$$f_d e^{i\delta_d} = \langle g | D | E\hat{k}_1^- \rangle, \quad (1)$$

where D is the dipole operator, E is the total energy, \hat{k} is the scattering angle of the electron, $|E\hat{k}_1^-\rangle$ denotes a scattering state of the field free Hamiltonian, the $-$ superscript signifies incoming wave boundary conditions, and f_d and δ_d are real. A second path consists of excitation to a state $|i\rangle$ which is embedded in the continuum. The probability amplitude for this resonance-mediated path is given by the product of two functions. The first of these is

$$f_i e^{-i\delta_i} = (E - E_i - \Delta_i - i\Gamma_i/2)^{-1}, \quad (2)$$

where E_i is the zero-order energy of the discrete state, Δ_i is the shift of this zero-order energy induced by the continuum, Γ_i is the width of the

resonance, and δ_i is the Breit-Wigner phase [1]. Expressing the displacement from the center of the resonance in reduced units,

$$\epsilon = \frac{E - E_i - \Delta_i}{\Gamma_i/2}, \quad (3)$$

we can write

$$\cot \delta_i = -\epsilon \quad (4)$$

and

$$f_i = \frac{2}{\Gamma_i} (1 + \epsilon^2)^{-1/2}. \quad (5)$$

The second function is given (in the limit of a weak field) by

$$f_r e^{i\delta_r} = \langle g | D\mathcal{F}(E) | i \rangle \langle i | H_M | E \hat{k}_1^- \rangle, \quad (6)$$

where $\mathcal{F}(E) = I + (E^- - PH_M P)^{-1} PH_M$, P projects onto the scattering manifold, I is the identity operator, and H_M is the (field free) matter Hamiltonian [2]. The operator $\mathcal{F}(E)$ mixes the zero-order (real) state with the continuum, thus broadening and shifting its eigenenergy. It is evident from Eq. (6) that the phase δ_r is the sum of the phases of the two matrix elements, δ_{g-i} , which depends only on the resonance properties,¹ and δ_{i-s} , which depends on the phase of the continuum wave function in the second matrix element. The total transition probability is proportional to the square of the sum of these two terms,

$$p = |f_d e^{i\delta_d} + f_i f_r e^{i(\delta_r - \delta_i)}|^2. \quad (7)$$

This result is shown in Ref. [2] to be equivalent to the well-known Fano [3] profile.

The above analysis is readily extended to other types of bound-to-continuum transitions such as molecular photodissociation [5]. The formalism can also be generalized to include the coupling of one (or more) resonant state(s) to several continua, so that photoexcitation can lead to different possible reaction products with an energy-dependent branching ratio [2]. The product ratio may be changed by varying the excitation energy (i.e., by changing $f_i e^{-i\delta_i}$). Altering the product distribution in this way is a form of *passive* control. This type of control is passive in the sense that for a given energy the amplitudes of the various paths are fixed.

This analysis raises the interesting possibility that *active* control of the reaction could be achieved by choosing the properties of the electromagnetic field in such a way as to manipulate the independent excitation paths

¹As discussed in [4], δ_{g-i} can also depend on the properties of D . For a *multiphoton* transition, D will be complex if any of the virtual intermediate states are not discrete.

[6, 7]. A simple example of such a manipulation is the altering of the relative phases of the independent paths. A decade ago Shapiro, Hepburn, and Brumer [8] proposed a scheme in which two phase-locked light sources are used, one inducing a three-photon transition to the continuum at a frequency² ω_1 and a second inducing a one-photon transition at frequency $\omega_3 = 3\omega_1$. This method has since been employed in a number of laboratories to control the transition rates [9, 10, 11, 12] and branching ratios [13, 14] of a variety of atomic and molecular processes.

The yield of channel S in the presence of a bichromatic field by both direct and resonance-mediated paths is given by

$$p^S = |f_{S,d}^{(1)}e^{i\delta_{S,d}^{(1)}} + f_i f_{S,r}^{(1)}e^{i(\delta_{S,r}^{(1)} - \delta_i)} + e^{i\phi}(f_{S,d}^{(3)}e^{i\delta_{S,d}^{(3)}} + f_i f_{S,r}^{(3)}e^{i(\delta_{S,r}^{(3)} - \delta_i)})|^2, \quad (8)$$

where ϕ is the relative phase of the two laser fields,³ subscript $(j) = (1)$ or (3) denotes the number of photons absorbed, and superscript S denotes product channels A or B . Expanding the square in this expression and integrating over all scattering angles gives the general result

$$\bar{p}^S = \bar{p}_1^S + \bar{p}_3^S + 2\bar{p}_{13}^S \cos(\phi + \delta_{13}^S), \quad (9)$$

where \bar{p}_m^S is the probability of obtaining product S by excitation path m , \bar{p}_{13}^S is an intensity-dependent quantity, and the constant δ_{13}^S is referred to as the *phase shift* for that channel. The difference between the phase shifts for the two channels is referred to as the *phase lag*,

$$\Delta\delta = \delta_{13}^A - \delta_{13}^B. \quad (10)$$

It is clear from eq. (9) that the yield of channel S may be maximized by setting the laser phase ϕ equal to $-\delta_{13}^S$. The objective of this paper is to understand the physical origin of the phase shift, and particularly how it depends on the Breit-Wigner phase, δ_i , and on the the so-called *molecular phases*, $\delta_{S,d}$ and δ_{i-S} .

2. Source of the Phase Shift

Before exploring the origin of the phase shift, it is important to realize that it is possible to control the branching ratio even when there is no phase

²In keeping with the convention used in nonlinear optics, we will use subscripts 1 and 3 to denote, respectively, the three- and one-photon paths, such that $\omega_3 = 3\omega_1$. But it will also be convenient to use the parenthetical superscript (j) to denote a j -photon transition; e.g., $D^{(3)}$ denotes the three-photon dipole operator.

³That is, $\phi = \phi^{(1)} - \phi^{(3)} = \phi_3 - 3\phi_1$, where ϕ_1 is the phase of the three-photon field and ϕ_3 is the phase of the one-photon field.

lag whatsoever. This fact may be ascertained by examining the structure of eq. (9). The intensity-dependence of the coefficients in this expression is given by

$$\bar{p}_1^S = I_1^3 F_1^S, \quad (11)$$

$$\bar{p}_3^S = I_3 F_3^S, \quad (12)$$

and

$$\bar{p}_{13}^S = (I_1^3 I_3)^{1/2} F_{13}^S, \quad (13)$$

where I_m is the intensity of the electromagnetic field used in path m , F_m^S is the angle-averaged matrix element of the transition operator for that path, and F_{13}^S is a cross term.

We define the following parameters: the ratio of the one- to three-photon yields for each channel,

$$R_S = \frac{I_3 F_3^S}{I_1^3 F_1^S}, \quad (14)$$

the Schwartz-inequality parameters,

$$\lambda_S = \frac{F_{13}^S}{(F_1^S F_3^S)^{1/2}}, \quad (15)$$

and the relative ratios of the one- to three-photon yields for the two channels,

$$g = \frac{F_3^B/F_1^B}{F_3^A/F_1^A}. \quad (16)$$

The significance of these parameters is as follows. The maximum modulation of the product yield in a particular channel obtainable by varying the laser phase ϕ occurs when the one- and three-photon yields for that channel are equal. We refer to this condition as "doubling the signal." For either of the product channels, say channel A , the signal may be doubled by setting the values of I_1 and I_3 such that $R_A = 1$. Under this condition the value of R_B is given by g , which is a measure of the feasibility of doubling the signals of both channels simultaneously. The amount of modulation that can actually be achieved depends on the value of the Schwartz-inequality parameters, with 100% modulation achievable for $\lambda_S = 1$. This limiting condition can be achieved, for instance, for a bound-to-bound transition. In general, however, λ_S is less than unity.

The ratio of the product yields expressed in terms of these parameters is given by [15]

$$\frac{\bar{p}^A}{\bar{p}^B} = \frac{F_1^A}{F_1^B} \frac{1 + R_A + 2R_A^{1/2} \lambda_A \cos(\tilde{\phi} + \Delta\delta)}{1 + gR_A + 2(gR_A)^{1/2} \lambda_A \cos \tilde{\phi}}, \quad (17)$$

where $\tilde{\phi} = \phi - \delta_{13}^B$. Contour plots of the product branching ratio, $\bar{p}^A/(\bar{p}^A + \bar{p}^B)$, are shown in Figure 1 for various values of these parameters. The two control parameters are the laser phase, $\tilde{\phi}$, and the intensity ratio, $Z = R_A/(1 + R_A)$. Throughout we set $F_1^A/F_1^B = 1$. In the top panel, where $\Delta\delta = 0$, significant control of the branching ratio is achieved, with the maximum relative yields occurring for the individual channels at $\tilde{\phi} = 0$ and π . The middle and bottom panels show even greater levels of control for $\Delta\delta = \pi/2$. For $g = 1$ the maximum relative yields for each channel are obtained by setting $Z = 1/2$ and varying $\tilde{\phi}$, whereas for $g \neq 1$ the contour plot is asymmetric in Z .

Inasmuch as $\Delta\delta \neq 0$ is a sufficient (but not necessary) condition for control, as a practical matter it is much easier to determine experimentally the extent of control by measuring the phase lag. Further, as discussed later in this paper, the magnitude and wavelength dependence of $\Delta\delta$ yield valuable information about the control mechanism as well as about the electronic properties of the excited molecule.

We turn now to the question of the origin of the phase shift, and to the role played by the molecular phases. Consider for simplicity the limiting case where only a direct path to the continuum exists. In this case the angle-averaged cross term in eq. (9) becomes

$$\bar{p}_{13}^S = \int d\hat{k} \langle g | \bar{D}^{(1)} | E S \hat{k}_1^- \rangle \langle E S \hat{k}_1^- | \bar{D}^{(3)} | g \rangle \quad (18)$$

where $D^{(j)}$ are effective j -photon dipole operators and $\bar{D}^{(j)} = e^{-i\phi^{(j)}} D^{(j)}$. One source of the molecular phase derives from the fact that the continuum wave function, $|E S \hat{k}_1^- \rangle$, is complex. This phase cancels out upon integration in certain limits [16] but not in the general case. Specifically, if a partial wave decomposition of the scattering state is such that each wave is given as the product of a (real) amplitude and a coordinate-independent phase that depends only on the partial wave, then \bar{p}_{13}^S is real.

In another limiting case only the resonance-mediated path exists. Ref. [2] shows that for a single, isolated resonance the cross term is given by

$$\bar{p}_{13}^S = \int d\hat{k} \frac{\langle g | D^{(1)} | i \rangle \langle i | H_M | E S \hat{k}_1^- \rangle \langle E S \hat{k}_1^- | H_M | i \rangle \langle i | D^{(3)} | g \rangle}{(E - E_i - \Delta_i)^2 + (\Gamma_i/2)^2}, \quad (19)$$

Because $|i\rangle$ is real,⁴ we see that $\delta_{S,r}^{(j)}$ cancels out. In the absence of a direct path, $\mathcal{F}(E) = 1$, so that $\delta_{g-i} = 0$, and the molecular phase δ_{i-S} cancels identically. Another way of stating this result is that when the

⁴The function $|i\rangle$ is an eigenstate of (the Hermitian) $Q H_M Q$, Q being a projector onto the bound manifold.

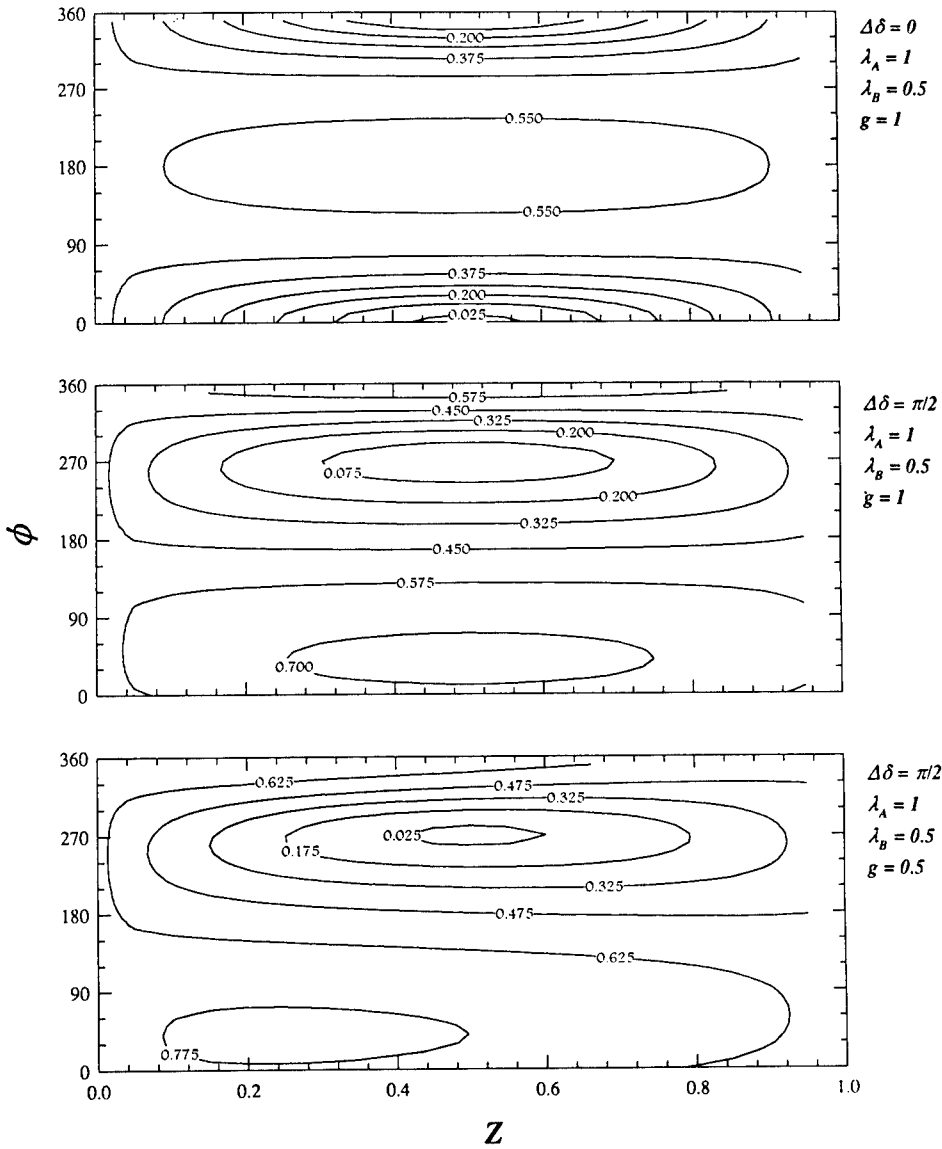


Figure 1. Contour plots of the product branching ratio for various combinations of the parameters described in the text. In the top panel the phase lag is set equal to 0, whereas in the bottom two panels it is equal to $\pi/2$. In the top two panels the doubling parameter $g = 1$, whereas in the bottom panel it is set equal to 0.5.

resonance-mediated path dominates, the atom or molecule "forgets" the phase information contributed by the excitation step, which is uncoupled from the transition to the continuum.

The most general case is obtained by retaining all four terms in Eq. (8). Expansion of the square of the sum of terms yields a cross term, which, before angle-averaging, has a phase shift given by

$$\begin{aligned} \tan \delta_{13}^S = & -[f_{S,d}^{(1)} f_{S,d}^{(3)} \sin(\delta_{S,d}^{(1)} - \delta_{S,d}^{(3)}) + f_i^2 f_{S,r}^{(1)} f_{S,r}^{(3)} \sin(\delta_{S,r}^{(1)} - \delta_{S,r}^{(3)}) \\ & + f_i f_{S,r}^{(1)} f_{S,d}^{(3)} \sin(\delta_{S,r}^{(1)} - \delta_{S,d}^{(3)} - \delta_i) + f_i f_{S,d}^{(1)} f_{S,r}^{(3)} \sin(\delta_{S,d}^{(1)} - \delta_{S,r}^{(3)} + \delta_i)] \\ & [f_{S,d}^{(1)} f_{S,d}^{(3)} \cos(\delta_{S,d}^{(1)} - \delta_{S,d}^{(3)}) + f_i^2 f_{S,r}^{(1)} f_{S,r}^{(3)} \cos(\delta_{S,r}^{(1)} - \delta_{S,r}^{(3)}) \\ & + f_i f_{S,r}^{(1)} f_{S,d}^{(3)} \cos(\delta_{S,r}^{(1)} - \delta_{S,d}^{(3)} - \delta_i) + f_i f_{S,d}^{(1)} f_{S,r}^{(3)} \cos(\delta_{S,d}^{(1)} - \delta_{S,r}^{(3)} + \delta_i)]^{-1}. \end{aligned} \quad (20)$$

It is evident that the phase shift arises from three sources: interference between the direct one- and three-photon paths with amplitude $f_{S,d}^{(1)} f_{S,d}^{(3)}$, interference between the resonance-mediated one- and three-photon paths with amplitude $f_i^2 f_{S,r}^{(1)} f_{S,r}^{(3)}$, and "double" cross terms with amplitudes $f_i f_{S,r}^{(1)} f_{S,d}^{(3)}$ and $f_i f_{S,d}^{(1)} f_{S,r}^{(3)}$. Far from the resonance only the first source contributes, so that if we set $f_1^{S,r} = f_{S,r}^{(3)} = 0$, the phase shift is given by $\delta_{13}^S = \delta_{S,d}^{(1)} - \delta_{S,d}^{(3)}$. On the other hand, in the absence of a direct path ($f_{S,d}^{(1)} = f_{S,d}^{(3)} = 0$), we obtain $\delta_{13}^S = \delta_{S,r}^{(1)} - \delta_{S,r}^{(3)}$. If both direct and resonance mediated paths are present, but only a single resonance contributes, the absolute value of the phase shift will reach a *minimum* near the center of the resonance, where the resonance-mediated path dominates. If however, the molecular phases do not contribute to the phase shift (i.e., $\delta_{S,d}^{(1)} = \delta_{S,d}^{(3)} \equiv \delta_{S,d}$, and $\delta_{S,d} = \delta_{i-S}$), then the double cross terms will dominate, and the absolute value of the phase shift will reach a *maximum* near the center of the resonance.

What then are the sufficient conditions for the molecular phases to contribute to the phase shift of the cross term? This question has been dealt with in Ref. [2], and we summarize here the conclusions of that study:

1. A direct path induces a phase shift unless the scattering Hamiltonian gives rise to elastic scattering only (and the scattering angles are integrated over). For instance, channel coupling in the continuum is sufficient to produce a phase lag in the direct path.

2. In the absence of a direct path, δ_{13}^S may be nonzero if there are two or more coupled resonances present (Ref. [2], eq (25)). If the resonances are uncoupled, however, and the product channels are rotational states, $\delta_{13}^{S,r}$ will vanish after integration over scattering angles.

3. A complex state at the one- or two-photon level can contribute to $\delta_{S,d}^{(3)}$ and $\delta_{S,g-i}^{(3)}$ [4]. If this contribution is the same for both channels, however, it will have no effect on $\Delta\delta$.

If the molecular phases cancel out, a phase shift may still arise from the Breit-Wigner phase that appears in the double cross terms. A necessary and sufficient condition for this effect is that the Fano asymmetry parameters, $q_S^{(j)}$, differ for the one- and three-photon paths.

3. Experimental Results

We present in this section experimental data which illustrate some of the principles developed above. In these experiments a molecular beam of either *HI* or *DI* molecules was irradiated simultaneously with an ultraviolet laser beam of frequency ω_1 and its third harmonic (VUV frequency of $\omega_3 = 3\omega_1$). The latter was generated by focusing the UV beam into a cell containing *Xe* gas. The wavelength of the UV laser was tuned over the range 353.4 to 354.3 nm, which encompasses the $5s\sigma$ Rydberg state of these molecules. This state, which lies just above the lowest ionization threshold of *HI*, autoionizes to produce HI^+ (or DI^+) and also predissociates to produce ground state *H* (or *D*) atoms and an electronically excited *I* atom. Subsequent absorption of one or more UV photons by the *I* atom yields an I^+ ion. The ions were produced between the electrodes of a Wiley-McLaren [17] time-of-flight mass spectrometer and were detected by a pair of microchannel plates. The relative phase of the UV and VUV beams was varied by passing both laser beams through a cell containing *H*₂ gas, which has a different refractive index at ω_3 and ω_1 . Further details of the experiment may be found in the literature [10], [13].

A typical experimental result is illustrated in Figure 2, which shows the modulation of the HI^+ and I^+ signals that is produced by a variation of ϕ . In this case there is a phase lag of approx. 150°. Figure 3 shows the wavelength dependence of the phase lag. Also shown are the photoionization spectra of both molecules, in which the $5s\sigma$ resonance is clearly visible. The fine structure of these spectra is of rotational origin. The most striking result of this figure is that $\Delta\delta$ attains large values far from the resonance and has a deep minimum near the center of the resonance. This behavior is in accord with our theoretical prediction for an isolated resonance in the case that the resonance-mediated path dominates the direct path near the center of the resonance.

Which channel is responsible for the phase lag, or do both contribute? Based on the theoretical work of Lefebvre-Brion [18], it appears that the phase shift for ionization of *HI* vanishes, implying that the phase lag is caused by the dissociation channel. The large phase lag far from the reso-

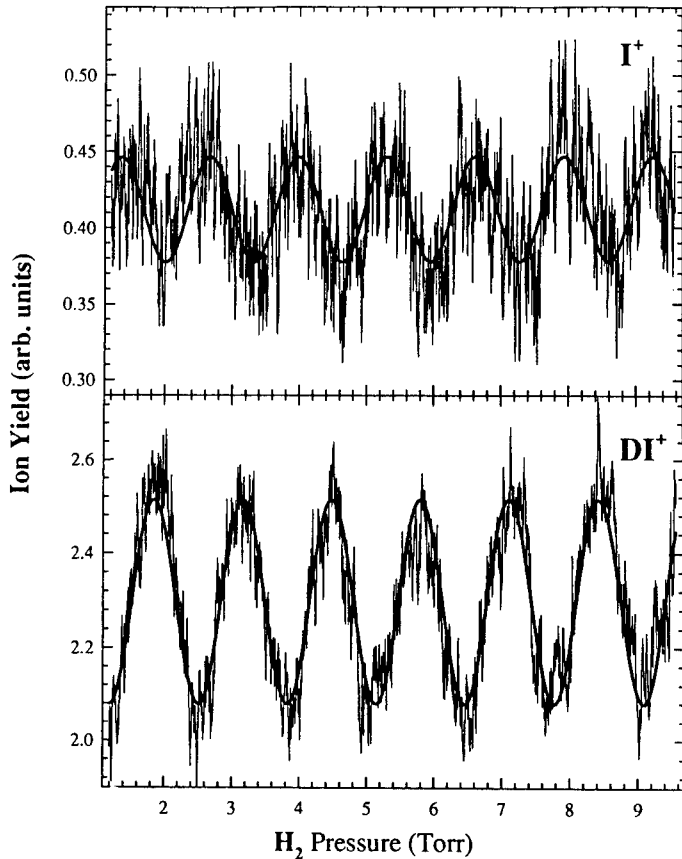


Figure 2. Modulation curves for DI^+ and I^+ recorded at $\lambda_1 = 353.69$ nm.

nance implies that the molecular phases in the direct path do not cancel. This effect is caused by the coupling of different nuclear channels (so-called "exit channel effects" [19]). One way to test this interpretation of the data is to measure the phase lag for the ionization of a mixture of HI and some other molecule. If the phase shift for the ionization of the other molecule is also zero, and if there is no resonance present in the spectrum of the second molecule, then the absolute value of the observed phase lag should display a *maximum* near the center of the HI resonance. An experiment to test this prediction is under way.

The large isotope effect displayed in Figure 3 is as yet unexplained. If indeed the phase lag is caused by the dissociation channel, the factor of 2 difference in reduced masses of the two isotopomers could well be involved in this effect. A key step for understanding the mechanism is to resolve the rotational structure present in the ionization and dissociation spectra

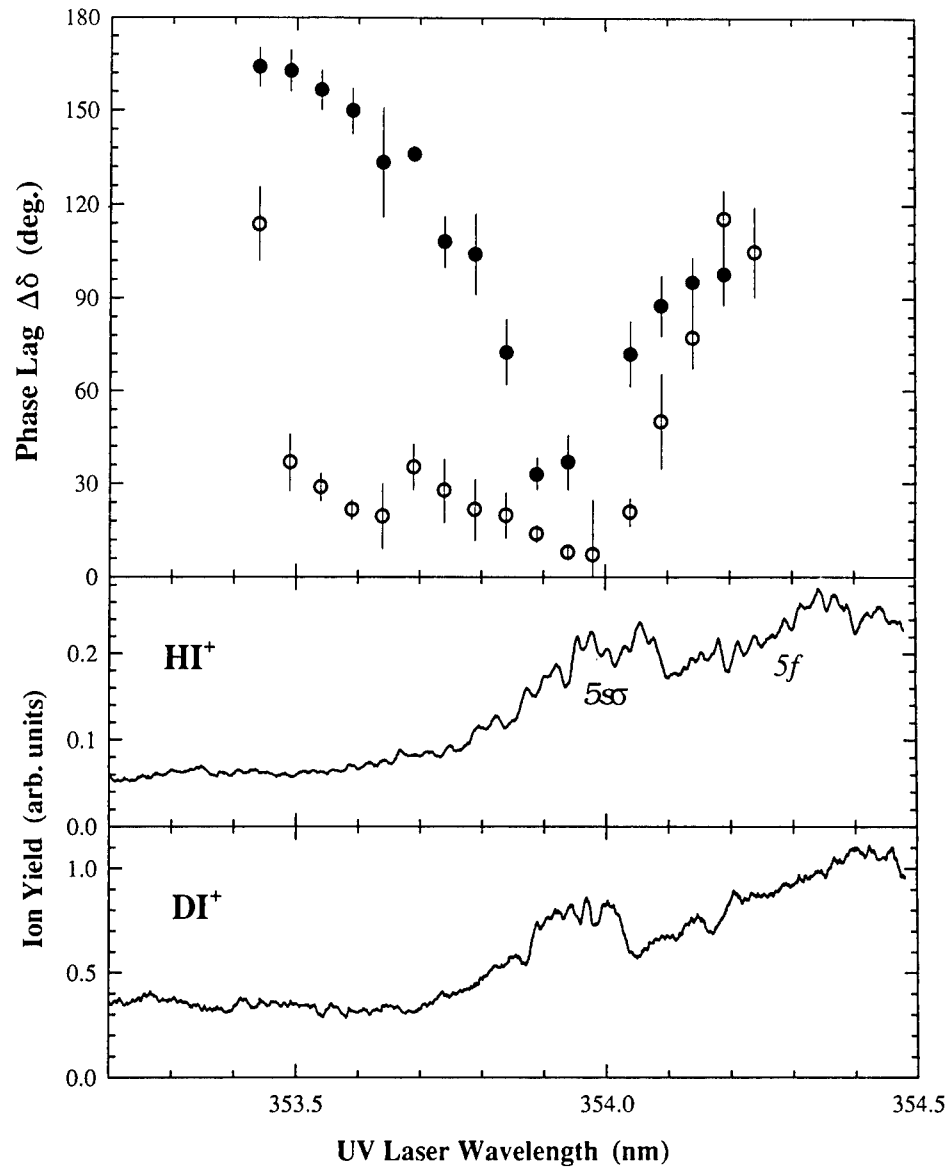


Figure 3. Phase lag between the dissociation and ionization channels for HI (open symbols) and DI (closed symbols). The one-photon (ω_3) spectra for the ionization of HI and DI are shown in the bottom panels.

of these molecules. Double-resonance experiments are planned with this objective in mind.

Support by the National Science Foundation is gratefully acknowledged.

References

1. J.J. Sakurai, *Modern Quantum Mechanics* (Addison-Wesley, Reading, 1994).
2. T. Seideman, *J. Chem. Phys.* **108**, 1915 (1998).
3. U. Fano, *Phys. Rev.* **124**, 1866 (1961).
4. S. Lee, *J. Chem. Phys.* **107**, 2734 (1997).
5. H. Lefebvre-Brion and R. W. Field, *Perturbations in the Spectra of Diatomic Molecules* (Academic Press, New York, 1986).
6. R.J. Gordon and S.A. Rice, *Ann. Rev. Phys. Chem.* **48**, 595 (1997).
7. M. Shapiro and P. Brumer, *J. Chem. Soc., Trans. Faraday Soc.* **93**, 1263 (1997).
8. M. Shapiro, J.W. Hepburn, and P. Brumer, *Chem. Phys. Lett.* **149**, 451 (1988).
9. C. Chen, Y.-Y. Yin, D.S. Elliott, *Phys. Rev. Lett.* **64**, 507 (1990).
10. S. Lu, S.M. Park, Y. Xie, and R.J. Gordon, *J. Chem. Phys.* **96**, 6613 (1992).
11. X. Wang, R. Bersohn, K. Takahashi, M. Kawasaki, and H.L. Kim, *J. Chem. Phys.* **105**, 2992 (1996).
12. N.E. Karapanagioti, D. Xenakis, D. Charalambidis, and C. Fotakis, *J. Phys. B* **29**, 3599 (1996).
13. L. Zhu, V. Kleiman, X. Li, S. Lu, K. Trentelman, and R.J. Gordon, *Science* **270**, 77 (1995).
14. L. Zhu, K. Suto, J.A. Fiss, R. Wada, T. Seideman, and R.J. Gordon, *Phys. Rev. Lett.* **79**, 4108 (1997).
15. P. Brumer and M. Shapiro, *Faraday Disc.* **82**, 177 (1986).
16. T. Nakajima, J. Zhang, and P. Lambropoulos, *J. Phys. B* **30**, 1077 (1997).
17. W.C. Wiley and I.H. McLaren, *Rev. Sci. Instr.* **26**, 1150 (1955).
18. H. Lefebvre-Brion, *J. Chem. Phys.* **106**, 2544 (1997).
19. M.H. Alexander, X. Li, R. Liyanage, and R.J. Gordon, *Chem. Phys.* **231**, 331 (1998).

COHERENT CONTROL OF ATOMIC PHOTOIONIZATION AND AUTOIONIZATION

P. LAMBROPOULOS^{1,2} and TAKASHI NAKAJIMA³

¹*Max-Planck-Institut für Quantenoptik*

85748, Garching, Germany

²*F.O.R.T.H., Institute of Electronic Structure and Laser
and Department of Physics, University of Crete*

P.O. Box 1527, Heraklion 711 10, Crete, Greece

³*Institute of Advanced Energy, Kyoto University
Gokasho, Uji, Kyoto 611-0011, Japan*

The control of the products of photoabsorption through the relative phase of two fields represents one of the schemes of coherent control which has been under continuing study and evolution over the last few years [1-8]. Its general aspects as well as a number of specific issues pertaining to small molecules are usefully reviewed and summarized in this volume by Gordon et al. With the intention of avoiding duplication of discussion and minimizing the overlap with their article, we focus our review and remarks on certain aspects of phase control in atoms. There are we believe two main motivations for studying phase control in photoabsorption. One has to do with the desire to control branching ratios of products, as amply illustrated experimentally and theoretically by Gordon et al. The other has to do with the possibility of probing atomic and molecular properties and interactions with radiation. We emphasize here the second.

First, recall the fundamental scheme based on the simultaneous action of a single- and a three-photon transition induced by fields of respective frequencies 3ω and ω , under the assumption that the relative phase (phase difference) of the two fields can be controlled through well-established techniques. Thus a fundamental general equation governing the dependence of the yield, leading to some product S , on the relative phase ϕ can be written as,

$$p^S = p_\omega^S + p_{3\omega}^S + 2(I_\omega^3 I_{3\omega})^{1/2} |F_{13}^S| \cos(\phi + \delta_{13}^S), \quad (1)$$

where F_{13}^S is a third frequency-dependent system-parameter whose magnitude determines the strength of the interference. The quantity $\phi = \phi_3 - 3\phi_1$ is the phase difference of the complex fields entering the respective transition amplitudes, while δ_{13}^S represents whatever phase appears in the amplitudes for product S . As long as F_{13}^S is different from zero, the signal p^S will exhibit a modulation as a function of ϕ even if δ_{13}^S is zero.

As has been established some time ago, the product yield will generally oscillate as a function of ϕ irrespective of whether this yield represents the population of a discrete state or the amount of decay into some continuum, such as ionization. It has been pointed out that in the case of transition into a smooth continuum [4], phase control can be employed to minimize (and in principle cancel) the contribution of one of the two partial waves into which the three-photon transition leads; since the single-photon transition leads only to one partial wave whose contribution can be interfered with.

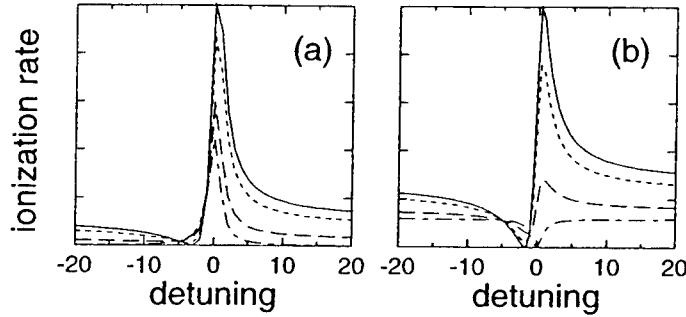


Figure 1: Two examples of autoionization line-shape in a weak field as a function of dimensionless detuning. Relative phase $\phi = 0$ (solid), $\pi/3$ (dotted), $2\pi/3$ (dashed), and π (dot-dashed). In (a) the direct transition to the continuum has been cancelled at $\phi = \pi$, while in (b) the transition to the discrete state has been cancelled at $\phi = \pi$.

The case of one autoionizing resonance decaying into one continuum represents the next level of interesting complication. Through a judicious choice of the single- and three-photon coupling to an initial (say the ground) state, in combination with controlled variation of the relative phase of the two fields, one can alter the line-shape in a rather drastic fashion [5, 6]. An asymmetric line-shape can be changed to completely symmetric or to a pure minimum in a smooth background - also known as window resonance. Simple analytical expressions provide a physical interpretation of this type of effect. Thus the transformation of an asymmetric line-shape to symmetric implies that the direct transition into the continuum (whose presence made the shape asymmetric) has been cancelled (see Fig.1(a)). The transformation to a pure minimum implies that the transition to the discrete state has been cancelled (see Fig.1(b)), reducing thus the process to the excitation of a discrete

state which decays into a continuum without interference with an other path. We know of no other way that the line-shape of an autoionizing state resonance can be manipulated in this fashion. Of course, the three-photon transition will as always involve an additional incoherent decay into a partial wave of higher angular momentum which does not interfere with any other transition. This acts as a smooth background on top of which the interference effects are superimposed. Questions of the degree of observability of the interferences then have to do with signal to noise considerations.

If we are to consider two different products, say A and B , however, each will obey an equation of the form of Eq.(1) and only if $\delta_{13}^A \neq \delta_{13}^B$ will the modulation of these two product signals be out of phase. It should be noted at this point that, whether the two product signals are in phase or out of phase, the branching ratio can be controlled through the manipulation of ϕ .

The term molecular phase [8] has been employed for the quantity δ_{13}^S ever since the first theoretical articulation of the idea. Although never pinpointed, it has often appeared in the equations. It is of course well known that transition amplitudes involving continua do contain the phase shift of the respective continuum. In a recent paper [7], based on a simple model for two channels *which are not directly coupled*, we have shown that such phases cancel out, while in a study involving transitions in a molecule, an identical conclusion has been reached [9]. The issue has been revisited and brought to a sharper focus in Refs.[10, 11], where a distinction has been made between their conclusions and previous work [7, 9].

In order to underscore the common features and similarities between the models, we consider the central equation for p^S derived in Ref.[10], namely,

$$p^S = \left| f_1^{S,d} e^{i\delta_1^{S,d}} + f_1^{S,r} f e^{i(\delta_1^{S,r} + \delta)} + e^{i\phi} \left(f_3^{S,d} e^{i\delta_3^{S,d}} + f_3^{S,r} f e^{i(\delta_3^{S,r} + \delta)} \right) \right|^2, \quad (2)$$

where $f_1^{S,d}$, $f_1^{S,r}$, $\delta_1^{S,d}$, and $\delta_1^{S,r}$ are the real parts of the direct and resonant transition amplitudes by a single-photon absorption and associated phase factors, respectively. Analogous quantities for a three-photon absorption, namely, $f_3^{S,d}$, $f_3^{S,r}$, $\delta_3^{S,d}$, and $\delta_3^{S,r}$ also appear in the above equation. As expected, the factor $e^{i\phi}$ containing the phase difference between the two fields multiplies one of the terms and will be responsible for the interference in the cross term, when the right hand side of Eq.(2) is written out explicitly in three terms as in Eq.(1). The corresponding equation of Ref.[7] for the photoionization rate into the continuum $|c_j\rangle$ ($j = 1, 2$), as given in Eq.(31) of that paper, reads,

$$\frac{dR_j}{d\tau} = 2\pi \left| \frac{\left(D_{c_j g}^{(3)} + e^{i\phi} \mathcal{D}_{c_j g} \right) (\Delta + i\Gamma/2) + V_{c_j a} \left\{ \Omega^{(3)}(1 - i/q^{(3)}) + e^{i\phi} \Omega(1 - i/q) \right\}}{\Delta + i\Gamma/2} \right|^2 \quad (j = 1, 2), \quad (3)$$

where we have used the notation Δ for the detuning instead of the δ used in Ref.[7]. The quantities $D_{c_j g}^{(3)}$, $\mathcal{D}_{c_j g}$, and $V_{c_j a}$ represent, respectively, the three-photon bound-free dipole matrix element coupling the initial state $|g\rangle$ to the $|c_j\rangle$ continuum, the single-photon bound-free dipole matrix element coupling $|g\rangle$ to the same continuum, and the matrix element of the configuration interaction V coupling the resonant state $|a\rangle$ to the same continuum. The width of the resonance is $\Gamma = 2\pi \sum_j |V_{c_j a}|^2$. The initial state is also coupled directly to the resonance via single-photon and three-photon amplitudes Ω and $\Omega^{(3)}$, respectively, each of which is accompanied by its own asymmetry parameter, i.e., q and $q^{(3)}$. *It is very important to stress that, in the above description, there is no direct coupling between $|c_1\rangle$ and $|c_2\rangle$ continua.* Those two continua communicate only through the couplings to the resonant state $|a\rangle$, i.e., via $V_{c_1 a}$ and $V_{c_2 a}$. The way these two continua interact with the resonant state $|a\rangle$ can be characterized by introducing correlation coefficients ρ and $\rho^{(3)}$ for the single- and the three-photon processes, respectively, as

$$\rho \equiv \frac{\sum_j V_{a c_j} \mathcal{D}_{c_j g}}{\sqrt{\sum_j |V_{c_j a}|^2} \sqrt{\sum_j |\mathcal{D}_{c_j g}|^2}} = \frac{2}{\sqrt{\gamma \Gamma}} \frac{\Omega}{q}, \quad (4)$$

$$\rho^{(3)} \equiv \frac{\sum_j V_{a c_j} D_{c_j g}^{(3)}}{\sqrt{\sum_j |V_{c_j a}|^2} \sqrt{\sum_j |D_{c_j g}^{(3)}|^2}} = \frac{2}{\sqrt{\gamma^{(3)} \Gamma}} \frac{\Omega^{(3)}}{q^{(3)}}, \quad (5)$$

where

$$\gamma \equiv 2\pi \sum_j |\mathcal{D}_{c_j g}|^2, \quad (6)$$

$$\gamma^{(3)} \equiv 2\pi \sum_j |D_{c_j g}^{(3)}|^2. \quad (7)$$

Clearly, the correlation coefficients are equal to unity if a single continuum is considered. The deviation of the absolute values of these coefficients from unity indicates that the coupling of the two continua $|c_1\rangle$ and $|c_2\rangle$ to $|a\rangle$ is different. The ionization line-shapes from each continuum as a function of laser detuning Δ are quite different if ρ and $\rho^{(3)}$ deviate from unity.

Since there is no direct coupling between the two continua $|c_1\rangle$ and $|c_2\rangle$ in our model employed in Ref.[7], it has been assumed that the continua can be prediagonalized. Thus the phase factors associated with the continuum wavefunctions $|c_j\rangle$ ($j = 1, 2$), common to all matrix elements $D_{c_j g}^{(3)}$, $\mathcal{D}_{c_j g}$, and $V_{c_j a}$ in the above equation, can be factored out, and we obtain,

$$\frac{dR_j}{d\tau} = 2\pi \left| \left(|D_{c_j g}^{(3)}| + e^{i\phi} |\mathcal{D}_{c_j g}| \right) + \frac{1}{\Delta + i\Gamma/2} |V_{c_j a}| \left\{ \Omega^{(3)} (1 - i/q^{(3)}) + e^{i\phi} \Omega (1 - i/q) \right\} \right|^2 \quad (j = 1, 2). \quad (8)$$

A couple of remarks are relevant here. In the above model, we have assumed that the two continua $|c_j\rangle$ correlate to the same photoabsorption product, which is nothing but an ion in the case of atom or molecule. The above treatment can be immediately extended to the case in which the two continua correlate to two different photoabsorption products, which may be, for example, two different ionic states in the case of an atom, and two different photoionization states or one photoionization state and one photodissociation state in the case of a molecule. If the two continua correlate to the two different ionic states and they may still be assumed to be prediagonalized, the total ionization rate $dR/d\tau$ is simply given by

$$\frac{dR}{d\tau} = 2\pi \sum_{j=1,2} \left| (D_{c_j g}^{(3)} + e^{i\phi} \mathcal{D}_{c_j g}) + \frac{1}{\Delta + i\Gamma/2} V_{c_j a} \left\{ \Omega^{(3)}(1 - i/q^{(3)}) + e^{i\phi} \Omega(1 - i/q) \right\} \right|^2 \quad (9)$$

If the two continua happen to be non-prediagonalized as is often the case in molecules [11], i.e., if the eigenstates of the total Hamiltonian are given as a linear combination of two continua, the matrix elements $D_{c_j g}^{(3)}$ and $\mathcal{D}_{c_j g}$ in Eq.(9) must be replaced by the corresponding linear combinations of $D_{c_1 g}^{(3)}$ and $D_{c_2 g}^{(3)}$, and $\mathcal{D}_{c_1 g}$ and $\mathcal{D}_{c_2 g}$ with appropriate weighting factors and the difference of phase shifts between two continua. It would be too artificial, however, if we attempted to incorporate such a possibility in this simple model of one isolated resonance. We prefer instead to present in this paper the treatment of an analogous but realistic context for this kind of coupling in the atoms of Xe and Ca.

We now come back to the Eq.(8). In order to compare this equation with that derived in Ref.[10], we redefine the following quantities:

$$f e^{i\delta} \equiv \frac{1}{\Delta + i\Gamma/2}, \quad (10)$$

$$f_1^{j,r} e^{i\delta_1^{j,r}} \equiv |V_{c_j a}| \Omega \left(1 - \frac{i}{q} \right), \quad (11)$$

$$f_3^{j,r} e^{i\delta_3^{j,r}} \equiv |V_{c_j a}| \Omega^{(3)} \left(1 - \frac{i}{q^{(3)}} \right), \quad (12)$$

$$f_1^{j,d} e^{i\delta_1^{j,d}} \equiv \mathcal{D}_{c_j g}, \quad (13)$$

$$f_3^{j,d} e^{i\delta_3^{j,d}} \equiv D_{c_j g}^{(3)}. \quad (14)$$

Not surprisingly, our bound-free matrix elements correspond to what Zhu *et al.* have called direct components, while our bound-resonance matrix elements correspond to what they have called resonant components [10]. Using these quantities, Eq.(8) can be recast into the following form:

$$\frac{dR_j}{d\tau} = 2\pi \left| f_3^{j,d} e^{i\delta_3^{j,d}} + f_3^{j,r} f e^{i(\delta_3^{j,r} + \delta)} + e^{i\phi} \left(f_1^{j,d} e^{i\delta_1^{j,d}} + f_1^{j,r} f e^{i(\delta_1^{j,r} + \delta)} \right) \right|^2, \quad (15)$$

which is identical to Eq.(4) of the paper by Zhu *et al.* [10]. *As long as there is no direct coupling between the two continua*, the form of our equations makes it clear that one can always take $\delta_1^{j,d}, \delta_3^{j,d} = 0$, as is evident in going from Eq.(3) to Eq.(8). Thus the only phases that survive in the sense that they affect the modulation of each product are $\delta_1^{j,r}$ and $\delta_3^{j,r}$ which are due to the coupling of the resonance to the continuum. They in fact vanish in the limit of $q, q^{(3)} \rightarrow \infty$, which corresponds to a symmetric resonance. It follows then that a reasonably asymmetric resonance is desirable for efficient control through the phase of the field in a scheme such as that of Refs.[7, 10, 12]. This is compatible with the finding in Ref.[10] to the effect that “in the limit of a single resonance and no direct component the molecular phase vanishes”.

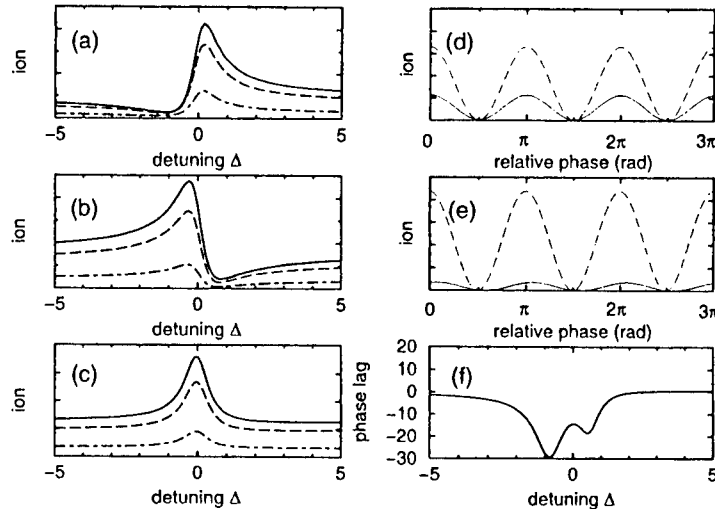


Figure 2: Example of calculated results based on a two-channel model employed in Ref.[7]. Ionization spectra of (a) channel 1, (b) channel 2, and (c) a sum of both as a function of dimensionless detuning Δ at relative phase $\phi = 0$ (solid), $\phi = \pi/3$ (dashed), and $\phi = 2\pi/3$ (dot-dashed). Modulation of ionization signals into channel 1 (solid) and channel 2 (dashed) at (d) $\Delta = -5$ and (e) $\Delta = -1$ as a function of relative phase. (f) Phase lag plotted as a function of detuning Δ .

A couple of further details are relevant here. Consider the phase lag between the two channels (products) studied in Ref.[7], shown here in Fig.2. Figs.2(a) and (b) show the ionization spectra into channels 1 and 2, respectively. The asymmetries in Figs.2(a) and (b) are almost reversed, which is simply due to the choice of the

parameters used for this specific calculations in which the correlation coefficients $\rho = -0.17$ and $\rho^{(3)} = -0.1$. Both of these values are very different from unity. The asymmetry parameters, however, are $q = -9.1$ and $q^{(3)} = -12$, respectively, which lead to the fairly symmetric total ionization spectra, as shown in Fig.2(c). Figs.2(d) and (e) show the modulation of ionization into channels 1 (solid) and 2 (dashed) at dimensionless detunings $\Delta = -5$ and $\Delta = -1$, respectively. Note that the phase lag has an extremum near the resonance, changing sharply away from resonance, exhibiting another extremum before approaching its zero value at large detuning. The appearance of the double-peak in Fig.2 is due to the deviation of the correlation factors, as defined in Eqs.(16)-(17) of Ref.[7], from unity, which may take different values case by case. The structure of the phase lag persists over a frequency range of about 3 autoionization widths. Needless to say, that, as correctly noted in Ref.[10], more than one closely spaced resonances will add structure, but that would be a complication to be dealt with if necessary. There is however another possible cause of structure in the phase lag, namely the presence of real intermediate states near two-photon resonance in the three-photon amplitudes whose sign reverses as the laser frequency is varied around such an intermediate resonance. A width should also appear in the denominator involving the detuning from such a resonance. All this accounts to an additional phase difference as the laser frequency crosses the position of the resonance. These details should be kept in mind when experimental data are analyzed. But as already noted, and appropriately stressed in Ref.[10], in the context of above model, the phase lag vanishes in the limit of large detuning, independently of the values of ρ and $\rho^{(3)}$.

The remaining question now is whether a non-vanishing phase lag for large detuning obtains only when a dissociation channel is coupled to ionization, or the effect is more basic and general. We demonstrate now that it indeed is more general, the minimum requirement being the coupling of two continua. As such, the effect is also present in atoms, as documented below through two quantitative examples, in two quite different atoms.

The first refers to photoionization in Xe, above the two fine-structure ionic thresholds $\text{Xe}^+ 5p^5 2P_{3/2}$ and $2P_{1/2}$, which represent the two products. This problem is handled through multichannel quantum defect theory (MQDT), as we have shown in earlier work [6]. In the framework of MQDT, given the quantum defects μ_α 's and transformation matrix $U_{\alpha i}$, we can expand the final state wave function in terms of spherical harmonics Y_{lm_i} . Namely, the continuum wavefunction can be written as,

$$|f_{m_s, m_{J_c}, J_c}(\hat{k}, r)\rangle = \sum_{l, m_l} i^l e^{-i\delta_l} Y_{lm_l}^*(\hat{k}) \sum_{j, J, \alpha} e^{-i\pi\mu_\alpha} (\alpha | J_c j J M_J) \times (J_c j J M_J | J_c m_{J_c} j m_j) (J_c m_{J_c} j m_j | l m_l s m_s) |\alpha\rangle, \quad (16)$$

where δ_l is the Coulomb phase shift, and $\hat{k} = (\theta, \varphi)$ and m_s are the direction of the photoelectron with respect to the laser polarization axis for linear polarization and

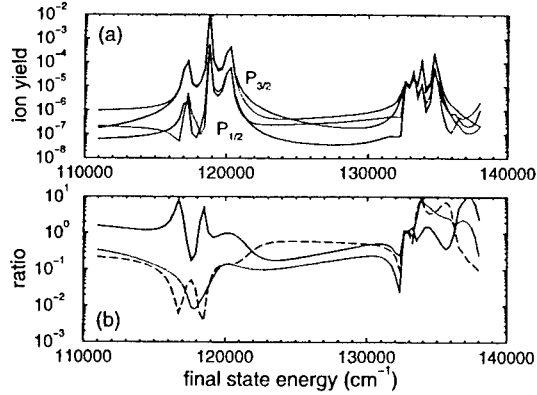


Figure 3: Ionization yield and branching ratio of Xe as a function of final state energy. $I_{3\omega} = 10 \text{ W/cm}^2$ and $I_\omega = 10^8 \text{ W/cm}^2$. (a) Ionization yield into channels $\text{Xe}^+ \ ^2P_{3/2}$ and $^2P_{1/2}$. Relative phase is set to $\phi = 0$ (solid) or $\phi = \pi$ (dashed). (b) Branching ratio at $\phi = 0$ (dotted) or $\phi = \pi$ (dashed). In (b), the ratio of branching ratios at $\phi = 0$ and $\phi = \pi$ has also been plotted (solid line).

the projection of the spin onto the quantization axis. The ionic core is described by the total angular momentum J_c and its projection m_{J_c} . The N-photon partial ionization amplitude is now written as

$$M^{(N)}(\hat{k})[m_s, m_{J_c}, J_c] = \sum_{l, m_l, j, J, \alpha} i^l (-1)^{1/2 - m_j - j + J_c - M_J} e^{i\delta_l + i\pi\mu_\alpha} Y_{lm_j}(\hat{k}) [(2j + 1)(2J + 1)]^{1/2} \times \begin{pmatrix} l & s & j \\ m_l & m_s & -m_j \end{pmatrix} \begin{pmatrix} j & J_c & J \\ m_j & m_{J_c} & -M_J \end{pmatrix} Z_{i\alpha} D_\alpha^{(N)}. \quad (17)$$

The differential ionization rate under the presence of two fields with the intensities $I_{3\omega}$ and I_ω (both in W/cm²) is given by,

$$\frac{dR}{d\Omega_s} = \sum_{m_s, m_{J_c}} \left| n_1 M^{(1)}(\hat{k})[m_s, m_{J_c}, J_c] \sqrt{I_{3\omega}} + e^{i\phi} n_3 M^{(3)}(\hat{k})[m_s, m_{J_c}, J_c] \sqrt{I_\omega^3} \right|^2, \quad (18)$$

where $n_1 = 0.767$ and $n_3 = 5.47 \times 10^{-18}$ are the conversion factors to the appropriate units (sec⁻¹).

The total ionization rate R is now obtained by integrating the calculated differential ionization rate $dR/d\Omega_s$ over the solid angle Ω_s . Obviously, the interference due to the two laser fields occurs between the states with the *same* Y_{lm_l} for R and between *any* states with *any* Y_{lm_l} for $dR/d\Omega$. From the equations given above,

it should be clear that this formalism is a generalization of the equation we have shown in Eq.(8)

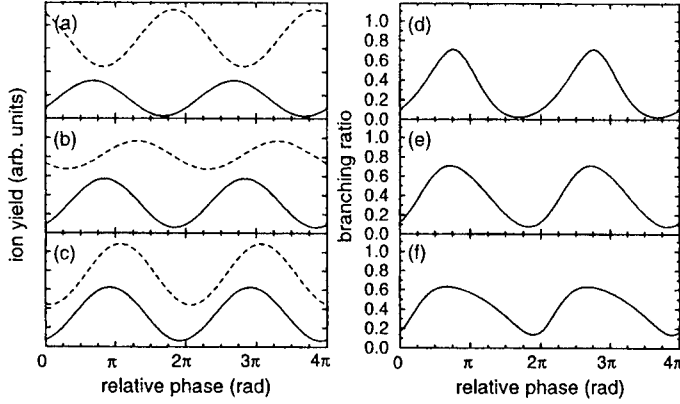


Figure 4: Modulation of the photoionization signals for $\text{Xe}^+ 5p^5 \ ^2P_{3/2}$ (solid) and $^2P_{1/2}$ (dashed) ion at three different final state energies (a) 123000cm^{-1} , (b) 125100cm^{-1} , and (c) 127100cm^{-1} above the atomic ground state as a function of the relative phase ϕ . The laser intensities are chosen to be $I_{3\omega} = 10\text{W/cm}^2$ and $I_\omega = 10^{10}\text{W/cm}^2$. (d)-(f) Branching ratios as a function of the relative phase ϕ . Graphs (d)-(f) correspond to graphs (a)-(c), respectively.

There are no resonances in the energy range $120000\text{-}130000\text{ cm}^{-1}$ above the atomic ground state, and there are no near-two-photon resonances with intermediate bound states either. We have thus a clear case of two coupled continua. Choosing the intensities $I_{3\omega} = 10\text{ W/cm}^2$ and $I_\omega = 10^{10}\text{ W/cm}^2$, we have calculated the product yields as well as the branching ratio as a function of final state energy. The result is presented in Fig.3. In Fig.4, we now show the modulation of two products $\text{Xe}^+ 5p^5 \ ^2P_{3/2}$ (solid) and $^2P_{1/2}$ (dashed) as a function of the relative phase ϕ at three different final state energies. We have, in addition, plotted in Fig.5 the phase lag between the two products as a function of final state energy. Clearly, the phase lag varies drastically over the energy range $120000\text{-}130000\text{ cm}^{-1}$, which lies in a smooth continuum very far away from resonances of any type. Note, however, that in the same figure, we have included the phase lag slightly outside the smooth region to illustrate the effect of intermediate two-photon resonances, mentioned earlier.

As a second example, we have calculated and plotted in Fig.6 the variation of the branching ratio of the two products $\text{Ca}^+(4s)$ and $\text{Ca}^+(3d)$, starting from the ground state $4s^2$ of Ca, as a function of final state energy under the presence of two laser fields with frequencies ω and 3ω with well-defined relative phase ϕ . Modulation of each product is plotted in Fig.7 as a function of the relative phase ϕ at two different final state energies. We have now employed the complete channel

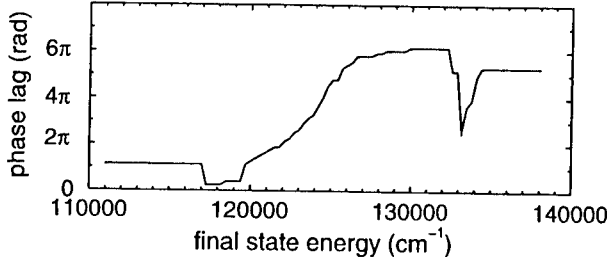


Figure 5: Variation of the phase lag of the two products $\text{Xe}^+ 5p^5 2P_{3/2}$ and $2P_{1/2}$ due to photoionization as a function of final state energy. All parameters are chosen to be the same as those for Fig.4.

functions, as obtained through an L^2 basis [13]. The results shown in Fig.7 again clearly demonstrate a phase lag between the two products far away from resonance (Fig.7(a)), and for comparison near the resonance (Fig.7(b)). Note that Eqs.(3) and (8) would have predicted zero phase lag for the case of Fig.7(a).

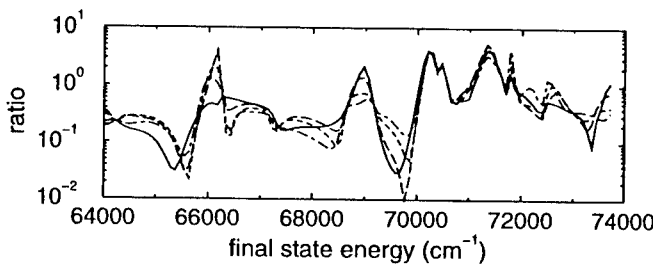


Figure 6: Variation of the branching ratio of $\text{Ca}^+ 4s$ and $3d$ ions for four different relative phases $\phi = 0$ (solid), $\pi/3$ (dashed), $2\pi/3$ (dotted), and π (dot-dashed). Laser intensities are chosen to be $I_{3\omega} = 10^2 \text{ W/cm}^2$ and $I_\omega = 10^8 \text{ W/cm}^2$.

In summary and conclusion, formation of products through photoabsorption involves continua. Efficient control of branching ratios of products through the relative phase of the two fields, irrespective of the presence of resonances, is much more flexible if a phase lag in the modulation of the two products, as a function of the relative phase of the fields, is non-zero. The general condition for this to occur is that the two continua be coupled through some intra-system interaction. The coupling between dissociation and ionization, as modeled in Ref.[10, 11], is one case in point. As we have shown above, the effect is to be found in atoms as well. We

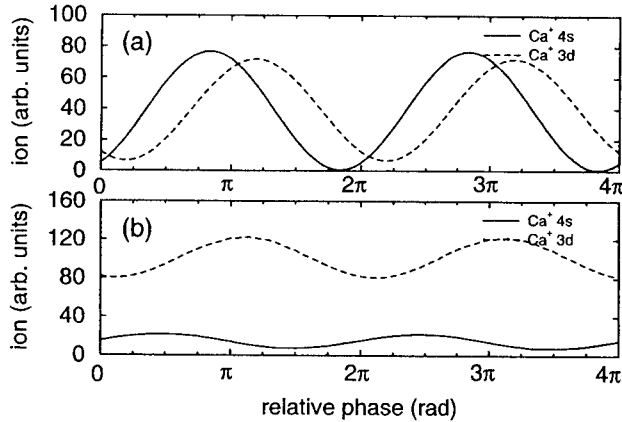


Figure 7: Modulation of the photoionization yield of Ca^+ 4s and 3d ions at two different final state energies. Laser intensities are the same as those for Fig.6. Final state energies are chosen to be (a) 66167cm^{-1} and (b) 68010cm^{-1} .

would thus suggest that, in order to emphasize the generality of the effect, it may be preferable to use the term channel phase. This also implies that, in addition to its relevance to product control, the effect may be a useful tool for the direct study of the relative phase of coupled channels, in atoms as well as molecules. Finally, in view of recent work on quantum confined Fano interference [14], in quantum wells, it may be worthwhile to ponder whether these issues of coherent control can be extended to such phenomena; although at first sight, it might seem that the necessary wavelength range may for the moment be inconvenient for phase control that requires some fundamental in the range of photon energy around 0.5eV and its third harmonic.

References

1. Gordon, R.J. and Rice, S.A. (1997) Active Control of the Dynamics of Atoms and Molecules, *Ann. Rev. Phys. Chem.* **48**, 601-641.
2. Chen, C., Yin, Y.-Y., and Elliott, D.S. (1990) Interference between Optical Transitions, *Phys. Rev. Lett.* **64**, 507-510.
3. Park, S.M., Lu, S.-P., and Gordon, R.J. (1991) Coherent laser control of the resonance-enhanced multiphoton ionization, *J. Chem. Phys.* **94**, 8622-8624.
4. Nakajima, T., Lambropoulos, P., Cavalieri, S., and Matera, M. (1992) Modulating ionization through phase control, *Phys. Rev. A* **46**, 7315-7318.

5. Nakajima, T. and Lambropoulos, P. (1993) Manipulation of the Line Shape and Final Products of Autoionization through the Phase of Electric Fields, *Phys. Rev. Lett.* **70**, 1081-1084.
6. Nakajima, T. and Lambropoulos, P. (1994) Effects of the phase of laser fields on autoionization, *Phys. Rev. A* **50**, 595-610.
7. Nakajima, T., Zhang, J. and Lambropoulos, P. (1997) Phase control through channels involving multiple continua and multiple thresholds, *J. Phys. B* **30**, 1077-1095.
8. Shapiro, M., Hepburn, J.W. and Brumer, P. (1988) Simplified laser control of unimolecular reactions simultaneous (ω_1, ω_3) excitation, *Chem. Phys. Lett.* **149**, 451-454.
9. Lefebvre-Brion, H. (1997) Study of the origin of the phase lag between signals in coherent laser control, *J. Chem. Phys.* **106**, 2544-2546.
10. Zhu, L., Suto, K., Fiss, J.A., Wada, R., Seideman, T. and Gordon, R.J. (1997) Effect of Resonances on the Coherent Control of the Photoionization and Photodissociation of HI and DI, *Phys. Rev. Lett.* **79**, 4108-4111.
11. Seideman, T. (1998) The role of a molecular phase in two-pathway excitation schemes, *J. Chem. Phys.* **108**, 1915-1923.
12. Zhu, L., Kleiman, V., Li, X., Lu, S., Trentelman, K. and Gordon, R.J. (1995) Coherent Laser Control of the Product Distribution Obtained in the Photoexcitation on HI, *Science* **270**, 77-80.
13. Lambropoulos, P., Maragakis, P. and Zhang, J. Two-Electron Atoms in Strong Fields, *Physics Reports* (to be published).
14. Bar-Ad, S., Kner, P., Marquezini, M.V., Mukamel, S., and Chemla, D.S. (1997) Quantum Confined Fano Interference, *Phys. Rev. Lett.* **78**, 1363-1366

LASING WITHOUT INVERSION VIA INTERFERENCE OF DOUBLE-DARK RESONANCES IN ATOMIC AND QUANTUM WELL SYSTEMS

M. O. SCULLY^{1,2}, M. FLEISCHHAUER^{1,3}, E. S. FRY^{1,2}, A. IMAMOĞLU⁴,
M. D. LUKIN^{1,2,5}, D. NIKONOV⁴, TH. WALTHER¹ AND S. F. YELIN^{2,3}

¹*Department of Physics, Texas A&M University, College Station,
TX 77843*

²*Max-Planck-Institut für Quantenoptik, 85748 Garching, Germany*

³*Sektion Physik, Ludwig-Maximilians-Universität München, D-
80333 Germany*

⁴*Dept. of Electr. and Comp. Eng., Univ. of CA, Santa Barbara,
CA 93106*

⁵*ITAMP, Harvard University, Cambridge, MA 02138*

Abstract. Three level systems driven by two coherent fields result in dark state (coherent population trapped) resonances. Such states are in many instances the basis for electromagnetically induced transparency (EIT) and lasing without inversion (LWI). Inhomogeneous broadening due to atomic motion in gases, or different effective masses for various levels in quantum wells presents a minor problem for EIT, but is more serious in the case of LWI. However, recent work involving four level systems driven by three coherent fields results in certain sharp features (interference between double-dark resonances) in the optical response. We here show that such double-dark states are interesting and potentially useful in mitigating the effects of inhomogeneous broadening in atomic and semiconductor quantum well systems.

1. Introduction

Fano interferences [1] between photons spontaneously emitted from the $|\pm\rangle$ dressed states of a Λ -system is the basis of EIT [2], see Fig. 1. When the $b \rightarrow a$ and $c \rightarrow a$ transitions are inhomogeneously broadened, but remain in two-photon Raman resonance, EIT persists. Moreover, when atoms are

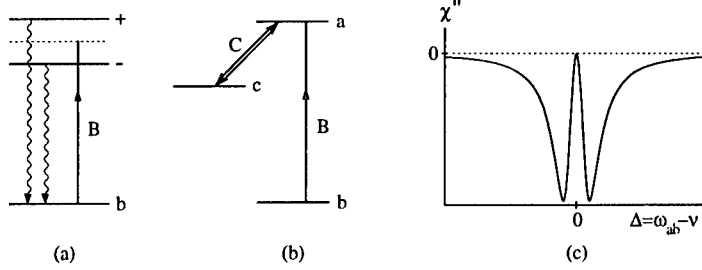


Figure 1. The dressed states $|\pm\rangle = (|a\rangle \pm |c\rangle)/\sqrt{2}$ in (a) are prepared by a coherent drive C coupling $|c\rangle$ and $|a\rangle$ as indicated in (b). This results in EIT (c). $B(C)$ is the Rabi-frequency for the $b \leftrightarrow a$ ($c \leftrightarrow a$) transition, respectively and ν denotes the probe frequency.

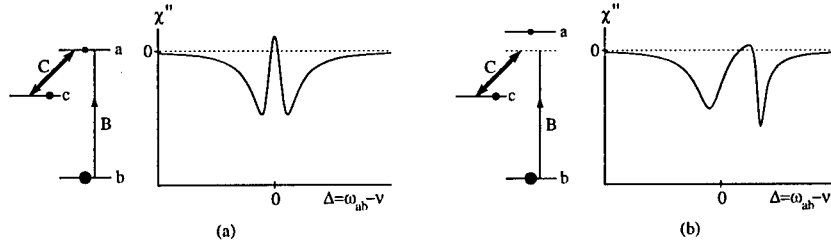


Figure 2. (a) Gain can be produced even when N_b is larger than N_a and N_c . When level $|a\rangle$ is “detuned”, as indicated in (b), a larger Rabi-frequency C is required to obtain LWI and gain is reduced due to “Stark broadening” (power broadening) of level $|a\rangle$.

injected in the upper levels $|c\rangle$ and $|a\rangle$, LWI [3] may occur (c.f. Fig. 2a). When level $|a\rangle$ is inhomogeneously broadened, LWI gain can be markedly reduced, as suggested in Fig. 2b; the broadening mechanism may be Doppler or effective mass broadening, etc., as indicated in Fig. 3.

2. Lasing without inversion in quantum well structures

Consider the situation depicted in Fig. 4. The atomic polarization $P_{ab} = \varphi \rho_{ab} N$ governs the gain or loss of the laser field B , where φ is the dipole matrix element, ρ_{ab} is the off-diagonal matrix element containing the physics, and N is the effective density of atoms or electrons. For the system of Fig. 4 the driving polarization is given by

$$\rho_{ab} = \frac{iB}{\Gamma_{ab}\Gamma_{cb} + |C|^2} \left[\Gamma_{cb}(\rho_{aa}^{(0)} - \rho_{bb}^{(0)}) + \frac{|C|^2}{\Gamma_{ca}}(\rho_{cc}^{(0)} - \rho_{aa}^{(0)}) \right], \quad (1)$$

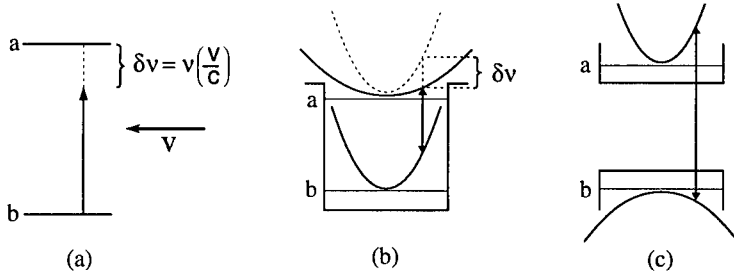


Figure 3. Inhomogeneous broadening due to differing atomic velocities for a gas (a), or different band curvatures (b,c). Artistic license has been taken in (b), since the electronic motion associated with sub-bands $|a\rangle$ and $|b\rangle$ is perpendicular to the page. (c) depicts the case of valence to conduction band transitions in which the curvature has a different sign.

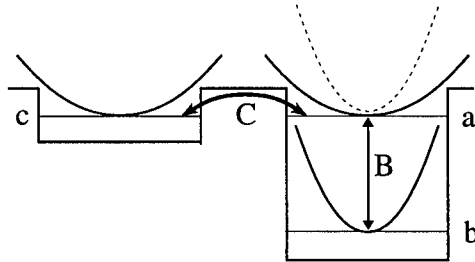


Figure 4. Quantum well LWI setup. Resonant tunneling with rate C couples states $|c, k\rangle$ and $|a, k\rangle$, laser Rabi rate B describes the frequency of the $b \leftrightarrow a$ transition

where the notation is defined in Table 1.

For EIT, $\rho_{aa}^{(0)} = \rho_{cc}^{(0)} = 0$ and when B and C are in two-photon Raman resonance ($\Delta_{ab} = \Delta_{ac}$) $\Gamma_{cb} = \gamma_{cb} \approx 0$. Thus ρ_{ab} is close to zero, i.e. absorption vanishes. We note that the effects of “stark broadening” of level $|a\rangle$ are contained in the denominator of Eq.(1). Since the stark denominator is multiplying the term in square brackets, which in the ideal case ($\gamma_{cb} = 0$) is zero, it has no effect on ρ_{ab} , i.e. stark broadening does not weaken EIT.

The situation is different for LWI. Now, we arrange for the term in square brackets to be positive (on resonance) which corresponds to gain. This occurs just by making $|C|^2$ large enough, even if the LWI condition, $\rho_{bb}^{(0)} > \rho_{cc}^{(0)} > \rho_{aa}^{(0)}$, is satisfied. But now the stark denominator is important and will lead to a saturation of gain, if $|C|^2 \gg |\Gamma_{cb}\Gamma_{ab}|$, as is clear from Eq.(1).

Consider now the case in which the upper $|a\rangle$ sub-band is inhomogeneously broadened as in Fig. 3. The effect of detuning comes into play via

Symbol	Parameter
$\rho_{\alpha\alpha}^{(0)}$	population in $ \alpha\rangle$ to zeroth order in B
Γ_{ab}	$\gamma_{ab} + i\Delta_{ab}$
Γ_{ca}	$\gamma_{ca} + i\Delta_{ca}$
Γ_{cb}	$\gamma_{cb} + i(\Delta_{ab} - \Delta_{ac}) \equiv \gamma_{cb} + i(\Delta_{ab} + \Delta_{ca})$
Γ_{cd}	$\gamma_{cd} + i\Delta_{cd}$
$\gamma_{\alpha\beta}$	$(\gamma_\alpha + \gamma_\beta)/2 + \gamma_{\text{ph}}$
γ_α	decay rate out of $ \alpha\rangle$
γ_{ph}	phase decay rate
Δ_{ab}	detuning of the probe B : $\omega_{ab} - \nu_B$
Δ_{ac}	detuning of the drive C : $\omega_{ac} - \nu_C$
Δ_{cd}	detuning of D : $\omega_{cd} - \nu_D$
α, β	a, b, c or d

TABLE 1. Notation used throughout the text.

the Γ_{cb} , Γ_{ca} and Γ_{ab} factors of Eq.(1). In fact, depending on the specific model of pumping, the zeroth order populations also depend on the inhomogeneous broadening. However, in order to simplify the following discussion, we assume a “clamped”, i.e. fixed population. If only the state $|a, k\rangle$ contributes to inhomogeneous broadening, i.e., only the energy E_a varies as in Fig. 3a and 3c, Γ_{cb} is not affected by the spread. Specifically,

$$\Gamma_{cb} = \gamma_{cb} + i[(\nu_B - \omega_{ab}) - (\nu_C - \omega_{ac})] = \gamma_{cb} + i[(\nu_B - \nu_C) - \omega_{cb}], \quad (2)$$

since $\omega_{ab} - \omega_{ac} = \omega_{cb}$. In this situation, we see that inhomogeneous broadening enters only through the Γ_{ab} and Γ_{ca} terms in Eq.(1). Thus, we can tune the fields such that $\Gamma_{cb} = \gamma_{cb}$ (two-photon resonance), and choose $|C| \geq \sqrt{\gamma_{cb}|\Gamma_{an}|}$, where $n = b, c$ to make the LWI term in Eq.(1) dominate. However, for sufficiently large values of C the polarization is strongly diminished. Thus, inhomogeneous broadening of the $|a\rangle$ -state frequency leads to a reduction of gain just like in a two-level system. Moreover in order to fulfill the LWI-gain condition

$$|C| \geq \sqrt{\gamma_{cb}|\Gamma_{an}|} \quad (3)$$

in the non-ideal case, $\gamma_{cb} \neq 0$, large resonant tunneling rates are required. This is where double-dark LWI comes into play.

3. Double-dark LWI

Usually any perturbation on a dark state results in an undesirable loss of coherence. However, as was first shown in the study of short-wavelength LWI [4], the introduction of a coherently coupled fourth level can improve LWI performance. More recently we have studied the system of Fig. 5a in detail and found sharp new features in the resonant optical susceptibility for LWI as shown in Fig. 5b [5]. The sharp spike in Fig. 5b can be understood by writing the dressed states for Fig. 5a to first order in D (c.f. Fig. 5c), namely

$$|+\rangle = \frac{1}{\Omega} \left[-\omega_+ |a\rangle + C \left(|c\rangle + \frac{D}{\omega_0 - \omega_+} |d\rangle \right) \right], \quad (4)$$

$$|-\rangle = \frac{1}{\Omega} \left[C |a\rangle + \omega_+ \left(|c\rangle + \frac{D}{\omega_0 - \omega_-} |d\rangle \right) \right], \quad (5)$$

$$|0\rangle = |d\rangle - \frac{DC}{\tilde{\Omega}^2} |a\rangle + \frac{D(\Delta_{cd} + \Delta_{ac})}{\tilde{\Omega}^2} |c\rangle, \quad (6)$$

$$\omega_{\pm} = -\frac{\Delta_{ac}}{2} \mp \sqrt{C^2 + \frac{\Delta_{ac}^2}{4}}, \quad (7)$$

$$\omega_0 = \Delta_{cd}, \quad (8)$$

where $\Omega^2 := C^2 + (\Delta_{ac}/2 + \sqrt{C^2 + \Delta_{ac}^2/4})^2$, and we have assumed, that $|\tilde{\Omega}^2| := |C^2 - \Delta_{cd}(\Delta_{cd} + \Delta_{ac})| \gg D^2$.

In the limit of $D = 0$ the states $|\pm\rangle$ are those defined in Fig. 1 and the energies are those given by Eqs. (7) and (8). But for $D \neq 0$ we now have a new sharp state $|0\rangle$ weakly coupled to $|b\rangle$, with a radiative decay rate going as $|D|^2/|C|^2$. Thus, the sharp spike is due to decays from $|0\rangle$ to $|b\rangle$, with a width limited by the decoherence of the metastable $|d\rangle$ and $|b\rangle$ states.

To proceed we need the double-dark extension of Eq.(1). It is given by

$$\rho_{ab} = \frac{iB}{\Gamma_{ab}} F_{cd} \left[\begin{aligned} & F_d (\rho_{aa}^{(0)} - \rho_{bb}^{(0)}) + \frac{C^2}{\Gamma_{cb}\Gamma_{ca}} R (\rho_{cc}^{(0)} - \rho_{aa}^{(0)}) \\ & - \frac{|C|^2}{\Gamma_{dc}\Gamma_{cb}} \frac{|D|^2}{\Gamma_{da}\Gamma_{db}} \frac{1}{F_c} \left(1 + \frac{\Gamma_{db}}{\Gamma_{ca}} R \right) (\rho_{cc}^{(0)} - \rho_{dd}^{(0)}) \end{aligned} \right], \quad (9)$$

where

$$R = \frac{1 + |C|^2/(\Gamma_{da}\Gamma_{dc}) - |D|^2/(\Gamma_{db}\Gamma_{da})}{1 + |C|^2/(\Gamma_{da}\Gamma_{dc}) + |D|^2/(\Gamma_{ca}\Gamma_{da})}, \quad (10)$$

$$F_c = 1 + |C|^2/(\Gamma_{da}\Gamma_{dc}), \quad (11)$$

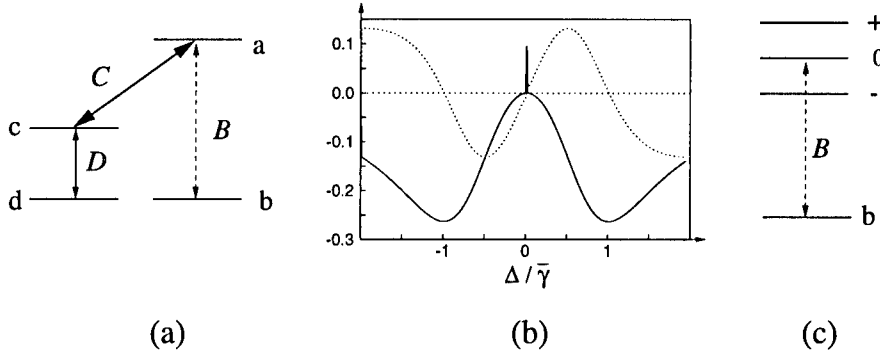


Figure 5. The four levels in (a) are coupled by Rabi-frequencies B , C , and D . (b) The solid and dotted lines are the imaginary and real part of the susceptibility (as a function of $\Delta \equiv \Delta_{ab}$ with $\Delta_{ac} = \Delta_{cd} = 0$), respectively. The imaginary part shows sharp spikes at $\Delta = 0$. (c) The physics is explained below in terms of the dressed states $|\pm\rangle$ and $|0\rangle$.

$$F_d = 1 + |D|^2/(\Gamma_{cb}\Gamma_{db}), \quad (12)$$

$$F_{cd} = \frac{1}{1 + |C|^2/(\Gamma_{ab}\Gamma_{cb}) + |D|^2/(\Gamma_{cb}\Gamma_{db})}, \quad (13)$$

and $\Gamma_{ab} = \gamma_{ab} + i\Delta_{ab}$, $\Gamma_{ca} = \gamma_{ca} + i\Delta_{ca}$, $\Gamma_{cb} = \gamma_{cb} + i(\Delta_{ab} + \Delta_{ca})$, $\Gamma_{db} = \gamma_{db} + i(\Delta_{ab} + \Delta_{ca} - \Delta_{cd})$, exactly analogous to the parameters in Table 1.

4. Inhomogeneous broadening, the double-dark state, and LWI

Note that a shift of the $|a\rangle$ state (i.e. inhomogeneous broadening of $|a\rangle$) does not affect ω_0 as given by Eq.(8) (valid in the weak D limit), i.e. ω_0 is independent of the energy of state $|a\rangle$ for weak D . Fig. 6 shows the dressed state frequencies as a function of excited state detuning for $D = 0.5$ and $C = 1$. One can see that the maximum shift of the $|0\rangle$ -state is $\pm D$.

Guided by the fact that the dressed-state resonance in the double-dark system remains narrow in the presence of inhomogeneous broadening, we plot ρ_{ab} as given by Eq.(9) for several values of the upper-state detuning. We see that indeed the LWI peak remains sharp and strong, even for substantial detuning of the $|a\rangle$ level (c.f. Fig. 7).

In order to convey the potential of the double-dark state system, let us conclude this section with a comparison of the effects of inhomogeneous broadening on gain in the case of 2-level, dark, and double-dark systems as shown in Fig. 8. To this end we consider the case in which we “clamp” the populations ρ_{aa} , ρ_{bb} , ρ_{cc} , and ρ_{dd} . This should be regarded as a “best case” limit for the double-dark states. As noted above, in real experiments, the populations will be influenced by atomic detuning, which strongly depends on the pump mechanisms. This will be discussed in more detail elsewhere.

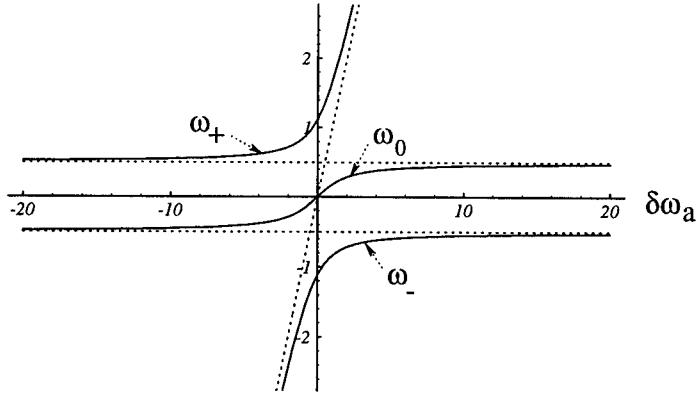


Figure 6. The frequencies of the dressed states $|\pm\rangle$ and $|0\rangle$ as a function of the detuning $\delta\omega_a$ of the excited-state. Dotted lines correspond to dressed state frequencies $\pm D$ and $\delta\omega_a$, when $C=0$. The parameters are $C = 1$ and $D = 0.5$, respectively. The frequency unit is γ_{ab} .

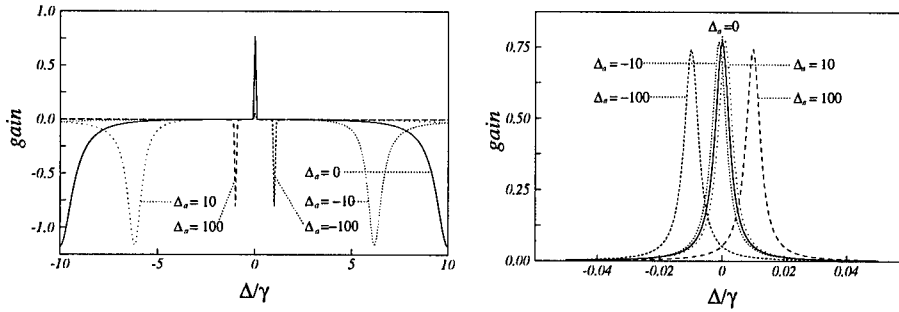


Figure 7. The gain as a function of $\Delta = \Delta_{ab} - \Delta_{ac}$ for several values of the detuning Δ_a of the upper level (in units of $\gamma = \gamma_{ab}$). The right shows an enlargement of the central peak in the left figure.

That double-dark resonances can reduce the influence of inhomogeneous broadening of the excited state $|a\rangle$ on the gain is illustrated again in Fig. 8c where the average gain in the presence of inhomogeneous broadening is shown as a function of the normalized width $\Delta\omega_a/\gamma_{ab}$ for different Rabi-frequencies. Fig. 8c is to be compared and contrasted to Figs. 8a and 8b and shows the potential advantage of double-dark resonances.

5. Inhomogeneous broadening in quantum well LWI

As noted earlier, different effective masses can result in inhomogeneous broadening and reduction of gain in semiconductor quantum well lasers. For example, consider a scheme similar to that considered by the Imamoğlu

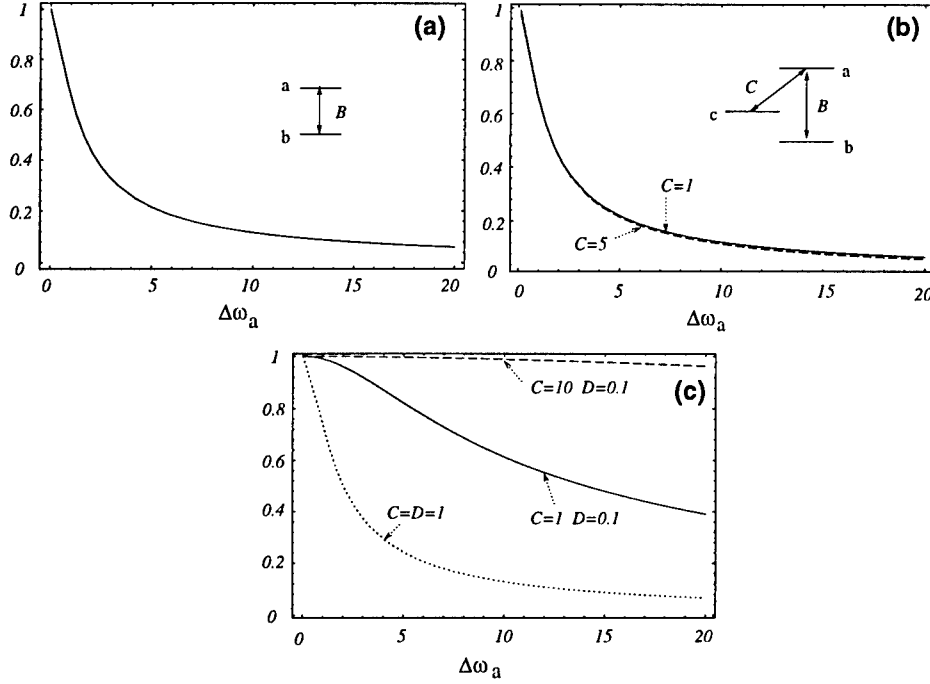


Figure 8. (a) The gain in a two-level system as a function of the width $\Delta\omega_a$ of a Gaussian distribution of excited state frequencies. The frequency unit is the coherence decay rate γ_{ab} . (b) The gain in a Λ -system for $C = 1$ (solid line) and $C = 5$ (dashed line) as a function of the inhomogeneous width $\Delta\omega_a$ of a Gaussian distribution of excited state frequencies. The frequency unit is $\gamma_{ab} = \gamma_{ac}$. (c) The gain in the double-dark system for $C = D = 1$ (dotted), $C = 1$, $D = 0.1$ (solid) and $C = 10$ and $D = 0.1$ (dashed) as a function of the inhomogeneous width $\Delta\omega_a$ of a Gaussian distribution of excited state frequencies. The frequency is in units of $\gamma = \gamma_{ab}$

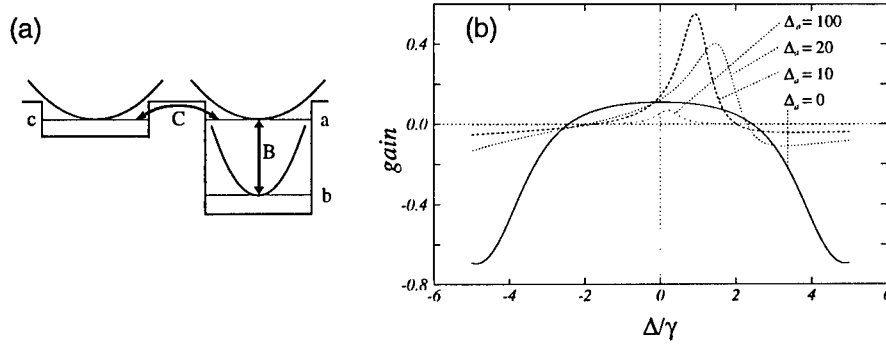


Figure 9. (a) Tunnel coupled $|a\rangle$ and $|c\rangle$ states with different effective mass for $|a\rangle$. (b) The gain for the system in (a) for different energies of the excited state.

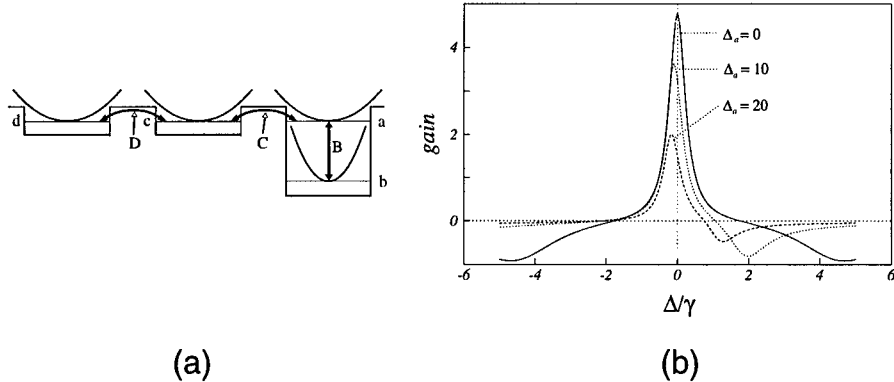


Figure 10. (a) A four-level tunnel coupled structure analogous to the atomic double-dark problem. (b) Gain for a double-dark “quantum well” like system as shown in (a) for various detunings.

group [6] depicted in Fig. 9a. When we carry out calculations for related systems (we actually do atoms), we obtain a gain which is strongly dependent on the upper level detuning (which is so to say different gain for different k values; c.f. Fig. 9b). Similarly, we find for the double-dark semiconductor system (again, we carry out appropriate atomic analog calculations) of Fig. 10a the gain curve shown in Fig. 10b.

Comparing Figs. 9 and 10, we see that double-dark states in quantum well structures hold promise and merit further study. One example of such studies is the interband LWI/Raman system of Fig. 11.

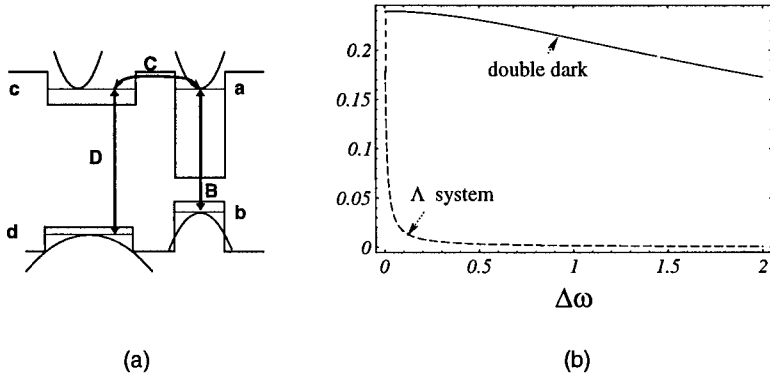


Figure 11. (a) Quantum well interband laser without inversion based on double-dark resonances. (b) The dependence of the gain for Λ (dashed) and double-dark configurations (solid line) on the normalized width $\Delta\omega$ of Gaussian inhomogeneous distributions. The injection rate is $r = 0.001$; the radiative decay on the laser transition is $\gamma = 1$; the removal rate from the $|b\rangle$ -state is $\gamma_0 = 0.01$; the Rabi-frequencies are $C = 5$, $D = 0.1$. (Optimized detuning for Λ)

In Fig. 11a we show a quantum well system, where the $|a, k\rangle$ and $|c, k\rangle$ states are in the conduction band and have a curvature opposite to that of the $|b, k\rangle$ and $|d, k\rangle$ states in the valence band. $|c, k\rangle$ and $|a, k\rangle$ are coupled via resonant tunneling and $|c, k\rangle$ and $|d, k\rangle$ by a weak electro-magnetic field D . Fig. 11b compares the dependence of the gain on inhomogeneous broadening for the case of a Λ system ($D = 0$ and injection into $|c\rangle$) and the double-dark system ($D \neq 0$ and injection into $|d\rangle$).

Acknowledgment

The authors gratefully acknowledge the support from the Office of Naval Research, the Welch Foundation, the Texas Advanced Research and Technology Program and the Rome Laboratories.

References

1. U. Fano, Phys. Rev. **124**, 1866 (1961); S. E. Harris, Phys. Rev. Lett. **62**, 1033 (1989); A. Imamoğlu, Phys. Rev. A **40**, 2835 (1989); M. Fleischhauer, C. H. Keitel, L. M. Naroducci, M. O. Scully, S.-Y. Zhu, and M. S. Zubairy, Opt. Comm. **94**, 599 (1992);
2. K. J. Boller, A. Imamoğlu, and S. E. Harris, Phys. Rev. Lett. **66**, 2593 (1991); for a review of the subject, see S. E. Harris, Physics Today **50**, 7, 36 (1997).
3. O. A. Kocharovskaya and Ya. I. Khanin, Pis'ma Zh. Exp. Teor. Fiz. **48**, 581 (1988) [JETP Lett. **48**, 630 (1988)]; S. E. Harris, Phys. Rev. Lett. **62**, 1033 (1989); M. O. Scully, S.-Y. Zhu, A. Gavrielides, Phys. Rev. Lett. **62**, 2813 (1989);
4. A. S. Zibrov, M. D. Lukin, D. E. Nikonov, L. Hollberg, M. O. Scully, V. L. Velichansky, and H. G. Robinson, Phys. Rev. Lett. **75**, 1499 (1995).
5. M. D. Lukin, S. F. Yelin, M. Fleischhauer, and M. O. Scully, "Interference between double dark resonances: an optical response induced by coherently altered quantum superpositions" (submitted)
6. A. Imamoğlu, and R. J. Ram, Opt. Lett. **19**, 1744 (1994);

PART II: Coherent Control in Semiconductors

COHERENCE CONTROL OF FREE CARRIERS IN BULK SEMICONDUCTORS

HENRY M. van DRIEL, JOHN E. SIPE,
ALAIN HACHÉ and JAMES M. FRASER
*Department of Physics, University of Toronto
and
Photonics Research Ontario
Toronto, Canada, M5S 1A7*

Abstract. We review our recent experimental and theoretical work on the use of optically-induced quantum interference to generate and control electrical currents and free carrier populations in bulk, low-temperature-grown GaAs at room temperature. Using phase-related nanosecond, picosecond or femtosecond pulses at 1550 and 775 nm and the quantum interference between single and two photon interband absorption pathways, we produce peak current densities of $\sim 10 \text{ Acm}^{-2}$ for only 10^{14} cm^{-3} carriers in GaAs (001). Within a nonlinear optics context, the induced coherence effect can be understood in terms of a divergent piece of a $\chi^{(3)}$. With 150 fs optical pulses at wavelengths similar to those used in current control we are also able to use quantum interference effects to achieve control of electron-hole populations in GaAs (111). The nonlinear susceptibility responsible for this type of interference is $\chi^{(2)}_{xyz}$.

1. Introduction

Optical phase is not normally thought of as a control parameter, although it is widely recognized that phase manifests itself passively in a wide variety of physical experiments, especially those involving light interference. Manykin and Afanas'ev [Manykin, 1967] were perhaps the first to recognize that optical phase could also be used actively to bring about interference between quantum mechanical processes such as simultaneous absorption of one and three photons connecting the same initial and final states in atoms. The population of the excited state and

hence the absorption is controlled by interference in the quantum mechanical amplitudes associated with the two pathways through the relative phase of the two optical beams. In the last decade, partly because of advances in laser technology, interest in coherence control (CC) of matter has increased particularly for atomic and molecular processes and chemical reactions [Brumer, 1989; Warren; 1993; Chen, 1992; Zhu, 1995]. Coherence effects have also been used to propose spatially asymmetric ejection of photoelectrons from impurities in fibers [Dianov, 1989; Anderson, 1991], and these effects have also been observed from atoms [Yin, 1992], from impurities in semiconductors [Kurizki, 1989] and from semiconductor quantum wells [Dupont, 1995]. Coherence control of exciton populations in quantum wells has been observed by Heberle et al. [Heberle, 1995] using phase related femtosecond pulses of the same frequency and, more recently, Pötz [Pötz, 1997] has shown theoretically population control for intersubband transitions in quantum wells using visible and microwave radiation.

Nearly all coherence control effects proposed or observed involve discrete states. However Éntin [Éntin, 1989] pointed out that one could also use *intraband* absorption of harmonically related beams in a metal or doped semiconductor to coherently control an electrical current. To date, these processes have not been observed. A number of years ago we proposed [van Driel, 1994; Atanasov, 1996] and later observed [Haché, 1997; Haché, 1998] coherence generation and control of photocurrents via *interband* transitions in a bulk semiconductor such as GaAs or low-temperature-grown GaAs (LT-GaAs).

We now consider the salient features associated with the generation and control of photocurrents in LT-GaAs at room temperature using femtosecond, picosecond and nanosecond optical pulses at 1550 and 775 nm. We also demonstrate partial population control in GaAs using similar pulses. Ironically, the use of quantum mechanics and the superposition principle allows for the generation of classical-like states that are difficult to generate otherwise. However, since the states are generated by simultaneous linear and nonlinear optical absorption processes, it should not come as a surprise that one can therefore develop a macroscopic description of these processes based on nonlinear optics. In the case of current control, we can understand the underlying physics in terms of a divergent piece of a $\chi^{(3)}$ process, while population control involving harmonically-related beams can be understood in terms of a $\chi^{(2)}$ process.

2. Coherently Controlled Currents in LT-GaAs

Figure 1 illustrates generation of electron-hole pairs via simultaneous single and two photon absorption of coherently related beams of frequency ω and 2ω , for the case where $\hbar\omega < E_g < 2\hbar\omega$ with E_g being the semiconductor band-gap energy. For single photon absorption of 2ω photons coupling valence (v) and conduction (c) band states, the transition amplitude is $a^{2\omega} \propto \langle \psi_v | E^{2\omega} \cdot p | \psi_c \rangle = p_{vc} \cos\theta E_0^{2\omega} \exp(i\phi_{2\omega})$ where $E_0^{2\omega}$ is the amplitude of the light field, p is the momentum operator and θ is the angle between a linearly polarized field direction and the direction of a Bloch k -vector. (This expression is strictly only true for light hole bands and Kane wave functions but related anisotropic state filling effects are also obtained for heavy-hole bands). For two photon absorption (of “ ω ” photons) from an optical beam polarized along the x-direction, the preferred pathway is an interband virtual transition and then a self-transition in the conduction band. Neglecting other bands of the semiconductor and other possible intermediate states, one then has:

$$\begin{aligned} a^\omega &\propto C(\omega) \langle \psi_v | E^\omega \cdot p | \psi_c \rangle \langle \psi_c | E^\omega \cdot p | \psi_c \rangle \\ &= C(\omega) p_{vc} \cos\theta (E_0^\omega)^2 \exp(2i\phi_{2\omega}) \hbar k_x \end{aligned} \quad (1)$$

where $C(\omega)$ is purely imaginary and contains a frequency dependent denominator accompanying the virtual transition amplitude. Adding the single and two photon transition amplitudes we have

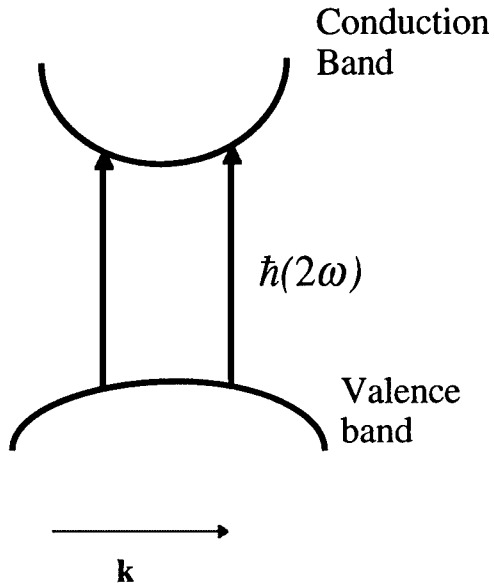
$$a^\omega + a^{2\omega} \propto p_{vc} \cos\theta \{ (E_0^{2\omega} \exp(i\phi_{2\omega}) + C(\omega) (E_0^\omega)^2 \exp(2i\phi_{2\omega}) \hbar k_x \} \quad (2)$$

The transition probability $|a^\omega + a^{2\omega}|^2$ contains an interference term $\propto \hbar k_x \sin(2\phi_{2\omega} - \phi_{2\omega})$ which results in a polar distribution of electrons and holes in momentum space. This is synonymous with an electrical current.

From a macroscopic viewpoint, it was shown [Atanasov, 1996] that the interference of quantum mechanical pathways leads to an electron and hole (e,h) current *injection* process whose rate $\mathbf{j}_{e,h}^I$ is related to the two optical electric fields [25], $\mathbf{E}^\omega, \mathbf{E}^{2\omega}$ by:

$$\mathbf{j}_{e,h}^I = \tilde{\eta}_{e,h} : \mathbf{E}^\omega \mathbf{E}^\omega \mathbf{E}^{-2\omega} + \text{c.c.} \quad (3)$$

Single Photon Absorption



Two Photon Absorption

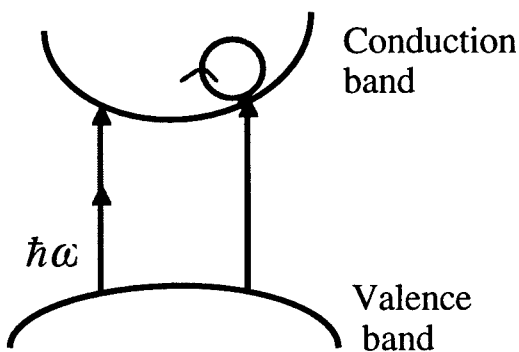


Figure 1. Schematic illustration of single (top) and two photon processes in semiconductors. The right side of the bottom figure illustrates typical states coupled via the virtual transitions.

where $\eta_{e,h}$ is a purely imaginary, fourth-rank tensor. For a semiconductor with zinc-blende symmetry, such as GaAs, this tensor has four independent components, the largest typically being $(\eta_{e,h})_{xxxx}$.

Equation 3 is based on a Fermi's Golden Rule approach since the current relaxation time (typically 100 fs) is long compared to the period of the optical beams; decay effects can be treated separately to a first approximation. We do so phenomenologically by writing a dynamical equation for the evolution of the current density $J_{e,h}$ as

$$\dot{J}_{e,h} = \dot{J}_{e,h}^l - J_{e,h}/\tau_{e,h} \quad (4)$$

where $\tau_{e,h}$ is the current relaxation time. For both beams polarized along the crystalline x axis, the current can be related to $(\eta_{e,h})_{xxxx}$ and, from Eq. 3, also to the phase parameter $\Delta\phi = 2\phi_\omega - \phi_{2\omega}$.

The generated current differs from a conventional current which occurs in a semiconductor when *pre-existing* carriers move in response to a DC electric field. In the case of a CC current, electrons (we ignore the smaller contribution made by holes to the current) are *optically injected* into conduction band states with a speed determined by 2ω , E_g and the electron and hole effective masses respectively. In GaAs this speed is 850 kms^{-1} for a 150 meV electron-hole excess energy (corresponding to single photon absorption at 775 nm). When the single and two photon absorption amplitudes are balanced, this speed is associated with electrons which are also moving in nearly the same direction. For $(\eta_{e,h})_{xxxx} = 20 \text{ s}^{-2} \text{ mCV}^{-3}$, $I_0^\omega = 100 \text{ MWcm}^{-2}$ and $I_0^{2\omega} = 15 \text{ kWcm}^{-2}$ (these intensities will balance single and two photon absorption process so as to optimize the current per carrier generated) with Gaussian pulse widths $\tau_\omega = \tau_{2\omega} = \tau_e = 100 \text{ fs}$, one obtains a surprisingly large peak current $\sim 1 \text{ kAcm}^{-2}$ for a carrier density of only $\sim 10^{14} \text{ cm}^{-3}$. Of course, relaxation effects during the optical pulse as well as beam phase-mismatch effects upon entering the sample can reduce this [Haché, 1998]. In the latter case, for GaAs the single photon absorption depth ($\sim 1 \mu\text{m}$) is nearly the same as the coherence length.

The CC currents do not occur as a result of an optical rectification field acting on pre-existing or optically generated carriers. Rectification effects occur via virtual interband transitions through a 4th rank tensor which has symmetry and phase characteristics similar to $\eta_{e,h}$. However the $\eta_{e,h}$ tensor is related to a *divergent* piece of $\chi^{(3)}(-\varepsilon; \omega, \omega, -2\omega + \varepsilon)$, i.e.,

$$\tilde{\eta} \propto \varepsilon^2 \lim_{\varepsilon \rightarrow 0} \tilde{\chi}^{(3)}(-\varepsilon; \omega, \omega, -2\omega + \varepsilon). \quad (5)$$

More importantly, the CC process is fundamentally different from field-induced acceleration. For CC currents, the carriers are born at high speed and thereafter decelerate. Overall the CC process therefore may offer advantages for physical effects involving rapid current generation, such as more efficient techniques for THz generation [Khurkin, 1995].

We have observed CC currents using harmonically related femtosecond, picosecond and nanosecond pulses with the fundamental beam having a wavelength near 1550 nm. A typical experimental arrangement is shown in Fig. 2. The experimental details are given elsewhere [Haché, 1998]. Phase control of the two beams is achieved with

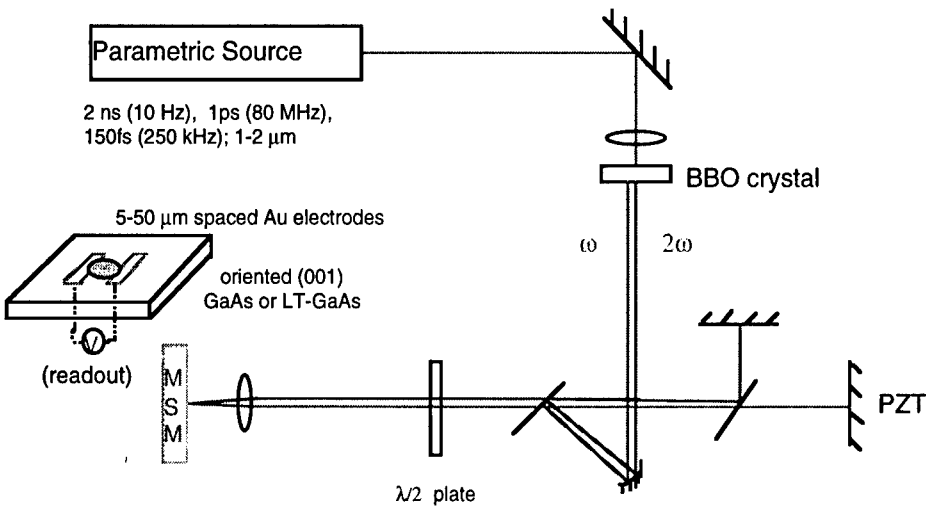


Figure 2. Experimental geometry used to observe steady-state current flow in GaAs.

a modified Michelson interferometer. In our experiments we have observed the currents by monitoring the steady voltage across a metal-semiconductor-metal (MSM) structure as charge accumulates on the metal electrodes. The semiconductor of choice is LT-GaAs since the rapid recombination time (~ 1 ps) prevents the MSM capacitor from discharging between pulses, whose repetition rate was varied from 10 Hz to 80 MHz. CC currents were observed with GaAs only with the 250 kHz repetition rate system. In principle one could also expect to observe CC current in centrosymmetric semiconductors such as Ge or Si as well since η is a 4th rank tensor. To date all experiments have been carried out at room temperature. Figure 3 illustrates the phase dependence of the modulated current when a GaAs (001) sample is illuminated with 150 femtosecond from an 80 MHz optical

parametric oscillator system with an average power of 50 mW (1550 nm) and 2 μ W (775 nm) and an illumination spot size of $\sim 50 \mu\text{m}$. The pulses are linearly co-polarized across the gap of the metal-semiconductor-metal structure, along the (100) direction to take advantage of the large η_{xxxx} tensor element. The data of Fig. 3 is obtained after a $\sim 25\%$ background effect (due to space-charge effects in the vicinity of the electrodes) was subtracted. The peak carrier density is estimated at $\sim 10^{14} \text{ cm}^{-3}$ while the peak current density (within the $\sim 0.5 \mu\text{m}$ absorption depth of the GaAs) is estimated at near 10 A cm^{-2} . We have verified the scaling of the CC current with MSM gap width, with optical field amplitudes and have observed high current generation for carrier density up to 10^{18} cm^{-3} . The peak currents generated are typically less than, but within an order of magnitude of, the theoretical predictions.

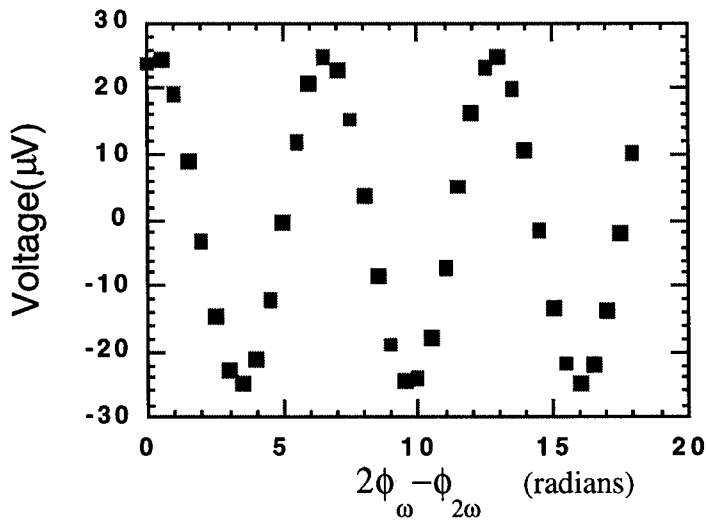


Figure 3. Phase dependence of steady state current measured via the voltage across a metal-semiconductor-metal device employing LT-GaAs.

3. Coherence Control of Electron-hole Populations in GaAs

Coherent control of population has been demonstrated via discrete states in both atomic [Chen, 1992] and quantum well semiconductors

[Heberle, 1995]. One of the questions we have asked ourselves is to what extent similar effects can be observed in bulk semiconductors based on band-band transitions, and in particular whether a density modulation is simultaneously induced in our current control experiments. Because of the rapid carrier dephasing associated with continuum states, it makes little sense to attempt to control such population with pulses of the same frequency, since for all but the shortest pulses, these pulses would have to be overlapped in space and time to overcome dephasing effects and the influence of inhomogeneous broadening associated with the bands (the macroscopic electron and hole interband polarization will decay on a time scale related to the inverse of the optical pulse bandwidth). Coherence control is then trivial as the fields themselves constructively or destructively interfere as they are delayed relative to each other. Rather we have attempted to control a population of carriers, N , using harmonically related pulses. Ignoring dephasing effects, the rate of change of the population can be understood in terms of the power deposited into the sample:

$$2\hbar\omega\dot{N} = \left\langle [\bar{E}^\omega(t) + \bar{E}^{2\omega}(t)] \cdot \frac{d}{dt} [\bar{P}^\omega(t) + \bar{P}^{2\omega}(t)] \right\rangle \quad (6)$$

where the $\langle \rangle$ brackets indicate a time average and P^ω and $P^{2\omega}$ are the linear and nonlinear polarizations induced by the ω and 2ω beams respectively. One then has single photon absorption processes (at 2ω), two photon absorption processes (at ω) and the interference between these process so that the power deposited can be represented as:

$$2\hbar\omega\dot{N} = W_{1-p_t}^{2\omega} + W_{2-p_t}^\omega + W_{int}^{\omega,2\omega} \quad (7)$$

The interference process can be understood within a nonlinear optics formalism as:

$$W_{int}^{\omega,2\omega} = \omega\epsilon_0(Im\chi_{ijk}^{(2)}(-2\omega;\omega,\omega)E_i^{-2\omega}E_j^\omega E_k^\omega \cos(\phi_i^{2\omega} - \phi_j^\omega - \phi_k^\omega)) \quad (8)$$

For a zincblende material such as GaAs, the only nonzero element of $\chi^{(2)}$ is $\chi_{xyz}^{(2)}$. Therefore, in our current control experiments conducted with GaAs (001), there is no density modulation induced by beams which are all of the same polarization. For this reason our efforts to observe population control have involved a GaAs (111) sample used illuminated by perpendicularly polarized beams at normal incidence, although even here the

effective $\chi^{(2)}$ is $0.4\chi_{xyz}^{(2)}$. Figure 4 illustrates the experimental set-up used to measure the CC density changes.

The experiments were carried out with 150 fs pulses with peak irradiance of 800 MWcm^{-2} (1550 nm) and 20 MWcm^{-2} (775 nm) respectively. The peak carrier density generated is $\sim 10^{18} \text{ cm}^{-3}$. In our experiments the density was monitored in two different ways. In the first method we simply observed the transmission of the 775 nm beam, whose total absorption is dictated by its relative phase with the 1550 nm beam. In the second method we used a probe beam at $\sim 870 \text{ nm}$, derived from the

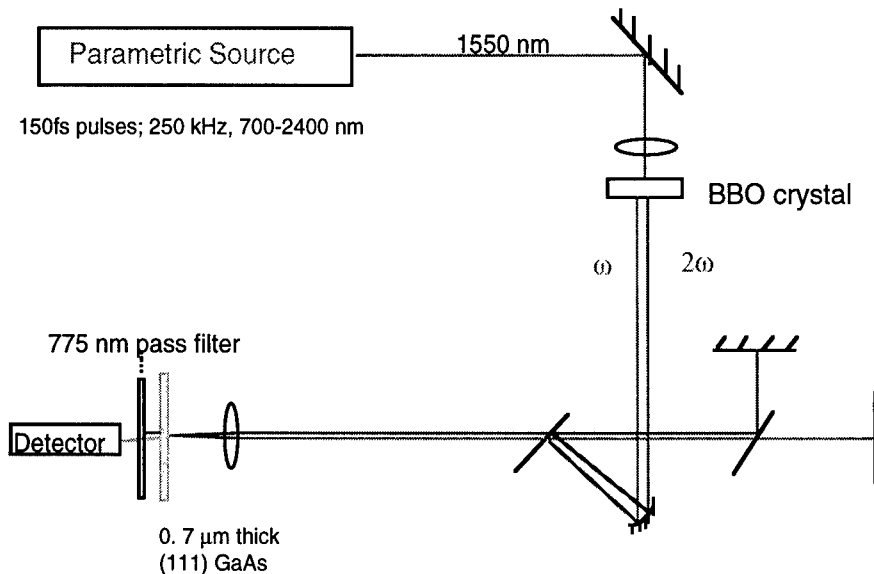


Figure 4. Schematic illustration of experimental geometry used to observe coherent control of carrier density in GaAs.

same optical parametric generator used to generate the 1500 nm beam, to probe the near-band-edge transmission (where state filling effects are largest) of the GaAs. This was done $\sim 5 \text{ ps}$ after the two other pulses were incident on the samples and the carriers had a chance to cool to the band edge. Both methods give similar results. Fig. 5 shows the modulated transmission of the 775 nm beam as a function of the CC phase parameter, $\Delta\phi$.

Note that the phase dependence observed in Fig. 5 can also be induced via a cascaded harmonic generation process as well. In such a process one has a flow of energy between the 1550 and 775 nm beams via a upconversion or downconversion within the GaAs sample *prior* to

absorption of the beams. Such a process leads to a similar phase dependence of the carrier density as that given by Eq. 8, except for a sinusoidal dependence on the phase parameter $\Delta\phi$. This type of process itself is a form of coherence control of carrier generation involving also the real part of $\chi^{(2)}$. We are presently performing careful phase dependent studies of the density control experiments, including sample thickness dependence to separate these two contributors to coherent control of carrier density.

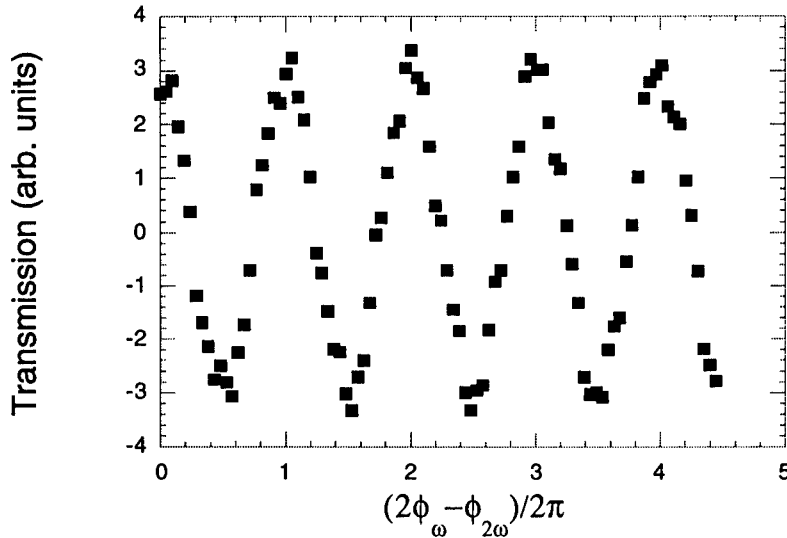


Figure 5. Modulated carrier density in GaAs observed via the transmission of the 775 nm pump beam.

Unlike the current experiments where, in principle it is possible to have all carriers contribute to current flow in a given direction (by balancing single and two photon absorption rates), it is not possible to achieve 100% modulation of the carrier density via coherent control in GaAs(111). Indeed we estimate our transmission modulation in these experiments to be of the order of a few percent. Part of the reason for this is simply related to obvious dephasing effects during the pulse which compete with coherence control. In addition, it is not possible to make use of the full value of $\chi_{xyz}^{(2)}$ for GaAs (111). More fundamentally, since the microscopic pathways which are embedded in $\chi^{(2)}$ are based on interference between those processes connected with single and two photon absorption,

the relative phase of the associated matrix elements and the symmetry of the crystal will dictate the strength of the interference terms in $\chi^{(2)}$ relative to those in $\chi^{(1)}$ and $\chi^{(3)}$. Note that for centrosymmetric systems such as atoms the density control processes discussed here do not occur and $\chi^{(2)}$ is identically zero although $\chi^{(1)}$ and $\chi^{(3)}$ are non-zero. For semiconductors one could optimize the density control by choosing materials with different symmetry classes. In addition density control efficiency may be improved by interfering absorption pathways of fundamental and third harmonic beams via $\chi^{(5)}$ and $\chi^{(1)}$ processes.

4. Summary and Conclusions

In this article we have reviewed our recent efforts to control electrical currents and carrier populations in bulk semiconductors. We have shown how the coherence control effects can be understood in terms of interference of absorption pathways. In addition since the results achieved are based on macroscopic fields, carrier currents and carrier densities, a practical way of understanding the processes is through conventional nonlinear optics. However, even here, the terms we have identified are not typically discussed within conventional nonlinear optics. We have also emphasized how symmetry properties of the crystals dictate the polarization properties of the effects as well as their magnitude.

5. Acknowledgments

We gratefully acknowledge financial support for this work from the Natural Sciences and Engineering Research Council of Canada and Photonics Research Ontario. HMvD also is thankful for financial support from the Killam Program of the Canada Council.

6. References

Anderson, D. Z., Mizrahi, V. and Sipe, J. E., 1991, Model for Second-harmonic Generation in Glass Optical Fibers Based on Asymmetric Photoelectron Emission from Defect Sites, *Opt. Lett.* **16**, 796.

Atanasov, R., Haché, A., Hughes, J. L. P., van Driel, H.M., and Sipe, J.E., 1996, Coherent Control of Photocurrent Generation in Bulk Semiconductors, *Phys. Rev. Lett.* **76**, 1703.

Brumer, P., and Shapiro, M., 1989, Coherence Chemistry: Controlling Chemical Reactions with Lasers, *Accts. of Chem. Res.* **22**, 407.

Chen, C., Yin, Y.Y., and Elliott, D.S., 1992, Interference Between Optical Transitions, *Phys. Rev. Lett.* **64**, 507.

Dianov, E. M., Kazanski, P. G. and Stepanov, D. Y., 1989. Problem of the Photoinduced Second Harmonic Generation in Optical Fibers, *Sov. J. Quantum Electronics*.**19**, 575-76 (Kvantovaya, Elektron. **16**, 887-8 (1989)).

Dupont, E., Corkum, P. B., Liu, H.C., Buchanan, M., and Wasilewski, Z. R., 1995, Phase Coherent Control of Photocurrent Directionality in Semiconductors, *Phys. Rev. Lett.* **74**, 3596.

Éntin, M. V., 1989, Theory of the Coherent Photogalvanic Effect, *Sov. Phys. Semicond.* **23**, 664 (Fiz. Tekh. Poluprovodn. **23**, 1066-69 (1989)).

Haché, A., Kostoulas, Y., Atanasov, R., Hughes, J. L. P., Sipe, J. E., and van Driel, H. M., 1997, Observation of Coherently Controlled Photocurrents in GaAs, *Phys. Rev. Lett.* **78**, 306.

Haché, A., Sipe, J.E., and van Driel, H. M., 1998, Quantum Interference Control of Electrical Currents in GaAs, *I.E.E.E. J. Quant. Elec.* **34**, 1144..

Heberle, A. P., Baumberg, J.J., and Köhler, K., 1995, Ultrafast Coherent Control and Destruction of Excitons in Quantum Wells, *Phys. Rev. Lett.* **75**, 2598.

Khurgin, J., 1995, Generation of the Terahertz Radiation Using the $\chi^{(3)}$ in Semiconductors, *J. of Nonlinear Opt. Phys. and Materials* **4**, 163.

Kurizki, G., Shapiro, M., and Brumer, P., 1989, Phase Controlled Current in Semiconductors, *Phys. Rev. B*, **39**, 3435.

Manykin, E.A., and Afanas'ev, A.M. ,1967, On the Possibility of Making a Medium Transparent by Multiquantum Resonance, *Sov. Phys. JETP* **25**, 828 (J. Exptl. Theor. Phys. (USSR) **52**, 1246 (1967)).

Pötz, W., 1997, Manipulation of Final State Population in Semiconductor Heterostructures by Pulsed Laser Fields, *Appl. Phys. Lett.*, **71**, 395.

van Driel, H. M., and Haché, A., 1994, Control of Photocurrent Directionality via Interference of Single and Two Photon Absorption in a Semiconductor, *OSA/IEEE Conference on Nonlinear Optics; Materials, Fundamentals and Applications*, Waikaloa, Hawaii.

Warren, W. S., Rabitz, H., and Dahleh, M., 1993, Coherent Control of Quantum Dynamics: The Dream is Alive, *Science* **259**, 1581.

Yin, Y., Chen, C., Elliott, D. S., and Smith, A. V., 1992, Asymmetric Photoelectron Angular Distributions from Interfering Photoionization Processes, *Phys. Rev. Lett.* **69**, 2353.

Zhu, L., Kleiman, L., Li, X., Lu, S. P., Trentelman, K., and Gordon, R.J., 1995, Coherent Laser Control of the Product Distribution Obtained in the Photoexcitation of HI, *Science* **270**, 77.

COHERENT CONTROL OF 2D EXCITONS PROBED BY TIME-RESOLVED SECONDARY EMISSION

X. MARIE, T. AMAND, P. LE JEUNE, M. BROUSSEAU, J. BARRAU
*Laboratoire de Physique de la Matière Condensée, CNRS - UMR 5830,
Complexe Scientifique de Rangueil, F-31077 Toulouse Cedex 04, France*

1. Introduction

The coherent control of a quantum system by light relies on the possibility to control both the amplitude and the phase of its photoexcited states. It consists in producing interferences between different excitation quantum paths, each one resulting from the interaction of the electromagnetic field with the system. Among the different kinds of control investigated, the use of a sequence of two time delayed ultrashort optical pulses allows to create two temporally separated excitation paths. *Temporal coherent control* is based on the interferences between these two excitation paths. It can be achieved if the excited system stays coherent for a time longer than the time delay between the two excitation pulses. Coherent control was introduced more than one decade ago in atomic and molecular physics [1, 2]. In solids, particularly in semiconductors and their related quantum structures, the phase relaxation times are in the picosecond range, so the investigation of coherent phenomena requires the use of the stable ultrafast laser sources only recently developed.

The coherence decay of optically excited electronic systems such as excitons in semiconductors provides one of the most powerful tools to investigate interaction processes of excited states [3]. Two types of coherence can be distinguished. One is the *optical coherence* between the ground and excited states whereby the electronic excitations are coupled to the phase of an electromagnetic wave. The other one is *quantum coherence* between the excited electronic states that are closely adjacent in energy. The optical coherence phenomena in solids are usually investigated by non-linear techniques such as Four Wave Mixing (FWM) [4-6], photon echo [7], and more recently reflectivity [8] experiments. Exciton-exciton, exciton-free carriers or exciton-phonon scattering have been explored in recent years with these techniques. We demonstrate in this communication that the coherent control of electronic excitations in semiconductors can also be monitored through the secondary emission following the excitation, yielding a direct measurement of the optical dephasing time. We show that the populations, alignment and spin orientation of excitons can be coherently controlled and directly observed in a Time Resolved Secondary Emission (TRSE) experiment. In contrast to recent reflectivity experiments [8] or resonant Rayleigh

interferometric experiments [9], which demonstrate the coherent destruction of carriers, the present work deals with a pure phase of cold excitons photogenerated under resonant excitation. As shown recently this is a condition for the stability of the exciton states [10], a decisive point in the present study which deals with the manipulation of these states. We demonstrate that the experiment relies on quantum interferences (*QI*) and not on optical interferences (*OI*). In dense and polarized exciton systems, this technique evidences the spin dependent mutual interactions between excitons.

2. Experimental set up and conditions

We present the results on a *GaAs / AlGaAs* Multiple Quantum Well (MQW) which consists of 30 periods of non-intentionally doped 10 nm *GaAs* wells and 20 nm *Al_{0.6}Ga_{0.4}As* barriers grown by molecular beam epitaxy on a (100) substrate. The cw photoluminescence linewidth is 0.9 meV at 1.7 K and the shift between the heavy-hole exciton (XH) absorption and the luminescence peaks is about 0.1 meV denoting the high quality of the sample. Similar observations have been made in other high quality *GaAs / AlGaAs* with sufficiently narrow linewidths.

A sequence of two optical pulses of opposite helicities σ^+ and σ^- split from a mode locked Ti : Sapphire laser beam (pulse width 1.6 ps) resonantly excites the heavy hole excitons at energy E_{XH} . This sequence is produced by a Mach-Zender type interferometer [Fig. 1(a)]. The temporal separation between the two pulses is controlled on two different time scales : a coarse tuning sets the delay t_1 between the two pulses on a picosecond scale; a fine tuning adds the delay t_2 on a femtosecond scale, allowing a very accurate control of the relative phase. The t_2 variation is achieved through the symmetrical rotation of two glass plates in opposite directions resulting in the variation of the optical path of the beam which travels across. The resolution on the optical path difference between the two interferometer arms is better than $\lambda/20$ where λ is the excitation wavelength. The exact delay between the two pulses is then $t_1 + t_2$, and it is convenient to calibrate the time scale so that t_1 is an exact multiple of λ/c . The TRSE kinetics are recorded by up-converting the emission signal in a *LiIO₃* non linear crystal with the output from an optical parametric oscillator (OPO) synchronously pumped by the same Ti:Sapphire laser which is used for the sample excitation. The temporal pulse-width of the OPO measured from a cross-correlation is 1.5 ps. The detection direction is set along the normal to the sample surface, 20° from the excitation specular reflexion. The acceptance solid angle of our up-conversion system is about 10^{-3} steradians. This two colours up-conversion technique is necessary to record the dynamics of excitons photocreated resonantly [11]. We used picosecond pulses rather than femtosecond ones in order to selectively excite the XH excitons: this is a crucial difference with previous experiments in which light-hole excitons and free carriers are also excited simultaneously. [8,11,12]. It is now well known that the exciton dephasing is strongly modified with the presence of free electrons and holes [6]. All the measurements were carried out at a temperature of 10 K and the photogenerated exciton density is varied from about 10^9 cm⁻² to 3×10^{10} cm⁻².

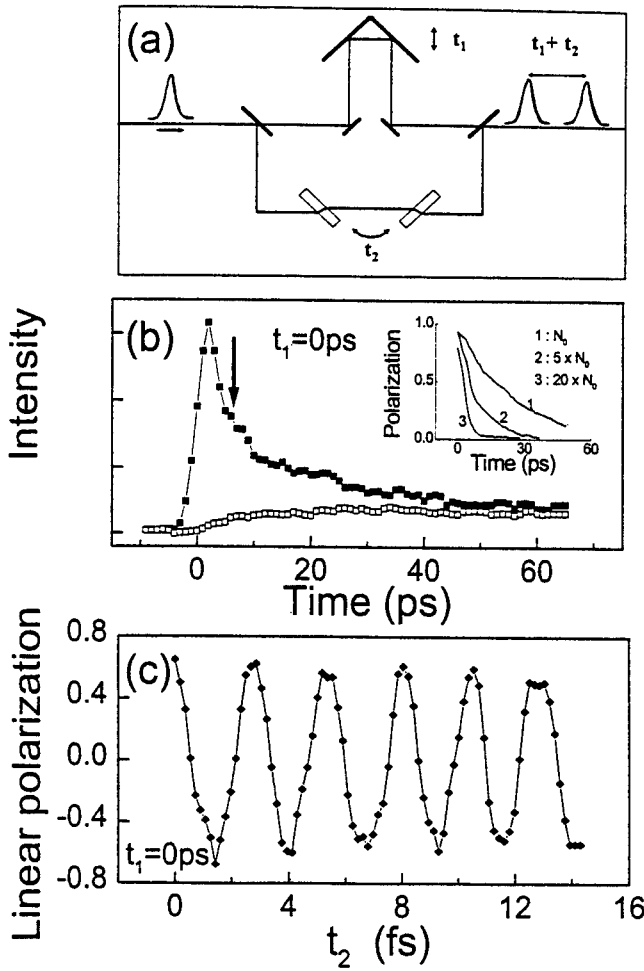


Figure 1.(a) Schematic excitation arrangement. In (b) and (c) the sequence configuration is (σ^+, σ^-) and $t_1 = 0$. (b) The time evolution of I^X (■) and I^Y (□) for $t_2 = m\lambda/c$. Inset: dependence of the linear polarization decay (characteristic time T_{sc}) as a function of the photocreated exciton density, $N_0 \approx 10^9 \text{ cm}^2$. (c) Linear polarization P' , measured 4 ps after the excitation [arrows in (b)], as a function of the fine temporal separation t_2 between the two excitation pulses.

For a (100)-grown QW, the relevant symmetry is D_{2d} . The growth direction Oz is taken as the quantization axis for the angular momentum. The conduction band is s-like, with two spin states $s_z = \pm 1/2$. The upper valence band is split into an heavy-hole band with the total angular momentum projection $j_z = \pm 3/2$ and a light-hole band with $j_z = \pm 1/2$. As the heavy-hole/light-hole splitting in the investigated sample is greater than the exciton binding energy, the exciton states can be described using the heavy-hole subspace only. The appropriate basis is then $\{|J_z\rangle \equiv |j_z + s_z\rangle\}$ i.e. $\{|+1\rangle, |-1\rangle, |+2\rangle, | -2\rangle\}$. In the time domain investigated in this work ($t < 25 \text{ ps}$), and

at low exciton density, only the optically active subspace $\{|+1\rangle, |-1\rangle\}$ is explored by the excitons due to the much longer electron and hole single particle spin-flip times [10,13]. A circularly polarized light σ^{\pm} creates excitons on states $|\pm 1\rangle$ (the "circular excitons" in the following), and a linearly σ^X or σ^Y polarized light, creates excitons on the coherent states $|X\rangle = (|1\rangle + |-1\rangle)/\sqrt{2}$ and $|Y\rangle = (|1\rangle - |-1\rangle)/i\sqrt{2}$ respectively (the "linear excitons") [14].

3. Coherent control of excitation alignment, spin and population.

We present in this section coherent control experiments performed at low exciton densities, typically about 10^9 cm $^{-2}$. First, when the main delay between the two excitation pulses is $t_1 = 0$ and the intensities are strictly equal, their optical interference results in a linearly-polarized light excitation. The polarization direction in the QW plane depends on t_2 . Figure 1(b) shows the time dependence of the two linearly polarized luminescence components $I^X(t)$ and $I^Y(t)$ and the resulting linear polarization $P(t) = (I^X - I^Y)/(I^X + I^Y)$ for $t_2 = m\lambda/c$ (where m is an integer), i.e. when the interference of the two laser pulses in the plane results in a linearly σ^X -polarized optical excitation. The recorded linear polarization, initially almost equal to 1, decays with a characteristic time $T_{s2} \approx 20$ ps, the so-called "transverse spin-relaxation time" [15]. This transverse spin relaxation time is the decay time of the quantum spin coherence. It is generally longer than "the optical dephasing time" T_2^o of excitons [5,6]. It is recognized now that, at low density, T_{s2} is driven by the intra-exciton exchange interaction [15]. It has been demonstrated recently that, when the density increases, a much more efficient spin relaxation process takes place, driven by the inter-exciton exchange interaction [16]. This effect of the density on the linear polarization decay is illustrated in the inset of Fig. 1(b). The exciton population lifetime measured in Fig. 1(b) ($T_1 \approx 15$ ps) is consistent with other measurements and theoretical calculations of the free exciton radiative recombination time on high quality MQWs [17].

Figure 1(c) displays the linear polarization dependence versus the fine temporal separation between the two pulses $P'(t_2)$. This recording, as all the similar recordings in this section, has been taken 4 ps after the second pulse to avoid any perturbation due to back-scattered laser light from the sample surface (as a consequence, a systematic small polarization loss occurs). The oscillations of the luminescence polarization observed in Fig. 1(c) at the period $T = \hbar / E_{XH}$ merely reflect the rotation of the excitation light polarization in the QW plane driven by t_2 which results in the photogeneration of linear excitons in states:

$$|\psi'(t_2)\rangle = \cos(\omega t_2 / 2)|X\rangle + \sin(\omega t_2 / 2)|Y\rangle. \quad (1)$$

As a matter of fact, the linear polarization of the exciton luminescence is $P' = \cos \omega t_2$, where $\omega = E_{XH} / \hbar$.

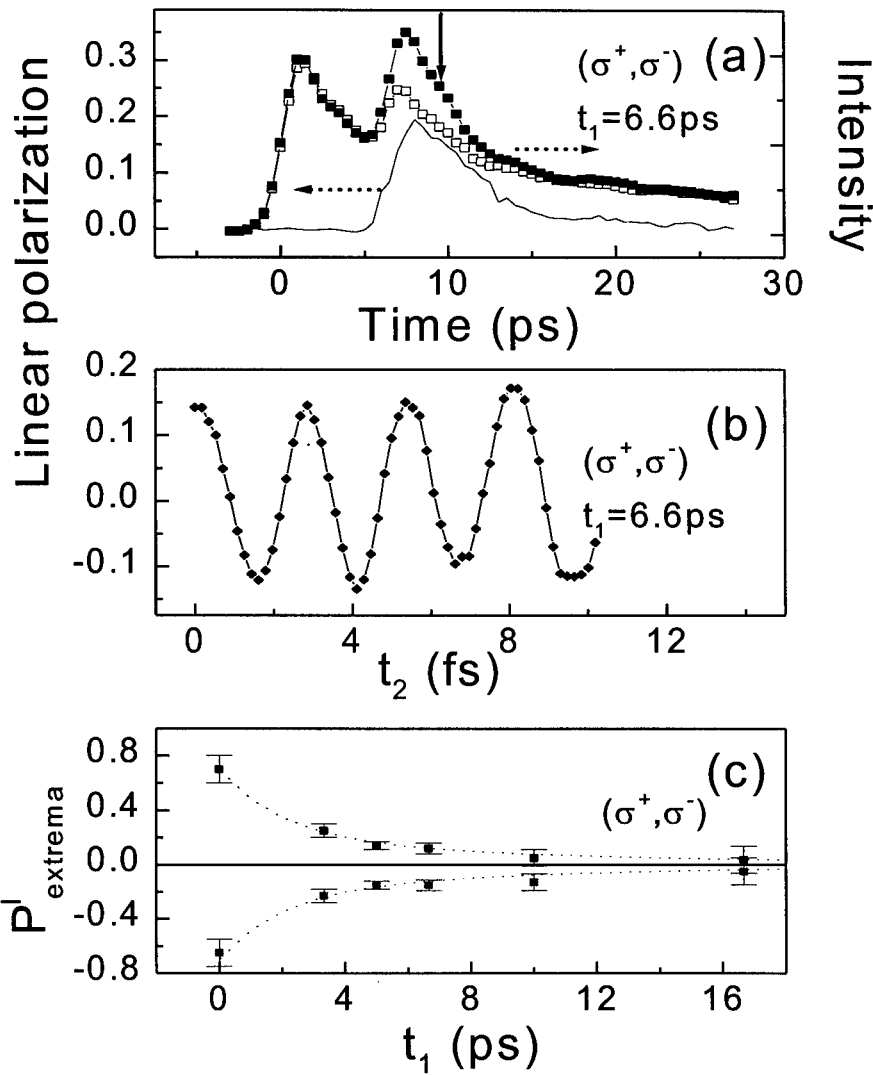


Figure 2. The configuration is (σ^+, σ^-) and $t_1 = 6.6$ ps. (a) The time evolution of I^X (■), I^Y (□) and the linear polarization P' (full line) for $t_2 = m\lambda/c$ (the back-scattered laser light from the sample surface is negligible). (b) The linear polarization P' measured 4 ps after the second excitation pulse [arrow in (a)], as a function of the fine temporal separation t_2 between the two excitation pulses. (c) The maxima and minima of the linear polarization oscillations as a function of t_1 (the dotted line is a guide for the eyes).

Now, the delay between the two excitation pulses is set to 6.6 ps, so that there is no temporal overlap between the two pulses. Figure 2(a) presents the secondary emission dynamics. The excitation with the second laser pulse results in a sharp rise of the linear polarization of the excitonic luminescence which then decays with the characteristic time T_{s2} . We have checked that, as expected, no linear polarization can be detected at any time delay when the sample is excited by the first or the second pulse independently. Obviously, this linear polarization originates from the interaction of the second pulse with the coherent excitonic polarization created in the crystal by the first pulse. The linear polarization (measured again 4 ps after the second pulse) is displayed as a function of t_2 in Fig. 2(b). The clear oscillations which are observed again are interpreted as follows.

The first optical pulse (σ^+ -polarized) sets up a material polarization in the crystal, built with $|+1\rangle$ excitons, which is coherent with the laser electromagnetic field. The interference of the second optical pulse (σ^- -polarized) with this material polarization at time t_2 results in a coherent polarization of linear excitons on $|\psi'(t_2)\rangle$ states. The oscillations as a function of time t_2 of the linear polarization of the luminescence reflects the rotation of the orientation of these linear excitons in the QW plane. The emission amplitude arising from these excitons $|\psi'(t_2)\rangle$ is a decreasing function of the delay t_1 between the two pulses, which reflects the decay of the coherent polarization of the matter. As a consequence, the amplitude of the oscillations of the linear polarization of the luminescence observed in Fig. 2(b), proportional to the fraction of excitons promoted on states $|\psi'(t_2)\rangle$ is directly proportional also to the fraction of the excitons created by the first pulse which still oscillate in phase with their photogenerating optical field at time t_1 . Figure 2(c) displays the minima and maxima of the linear polarization oscillations as a function of t_1 . Thus the amplitude decay of these oscillations follows the decay of the coherent exciton population created by the first pulse ; it directly reflects the optical dephasing of excitons in the time interval $[0, t_1]$ even in the presence of inhomogeneous broadening, as we shall see hereunder [9, 18]: the decay time is the so-called "optical dephasing time" (T_2^o). We measure $T_2^o = 6 \pm 1$ ps. The result is in agreement with previous measurements by the Four Wave Mixing technique [3].

Here the question arises how the inhomogeneous broadening influences the decay time of the polarization oscillations when t_1 increases. Following recent works by Zimmerman [19], Citrin [20], and Haacke et al. [21], the secondary emission after the coherent excitation of excitons by an ultra-fast optical pulse includes both disorder-induced Resonant Rayleigh Scattering (RRS), which is coherent with the resonant excitation, and incoherent photoluminescence (PL) from excitons which have experienced energy or phase relaxation. Actually excitons $|\psi'(t_2)\rangle$ are detected 4 ps after their generation at time t_1 , when a fraction of them has lost the optical phase. However, the secondary emission is here still dominated by RRS [21]. If the secondary emission was dominated by incoherent luminescence, the inhomogeneous broadening

would reduce the amplitude of the oscillations when t_1 increases by a factor of the order of $\exp(-\sigma_{inh}^2 t_1^2 / 2)$ where $\sigma_{inh} = \Gamma_{inh} / (\hbar \sqrt{8 \ln 2})$ and Γ_{inh} is the inhomogeneous exciton linewidth in a gaussian description. Taking $\Gamma_{inh} = 0.9$ meV leads to a much faster amplitude decay than the observed one [22].

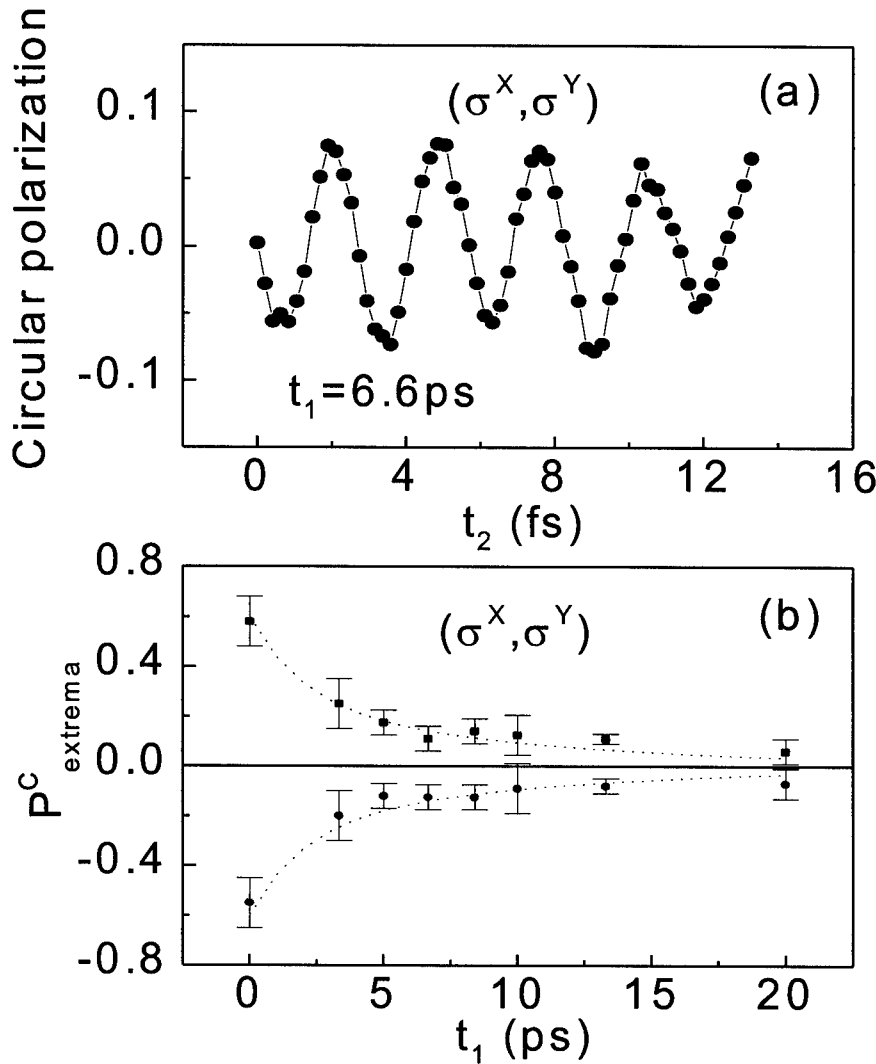


Figure 3. The configuration is (σ^x, σ^y) and $t_1 = 6.6$ ps. (a) The circular polarization $P_c^c = (I^+ - I^-) / (I^+ + I^-)$, as a function of the fine temporal separation t_2 between the two pulses (I^{\pm} are the circularly polarized luminescence components). (b) The maxima and minima of the circular polarization oscillations as a function of t_1 (the dotted line is a guide for the eyes).

Consider now a different experimental configuration in which we use a sequence of two linearly cross-polarized optical pulses, σ^x and σ^y successively. Here, the interference of the second pulse with the coherent material polarization created by the first one results in a coherent material polarization of "elliptic excitons" which occupy the states [14] :

$$|\psi^e(t_2)\rangle = \cos(\omega t_2 - \pi/4) |+1\rangle - i \sin(\omega t_2 - \pi/4) |-1\rangle \quad (2)$$

These excitons, which are characterized by a circular polarization $P^c = \sin \omega t_2$, contribute to the circular polarization of the luminescence. This effect can be compared to the observation of Faraday rotation of a linearly polarized light probe after the excitation by a sequence of two cross-polarized pump pulses [12]. Here, the circular polarization rate P^c decays in a characteristic time T_{sl} , the so-called "longitudinal spin relaxation time" of excitons [13,15] : we measure $T_{sl} = 30$ ps. It is shown in Fig. 3(a) that this circular polarization oscillates at the pulsation ω as a function of t_2 when $t_1 = 6.6$ ps. In this configuration also the minima and maxima of the circular polarization oscillations decay when t_1 increases with the characteristic time T_2^o , providing again the direct measurement of the optical dephasing time of excitons. We find again $T_2^o = 6 \pm 1$ ps [Fig. 3(b)].

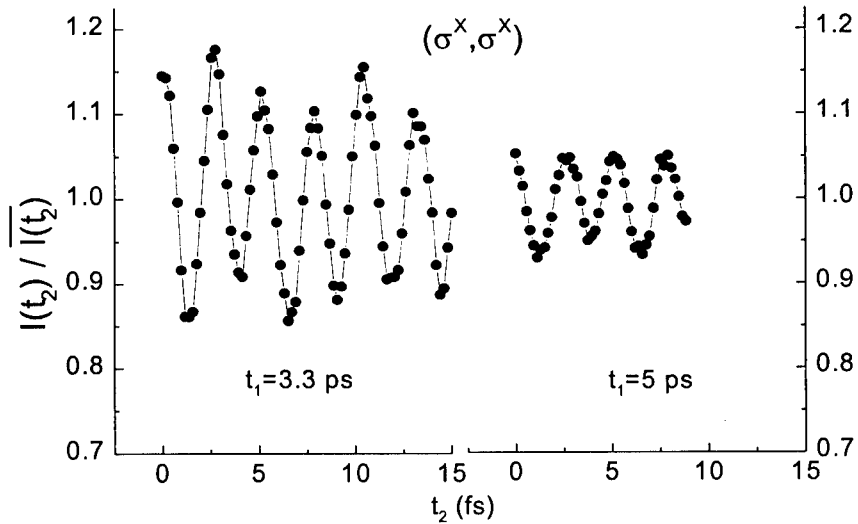


Figure 4. The configuration is (σ^x, σ^x) . The total secondary emission intensity $I(t_2)$ when (a) $t_1 = 3.3$ ps and (b) $t_1 = 5$ ps. In order to show the damping of the oscillations as a function of t_1 , the total luminescence intensity has been divided by its average value $\bar{I} = \bar{I}(t_2)$.

Finally we consider the experimental configuration in which we use a sequence of two linearly co-polarized optical pulses. In contrast to the previous configurations which relied on coherent control of the exciton alignment or orientation, it is now the exciton density which is coherently controlled, as in Ref. [8]. Constructive and destructive interferences between the second optical pulse and the coherent excitons surviving from the first pulse modulate the total exciton density, as demonstrated by the oscillations of the luminescence intensity as a function of t_2 at a fixed delay t_1 . This is illustrated in Fig. 4. The decay of this modulation amplitude as a function of t_1 reflects the decay of the coherent exciton population after its generation by the first optical pulse; the decay time is in agreement with the T_2^o measured in the other configurations. Similar observations have been done when the sample is excited by a sequence of two circularly co-polarized optical pulses.

4. Quantum interferences versus optical interferences

The question addressed here is fundamental : do the observed phenomena result from Optical Interferences (*OI*) or Quantum Interferences (*QI*)? This question arises when evaluating the macroscopic polarization of the sample after the excitation sequence. This polarization is now evaluated. We write the system hamiltonian as $H = H_0 + H_{int}(t)$, where H_0 is the unperturbed hamiltonian and $H_{int}(t)$ the interaction hamiltonian with light. Both hamiltonian are restricted to the heavy-hole exciton subspace. For a (σ^x, σ^y) excitation sequence, a possible basis is $\{|\emptyset\rangle, |X\rangle, |Y\rangle\}$ where $|\emptyset\rangle$ is the ground state. In the dipolar approximation, $H_{int}(t) = -\hat{\mu} \cdot \mathbf{E}(t)$ where $\hat{\mu}$ is the dipolar operator for the heavy-hole exciton, and $\mathbf{E}(t) = \mathbf{E}_1(t) + \mathbf{E}_2(t-\tau)$ is the electric field amplitude ($\tau = t_1 + t_2$). To the first order approximation with respect to the electric field amplitudes, and for short pulses, the excited state after the second pulse is given in the *QI hypothesis* by the coherent superposition:

$$|\psi(t)\rangle \approx |\emptyset\rangle + \theta_X e^{-i\omega_H t} |X\rangle + \theta_Y e^{-i\omega_H(t-\tau)} |Y\rangle, \quad t > \tau \quad (3)$$

where $\theta_i = \mu_{i,\emptyset} E_i(\omega_H) / \hbar$ ($i = X, Y$), $\theta_i \ll 1$, and $\mathbf{E}(\omega_H)$ is the Fourier transform of the electric field at the heavy-hole exciton pulsation ω_H . In the *OI* hypothesis, the two pulses create *independent* excitonic states, and two types of linear excitons will be created, namely:

$$|\psi_1(t)\rangle \approx |\emptyset\rangle + \theta_X e^{-i\omega_H t} |X\rangle, \quad t > 0 \quad (4a)$$

$$|\psi_2(t)\rangle \approx |\emptyset\rangle + \theta_Y e^{-i\omega_H(t-\tau)} |Y\rangle, \quad t > \tau \quad (4b)$$

and no microscopic coherence appears between $|X\rangle$ and $|Y\rangle$ states. The experiment could be then interpreted in terms of optical interferences of the secondary emission of these states.

In both cases, the first order *macroscopic* polarization $\mathbf{P}^{(1)} = \mathbf{P}_1^{(1)} + \mathbf{P}_2^{(1)}$ is given (with $\mathbf{e}_X, \mathbf{e}_Y$ unitary vectors) by : $\mathbf{P}^{(1)}(t) = \rho_{X,\emptyset}(t)\mu_{\emptyset,X}\mathbf{e}_X + \rho_{Y,\emptyset}(t)\mu_{\emptyset,Y}\mathbf{e}_Y$, where $\rho_{i,\emptyset}(t)$ are the coherence terms of the density operator $\hat{\rho}(t)$ of the system. Assuming $|\mu_{\emptyset,X}| = |\mu_{\emptyset,Y}| \equiv |\mu|$, we obtain:

$$\mathbf{P}^{(1)}(t) = \frac{|\mu|^2}{\hbar} e^{-i\omega_H t} [E_X(\omega_H)\mathbf{e}_X + e^{i\omega_H \tau} E_Y(\omega_H)\mathbf{e}_Y], \quad t > \tau \quad (5)$$

so that the two cases lead *a priori* to the same polarization. The distinction will come, as we shall see in the following, from the different coherence relaxation times of the density matrix.

The density operator of the $\hat{\rho}(t)$ satisfies the evolution equation given by :

$$\frac{d\hat{\rho}}{dt} = -\frac{i}{\hbar} [H(t), \hat{\rho}] + \left. \frac{d\hat{\rho}}{dt} \right|_{relax} \quad (6)$$

where the phenomenological terms $\left. \frac{d\hat{\rho}}{dt} \right|_{relax}$ describe the relaxation of the system towards the thermodynamical equilibrium. Within the relaxation time approximation, the relaxation of population terms writes in the basis $\{|\emptyset\rangle, |+1\rangle, |-1\rangle\}$:

$$\left. \frac{d\rho_{\pm 1, \pm 1}}{dt} \right|_{relax} = -\frac{1}{T_1} \rho_{\pm 1, \pm 1} - \frac{1}{2T_{s1}} (\rho_{\pm 1, \pm 1} - \rho_{\mp 1, \mp 1}) \quad (7a)$$

$$\left. \frac{d\rho_{0,0}}{dt} \right|_{relax} = \frac{1}{T_1} (\rho_{1,1} + \rho_{-1,-1}) \quad (7b)$$

where T_1 is the intrinsic radiative exciton lifetime, while T_{s1} is the longitudinal exciton spin relaxation time [15]. The coherences decay is given by the non-diagonal relaxation terms:

$$\left. \frac{d\rho_{-1,1}}{dt} \right|_{relax} = -\left(\frac{1}{T_1} + \frac{1}{T_{s2}} \right) \rho_{-1,1} \quad (8a)$$

$$\left. \frac{d\rho_{\emptyset,\pm 1}}{dt} \right|_{\text{relax}} = -\frac{1}{T_2^o} \rho_{\emptyset,\pm 1} \quad (8b)$$

where T_2^o is the optical dephasing time of optically active excitons, and T_{s2} is the exciton transverse spin relaxation time [15]. Corresponding expressions can be obtained in the $\{|\emptyset\rangle, |X\rangle, |Y\rangle\}$ basis. The equation of the density matrix can be solved analytically for a (σ^X, σ^Y) excitation sequence in the case where $\tau, T_2^o \ll T_1, T_{s2}$.

In the case of *QI hypothesis*, the circular polarisation detected after the second pulse is given by: $P^c(t) = (\rho_{1,1} - \rho_{-1,-1}) / (\rho_{1,1} + \rho_{-1,-1})$ or $P^c(t) = (\rho_{X,Y} + \rho_{Y,X}) / (\rho_{X,Y} + \rho_{Y,X})$. We obtain, taking $|\theta_X| = |\theta_Y|$:

$$P^c(t) = \frac{2e^{-\tau/T_2^o} \sin \omega_H \tau}{e^{-\tau/T_1} + 1} e^{-(t-\tau)/T_{s1}} \propto \exp(-t/T_{s1}) \quad (9)$$

On the other hand, in the *OI hypothesis*, the detected circular polarization after the second pulse is proportional to: $P^c(t) = (\rho_{X,\emptyset} \rho_{\emptyset,Y} + \rho_{\emptyset,X} \rho_{Y,\emptyset}) / (\rho_{X,X} + \rho_{Y,Y})$. We obtain here:

$$P^c(t) = \frac{2e^{-(2t-\tau)/T_2^o}}{e^{-\tau/T_1} + e^{-(t-\tau)/T_1}} \sin \omega_H \tau \propto \exp(-2t/T_2^o) \quad (10)$$

The argument is based now on the experimental results displayed on Fig. 5 and the dephasing times of linear excitons measured in the previous section. Here, the time delay between the two linearly polarized excitation pulses σ^X and σ^Y , is $t_1 = 4$ ps (there is no temporal overlap) and the phase difference is precisely adjusted to a multiple integer of 2π . The right I^+ and left I^- circularly polarized secondary emission components and the corresponding circular polarization P^c are displayed on Fig. 5. We observe that the excitation with the second laser pulse results in a sharp rise of the circular polarization of the excitonic luminescence. As shown in the previous section, the amplitude of these oscillations decays as a function of the time delay t_1 with the optical dephasing time $T_2^o = 6 \pm 1$ ps. In the *OI hypothesis*, the circular polarization observed after the second pulse would originate from the interference in the detector of the secondary radiations from the $|X\rangle$ and $|Y\rangle$ excitons (created successively by the two pulses). In the *QI hypothesis*, the circular polarization originates from the secondary radiation of *elliptic excitons* (a coherent superposition of $|X\rangle$ and $|Y\rangle$ states) resulting from the interference of the second laser pulse with the material polarization created by the first one. In the *OI hypothesis*, the circular polarization P^c which appears after the second pulse should decay with $T_2^o/2$ (plotted in dotted line in

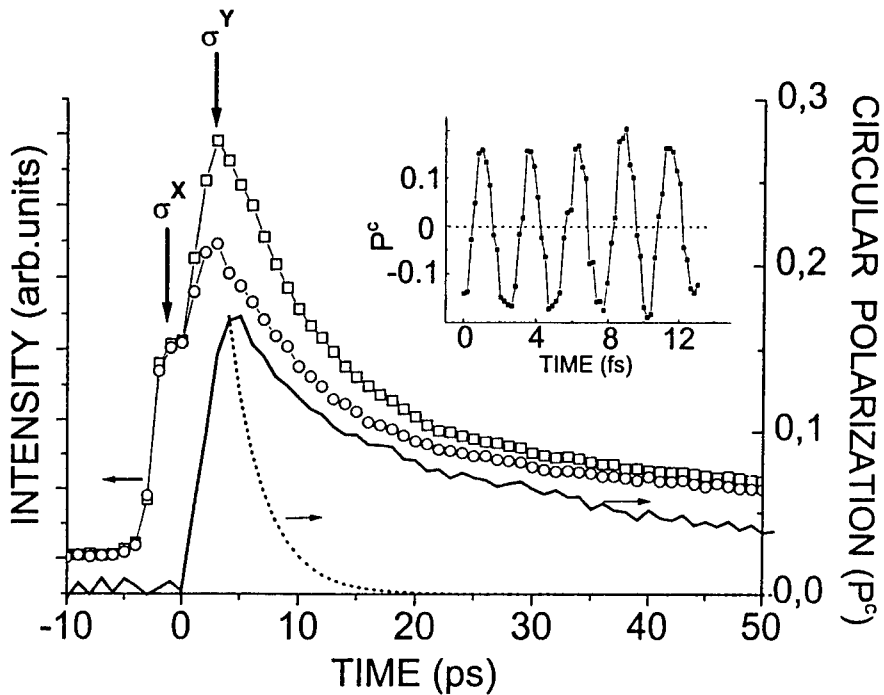


Figure 5. The configuration is (σ^x, σ^y) and $t_1 = 4$ ps. The time evolution of right I^+ (□) and left I^- (○) circularly polarized luminescence components and the corresponding circular polarization P^c (full line). Dotted line : expected circular polarization decay in the optical interference hypothesis, using the measured value $T_2^0 = 6$ ps. The inset displays the circular polarization oscillations (pulsation $\omega = E_{\text{XH}}/\hbar$) versus the fine temporal separation between the two pulses t_2 (the recording is taken just after the second pulse).

fig. 5 for comparison). In the *QI* hypothesis, the circular polarization should decay with the longitudinal exciton spin relaxation time T_{s1} , much longer than $T_2^0/2 \approx 3$ ps (a simple one pulse experiment yields $T_{s1} \approx 30$ ps in this sample). Fig. 5, which shows that the circular polarization decays with T_{s1} and not $T_2^0/2$, demonstrates the *QI* hypothesis. This result can be compared to the observation reported in [12] : the Faraday rotation of the reflected probe after an excitation sequence (σ^x, σ^y) demonstrates that a quantum superposition of exciton states is indeed achieved. Time resolved four wave mixing experiments allow also in principle to distinguish between *QI* and *OI* [23]. They are based on the analysis of the third order non-linear polarisability dynamics. We mention also that an experimental proof of *QI* hypothesis in a temporal coherent control experiment was recently obtained in atomic Cs [24]. It

relies on a two photon transition process. Here, we have demonstrated that, in condensed matter, the distinction between *QI* and *OI* can be made from an experiment which relies on the first order polarisation.

5. Spin dependent mutual interactions between excitons

Mutual interactions in dense exciton gas was first investigated by Four-Wave Mixing experiments using linearly polarized pulses [6,25]. In both references, the homogeneous exciton broadening was found to increase with the exciton density N , with a law which can be linearized in a moderate density range ($N \leq 2 \times 10^{10} \text{ cm}^{-2}$) according to :

$$\Gamma(N) = \Gamma_0 + \gamma_{xx} N \quad (11)$$

This linear behaviour was predicted in Ref. [26], but a discrepancy remains since the theoretical value for γ_{xx} is much lower than the experimentally determined one. In addition, we evidenced previously on the basis of photoluminescence experiments [16,27], that the mutual exciton interactions were strongly dependent on their polarization state, due to the effect of exchange interaction between their constitutive elements. We investigate here, as an application of our coherent control technique, the influence of the exciton density on the optical dephasing time $T_2^o = 2\hbar/\Gamma$, taking into account the spin state of the excitons. We recall that using a (σ^+, σ^-) sequence we measure the dephasing time of a *circular* exciton population, whereas with a (σ^x, σ^y) sequence we determine the dephasing time of a *linear* exciton population. At low photocreated exciton densities ($N \leq 10^9 \text{ cm}^{-2}$), we find the same value for T_2^o for both sequences ($T_2^o = 6 \pm 1 \text{ ps}$), i.e. for the two types of exciton populations. However, when the total photogenerated density increases, the measured phase coherence decay time decreases much faster in the (σ^x, σ^y) configuration than in the (σ^+, σ^-) one. Fig. 6 displays the density dependence of $1/T_2^o$ for circular or linear exciton populations. It demonstrates the spin dependence of the exciton mutual interactions.

The density dependence of the homogeneous broadening can be linearized for initial densities $N \leq 3 \times 10^{10} \text{ cm}^{-2}$ after equation (11). Here, Γ_0 is the non-density dependent homogeneous broadening which includes all dephasing mechanisms except the mutual exciton scattering, and γ_{xx} is the *collision broadening* parameter resulting from exciton-exciton scattering. The fit with the experimental data for linear excitons yields $\gamma_{xx} = 0.15 \text{ meV} \times 10^{-10} \text{ cm}^{-2}$ and $\Gamma_0 = 0.2 \text{ meV}$. The γ_{xx} value is similar to the collision broadening parameters measured in [6,25].

In contrast to the case of linear excitons, we see in Fig. 6 that the optical dephasing time of circular excitons depends very slightly on the exciton density in the range 10^9 - $3 \times 10^{10} \text{ cm}^{-2}$. This behaviour difference between the circular and linear excitons is interpreted as a manifestation of the spin dependent mutual exciton interactions [16,27].

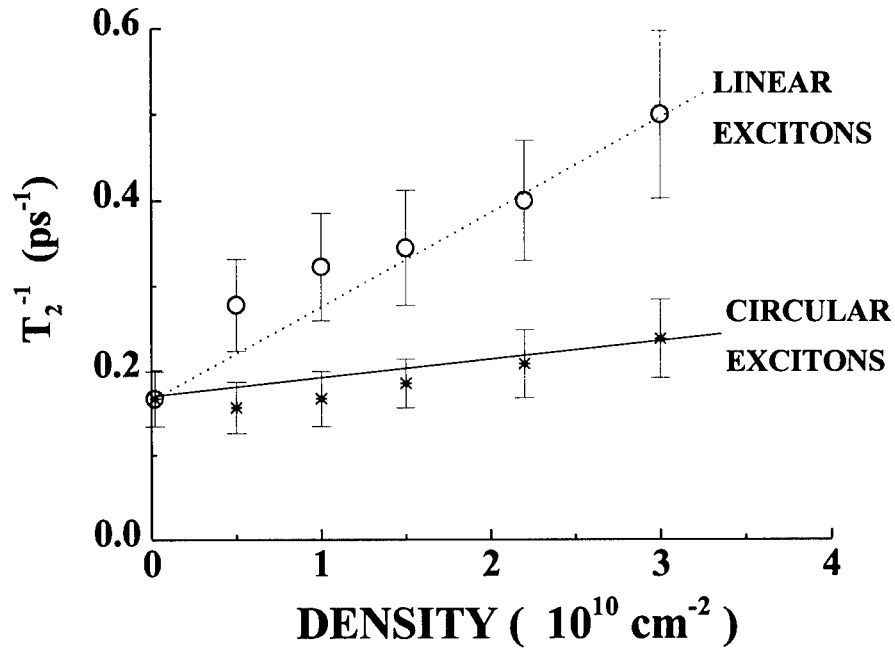


Figure 6. Inverse of the optical dephasing times T_2^o of circular (*) or linear (o) excitons as a function of the exciton density. Dashed line : linear fit of the experimental data for linear excitons. Full line : linear fit of the experimental data for circular excitons taking the broadening parameter calculated in [25] ; the low density value $1/T_2^o$ is the experimental one.

The stability of the pure circularly polarized exciton phase, with respect to these interactions, results in an optical dephasing time quasi-independant of the density. This behaviour difference can explain the discrepancy mentioned previously by Honold *et al.* [6] between the broadening parameter measured in FWM experiments (with linearly polarized pulses) and the calculated value in a many body approach by Manzke *et al.* [26]. The experimental γ_{xx} value for linear excitons is about four times larger than the theoretical one. The latter however agrees well with the broadening parameter we measure for circular excitons : the full line in Fig. 6 corresponds to the calculated broadening parameter by Manzke *et al.* [26]. The agreement between the theory and the experiment is here quite convincing. This is a satisfactory result since Manzke *et al.* did not include in their calculations the spin-dependent mutual exciton exchange interactions. In other words, their calculations is appropriate for circular and not for linear excitons.

6. Conclusion

In summary, we demonstrate in this work that coherent superposition of exciton states can be achieved by using a sequence of two phase-controlled optical excitation pulses. We show that the coherent control of excitons in semiconductors can be monitored by their secondary emission, yielding direct measurements of the optical dephasing time T_2^o . In contrast to Four-Wave-Mixing techniques in which the principle of measurement of T_2^o is based on the third order non-linear polarization effect, the present measurements rely on the linear response of the system. We have shown that the optical orientation of optically active excitons, their alignment and their populations can be coherently controlled on time scales shorter than the optical dephasing time and directly observed in a Time Resolved Secondary Emission experiment. The optical dephasing time T_2^o of excitons, their longitudinal and transverse spin relaxation times T_{s1} and T_{s2} and their radiative lifetime T_1 are measured in the same experiment with strictly the same experimental conditions. At high density, mutual exciton exchange interaction is evidenced, leading to a spin dependent collisional broadening parameter.

Acknowledgements : we are grateful to R. Planel for the growth of high quality samples. We thank A. Quattropani, C. Ciuti, C. Piermarocchi and V. Savona for fruitful discussions. It is also a pleasure to thank B. Deveaud and S. Haacke for stimulating discussion about RRS.

7. References

- [1] M. M. Salour and C. Cohen-Tannoudji, Observation of Ramsey's interference fringes in the profile of Doppler-free two-photon resonances, *Phys. Rev. Lett.* **38**, 757 (1977).
- [2] N. F. Sherer, A. Ruggiero, M. Du, and G. R. Fleming, Time resolved dynamics of isolated molecular systems studied with phase-locked femtosecond pulse pairs, *J. Chem. Phys.* **93**, 856 (1990); N. F. Scherer, R. J. Carlson, A. Matro, M. Du, A. J. Ruggiero, V. Romero-Rochin, J. A. Cina, G. R. Fleming, and S. A. Rice, Fluorescence-detected wave packet interferometry: time resolved molecular spectroscopy with sequences of femtosecond phase-locked pulses, *J. Chem. Phys.* **95**, 1487 (1991).
- [3] For a review, see *Coherent Optical Interactions in Semiconductors*, edited by R. T. Philips, NATO ASI Ser. B, Vol. 330 (Plenum Press, New York, 1994).
- [4] L. Shultheis J. Kuhl, and A. Honold, and C. W. Tu, Ultrafast phase relaxation of excitons via exciton-exciton and exciton-electron collisions, *Phys. Rev. Lett.* **57**, 1635 (1986).
- [5] E. O. Göbel, K. Leo, T. C. Damen, and J. Shah, S. Schmitt-Rink and W. Schäfer, J. F. Müller, K. Köhler, Quantum beats of excitons in quantum wells, *Phys. Rev. Lett.* **64**, 1801 (1990).
- [6] A. Honold, L. Shultheis, J. Kuhl, C. W. Tu, Collision broadening of two-dimensional excitons in GaAs single quantum well, *Phys. Rev. B* **40**, 6442 (1989).
- [7] G. Noll, U. Siegner, S. G. Shevel, and E. O. Göbel, Picosecond stimulated photon echo due to intrinsic excitations in semiconductor mixed crystals, *Phys. Rev. Lett.* **64**, 792 (1990).
- [8] A. P. Heberle, and J. J. Baumberg, K. Köhler, Ultrafast coherent control and destruction of excitons in quantum wells, *Phys. Rev. Lett.* **75**, 2598 (1995).
- [9] S. Ceccherini, F. Bogani, M. Gurioli, M. Colocci, Time-resolved interference of coherent polarization waves in semiconductors, *Opt. Commun.* **132**, 77 (1996).
- [10] T. Amand, X. Marie, M. Brousseau, P. Le Jeune, D. Robart, J. Barrau, R. Planel, Spin quantum beats of 2D-exciton, *Phys. Rev. Lett.* **78**, 1355 (1997).

[11] H. Wang, J. Shah, and T. C. Damen, L. N. Pfeiffer, Spontaneous emission of excitons in GaAs quantum wells: the role of momentum scattering, *Phys. Rev. Lett.* **74**, 3065 (1995).

[12] A. P. Heberle, J. J. Baumberg, E. Binder, T. Kuhn, K. Kohler, K. H. Ploog, Coherent control of exciton density and spin, *IEEE Journal on Selected Topics in Quantum Electron.* **2**, 769 (1996).

[13] A. Vinattieri, J. Shah, T. C. Damen, and D. S. Kim, L. N. Pfeiffer, M. Z. Maialle and L. J. Sham, Exciton dynamics in GaAs quantum wells under resonant excitation , *Phys. Rev. B* **50**, 10868 (1994).

[14] Since the $|X\rangle$ and $|Y\rangle$ exciton states are degenerated in type I quantum wells, the X - Y axis orientation is immaterial.

[15] M. Z. Maialle, E. A. de Andrade e Silva, and L. J. Sham, Exciton spin dynamics in quantum wells, *Phys. Rev. B* **47**, 15776 (1993).

[16] T. Amand, D. Robart, X. Marie, M. Brousseau, P. Le Jeune, and J. Barrau, Spin relaxation in polarized interacting exciton gas in quantum wells , *Phys. Rev. B* **50**, 9880 (1997).

[17] B. Deveaud and F. Clérot, N. Roy, K. Satzke, and B. Sermage, D. S. Katzer, Enhanced radiative recombination of free excitons in GaAs quantum wells, *Phys. Rev. Lett.* **67**, 2355 (1991); L. C. Andreani, Radiative Lifetime of free excitons in quantum wells , *Solid State Commun.* **77**, 641 (1991).

[18] H. Stoltz, D. Schwartze, and W. von der Osten, G. Weimann, Transient resonance Rayleigh scattering from electronic states in disordered systems: Excitons in GaAs/Al_xGa_{1-x}As multiple-quantum-well structures, *Phys. Rev. B* **47**, 9669 (1993).

[19] R. Zimmermann, Theory of resonant Rayleigh scattering of excitons in semiconductor quantum wells, *Nuovo Cimento* **17D**, 1801 (1995).

[20] D. S. Citrin, Time-domain theory of resonant Rayleigh scattering by quantum wells: early-time evolution, *Phys. Rev B* **54**, 14572 (1996).

[21] S. Haacke, R. A. Taylor, R. Zimmermann, I. Bar-Joseph, and B. Deveaud, Resonant femtosecond emission from quantum well excitons: The role of Rayleigh scattering and luminescence, *Phys. Rev. Lett.* **78**, 2228 (1997); S. Haacke, G. R. Hayes, R. A. Taylor, M. Kauer, and B. Deveaud, OSA series TOPS (1998), to be published.

[22] C. Ciuti, private communication

[23] M. Koch, J. Feldmann, G. Von Plessen, E. O. Göbel, and P. Thomas, K. Köler, Quantum beats versus polarization interference: an experimental distinction, *Phys. Rev. Lett.* **69**, 3631 (1992).

[24] V. Blanchet, C. Nicole, M.-A. Bouchene, and B. Girard, Temporal coherent control in two photon transitions: from optical interferences to quantum interferences, *Phys. Rev. Lett.* **78**, 2716 (1997).

[25] R. Eccleston, B. F. Feuerbacher, J. Kuhl, W. W. Rühle, and K. Ploog, Density-dependent exciton radiative lifetimes in GaAs quantum wells, *Phys. Rev B* **45**, 11403 (1992).

[26] G. Manzke K. Henneberger, and V. May, Many-exciton theory for multiple quantum-well structures, *Phys. Status Solidi (b)* **130**, 233 (1987)

[27] P. Le Jeune, X. Marie, T. Amand, F. Romstad, F. Perez, J. Barrau, and M. Brousseau, Spin-dependent exciton-exciton interactions in quantum wells, *Phys. Rev. B* (1998), to be published.

MANY-BODY EFFECTS IN THE ULTRAFAST POPULATION TRANSFER IN P-DOPED SEMICONDUCTOR QUANTUM WELLS

R. BINDER

*Optical Sciences Center, University of Arizona
Tucson, AZ 85721*

AND

M. LINDBERG

*Institutionen för Fysik, Åbo Akademi
Porthansgatan 3, 20500 Åbo, Finland*

Abstract. The influence of many-body effects due to the Coulomb interaction between charge carriers in semiconductors on the light-induced adiabatic population transfer is investigated. The population transfer under consideration involves heavy-hole (hh) and light-hole (lh) bands in p-doped semiconductor quantum wells. The investigation is a theoretical analysis and numerical evaluation of appropriate generalized multi-band semiconductor Bloch equations. Dynamic energy renormalizations due to Coulomb exchange interactions as well as quasi-thermalization of charge carriers is taken into account.

1. INTRODUCTION

In recent years considerable interest has been devoted to ultrafast adiabatic transfer of population between eigenstates of atoms or molecules [1, 2, 3, 4, 5]. It is possible to completely transfer population between two not-optically-coupled states by using a third state which is optically coupled to both the initial and the final state. The two states are coupled to the third state with two separate light pulses, one for each transition. The pulses have approximatively equal detunings and the band width of the pulse caused by the temporal change of the amplitude is small compared

with the detunings. In this way the eigenstates of the 3-level system become weakly mixed, except when they happen to cross each other. Consequently, the time evolution of the system is, most of the time, adiabatic. With suitably chosen parameters the crossing of the adiabatic energy levels leads to a Landau-Zener type transition [6, 7, 8]. The transfer seems to work best in the so-called counterintuitive pulse delay scheme in which the first pulse corresponds to the optical transition that includes the final state and, therefore, to a transition between two empty states. The exact resonance condition underlying the population trapping state is not necessary for the transfer to work. Only the crossing is essential since the population is switched at the crossing and it remains in its new state through the rest of the adiabatic evolution including the limit of vanishing light amplitudes (i.e., after the pulse sequence). If the states would be adiabatic at all times the population would remain in one of the adiabatic states and hence, after the pulse, would return to where it had started from.

The physical processes in semiconductor quantum wells, that can be characterized in terms of a conduction (c) and two valence (v) bands (i.e., one heavy-hole (hh) and one light-hole (lh) band) are much more complex than in atomic 3-level systems, because of band structure effects and because of the Coulomb interaction which yields excitonic and plasma-induced many-body effects. Nevertheless, the existence of non-radiative coherences in semiconductors has been proven experimentally (see [9] and references therein). Also, theoretical simulations predict the existence of the population-trapped state in semiconductors [10]. In the following, we study how many-body effects like band renormalization, renormalization of the dipole energy and Coulomb scattering influence the light-induced population transfer in semiconductors. This is an extension of our recent investigation of population transfer in semiconductors [11]. It includes a detailed analysis of the general results presented in Ref. [11] with special emphasis on the role of many-body effects. A related investigation of optical excitation of spatially indirect excitons in double quantum wells utilizing the counterintuitive pulse delay scheme is given in Ref. [12].

The system to be considered in the following is a p-doped semiconductor quantum well [13]. We assume that the $hh-lh$ splitting is sufficiently large so that the p-doping yields only heavy holes. A permanent heavy hole population and no light holes forms a Λ -like band structure analogous to the Λ -level structure in the quantum optics of atoms.

2. THEORETICAL BASIS

In this section we review the theoretical model, which is based on the screened HF-theory for optically excited semiconductor systems. For a gen-

eral review and more details about the foundation of the screened HF-theory of optically excited semiconductors see, for example, [14]. The contributions to this theory that describe the coherent nonlinear optical response have also been discussed in [10, 15]. The model discussed below is also the basis of Ref. [11].

The theory is based on equations-of-motion for the time-dependent optical polarization functions $P_{sj}(\vec{k})$ as well as the electron and hole distribution-coherence functions $f_{ss'}(\vec{k})$ and $f_{jj'}(\vec{k})$, respectively. The vector \vec{k} is the two-dimensional in-plane wave vector, the electron quantum numbers s, s' denote the spin-degenerate conduction bands with $s = \pm 1/2$, and the hole quantum numbers j, j' denote the two degenerate heavy-hole ($j = \pm 3/2$) and light-hole ($j = \pm 1/2$) bands. The equations-of-motion comprise the coherent Hartree-Fock contributions and incoherent dephasing and scattering contributions. If (as assumed in the following) biexcitonic effects are insignificant, the Hartree-Fock contributions to the nonlinear optical response constitute the ideal limit in the sense that optical pulses can in principle be shorter than typical incoherent scattering times, but the many-particle effects described by the Coulomb terms in the HF-theory cannot be neglected on any time-scale. Since typical femtosecond pulses don't quite reach this ideal limit, we have amended the HF-theory with dephasing contributions and a self-consistent multiband relaxation rate model.

The equation for $P_{sj}(\vec{k})$ reads ($\hbar = 1$):

$$\begin{aligned} i \frac{d}{dt} P_{sj}(\vec{k}) = & \sum_{s'j'} \{ [\delta_{ss'} \delta_{jj'} \varepsilon_{\vec{k}}^s + \delta_{ss'} \mathcal{H}_{jj'}(-\vec{k})] P_{s'j'}(\vec{k}) \\ & - \Omega_{s'j'}(\vec{k}) [\delta_{ss'} \delta_{jj'} - \delta_{jj'} f_{ss'}(\vec{k}) - \delta_{ss'} f_{jj'}(\vec{k})] \\ & + [\delta_{jj'} \Sigma_{ss'}(\vec{k}) + \delta_{ss'} \Sigma_{jj'}(-\vec{k})] P_{s'j'}(\vec{k}) \} \\ & + i \frac{d}{dt} P_{sj}(\vec{k}) \Big|_{scatt}, \end{aligned} \quad (1)$$

the one for the electron distribution is

$$\begin{aligned} i \frac{d}{dt} f_{ss'}(\vec{k}) = & \sum_j \{ \Omega_{s'j}^*(\vec{k}) P_{sj}(\vec{k}) - \Omega_{sj}(\vec{k}) P_{s'j}^*(\vec{k}) \} \\ & + \sum_{s''} \{ \Sigma_{ss''}(\vec{k}) f_{s''s}(\vec{k}) - f_{ss''}(\vec{k}) \Sigma_{s''s'}(\vec{k}) \}, \end{aligned} \quad (2)$$

and that for the hole distribution function is

$$i \frac{d}{dt} f_{jj'}(\vec{k}) = \sum_{j''} \{ \mathcal{H}_{jj''}(\vec{k}) f_{j''j'}(\vec{k}) - f_{jj''}(\vec{k}) \mathcal{H}_{j''j'}(\vec{k}) \}$$

$$\begin{aligned}
& + \sum_s \{ \Omega_{sj'}^*(-\vec{k}) P_{sj}(-\vec{k}) - \Omega_{sj}(-\vec{k}) P_{sj'}^*(-\vec{k}) \} \\
& + \sum_{j''} \{ \Sigma_{jj''}(\vec{k}) f_{jj''}(\vec{k}) - f_{jj''}(\vec{k}) \Sigma_{jj''}(\vec{k}) \} \\
& + i \frac{d}{dt} f_{jj'}(\vec{k}) \Big|_{scatt}. \tag{3}
\end{aligned}$$

Here, the electron energies are parabolic, $\varepsilon_k^s = \hbar^2 k^2 / 2m_e + \Sigma_{CH} + E_G$, where E_G is the bandgap of the undoped quantum well and Σ_{CH} is the Coulomb Hole self-energy (see, e.g., [16]).

The Luttinger Hamiltonian \mathcal{H} for the valence bands in the basis $\{j\} = (3/2, -1/2, 1/2, -3/2)$ reads

$$\mathcal{H} = \begin{pmatrix} H_{hh} & c^* & 0 & 0 \\ c & H_{lh} & 0 & 0 \\ 0 & 0 & H_{lh} & c^* \\ 0 & 0 & c & H_{hh} \end{pmatrix} \tag{4}$$

where The Luttinger Hamiltonian \mathcal{H} consists of two 2×2 matrices (compare with [15]) with elements $H_{hh} = (\hbar^2/2m_0)(\gamma_1 + \gamma_2)k^2$, $H_{lh} = (\hbar^2/2m_0)(\gamma_1 - \gamma_2)k^2 + \Delta_{hh-lh}$, and, within an isotropic approximation, $c = -(\hbar^2/2m_0)\sqrt{3}(\gamma_2(k_x^2 - k_y^2) - 2i\gamma_3 k_x k_y) \approx -(\hbar^2/4m_0)\sqrt{3}(\gamma_2 + \gamma_3)k^2$. Here, $\gamma_1, \gamma_2, \gamma_3$ are the Luttinger parameters. The energy renormalizations are given by (with $a = s$ or j)

$$\Sigma_{aa'}(k) = - \sum_{\vec{q}} V(\vec{q}) f_{aa'}(\vec{k} + \vec{q}). \tag{5}$$

and the renormalized dipole energy is

$$\Omega_{sj}(k) = \vec{\mu}_{sj} \cdot \vec{E} + \sum_{\vec{q}} V(\vec{q}) P_{sj}(\vec{k} + \vec{q}). \tag{6}$$

The interaction potential $V(q)$ is the statically screened Coulomb potential including the form factor $\mathcal{F}(q)$ according to the lowest-subband wavefunctions in an infinitely deep quantum well:

$$V(q) = \frac{2\pi e^2}{q} \mathcal{F}(q) \epsilon_q^{-1} \tag{7}$$

with

$$\mathcal{F}(q) = \frac{8}{(qL)^2 + 4\pi^2} \left[\frac{3qL}{8} + \frac{\pi^2}{qL} - \frac{(1 - e^{-qL})4\pi^4}{(qL)^2[(qL)^2 + 4\pi^2]} \right] \tag{8}$$

where L is the thickness of the quantum well. Within a simple time-independent screening model, the screened potential is given by the initial hh -density. The static screening function is

$$\epsilon_q^{-1} = 1 - \omega_{pl}^2(q)/\omega^2(q) \quad (9)$$

where

$$\omega^2(q) = \omega_{pl}^2(q) \left(1 + \frac{q}{\kappa} \right) + \epsilon_{hh}^2(q) \quad (10)$$

and

$$\omega_{pl}^2(q) = \frac{2\pi e^2 q n_{hh}}{m_{hh}} \quad (11)$$

are the two-dimensional (squared) plasmon dispersion and plasma frequency, respectively [16], and $\epsilon_{hh}^2(q)$ is the parabolic energy dispersion of the heavy-hole in the vicinity of the Γ -point and $m_{hh}/m_0 = (\gamma_1 + \gamma_2)^{-1}$ (m_0 = electron mass in vacuum).

The light pulses are denoted by \vec{E} . The dipole matrix elements $\vec{\mu}_{sj}$ contain the information of optical selection rules. The dipole matrix elements [17] are given by $\vec{\mu}_{1/2,3/2} = \sqrt{3}\vec{\mu}_{-1/2,1/2} = -\mu\vec{e}_+$ and $\vec{\mu}_{-1/2,-3/2} = \sqrt{3}\vec{\mu}_{1/2,-1/2} = -\mu\vec{e}_-$ where μ is the magnitude of the microscopic Cartesian dipole element. In the following we will call the transitions from $j = 3/2$ and $j = -1/2$ to $s = 1/2$ "spin +1 transitions" (and this subset of bands "spin +1 subset") and the transitions from $j = -3/2$ and $j = +1/2$ to $s = -1/2$ "spin -1 transitions" (and this subset of bands "spin -1 subset").

For the scattering contribution to the f -equations we use a relaxation time approximation (RTA). For a fermion system the linearization of the scattering integral leads to linear decay terms proportional to the difference between the individual populations of the states and corresponding thermal populations given by a Fermi distributions. The multiplying constant in the linearized decay term is called $1/T_1$. In general it would be temperature and density dependent but, for simplicity, we assume it to be a constant. A Fermi distribution is characterized by the single particle energy of the state and the global quantities temperature and chemical potential. Since the Coulomb interaction does not change the total energy or the particle numbers of the system involved in the scattering, the global quantities, temperature and the chemical potential, are determined by setting the total energy and the total particle numbers given by the Fermi distributions equal to the ones given by the temporal populations. Each separately conserved particle number corresponds to a separate chemical potential. The total energy and the particle numbers can then be changed

by other processes like absorption or recombination. If the other processes are not present the populations would be driven to these Fermi distributions asymptotically. As discussed above, the Coulomb interaction causes a renormalization of the single particle energies. The renormalization depends on populations and can be viewed as band shifts. We approximate the shifts by assuming them to be the same for each state in a given band but for them to be different in different bands. These rigid band shifts are given by selfenergies at $k = 0$. The rigid shift is evaluated using the thermal populations which makes the evaluation self consistent. Technically, the self-consistency is obtained by evaluating the zero density bands shifts (given constants) as a difference between the finite density band shifts and the corresponding rigid renormalizations. The temperature, the chemical potentials, and the band-renormalizations (shifts) are computed self consistently at each point in time since the total energy and the particle numbers are changed by the interaction with the optical fields. In the present case we assume that the spin +1 and spin -1 subsystems are not coupled by scattering processes since the spin flip times are typically in the ps rather than the fs regime, (see, for example, [18, 19]. Assuming, furthermore, that because of the high carrier density the fs-scattering processes are dominated by carrier-carrier scattering, the parameters characterizing the appropriate quasi-thermal equilibrium are (for each subsystem): the three band-offsets, two chemical potentials (one for the c-band and one for the v-bands), and the temperature. These parameters are uniquely and self-consistently determined by the zero-density band-offsets, the two densities (electron and total hole density), and the total electron-hole kinetic energy. Note that the renormalization of the bands due to the occupation-dependent screened exchange interaction influences the relative shift of the hh and the lh band in a complicated way. Note also that the off-diagonal elements of the quasi-thermal hole distribution (denoted by the superscript "F" for Fermi) $\tilde{f}_{jj'}^F(\vec{k})$ ($j \neq j'$) do not vanish. This is because we have written Eq. 3 in a basis that does not correspond to the true one-particle eigenstates of the system. A simple RTA of the form

$$\frac{d}{dt} \tilde{f}_{jj'}(\vec{k}) \Big|_{scatt} = -\frac{1}{T_1} \left(\tilde{f}_{jj'}(\vec{k}) - \delta_{jj'} \tilde{f}_j^F(\vec{k}) \right) \quad (12)$$

is possible only if the states labelled by j and \vec{k} are the one-particle eigenstates. To indicate this, we use a 'tilde' in Eq. 12, and the relation between \tilde{f} and f is given by $\tilde{f}_{jj'} = \sum_{ii'} u_{ij}^* u_{i'j'} f_{ii'}$, where u_{ij} is the eigenvector matrix of \mathcal{H} and we have suppressed the common index \vec{k} . Finally, in the scattering contribution to the equation for the optical polarization functions we use a simple dephasing constant $1/T_2$ to simulate the effects of carrier-carrier scattering.

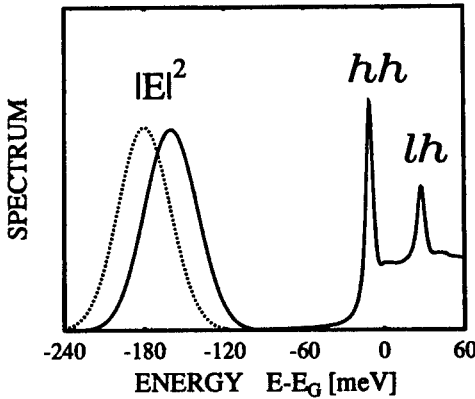


Figure 1. Sketch of the spectral intensities of the light-pulses and the $hh-lh$ absorption spectrum of the undoped semiconductor.

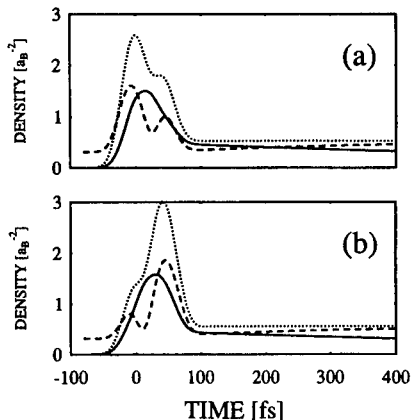


Figure 2. Density vs. time for the heavy-hole density (dashed line), light-hole density (solid line), and conduction band density (dotted line). The unit length is $a_0 = 135\text{\AA}$. In (a), $s = 1/2$ and $j = 3/2$ and $-1/2$, respectively, and in (b) $s = -1/2$ and $j = -3/2$ and $+1/2$. $T_1 = T_2 = 600\text{ fs}$.

3. RESULTS AND DISCUSSION

For the numerical investigation we use GaAs material parameters: $m_e = 0.067m_0$, $\epsilon_b = 12.7$ (background dielectric function entering the Coulomb potential), $\gamma_1 = 6.85$, $\gamma_2 = 2.1$, $\gamma_3 = 2.9$. We use a $hh-lh$ splitting of 40 meV and a well thickness of 50 \AA with infinite potential barriers. Unless otherwise noted, we use two 40 fs pulses (intensity FWHM), one left-handed circularly polarized pulse centered in time at $t = 0$ and in frequency at $\hbar\omega_0 = E_G - 180\text{ meV}$, and one right-handed circularly polarized pulse centered at $t = 40\text{ fs}$ and $\hbar\omega_1 = E_G - 160\text{ meV}$. The peak amplitudes are $\mu E_0 = 212\text{ meV}$. The doping density is chosen to be $3.42 \times 10^{11} \text{ cm}^{-2}$ at a temperature of 20 K.

In Fig. 1 we show the spectral intensities of the two light pulses and, for

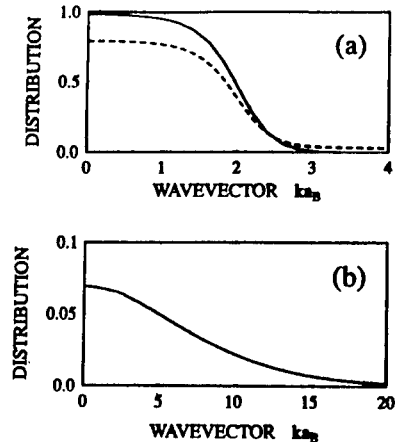


Figure 3. Distribution function before and shortly after the population transfer according to Fig. 2a. (a) Solid line: hh -distribution before the transfer, dashed line: lh -distribution after the transfer. (b) Electron distribution after the transfer.

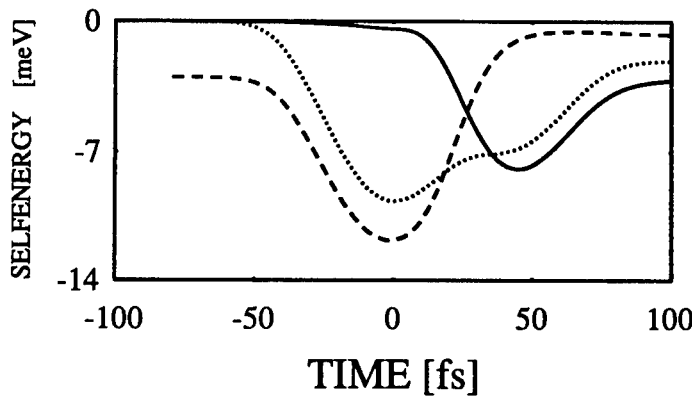


Figure 4. Statically screened exchange selfenergy vs. time according to Fig. 2a. (The line styles are same as in Fig. 2a)

reference, the hh and lh -exciton spectrum of the undoped semiconductor. Clearly, there is not much spectral overlap between the pulses and the excitonic absorption. This justifies use of a dephasing time that is larger than the inverse exciton width. Such an increase of dephasing time as function of increasing detuning models the typical non-Lorentzian lineshape of the optical transitions. For the numerical evaluations we choose $T_1 = T_2 = 600$ fs.

Fig. 2 shows the density responses of all six bands as function of time in the presence of non-zero dephasing and relaxation rates. The basic characteristics during the time of the pulses are similar to those discussed in [11] for vanishing dephasing and relaxation rates, i.e., the transfer works well for both spin subsystems. For later times, the relaxation causes the redistribution of holes toward the original occupation of heavy-holes due to

intervalence band scattering. Since, in our analysis, we model on carrier-carrier scattering, the original state cannot be reached because the transfer is related to an effective heating of the carriers, which can be reversed only if the carrier-phonon scattering allows for a reduction of the energy of the electronic system (i.e., electrons and holes). Carrier scattering with LO-phonons sets in on the time scale shown in Fig. 2 and eventually dominates the dynamics on the several-hundred-femtosecond timescale. Finally, on a picosecond time-scale, spin-flip processes contribute as well, leading to the vanishing of differences in the occupation of the two degenerate electron bands and the two hole subsystems.

Although in the presence of non-zero dephasing the density transfer is strongly reduced, and the final density of the conduction bands is significant, the basic transfer mechanism is not significantly altered. This is because the charge-carrier distribution due to the dephasing-induced absorption is different from the distribution taking part in the transfer. The latter is localized in the low-momentum states (because of our specific choice of initial conditions), whereas the former spreads of a wide range of momentum values. The range of this spread is determined by the detuning of the pulses, the curvature of the bands, and the dephasing rate (= broadening of the transitions), and it increases with increasing detuning and increasing dephasing rate. Fig. 3 illustrates this point. Although the comparison of the hh -distribution before the transfer and the lh -distribution after the transfer reveals that due to non-zero dephasing the transfer is not quite complete, it is still essentially intact. In contrast, the conduction band occupation, which is due to the dephasing-induced absorption, is generally quite small but spreads over a large range of momentum values.

Finally, we illustrate in Fig. 4 another semiconductor-specific effect: the dynamic renormalization of the optical transitions due to the light-induced dynamic energy renormalizations. Shown in the figure are the statically screened Hartree-Fock exchange energies of the three bands of the spin +1 subsystem. Due to the transient occupation of the bands, these shifts are large for all bands during the presence of the pulses. Before the transfer, only the hh -band is renormalized, and, ideally, after the transfer only the lh -band would be renormalized. However, due to absorption, there remains a non-zero renormalization of all the bands after the pulses are gone. Since this renormalization depends on the actual distribution of carriers and not only on the total density, it continues to change with time after the transfer because of the charge-carrier scattering.

4. ACKNOWLEDGEMENTS

This work is supported by grants from ARO, JSOP, Academy of Finland, COEDIP (Univ. Arizona), and grants for CPU time at CCIT, University of Arizona.

References

1. J. Oreg, F. T. Hio, and J. H. Eberly, *Phys. Rev. A* **29**, 690 (1984).
2. B. W. Shore, K. Bergmann, J. Oreg, and S. Rosenwaks, *Phys. Rev. A* **44**, 7442 (1991).
3. S. Schiemann, A. Kuhn, S. Steuerwald, and K. Bergmann, *Phys. Rev. Lett.* **71**, 3637 (1993).
4. N. Wang and H. Rabitz, *J. Chem. Phys.* **104**, 1173 (1996).
5. S. E. Harris, *Physics Today*, July 1997, p. 36.
6. N. V. Vitanov and S. Stenholm, *Opt. Commun.* **135**, 394 (1997).
7. N. V. Vitanov and S. Stenholm, *Phys. Rev. A* **55**, 648 (1997).
8. In the case of exact two-photon resonance, two of the three eigenvalues are degenerate in the absence of light. Away from the two-photon resonance, the degeneracy of these two eigenvalues in the absence of light is lifted. The temporal variation of these two eigenvalues as a consequence of the light pulses can then lead to a light-induced crossing, which can be viewed as being analogous to the Landau-Zener transition.
9. K. B. Ferrio and D. G. Steel, *Phys. Rev. Lett.* **80**, 786 (1998).
10. M. Lindberg and R. Binder, *Phys. Rev. Lett.* **75**, 1403 (1995).
11. R. Binder and M. Lindberg, (1998), submitted for publication.
12. W. Pötz, *Appl. Phys. Lett.* **71**, 395 (1997).
13. An alternative way to create a hole plasma is to optically pump a type-II semiconductor quantum well in which the electrons localize in a different well shortly after the excitation process. The advantage of such an approach lies in the greater flexibility in adjusting the hole density. We are grateful to Steven Cundiff for pointing that out to us.
14. R. Binder and S. Koch, *Prog. Quant. Electr.* **19**, 307 (1995).
15. R. Binder, *Phys. Rev. Lett.* **78**, 4466 (1997).
16. H. Haug and S. W. Koch, *Quantum Theory of the Optical and Electronic Properties of Semiconductors*, 2nd ed. (World Scientific, Singapore, 1993).
17. *Optical Orientation*, edited by F. Meier and B. Zakharchenya (North-Holland, Amsterdam, 1984).
18. D. W. Snoke, W. W. Rühle, K. Köhler, and K. Ploog, *Phys. Rev. B* **55**, 13789 (1997).
19. M. Z. Maialle, E. A. de Andrade e Silva, and L. J. Sham, *Phys. Rev. B* **47**, 15776 (1993).

COHERENT CONTROL OF HEAVY-LIGHT HOLE AND PHONON QUANTUM BEATS

T. KUHN, V.M. AXT AND M. HERBST

*Institut für Theoretische Physik II
Westfälische Wilhelms-Universität
Wilhelm-Klemm-Str. 10, 48149 Münster, Germany*

AND

E. BINDER

*Hitachi Cambridge Laboratory
Cavendish Laboratory
Madingley Road, Cambridge CB3 0HE, UK*

Abstract. The control of quantum beats by two phase-locked optical pulses is analyzed theoretically. We compare the case of heavy-light hole quantum beats as an example of a purely electronic coherence with the case of phonon quantum beats which are a characteristic feature of electron-phonon quantum kinetics. The maxima and minima of the beat amplitudes can be understood by the same arguments. For the case of phonon quantum beats an exactly solvable model is presented which allows us to analyze the role of the electron-phonon coupling constant.

1. Introduction

Coherent dynamics in semiconductors relies on the fact that a quantum mechanical system is not completely specified by the amplitude of the wave function related to an occupation probability, but also by its phase. In atomic physics such coherent experiments have a long tradition, in semiconductors, due to the short dephasing times, they have been possible only when sufficiently short laser pulses became available. Among the many types of coherent experiments one of the most direct ways to show the wave-like behavior are coherent control experiments which are based on the phenomenon of constructive or destructive interference. Essentially two

different classes of such experiments have been performed: The excitation by two simultaneous pulses with different frequencies allows one to control the final state of the system which is used, e.g., for the coherent control of photocurrent [1] or chemical reactions [2]. The excitation by two temporally non-overlapping pulses, on the other hand, gives a direct information on the phase memory introduced by the first pulse. Examples of this latter case are coherent control of exciton density, spin, and heavy-light hole (HL) beats [3, 4, 5], of THz emission due to quantum beats in asymmetric double quantum wells [6, 7], and of phonon quantum beats [8, 9]. In this contribution we will concentrate on the coherent control of quantum beats by comparing the case of HL beats which can be understood on the basis of the semiconductor Bloch equations (SBE) with the case of phonon quantum beats, which require a quantum kinetic treatment of carrier-phonon interaction. Besides a full quantum kinetic semiconductor model we investigate an analytically solvable model which allows us to study the effects of a stronger electron-phonon coupling.

2. Heavy-light hole quantum beats

The theoretical description of coherent dynamics in a semiconductor including heavy holes (HH) and light holes (LH) is based on the multiband SBE. The basic variables are the elements of the single particle density matrix $f_{\mathbf{k}}^e = \langle c_{\mathbf{k}}^\dagger c_{\mathbf{k}} \rangle$, $f_{ij,\mathbf{k}}^h = \langle d_{i,\mathbf{k}}^\dagger d_{j,\mathbf{k}} \rangle$, and $p_{i,\mathbf{k}} = \langle d_{i,-\mathbf{k}} c_{\mathbf{k}} \rangle$, where $c_{\mathbf{k}}^\dagger$ and $d_{i,\mathbf{k}}^\dagger$ ($c_{\mathbf{k}}$ and $d_{i,\mathbf{k}}$) denote the creation (annihilation) of electrons and holes with $i, j = h, l$ referring to HH and LH, respectively. The equations of motion for these variables are given by

$$\frac{d}{dt} f_{\mathbf{k}}^e = \frac{1}{i\hbar} \sum_i (\mathcal{U}_{i,\mathbf{k}} p_{i,\mathbf{k}}^* - \mathcal{U}_{i,\mathbf{k}}^* p_{i,\mathbf{k}}) + \frac{d}{dt} f_{\mathbf{k}}^e \Big|^{col}, \quad (1)$$

$$\begin{aligned} \frac{d}{dt} f_{ij,-\mathbf{k}}^h &= \frac{1}{i\hbar} \sum_l (\mathcal{E}_{jl,-\mathbf{k}}^h f_{il,-\mathbf{k}}^h - \mathcal{E}_{li,-\mathbf{k}}^h f_{lj,-\mathbf{k}}^h) \\ &\quad + \frac{1}{i\hbar} (\mathcal{U}_{j,\mathbf{k}} p_{i,\mathbf{k}}^* - \mathcal{U}_{i,\mathbf{k}}^* p_{j,\mathbf{k}}) + \frac{d}{dt} f_{ij,-\mathbf{k}}^h \Big|^{col}, \end{aligned} \quad (2)$$

$$\begin{aligned} \frac{d}{dt} p_{i,\mathbf{k}} &= \frac{1}{i\hbar} \sum_j (\mathcal{E}_{\mathbf{k}}^e \delta_{ij} + \mathcal{E}_{ij,-\mathbf{k}}^h) p_{j,\mathbf{k}} \\ &\quad + \frac{1}{i\hbar} \sum_j \mathcal{U}_{j,\mathbf{k}} (\delta_{ij} - \delta_{ij} f_{\mathbf{k}}^e - f_{ji,-\mathbf{k}}^h) + \frac{d}{dt} p_{i,\mathbf{k}} \Big|^{col}. \end{aligned} \quad (3)$$

Here, the Hartree-Fock renormalized energies

$$\mathcal{E}_{\mathbf{k}}^e = \epsilon_{\mathbf{k}}^e - \sum_{\mathbf{q}} V_{\mathbf{q}} f_{\mathbf{k}+\mathbf{q}}^e, \quad (4)$$

$$\mathcal{E}_{ij,\mathbf{k}}^h = \epsilon_{i,\mathbf{k}}^h \delta_{ij} - \sum_{\mathbf{q}} V_{\mathbf{q}} f_{ji,\mathbf{k}+\mathbf{q}}^h, \quad (5)$$

$\epsilon_{\mathbf{k}}^e$ and $\epsilon_{i,\mathbf{k}}^h$ denoting the single particle energies of electrons and holes and $V_{\mathbf{q}}$ being the Coulomb matrix element, include the effect of band gap renormalization, and the Hartree-Fock renormalized field

$$U_{i,\mathbf{k}} = -M_{i,\mathbf{k}} E_0(t) e^{-i\omega_L t} - \sum_{\mathbf{q}} V_{\mathbf{q}} p_{i,\mathbf{k}+\mathbf{q}}, \quad (6)$$

$M_{i,\mathbf{k}}$ being the dipole matrix element and $E_0(t)$ (ω_L) denoting the amplitude (central frequency) of the driving field, give rise to excitonic effects and Coulomb enhancement. In these equations only Coulomb terms conserving the number of carriers in each band have been taken into account which are the dominant terms due to their small- q behavior. Thus, contributions between conduction and valence bands leading, e.g., to Auger recombination and impact ionization as well as contributions leading to transitions between the valence bands are neglected. The resulting SBE are equivalent to the multisubband case given in [10].

The last term on the right hand side in each of the Eqs. (1)-(3) denotes the collision term. In the present section dephasing is treated in terms of simple relaxation time T_2 while relaxation processes of the distribution function are neglected. A detailed quantum kinetic treatment of the collision terms due to carrier-phonon interaction will be discussed in the following sections.

For the case of excitation mainly in the excitonic region of the spectrum the SBE give more insight into the coherent dynamics after transformation into the exciton basis.[10, 11] The frequency ω_n and wave function $p_{i,\mathbf{k}}^n$ of the exciton state $|n\rangle$ in \mathbf{k} -space representation are obtained by inserting the ansatz

$$p_{i,\mathbf{k}}(t) = p_{i,\mathbf{k}}^n e^{-i\omega_n t} \quad (7)$$

into the homogeneous part of Eq. (3), i.e., from the eigenvalue problem

$$(\epsilon_{\mathbf{k}}^e + \epsilon_{i,-\mathbf{k}}^h - \hbar\omega_n) p_{i,\mathbf{k}}^n - \sum_{\mathbf{q}} V_{\mathbf{q}} p_{i,\mathbf{k}+\mathbf{q}}^n = 0. \quad (8)$$

Then, the polarization can be expanded in the complete and orthogonal basis set of exciton states according to

$$p_{i,\mathbf{k}}(t) = \sum_n P_n(t) p_{i,\mathbf{k}}^n \quad (9)$$

where P_n denotes the amplitude of the n -th exciton state. After some calculations the SBE in the exciton basis are obtained:

$$\frac{d}{dt} f_{\mathbf{k}}^e = -\frac{1}{i\hbar} \sum_{i,n} (p_{i,\mathbf{k}}^{n*} M_{i,\mathbf{k}} E_0(t) e^{-i\omega_L t} P_n^* - p_{i,\mathbf{k}}^n M_{i,\mathbf{k}}^* E_0^*(t) e^{i\omega_L t} P_n) \quad (10)$$

$$- \frac{1}{i\hbar} \sum_{nn'} \sum_{i,k'} V_{k-k'} \left(p_{i,k}^{n*} p_{i,k'}^{n'} - p_{i,k'}^{n*} p_{i,k}^{n'} \right) P_n^* P_{n'} , \quad (10)$$

$$\begin{aligned} \frac{d}{dt} f_{ij,-k}^h &= \frac{1}{i\hbar} \sum_l (\mathcal{E}_{jl,-k}^h f_{il,-k}^h - \mathcal{E}_{li,-k}^h f_{lj,-k}^h) \\ &- \frac{1}{i\hbar} \sum_n \left(p_{i,k}^{n*} M_{j,k} E_0(t) e^{-i\omega_L t} P_n^* - p_{j,k}^n M_{i,k}^* E_0^*(t) e^{i\omega_L t} P_n \right) \\ &- \frac{1}{i\hbar} \sum_{nn'} \sum_{k'} V_{k-k'} \left(p_{i,k}^{n*} p_{j,k'}^{n'} - p_{i,k'}^{n*} p_{j,k}^{n'} \right) P_n^* P_{n'} , \end{aligned} \quad (11)$$

$$\begin{aligned} \frac{d}{dt} P_n &= -i\omega_n P_n - \frac{1}{i\hbar} \mu_n E_0(t) e^{-i\omega_L t} - \frac{P_n}{T_2} \\ &+ \frac{1}{i\hbar} \sum_{ij,k} p_{i,k}^{n*} M_{j,k} E_0(t) e^{-i\omega_L t} \left(\delta_{ij} f_{k}^e + f_{ji,-k}^h \right) + \frac{1}{i\hbar} \sum_{n'} P_{n'} \\ &\times \sum_{\substack{ij \\ kk'}} V_{k-k'} \left(\delta_{ij} f_{k}^e + f_{ji,-k}^h \right) \left(p_{i,k}^{n'*} p_{j,k'}^{n'} - p_{i,k'}^{n*} p_{j,k}^{n'} \right) . \end{aligned} \quad (12)$$

The coupling to the light field is now determined by the exciton dipole moment

$$\mu_n = \sum_{i,k} p_{i,k}^{n*} M_{i,k} . \quad (13)$$

The various terms in the equations of motion can be classified according to the order of the light field: The dominant contribution to the exciton amplitude P_n (first line in Eq. (12)) is of first order in the field. Thus, all driving terms in Eqs. (10), (11) are of second order in the field. The Coulomb terms cannot be neglected in the calculation of the carrier distribution even at low densities. However, these terms cancel in the equation of motion for the complete carrier (or exciton) density

$$N = n^e = n^h = \sum_{\mathbf{k}} f_{\mathbf{k}}^e = \sum_{i,k} f_{ii,k}^h \quad (14)$$

which, since $V_{\mathbf{k}-\mathbf{k}'} = V_{\mathbf{k}'-\mathbf{k}}$, is given by

$$\frac{d}{dt} N = -\frac{1}{i\hbar} \sum_n \left(\mu_n E_0(t) e^{-i\omega_L t} P_n^* - \mu_n^* E_0^*(t) e^{i\omega_L t} P_n \right) . \quad (15)$$

The second and third line in Eq. (12), which originate from phase space filling, band gap and renormalization, involve products of field or exciton amplitudes and distribution functions. Therefore they are at least of third order in the field. If screening is taken into account additional contributions appear due to the density-dependence of the Coulomb matrix elements

which, again, are at least of third order in the field. Thus, in the low density limit, i.e., up to second order in the field, the SBE in the exciton basis (Eqs. (12),(15)) agree with the optical Bloch equations for an ensemble of two-level systems with frequencies ω_n , N denoting the total occupation of the upper states. In this representation the linear response as well as the exciton density in second order are exactly determined by optical Bloch equations which enables one to interpret the results in terms of rotations of a Bloch vector [3, 5]. If higher order terms are included, this analogy does not hold anymore since the full \mathbf{k} -dependence of the distribution functions is required for the third-order contributions.

In a coherent control experiment, HL beats can be observed in the exciton density as a function of the pulse delay [4] and in the four wave mixing (FWM) signal [3]. They also modulate pump-probe signals like the differential transmission and reflection. In a coherent control FWM experiment two pulses in the direction \mathbf{k}_1 generate a polarization in the sample. A third pulse in the direction \mathbf{k}_2 interacts with this polarization and is self-diffracted in the direction $2\mathbf{k}_2 - \mathbf{k}_1$ where the FWM signal is measured. In a first approximation the FWM signal is a measure for the polarization induced by the first two pulses and, since the inhomogeneous broadening is eliminated by a time-reversal, the incoherently summed polarization $\sum_{j,\mathbf{k}} |p_{j,\mathbf{k}}|$ is a good measure for the signal in the sense that it contains the essential features. A full calculation of FWM signals is also possible, in the present case, however, calculations including three pulses for a large number of time delays are required which would be very time consuming.

Figure 1 shows the incoherently summed polarization for two series of time delays between the pulses one and two (150 fs pulses centered at the HH exciton), n referring to the number of HH exciton periods $T_{hh} = 2\pi/\omega_{hh}$ and n_l referring to the respective number of LH periods. For an integer value of n the polarization is enhanced by the second pulse (constructive interference), for an integer plus one half value it is reduced (destructive interference). Due to the dephasing ($T_2 = 2.5$ ps) it is not completely destroyed. The quantum beats, on the other hand, are determined by n_l because the light holes are excited much weaker. The beats vanish completely if n_l assumes an integer plus one half value since in this case the LH component is essentially destroyed by the second pulse.

3. Carrier-phonon quantum kinetics: Phonon quantum beats

On the semiclassical kinetic level interaction mechanisms lead to transitions between states, the transition rates being obtained from Fermi's golden rule. On this level, these mechanisms are a source of dephasing of coherent variables like interband, intersubband, and intervalence band

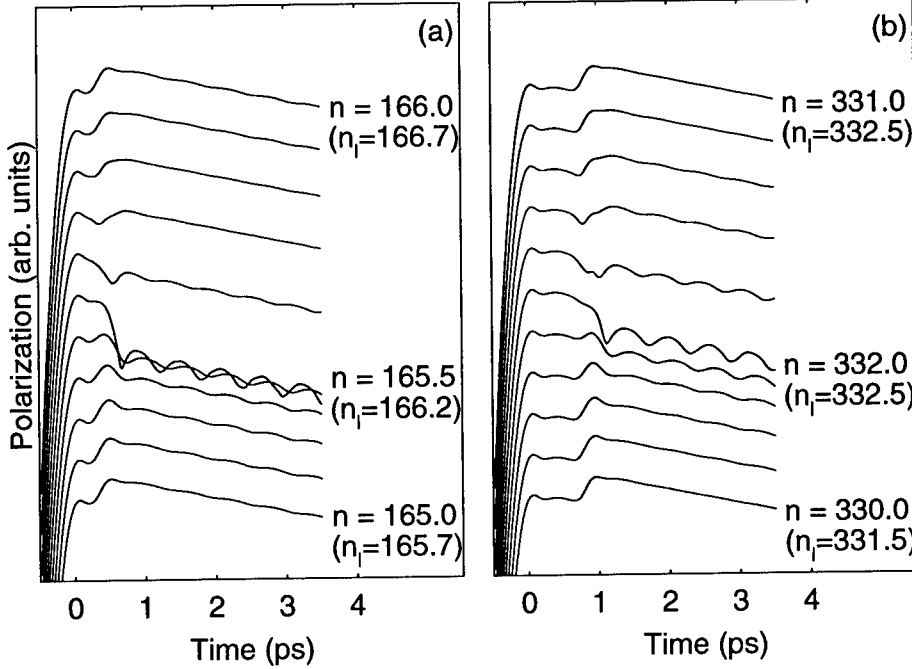


Figure 1. Coherent control of HL quantum beats in a single quantum well. The time delay between the pulses is given in units of the HH period (n) and the LH period (n_l).

polarizations. On a quantum mechanical level, on the other hand, they can also be a source of coherence due to the coupling between states. In the case of carrier-LO-phonon interaction it has been shown theoretically [12, 13, 14, 15] and experimentally [16] that in a quantum kinetic treatment the decay of the polarization exhibits an oscillatory contribution, the phonon quantum beats. Only recently it has been shown experimentally that also these beats can be coherently controlled [8, 9].

Carrier-phonon quantum kinetics in a two-band model can be described on various levels, in particular nonequilibrium Green's functions [12, 13] or the density matrix formalism [14, 15], both leading to the same equations of motion on certain approximation levels. The carrier-phonon Hamiltonian introduces new variables in the equations of motion of the single particle density matrices $f_{\mathbf{k}}^{e,h}$, $p_{\mathbf{k}}$ and $n_{\mathbf{q}} = \langle b_{\mathbf{q}}^{\dagger} b_{\mathbf{q}} \rangle$, these are the phonon assisted density matrices

$$S_{\mathbf{k}+\mathbf{q},\mathbf{k}}^e = \frac{i}{\hbar} g_{\mathbf{q}} \langle c_{\mathbf{k}+\mathbf{q}}^{\dagger} b_{\mathbf{q}} c_{\mathbf{k}} \rangle, \quad S_{\mathbf{k}+\mathbf{q},\mathbf{k}}^h = -\frac{i}{\hbar} g_{\mathbf{q}} \langle d_{\mathbf{k}+\mathbf{q}}^{\dagger} b_{\mathbf{q}} d_{\mathbf{k}} \rangle, \quad (16)$$

$$T_{\mathbf{k}+\mathbf{q},\mathbf{k}}^{(+)} = \frac{i}{\hbar} g_{\mathbf{q}} \langle d_{-(\mathbf{k}+\mathbf{q})} b_{\mathbf{q}} c_{\mathbf{k}} \rangle, \quad T_{\mathbf{k},\mathbf{k}+\mathbf{q}}^{(-)} = \frac{i}{\hbar} g_{\mathbf{q}} \langle d_{-\mathbf{k}} b_{\mathbf{q}}^{\dagger} c_{\mathbf{k}+\mathbf{q}} \rangle, \quad (17)$$

$g_{\mathbf{q}}$ being the coupling matrix elements and $b_{\mathbf{q}}^\dagger$ ($b_{\mathbf{q}}$) denoting phonon creation (annihilation) operators. They constitute the starting point of an infinite hierarchy of equations of motion involving higher order density matrices. In terms of a correlation expansion, this hierarchy is truncated by factorization on a certain level. A discussion of this factorization can be found in [17].

The Hamiltonian for a two-band model including carrier-carrier and carrier-phonon interaction is given by

$$\begin{aligned}
 H = & \sum_{\mathbf{k}} \left(\epsilon_{\mathbf{k}}^e c_{\mathbf{k}}^\dagger c_{\mathbf{k}} + \epsilon_{\mathbf{k}}^h d_{\mathbf{k}}^\dagger d_{\mathbf{k}} \right) + \sum_{\mathbf{q}} \hbar \omega_{op} b_{\mathbf{q}}^\dagger b_{\mathbf{q}} \\
 - & \sum_{\mathbf{k}} \left(M_{\mathbf{k}} E_0(t) e^{-i\omega_L t} c_{\mathbf{k}}^\dagger d_{-\mathbf{k}}^\dagger + M_{\mathbf{k}}^* E_0^*(t) e^{i\omega_L t} d_{-\mathbf{k}} c_{\mathbf{k}} \right) \\
 + & \sum_{\mathbf{k}, \mathbf{q}} g_{\mathbf{q}} \left(c_{\mathbf{k}+\mathbf{q}}^\dagger b_{\mathbf{q}} c_{\mathbf{k}} - c_{\mathbf{k}}^\dagger b_{\mathbf{q}}^\dagger c_{\mathbf{k}+\mathbf{q}} - d_{\mathbf{k}+\mathbf{q}}^\dagger b_{\mathbf{q}} d_{\mathbf{k}} + d_{\mathbf{k}}^\dagger b_{\mathbf{q}}^\dagger d_{\mathbf{k}+\mathbf{q}} \right) \\
 + & \sum_{\substack{\mathbf{k}, \mathbf{k}' \\ \mathbf{q}}} \frac{V_{\mathbf{q}}}{2} \left(c_{\mathbf{k}}^\dagger c_{\mathbf{k}'}^\dagger c_{\mathbf{k}'+\mathbf{q}} c_{\mathbf{k}-\mathbf{q}} + d_{\mathbf{k}}^\dagger d_{\mathbf{k}'}^\dagger d_{\mathbf{k}'+\mathbf{q}} d_{\mathbf{k}-\mathbf{q}} - 2c_{\mathbf{k}}^\dagger d_{\mathbf{k}'}^\dagger d_{\mathbf{k}'+\mathbf{q}} c_{\mathbf{k}-\mathbf{q}} \right). \quad (18)
 \end{aligned}$$

If all four-point correlations are neglected, this Hamiltonian gives rise to the equations of motion for the single particle density matrices

$$\begin{aligned}
 \frac{d}{dt} f_{\mathbf{k}}^e &= 2\text{Re} \left\{ \frac{i}{\hbar} \mathcal{U}_{\mathbf{k}}^* p_{\mathbf{k}} \right\} \\
 &+ \sum_{\mathbf{q}} \left[2\text{Re} \left\{ S_{\mathbf{k}+\mathbf{q}, \mathbf{k}}^e \right\} - 2\text{Re} \left\{ S_{\mathbf{k}, \mathbf{k}-\mathbf{q}}^e \right\} \right], \quad (19)
 \end{aligned}$$

$$\begin{aligned}
 \frac{d}{dt} f_{-\mathbf{k}}^h &= 2\text{Re} \left\{ \frac{i}{\hbar} \mathcal{U}_{\mathbf{k}}^* p_{\mathbf{k}} \right\} \\
 &+ \sum_{\mathbf{q}} \left[2\text{Re} \left\{ S_{-(\mathbf{k}+\mathbf{q}), -\mathbf{k}}^h \right\} - 2\text{Re} \left\{ S_{-\mathbf{k}, -(\mathbf{k}-\mathbf{q})}^h \right\} \right], \quad (20)
 \end{aligned}$$

$$\begin{aligned}
 \frac{d}{dt} p_{\mathbf{k}} &= -\frac{i}{\hbar} \left(\mathcal{E}_{\mathbf{k}}^e + \mathcal{E}_{-\mathbf{k}}^h \right) p_{\mathbf{k}} - \frac{i}{\hbar} \mathcal{U}_{\mathbf{k}} \left(1 - f_{\mathbf{k}}^e - f_{-\mathbf{k}}^h \right) \\
 &+ \sum_{\mathbf{q}} \left[T_{\mathbf{k}+\mathbf{q}, \mathbf{k}}^{(+)} - T_{\mathbf{k}-\mathbf{q}, \mathbf{k}}^{(-)} - T_{\mathbf{k}, \mathbf{k}-\mathbf{q}}^{(+)} + T_{\mathbf{k}, \mathbf{k}+\mathbf{q}}^{(-)} \right], \quad (21)
 \end{aligned}$$

$$\frac{d}{dt} n_{\mathbf{q}} = \sum_{\mathbf{k}} \left[2\text{Re} \left\{ S_{\mathbf{k}+\mathbf{q}, \mathbf{k}}^e \right\} + 2\text{Re} \left\{ S_{\mathbf{k}+\mathbf{q}, \mathbf{k}}^h \right\} \right]. \quad (22)$$

For the phonon assisted density matrix $T^{(+)}$ we obtain

$$\begin{aligned}
 \frac{d}{dt} T_{\mathbf{k}', \mathbf{k}}^{(+)} &= \frac{1}{i\hbar} \left(\mathcal{E}_{-\mathbf{k}'}^h + \mathcal{E}_{\mathbf{k}}^e + \hbar \omega_{op} \right) T_{\mathbf{k}', \mathbf{k}}^{(+)} - \frac{i}{\hbar} \left(1 - f_{-\mathbf{k}'}^h - f_{\mathbf{k}}^e \right) \tilde{T}_{\mathbf{k}', \mathbf{k}}^{(+)} \\
 &+ \frac{i}{\hbar} \left(\mathcal{U}_{\mathbf{k}'} S_{\mathbf{k}', \mathbf{k}}^e - \mathcal{U}_{\mathbf{k}} S_{-\mathbf{k}, -\mathbf{k}'}^h \right) - \frac{i}{\hbar} \left(p_{\mathbf{k}'} \tilde{S}_{\mathbf{k}', \mathbf{k}}^e - p_{\mathbf{k}} \tilde{S}_{-\mathbf{k}, -\mathbf{k}'}^h \right)
 \end{aligned}$$

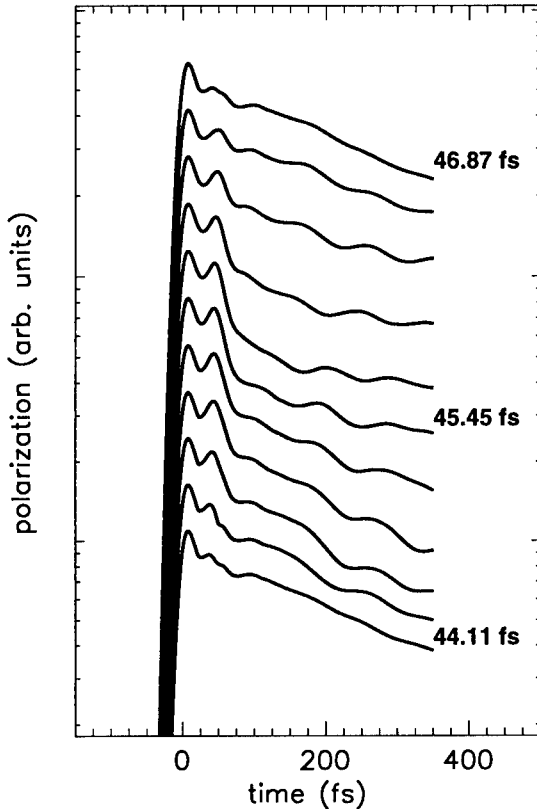


Figure 2. Coherent control of phonon quantum beats in a quantum wire for the case of excitation by two 15 fs pulses centered at the exciton frequency.

$$\begin{aligned}
 &+ \frac{1}{\hbar^2} |g_{\mathbf{k}'-\mathbf{k}}|^2 \left[(n_{\mathbf{k}'-\mathbf{k}} + 1) (1 - f_{\mathbf{k}}^e) + n_{\mathbf{k}'-\mathbf{k}} f_{\mathbf{k}}^e \right] p_{\mathbf{k}'} \\
 &- \frac{1}{\hbar^2} |g_{\mathbf{k}'-\mathbf{k}}|^2 \left[(n_{\mathbf{k}'-\mathbf{k}} + 1) (1 - f_{-\mathbf{k}'}^h) + n_{\mathbf{k}'-\mathbf{k}} f_{-\mathbf{k}'}^h \right] p_{\mathbf{k}}
 \end{aligned} \quad (23)$$

with the off-diagonal Hartree-Fock terms

$$\tilde{S}_{\mathbf{k}',\mathbf{k}}^{e,h} = - \sum_{\mathbf{q}'} V_{\mathbf{q}'} S_{\mathbf{k}'+\mathbf{q}',\mathbf{k}+\mathbf{q}'}^{e,h} + V_{\mathbf{k}'-\mathbf{k}} \sum_{\mathbf{q}'} \left(S_{\mathbf{k}'+\mathbf{q}',\mathbf{k}+\mathbf{q}'}^{e,h} + S_{\mathbf{k}'+\mathbf{q}',\mathbf{k}+\mathbf{q}'}^{h,e} \right) \quad (24)$$

$$\tilde{T}_{\mathbf{k}',\mathbf{k}}^{(\pm)} = - \sum_{\mathbf{q}'} V_{\mathbf{q}'} T_{\mathbf{k}'+\mathbf{q}',\mathbf{k}+\mathbf{q}'}^{(\pm)}, \quad (25)$$

and similar equations for the other phonon assisted density matrices.

Figure 2 shows the incoherently summed polarization for the case of a quantum wire excited by two 15 fs pulses centered at the exciton frequency.

The oscillations, which in the present case are due to a beating between the exciton and a phonon sideband above the exciton, can be clearly controlled by the relative phase of the second pulse. The beats are essentially absent for the lowest and the highest value of the time delay shown in the figure. These values correspond to 16.5 and 17.5 times the period of the phonon sideband which is determined by the sum of exciton and beat frequency. Thus, the behavior is the same as in the case of HL beats shown above. It is interesting to notice that the decay of the signal is modified by the second pulse, a feature which has been found also in the experiment [8, 9].

4. Non-perturbative treatment of carrier-phonon interaction

The quantum kinetic theory discussed in the previous section is based on a correlation expansion which assumes that correlations between an increasing number of quasiparticles are of decreasing importance. Since this expansion is related to an expansion in the carrier-phonon coupling matrix element, the analysis of systems with a stronger phonon coupling requires to take into account higher orders in the hierarchy. In this section we discuss an alternative method which has been proposed recently [18] and which avoids the hierarchy. This method will be applied to a simple model of a two-level system interacting with a single phonon mode. This model, which has already been shown to explain very well the coherent control of phonon quantum beats in the weak coupling limit [8, 9], can be solved exactly by the present method.

The basic idea is to substitute the single particle density matrices by generating functions defined according to, e.g.,

$$f_{\mathbf{k}\mathbf{k}'}^e(\{\alpha_{\mathbf{q}}\}, \{\beta_{\mathbf{q}}\}) = \langle c_{\mathbf{k}}^\dagger c_{\mathbf{k}'} \exp[\sum_{\mathbf{q}} \alpha_{\mathbf{q}} b_{\mathbf{q}}^\dagger] \exp[\sum_{\mathbf{q}} \beta_{\mathbf{q}} b_{\mathbf{q}}] \rangle, \quad (26)$$

$$p_{\mathbf{k}\mathbf{k}'}(\{\alpha_{\mathbf{q}}\}, \{\beta_{\mathbf{q}}\}) = \langle d_{\mathbf{k}} c_{\mathbf{k}'} \exp[\sum_{\mathbf{q}} \alpha_{\mathbf{q}} b_{\mathbf{q}}^\dagger] \exp[\sum_{\mathbf{q}} \beta_{\mathbf{q}} b_{\mathbf{q}}] \rangle \quad (27)$$

with complex numbers $\alpha_{\mathbf{q}}$ and $\beta_{\mathbf{q}}$. All phonon-related higher order density matrices can be obtained as partial derivatives with respect to $\alpha_{\mathbf{q}}$ and $\beta_{\mathbf{q}}$ taken at $\alpha_{\mathbf{q}} = \beta_{\mathbf{q}} = 0$. As a result, the hierarchy of equations of motion is transformed into a set of partial differential equations. While the treatment of a full semiconductor model is too complicated due to the high dimension of the equations, the following two-level model interacting with one phonon mode, which stands for a coupled exciton-phonon system, can be solved analytically.

The Hamiltonian including the coupling to the light field is given by

$$H = \hbar\Omega c^\dagger c + \hbar\omega_L b^\dagger b + \hbar g (b^\dagger + b) c^\dagger c - \hbar M_0 (E c^\dagger d^\dagger + E^* d c). \quad (28)$$

The dynamical variables in this case are the functions

$$p(\alpha, \beta, t) = \langle dc \exp(\alpha b^\dagger) \exp(\beta b) \rangle, \quad (29)$$

$$f(\alpha, \beta, t) = \langle c^\dagger c \exp(\alpha b^\dagger) \exp(\beta b) \rangle, \quad (30)$$

$$n(\alpha, \beta, t) = \langle \exp(\alpha b^\dagger) \exp(\beta b) \rangle, \quad (31)$$

which obey the following equations of motion:

$$i\partial_t p = [\Omega + \omega_L(\beta\partial_\beta - \alpha\partial_\alpha) + g(\beta + \partial_\alpha + \partial_\beta)]p - M_0 E(n - 2f), \quad (32)$$

$$i\partial_t f = [\omega_L(\beta\partial_\beta - \alpha\partial_\alpha) + g(\beta - \alpha)]f - M_0 [E p^T - E^* p], \quad (33)$$

$$i\partial_t n = \omega_L(\beta\partial_\beta - \alpha\partial_\alpha)n + g(\beta - \alpha)f, \quad (34)$$

with $p^T(\alpha, \beta) \equiv p^*(\beta^*, \alpha^*)$. By means of the transformations

$$\bar{p}(\alpha, \beta, t) = e^{i\bar{\Omega}t + \beta\gamma e^{i\omega_L t}} p(\alpha e^{-i\omega_L t} + \gamma, \beta e^{i\omega_L t} - \gamma, t), \quad (35)$$

$$\bar{f}(\alpha, \beta, t) = e^{\gamma(\beta e^{i\omega_L t} + \alpha e^{-i\omega_L t})} f(\alpha e^{-i\omega_L t}, \beta e^{i\omega_L t}, t), \quad (36)$$

$$\bar{n}(\alpha, \beta, t) = n(\alpha e^{-i\omega_L t}, \beta e^{i\omega_L t}, t), \quad (37)$$

$$\bar{E}(t) = M_0 \exp[i\bar{\Omega}t] E(t), \quad (38)$$

with $\bar{\Omega} = \Omega - \omega_L \gamma^2$, and $\gamma = g/\omega_L$ the partial derivatives are eliminated resulting in a set of three ordinary differential equations which can be further simplified by setting $\bar{y}(\alpha, t) = \bar{y}(-\alpha^*, \alpha, t)$ where y stands for p , f , and n . The final equations of motion are

$$\begin{aligned} \partial_t \bar{p}(\alpha) &= i\bar{E} [e^{\alpha\gamma e^{i\omega_L t}} \bar{n}(\alpha - \gamma e^{-i\omega_L t}) \\ &\quad - 2 e^{\alpha^*\gamma e^{-i\omega_L t}} \bar{f}(\alpha - \gamma e^{-i\omega_L t})], \end{aligned} \quad (39)$$

$$\begin{aligned} \partial_t \bar{f}(\alpha) &= ie^{-\gamma^2} [\bar{E} e^{\alpha\gamma e^{i\omega_L t}} \bar{p}^*(-\alpha + \gamma e^{-i\omega_L t}) \\ &\quad - \bar{E}^* e^{-\alpha^*\gamma e^{-i\omega_L t}} \bar{p}(\alpha + \gamma e^{-i\omega_L t})], \end{aligned} \quad (40)$$

$$\partial_t \bar{n}(\alpha) = -i\gamma \omega_L 2 \operatorname{Re}[\alpha e^{i\omega_L t}] e^{-\gamma 2i\operatorname{Im}[\alpha e^{i\omega_L t}]} \bar{f}(\alpha). \quad (41)$$

These equations have to be solved with the initial conditions $\bar{f}(\alpha, 0) = \bar{p}(\alpha, 0) = 0$ and $\bar{n}(\alpha, 0) = \exp[-n_L |\alpha|^2]$, n_L being the equilibrium (Bose) value of the phonon occupation. From the dynamical variables we obtain the polarization $P = \hbar M_0 e^{-(i\bar{\Omega}t + \gamma^2)} \bar{p}(\gamma e^{-i\omega_L t}, t)$ and the exciton density $N_e = \bar{f}(\alpha = 0, t)$.

The equations can be solved iteratively for the case of excitation by δ -pulses $E(t) = E_0 \delta(t)$. The linear polarization is given by

$$P_\delta^{(1)}(t) = i\hbar M_0^2 E_0 \theta(t) e^{-i\bar{\Omega}t + \gamma^2 (e^{-i\omega_L t} - 1 - n_L |e^{-i\omega_L t} - 1|^2)}. \quad (42)$$

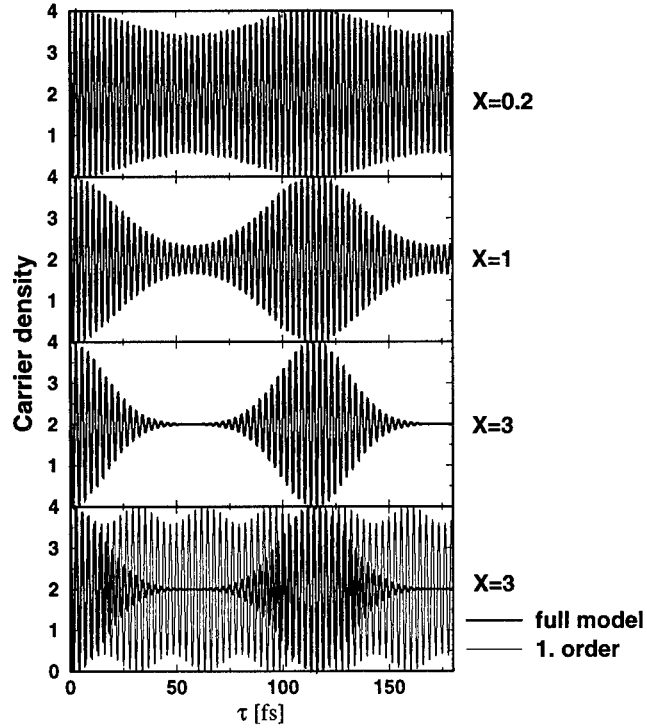


Figure 3. Coherent control of carrier density obtained from the two-level model for 15 fs pulses at $T = 10K$.

At zero temperature, where $n_L = 0$, this result can also be written as

$$P_{\delta}^{(1)}(t) = i\hbar M_0^2 E_0 \theta(t) \sum_{j=0}^{\infty} e^{-\gamma^2} \frac{\gamma^{2j}}{j!} e^{-i(\tilde{\Omega}+j\omega_L)t} \quad (43)$$

which shows the well-known result of phonon sidebands at multiples of the phonon frequency above the polaron shifted exciton energy. It is interesting to compare this exact result with the result obtained from the first order correlation expansion:

$$P_{\delta corr}^{(1)}(t) = \frac{i\hbar M_0^2 E_0 \theta(t)}{(1+2x)} \{(x+1)e^{-i[\Omega-\omega_L x]t} + xe^{-i[\Omega+\omega_L(1+x)]t}\} \quad (44)$$

with $x = (\sqrt{1+4\gamma^2} - 1)/2 \approx \gamma^2$. As expected, we find only one phonon sideband, the frequency however being shifted by a factor $(1+2x)$.

The exciton density up to $\mathcal{O}(E^2)$ generated by two δ -pulses with a time delay τ is given by

$$N_{e,\delta}^{(2)}(t, \tau) = |M_0 E_0|^2 \{ \theta(t) + \theta(t-\tau) \}$$

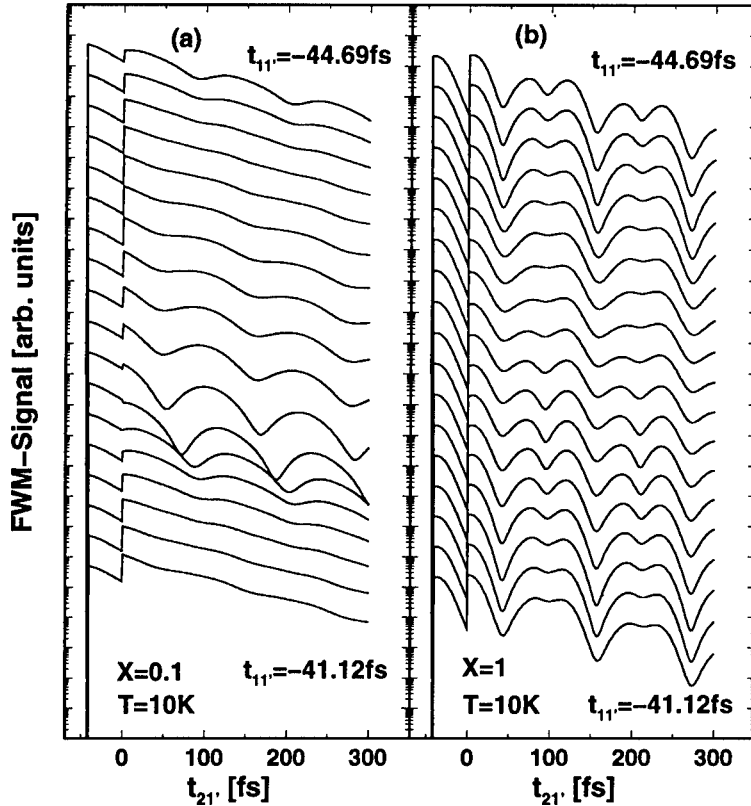


Figure 4. Coherent control of phonon quantum beats obtained from the two-level model for delta pulses at $T = 10\text{K}$.

$$\times [2\text{Re}[e^{-i\bar{\Omega}\tau+\gamma^2}(e^{-i\omega_L\tau-1-n_L}|e^{-i\omega_L\tau-1}|^2)] + 1]\} \quad (45)$$

exhibiting the fast coherent control oscillations at the polaron shifted exciton energy $\bar{\Omega}$ as well as additional structures related to the phonon coupling. In Fig. 3 the exciton density created by two 15 fs pulses at a temperature of 10 K is shown as a function of τ for three different values of the phonon coupling. For $x = 0.2$ we find a weak modulation with the phonon frequency. With increasing coupling the higher order terms do not show up as additional frequencies, instead the minima become more pronounced leading finally to a behavior similar to a “collapse and revival”. In the lowest part of the figure we compare the full model with the first order correlation expansion result which, of course, are quite different at this high value of x . Nevertheless it is interesting to notice that the very initial part below 20 fs is still in agreement which is consistent with the interpretation that the correlations are successively built up.

For the case of excitation by three δ -pulses the FWM signal can be calculated analytically. The polarization in the FWM direction is given by

$$\begin{aligned} P_{2k_2-k_1}^{(3)} = & -i\hbar M_0^2 E_0 |M_0 E_0|^2 \theta(t) e^{-i\bar{\Omega}t+2\gamma^2(\cos(\omega_L t)-1)} \\ & \times \{ \theta(-t_1) e^{-i\bar{\Omega}t_1+\gamma^2(2e^{-i\omega_L t_1}-e^{i\omega_L(t-t_1)}-1-n_L|2-e^{-i\omega_L t_1}-e^{-i\omega_L t}|^2)} \\ & + \theta(-t_{1'}) e^{-i\bar{\Omega}t_{1'}+\gamma^2(2e^{-i\omega_L t_{1'}}-e^{i\omega_L(t-t_{1'})}-1-n_L|2-e^{-i\omega_L t_{1'}}-e^{-i\omega_L t}|^2)} \} \end{aligned} \quad (46)$$

where the time of the pulse in direction k_2 has been set to zero. The FWM signal $P_{2k_2-k_1}^{(3)}$ for different time delays of the pulses in direction k_1 and for two values of the coupling constants are shown in Fig. 4. The results for the weak coupling are in agreement with those given in [8] and clearly show the coherent control of the quantum beats. By an expansion of the exponential (for $t = 0$, $n_L = 0$, $t_{21} > 0$, $t_{21'} > 0$) the signal can be written as

$$|P_{2k_2-k_1}^{(3)}|^2 = \text{const} \{ 1 + \cos(\bar{\Omega}t_{11'}) + \gamma^2 h(t_{21'}, t_{11'}) \} \quad (47)$$

with $h(t_{21'}, t_{11'}) = \cos \omega_L t_{21'} \{ \cos \omega_L t_{11'} + 1 + \cos(\bar{\Omega} + \omega_L)t_{11'} + \cos \bar{\Omega}t_{11'} \} + \sin \omega_L t_{21'} \{ \sin \omega_L t_{11'} + \sin(\bar{\Omega} + \omega_L)t_{11'} - \sin \bar{\Omega}t_{11'} \}$ which directly shows that the beat amplitude h vanishes for $(\bar{\Omega} + \omega_L)t_{11'} = (2n+1)\pi$ or $\bar{\Omega}t_{11'} = (2n+1)\pi$ in agreement with the results of the previous sections. In the case of a stronger phonon coupling the FWM signal in Fig. 4(b) exhibits higher harmonics of the phonon frequency. Since now more than two transitions are beating the oscillations cannot be anymore switched off completely.

5. Conclusions

We have presented a theoretical analysis of the coherent control of heavy-light hole and phonon quantum beats. In all cases the quantum beats are switched off by the second pulse if there is destructive interference for the weaker of the two beating transitions, which in the first case was the light hole and in the second case the phonon sideband. We have shown by an analytical solution of a two-level model coupled to a single phonon mode that for stronger phonon coupling higher harmonics appear in the FWM signal and a full control of the beats is not anymore possible.

Acknowledgements

This work has been supported by the Deutsche Forschungsgemeinschaft within the framework of the Schwerpunktprogramm *Quantenkohärenz in Halbleitern* and by the European Commission within the TMR network *Ultrafast Quantum Optoelectronics*. A grant for computer time at the HLRZ Jülich is gratefully acknowledged.

References

1. van Driel, H. M., J. E. Sipe, A. Haché, and R. Atanasov: 1997, 'Coherence control of photocurrents in semiconductors'. *phys. stat. sol. (b)* **204**, 3.
2. Brumer, P. and M. Shapiro: 1995, 'Laser control of chemical reactions'. *Sci. Am.* **272**(3), 34.
3. Heberle, A. P., J. J. Baumberg, and K. Köhler: 1995, 'Ultrafast coherent control and destruction of excitons in quantum wells'. *Phys. Rev. Lett.* **75**, 2598.
4. Baumberg, J. J., A. P. Heberle, K. Köhler, and K. Ploog: 1996, 'Ultrafast coherent carrier control in quantum wells'. *J. Opt. Soc. Am. B* **13**, 1246.
5. Heberle, A. P., J. J. Baumberg, E. Binder, T. Kuhn, K. Köhler, and K. H. Ploog: 1996, 'Coherent control of exciton density and spin'. *IEEE Journal of Selected Topics in Quantum Electronics* **2**, 769.
6. Planken, P. C. M., I. Brener, M. C. Nuss, M. S. C. Luo, and S. L. Chuang: 1993, 'Coherent control of terahertz charge oscillations in a coupled quantum well using phase-locked optical pulses'. *Phys. Rev. B* **48**, 4903.
7. Luo, M. S. C., S. L. Chuang, P. C. M. Planken, I. Brener, and M. C. Nuss: 1993, 'Coherent double-pulse control of quantum beats in a coupled quantum well'. *Phys. Rev. B* **48**, 11043.
8. Wehner, M. U., M. H. Ulm, D. S. Chemla, and M. Wegener: 1998a, 'Coherent control of electron-LO-Phonon Scattering in Bulk GaAs'. *Phys. Rev. Lett.* **80**, 1992.
9. Wehner, M. U., M. H. Ulm, D. S. Chemla, and M. Wegener: 1998b, 'Coherent dynamics in semiconductors on a 10 fs timescale: Coherent control of scattering processes'. *phys. stat. sol. (b)* **206**, 281.
10. Binder, E., T. Kuhn, and G. Mahler: 1994, 'Coherent intraband and interband dynamics in double quantum wells: Exciton and free carrier effects'. *Phys. Rev. B* **50**, 18319.
11. Chansungsan, C., L. Tsang, and S. L. Chuang: 1994, 'Coherent terahertz emission from coupled quantum wells with excitonic effects'. *J. Opt. Soc. Am. B* p. to be published.
12. Bányai, L., D. B. Tran Thoai, C. Remling, and H. Haug: 1992, 'Interband quantum kinetics with LO-phonon scattering in a laser-pulse-excited semiconductor'. *phys. stat. sol. (b)* **173**, 149.
13. Tran Thoai, D. B. and H. Haug: 1993, 'Band-edge quantum kinetics for coherent ultrashort-pulse spectroscopy in polar semiconductors'. *Phys. Rev. B* **47**, 3574.
14. Schilp, J., T. Kuhn, and G. Mahler: 1994, 'Electron-phonon quantum kinetics in pulse excited semiconductors: Memory and renormalization effects'. *Phys. Rev. B* **50**, 5435.
15. Schilp, J., T. Kuhn, and G. Mahler: 1995, 'Quantum kinetics of the coupled carrier-phonon system in photoexcited semiconductors'. *phys. stat. sol. (b)* **188**, 417.
16. Bányai, L., D. B. Tran Thoai, E. Reitsamer, H. Haug, D. Steinbach, M. U. Wehner, M. Wegener, T. Marschner, and W. Stolz: 1995, 'Exciton-LO-phonon quantum kinetics: Evidence of memory effects in bulk GaAs'. *Phys. Rev. Lett.* **75**, 2188.
17. Kuhn, T.: 1998, 'Density matrix theory of coherent ultrafast dynamics'. In: E. Schöll (ed.): *Theory of Transport Properties of Semiconductor Nanostructures*. London, p. 173.
18. Axt, V. M. and S. Mukamel: 1998, 'Nonlinear optics of semiconductor and molecular nanostructures; a common perspective'. *Rev. Mod. Phys.* **70**, 145.

COHERENT CONTROL SCHEMES IN SEMICONDUCTOR DOUBLE WELLS

XUEDONG HU AND WALTER PÖTZ

*Department of Physics, University of Illinois at Chicago
845 W. Taylor, Chicago, IL 60607*

Abstract. We present a brief overview of some of our theoretical studies of coherent control schemes in semiconductor heterostructures within Boltzmann–Bloch equations. The latter are obtained from Dyson’s equation within the Keldysh nonequilibrium Green’s function approach and allow a microscopic analysis of coherent control schemes in semiconductors. Feasibility of coherent control of charge oscillations, optical absorption, and optical gain is predicted. Most recent studies also indicate that coherent control of longitudinal optical (LO) phonon emission rates can be achieved.

1. Introduction

Coherent control is based on quantum interference between competing pathways as demonstrated, for example, in Young’s multi-slit experiment or the Aharonov–Bohm effect [1]. Original experimental work on coherent control in atoms, molecules, and solids has been based on variation of the relative phase between two coherent light fields, one of which promotes single photon absorption, the other leading to either two- or three-photon absorption. Within this scheme, coherent control of photo-ionization, photo-dissociation, and the direction of photocurrent has been demonstrated in experiments [2, 3, 4]. We proposed that coherent control of THz radiation from heterostructures can be achieved [5]. The principle of this coherent control scheme, illustrated in Fig. 1(a), can be explained with Fermi’s Golden Rule. It states that the probability for going from an initial state

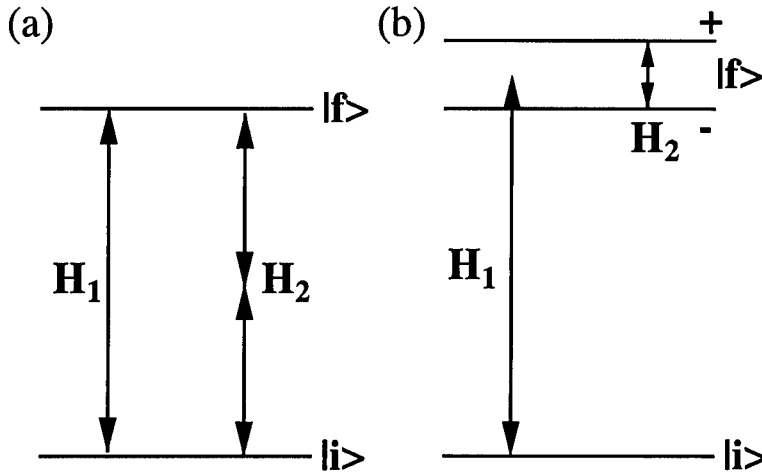


Figure 1. Schematic representation of two coherent control schemes: (a) the traditional scheme using the relative phase between two light fields; (b) a coherent control scheme based on a three-level system. Horizontal bars and vertical arrows indicate electronic bands and light fields, respectively.

$|i\rangle$ to a final state $|f\rangle$ is proportional to

$$P_{i \rightarrow f} \propto |\langle i | \sum_{i=1}^N H_i | f \rangle|^2 \quad (1)$$

when there are N ($N=2$, in the simplest case of coherent control) ways to couple $|i\rangle$ to $|f\rangle$. Adjusting the relative phase between individual Hamiltonians H_i allows manipulation of the magnitude of interference terms and hence the transition probability.

However, the quantum interference principle is much more general and is not limited to two-level situations or two perturbations. Consider, for example, a bulk semiconductor or a semiconductor nanostructure where electronic transitions occur between two or more *electronic (sub)bands*, *i.e.* between two continua. Such transitions can be promoted by various “built-in” many-body interactions, such as electron-electron, electron-phonon, and electron-photon interactions, as well as external perturbations. Generally, there is little external control over many-body interactions, although structural design can be used to suppress certain coupling mechanisms. For example, the LO phonon coupling can be suppressed by using minibands which are narrower than the LO phonon energy. Similarly, scattering contributions from the electron-electron Coulomb interaction can be reduced by working in the low density regime. Moreover, structural design allows tailoring of coupling matrix elements to some degree, which has been exploited in the design of quantum cascade lasers and Fano resonances [6].

Note also that recently an optical intracollisional-field effect has been used to manipulate the phonon emission rate [7]. This occurs when light pulse durations are significantly shorter than optical phonon emission times (≈ 200 fs in GaAs) so that collision duration times can be resolved. Here, however, we will confine ourselves to situations where pump and probe pulse durations are of the same order of magnitude (or larger) than characteristic scattering times. In this case, Boltzmann–Bloch equations (BBEs) give a good microscopic account of the physical processes that go on in a semiconductor upon subpicosecond (laser) excitation [8].

BBEs, or equivalently, density matrix equations can account for both coherence in the system, in the form of interband polarizations $f_{\alpha\beta}(\mathbf{k})$ (off-diagonal density matrix elements), and phase breaking in the system due to many-body interactions. For example, the basic electron–phonon scattering contributions are of the form

$$\begin{aligned}
& \partial_t f_{\alpha\beta}^>(t, \mathbf{k}) \Big|_{\text{e-p, scattering}} = \\
& \frac{1}{\hbar^2} \sum_{\gamma\nu\nu'\mathbf{k}_\nu} \int_0^t dt' \left\{ M_{\alpha\nu'}^{(\sigma)}(\mathbf{k} - \mathbf{k}_\nu) M_{\nu\gamma}^{(\sigma)}(\mathbf{k}_\nu - \mathbf{k}) \right. \\
& \left[\left(n_\sigma^<(t', \mathbf{k} - \mathbf{k}_\nu) e^{\frac{i(t-t')}{\hbar}(\epsilon_\beta(\mathbf{k}) - \epsilon_{\nu'}(\mathbf{k}_\nu) - \hbar\omega_\sigma(\mathbf{k} - \mathbf{k}_\nu))} \right) f_{\nu'\nu}^<(t', \mathbf{k}_\nu) f_{\gamma\beta}^>(t', \mathbf{k}) \right. \\
& + n_\sigma^>(t', \mathbf{k}_\nu - \mathbf{k}) e^{\frac{i(t-t')}{\hbar}(\epsilon_\beta(\mathbf{k}) - \epsilon_{\nu'}(\mathbf{k}_\nu) + \hbar\omega_\sigma(\mathbf{k}_\nu - \mathbf{k}))} \left. \right) \\
& - \left(n_\sigma^>(t', \mathbf{k} - \mathbf{k}_\nu) e^{\frac{i(t-t')}{\hbar}(\epsilon_\beta(\mathbf{k}) - \epsilon_{\nu'}(\mathbf{k}_\nu) - \hbar\omega_\sigma(\mathbf{k} - \mathbf{k}_\nu))} \right. \\
& + n_\sigma^<(t', \mathbf{k}_\nu - \mathbf{k}) e^{\frac{i(t-t')}{\hbar}(\epsilon_\beta(\mathbf{k}) - \epsilon_{\nu'}(\mathbf{k}_\nu) + \hbar\omega_\sigma(\mathbf{k}_\nu - \mathbf{k}))} \left. \right) f_{\nu'\nu}^>(t', \mathbf{k}_\nu) f_{\gamma\beta}^<(t', \mathbf{k}) \Big] \\
& + M_{\gamma\nu'}^{(\sigma)}(\mathbf{k} - \mathbf{k}_\nu) M_{\nu\beta}^{(\sigma)}(\mathbf{k}_\nu - \mathbf{k}) \left[\left(n_\sigma^<(t', \mathbf{k} - \mathbf{k}_\nu) e^{\frac{i(t'-t)}{\hbar}(\epsilon_\alpha(\mathbf{k}) - \epsilon_\nu(\mathbf{k}_\nu) - \hbar\omega_\sigma(\mathbf{k} - \mathbf{k}_\nu))} \right) f_{\nu'\nu}^<(t', \mathbf{k}_\nu) f_{\alpha\gamma}^>(t', \mathbf{k}) \right. \\
& + n_\sigma^>(t', \mathbf{k}_\nu - \mathbf{k}) e^{\frac{i(t'-t)}{\hbar}(\epsilon_\alpha(\mathbf{k}) - \epsilon_\nu(\mathbf{k}_\nu) + \hbar\omega_\sigma(\mathbf{k}_\nu - \mathbf{k}))} \left. \right) f_{\nu'\nu}^>(t', \mathbf{k}_\nu) f_{\alpha\gamma}^<(t', \mathbf{k}) \\
& - \left(n_\sigma^>(t', \mathbf{k} - \mathbf{k}_\nu) e^{\frac{i(t'-t)}{\hbar}(\epsilon_\alpha(\mathbf{k}) - \epsilon_\nu(\mathbf{k}_\nu) - \hbar\omega_\sigma(\mathbf{k} - \mathbf{k}_\nu))} \right. \\
& + n_\sigma^<(t', \mathbf{k}_\nu - \mathbf{k}) e^{\frac{i(t'-t)}{\hbar}(\epsilon_\alpha(\mathbf{k}) - \epsilon_\nu(\mathbf{k}_\nu) + \hbar\omega_\sigma(\mathbf{k}_\nu - \mathbf{k}))} \left. \right) f_{\nu'\nu}^>(t', \mathbf{k}_\nu) f_{\alpha\gamma}^<(t', \mathbf{k}) \\
& + 2i \sin[(t' - t)\omega_\sigma(0)] f_{\nu'\nu}^<(t', \mathbf{k}_\nu) M_{\nu\nu'}^{(\sigma)}(0)
\end{aligned}$$

$$\begin{aligned} & \times \left(M_{\gamma\beta}^{(\sigma)}(0) f_{\alpha\gamma}^<(t', \mathbf{k}) e^{\frac{i(t'-t)}{\hbar}(\epsilon_\alpha(\mathbf{k}) - \epsilon_\gamma(\mathbf{k}))} \right. \\ & \left. - M_{\alpha\gamma}^{(\sigma)}(0) f_{\gamma\beta}^<(t', \mathbf{k}) e^{\frac{i(t'-t)}{\hbar}(\epsilon_\gamma(\mathbf{k}) - \epsilon_\beta(\mathbf{k}))} \right) \} \end{aligned} \quad (2)$$

Here, $n_\sigma^<(t, \mathbf{k})$ is the phonon occupation number for phonon mode (σ, \mathbf{k}) and $n_\sigma^>(t, \mathbf{k}) = n_\sigma^<(t, \mathbf{k}) + 1$. Similarly, $f_{\alpha\gamma}^<(t, \mathbf{k}) = -f_{\gamma\alpha}(t, \mathbf{k})$ and $f_{\alpha\gamma}^>(t, \mathbf{k}) = \delta_{\alpha\gamma} - f_{\gamma\alpha}(t, \mathbf{k})$, with α, γ , and \mathbf{k} denoting subbands and the two-dimensional wave vector for in-plane motion, respectively. Here $f_{\gamma\alpha}$ are inter(sub)band polarizations, while $f_{\alpha\alpha}$ are carrier distribution functions in band α . Usually, the adiabatic and Markov approximation are also used. Equation (2) shows that the phonon-induced transition rates depend on interband polarizations, which in turn can be manipulated externally by suitable light fields. Hence, in the present situation the quantum interference principle mandates that transition probabilities are influenced by the relative phases of interband polarizations. This will be exploited in Sect. 2.4. Equivalently, phonon Boltzmann equations show that the net phonon emission rate depends on interband polarizations, as well as distribution functions.

Interband polarizations can most effectively be manipulated by external light fields and their relative phases. In our theoretical analysis we treat light fields classically within the dipole approximation. The light-electron coupling has the structure

$$H_{LF} = \sum_{\mathbf{k}, i, f} \left\{ a_{LF}(\mathbf{k}, t) \cos(\omega_{LF}t + \phi_{LF}) \hat{b}_f(\mathbf{k})^\dagger \hat{b}_i(\mathbf{k}) + h.c. \right\}, \quad (3)$$

where $\hat{b}_\alpha(\mathbf{k})$ are the single-electron field operators. ω_{LF} and ϕ_{LF} are frequency and phase of the light field. $a_{LF}(\mathbf{k}, t)$ is the effective coupling strength. Gaussian pulse shapes are used in our calculations. Such an interaction “generates” interband polarization $f_{if}(\mathbf{k})$, *i.e.*, coherence between states $|i\rangle$ and $|f\rangle$.

However, many-body interactions set a limit to phase control as they tend to “break” phase coherence. In other words, particles do not evolve according to the single-particle Schrödinger wave equation. They interact with each other in a complicated manner, causing the concept of phase to break down on a time scale larger than the characteristic scattering time. Another way of looking at phase breaking in a control process using the relative phase between two perturbations H_1 and H_2 is to include the many-body effects symbolically as a third perturbation in H_{MB} , so that the net transition probability in Eq. (1) is

$$|\langle i | H_1 + H_2 + H_{MB} | f \rangle|^2. \quad (4)$$

Hence, when the external perturbations are weak or of the same order of magnitude as many-body scattering from $|i\rangle$ to $|f\rangle$, coherent control is limited to time scales of the order of the characteristic scattering time in the system. Note that the relevant scattering time is the one from $|i\rangle$ to $|f\rangle$, *i.e.*, the one in direct competition with the transitions promoted by the external perturbations. This explains why coherent control works for inter(sub)band excitations even when pump pulse durations far exceed intraband scattering times [3, 4].

Recent advances in subpicosecond laser spectroscopy and microfabrication of semiconductor nanostructures provide a fertile ground for the study and exploitation of coherent control phenomena. The goal is twofold. Firstly, coherent control schemes provide a sensitive tool to explore the dynamics of many-body interactions and their role in “breaking the phase”. Secondly, coherent control schemes may be used as a tool to perform certain tasks, such as controlling the final state population in an interband transition [9], the optical gain of a device [10], THz emission [5, 11, 12], or photocurrents [3, 4].

In what follows we will use the two control schemes shown in Fig. 1. Such level schemes (subband structures) can be readily engineered in semiconductor nanostructures using modern growth techniques. Fig. 1(a) shows the traditional control scheme of variation of relative phase between two light fields which, respectively, couple the initial and final band by a single- and two-(or three-) photon processes. Depending on the nature of the system, the relative phase allows control of the absorption cross section, the branching ratio in a photo-chemical reaction, the photocurrent, or charge oscillations in a double well. Note that here the horizontal bars represent electronic bands rather than sharp electronic levels of an atom. The second scheme, Fig. 1(b), is based on a three-band model consisting of a doublet $+/-$ and a singlet of bands. Manipulation of the phase of the interband polarization $f_{+-}(\mathbf{k})$ of the doublet allows control of transitions between the singlet and the doublet provided that the period of the interband polarization $f_{+-}(\mathbf{k})$ is longer than the characteristic time constant of the coupling between the singlet and the doublet. The latter can be provided by a light pulse or simply by phonons or coupling via a continuum.

2. Numerical Results

2.1. COHERENT CONTROL OF CHARGE OSCILLATIONS IN ASYMMETRIC DOUBLE WELLS

Scheme Fig. 1(a) has been used to demonstrate feasibility of coherent control of charge oscillations in asymmetric double wells [5, 13]. In an asymmetric AlGaAs/GaAs double well (as sketched in Fig. 2, but without microwave

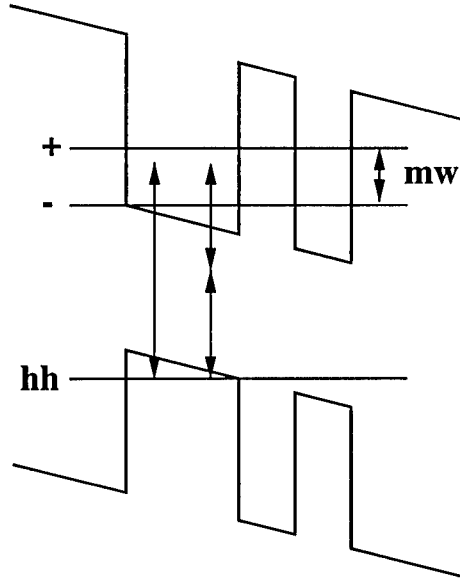


Figure 2. An illustration of a biased semiconductor double well.

(mw) driving field) the initial state $|i\rangle$ is the top heavy-hole band of the wide well. The final state $|f\rangle$ is the doublet of electron subbands which are biased into resonance by an external electric field [14]. Interference between single- and two-photon absorption between this subband doublet and the top heavy-hole band determines both the number of photo-excited electron-hole pairs, as well as their rate of generation. The light fields are treated classically and their coupling to the carriers is incorporated within the dipole approximation using the Hamiltonians

$$H_{1p} = \sum_{\mathbf{k}} \left\{ A_{1p}(\mathbf{k}, t) \hat{b}_L^\dagger(\mathbf{k}) \hat{b}_L(\mathbf{k}) - A_{1p}(\mathbf{k}, t) \hat{b}_H^\dagger(\mathbf{k}) \hat{b}_H(\mathbf{k}) \right. \\ \left. + [B_{1p}(\mathbf{k}, t) \hat{b}_L^\dagger(\mathbf{k}) \hat{b}_H(\mathbf{k}) + h.c.] \right\} \quad (5)$$

and

$$H_{2p} = \sum_{\mathbf{k}} \left\{ A_{2p}(\mathbf{k}, t) \hat{b}_L^\dagger(\mathbf{k}) \hat{b}_L(\mathbf{k}) - A_{2p}(\mathbf{k}, t) \hat{b}_H^\dagger(\mathbf{k}) \hat{b}_H(\mathbf{k}) \right. \\ \left. + [B_{2p}(\mathbf{k}, t) \hat{b}_L^\dagger(\mathbf{k}) \hat{b}_H(\mathbf{k}) + h.c.] \right\} \quad (6)$$

Here $A_i(\mathbf{k}, t) = 2\mathbf{k} \cdot \mathbf{P} / E_g a_i(t) \cos(\omega_i t + \phi_i)$, $i=1p, 2p$, where E_g , \mathbf{P} , and $a_i(t)$, respectively, are energy gap, the momentum matrix element [15], and the dipole matrix elements (times some constants) between hole (H) and left

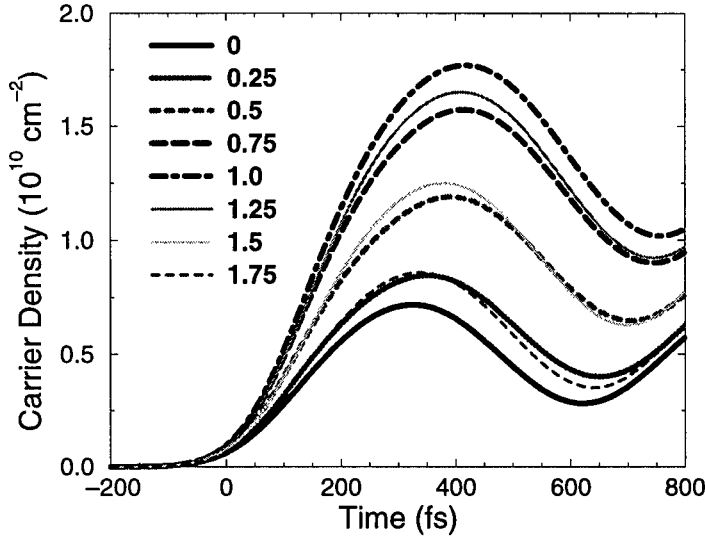


Figure 3. Number of electrons in the narrow well of a biased asymmetric 150Å-20Å-100Å double well versus time and phase of the light field providing single-photon absorption.

well (L) subband. $B_{ip}(\mathbf{k}, t) = a_i(t) \cos(\omega_i t + \phi_i)$ are the usual light-matter couplings, as used in Eq. (3). Note that Eq. (5) and Eq. (6) lead to kinetic equations which go beyond the usual semiconductor Bloch equations. They account for \mathbf{k} -dependent mixing of $|s\rangle$ and $|p\rangle$ states in valence and conduction band Bloch functions [16]. The pulse envelopes are Gaussians in time. ϕ_i is the phase of light field i . Within this Hamiltonian, the light fields are treated exactly. Standard techniques of harmonics generation using ω_{2p} as input frequency allow generation of phase-locked second harmonics of frequency $\omega_{1p} = 2\omega_{2p}$.

Fig. 3 shows the number of carriers in the narrow well as a function of time and phase of the high frequency pump field. The THz signal is proportional to the second time-derivative of this quantity [13]. In this low carrier density limit of less than 5×10^{10} carriers/cm², the pump pulse duration is limited by the tunneling period (≈ 400 fs) between left and right well. Note that this three-subband situation is distinctly more complicated than a(n atomic) three-level system due to the carrier-carrier Coulomb interaction which mixes particles in different \mathbf{k} states, leading to both coherent many-body effects, such as exciton formation, as well as incoherent many-body effects in the form of scattering. Similar control effects are obtained from interference between single- and three-photon absorption [12].

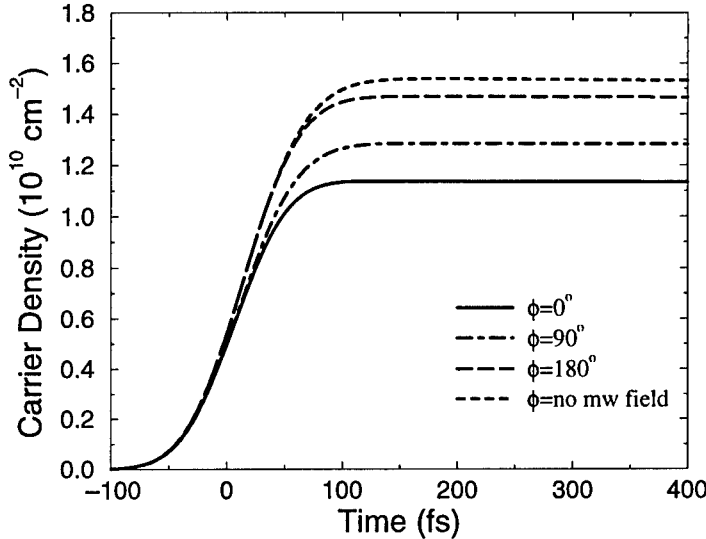


Figure 4. Number of electron-hole pairs generated in a biased asymmetric 150Å-25Å-100Å double well versus time and phase of the mw field.

2.2. COHERENT CONTROL OF OPTICAL ABSORPTION

If the duration of a pump pulse is shorter than the low frequency oscillation period of interband polarization $f_{+-}(\mathbf{k})$, the phase of the latter can be used to control optical absorption in a scheme sketched in Fig. 1(b) [12, 17]. Consider a situation where the pump pulse is in resonance with the direct exciton of the wide well in an asymmetric GaAs/AlGaAs double well and the lowest electron subband splitting is on the order of 10 meV. If this doublet is driven resonantly by a coherent microwave (mw) field, the phase of the mw field determines the phase of the $f_{+-}(\mathbf{k})$ interband polarization. Hence, for a pump pulse shorter than the doublet Rabi period, its arrival time determines the number of electron-hole pairs which are generated by the pump pulse. Fig. 4 shows the number of electron-hole pairs as a function of time and mw phase for a mw intensity of about 1 MW/cm² and a 200 fs pump pulse. Time “zero” marks the arrival of the peak of the pump pulse, whose shape is chosen to be a Gaussian. In the present case we find the effect to be periodic with π , indicating a break-down of the rotating-wave approximation for the mw field in contrast to atomic/molecular situations where the latter usually is a good approximation. Moreover, here we directly probe and control a many-body effect, namely, the Coulomb enhancement near the bandgap.

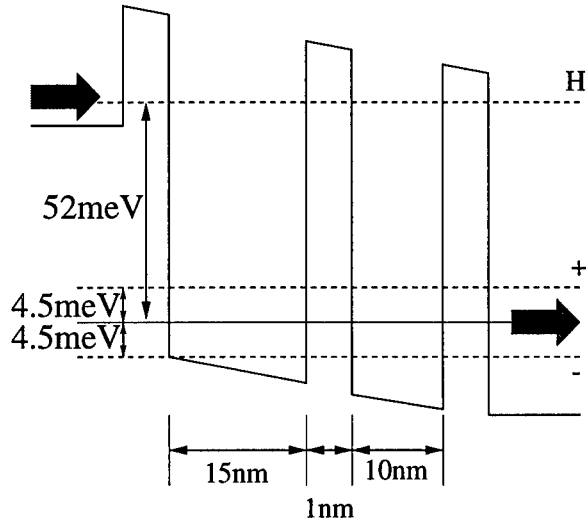


Figure 5. Here is an illustration of the asymmetric GaAs-GaAlAs double well we studied. The system is biased by a DC electric field so that the splitting of the electron subband doublet (“-” and “+”) is about 9 meV. The well and barrier widths are shown in the figure. The well depth is about 0.5 eV. Within a three-subband model we study the doublet (“-”, and “+”) and the next higher band “H”. The three subbands have the same parabolicity with carrier effective mass of $0.067m_e$. The dipole coupling between the top band “H” and the lowest subband “-” is about 65 percent of the strength of that between “H” and “+”.

2.3. COHERENT CONTROL OF OPTICAL GAIN

As a second application of scheme (b) in Fig. 1 we explore the possibility to coherently control optical gain in semiconductors. Here we consider a structure which is similar to the double-well (DW) structure which has been used as the building block of the quantum cascade laser [18]. We treat it within a three-electronic-subband model, as illustrated in Fig. 5. Its lower two subbands form a doublet whose separation is controlled by a static external field. Here the splitting is about 9 meV. The two subbands are coupled resonantly by a continuous wave (cw) mw field of intensity 1.5 MW/cm^2 (20 kW/cm^2 in the long probe pulse cases). A probe pulse couples a higher subband (H) to the doublet (“+” and “-”). Both mw driving field and the probe field propagate along the planes of the quantum wells, with their electric field along the growth direction. All light-field couplings are treated within the dipole approximation. For simplicity, we treat all three subbands with equal parabolicity, so that energy separations are independent of \mathbf{k} .

HF mean field corrections from the electron-electron interaction are taken into account. Electron-electron scattering is almost always neglected

in these calculations due to the low carrier densities and short time scale in the present situation. When we did include carrier–carrier scattering, we verified that it merely leads to small quantitative changes in our results for optical gain. We do account for the polar optical phonon contribution to the electron–phonon scattering. This is important because phonons provide an efficient means of transferring electrons between subbands which is in direct competition to (stimulated) photon emission (see Eq. (4)). Here, we solely consider confined phonon modes because they are the dominant ones for current well widths of ≥ 10 nm [19].

The initial carrier density in the DW is about 1×10^{10} carriers/cm² and is maintained by either current injection or optical pumping. One way to populate the top subband H is through optical pumping. For example, one may optically pump carriers from the heavy hole band directly into subband H. Here we have made the simplification assuming that such excitation using a short optical pulse with appropriate central frequency only populates the upper subband. In reality, all the subbands should be affected. The approximation of pumping only one subband greatly reduces the complexity of the problem, while it does not lead to a neglect of important physical processes.

Another scheme to populate the upper H subband is through current injection where the electron population is maintained by coupling to two outside reservoirs, as illustrated in Fig. 5. Tunneling is included via a Fermi golden rule calculation, with the tunneling matrix elements as adjustable constants. The latter are determined by structural design and they determine how fast the system reaches the steady state. Electron tunneling has two major effects on the dynamics of the system. It resupplies carriers to the upper subband and removes them from the lower subbands, thus maintaining a relatively constant population. It also causes the carriers to decoherence because tunneling means coupling the discrete states inside the double wells to a continuum of states in the reservoirs.

We determine the spectral gain by sending a probe pulse into the sample which couples the ground state doublet to the upper subband H. The detuning of the probe pulse is measured relative to the center of the doublet with negative detuning referring to smaller photon energy and positive detuning referring to larger photon energy of the probe pulse. Due to the short probe pulse duration of 200 fs, we calculate the optical gain directly from the induced population change in the electronic subbands. For given center frequency of the probe pulse, subtracting population changes due to tunneling and phonon emission, the remaining population change is due to carriers emitting or absorbing photons by jumping between subbands. This approach is consistent with the dipole approximation which we make, where spatial dispersion is neglected.

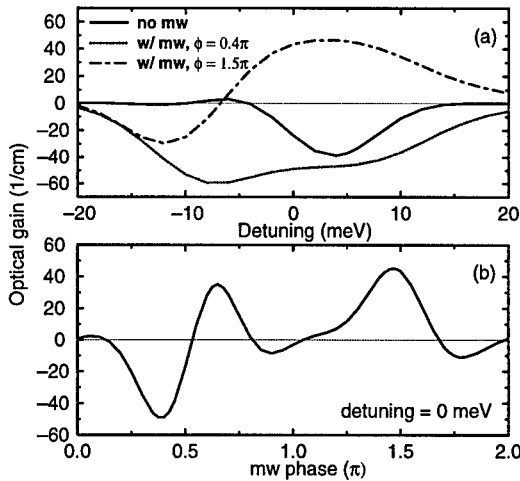


Figure 6. Optical gain with and without a mw driving field, for a short probe pulse (200 fs) in a closed system. (a) shows the optical gain profile's dependence on the mw field and its phase, while (b) shows the mw phase dependence of optical gain at a certain detuning (0 meV). As shown, the optical absorption is sensitive to the phase of the mw field.

2.3.1. Closed System

To demonstrate the coherent effect of a mw driving field, we first consider a closed three-subband system. Here we do not turn on any dissipation mechanism, but include Coulomb Hartree-Fock mean field corrections. Going from the highest to the lowest subband, the initial subband occupancies are, respectively, 0.30, 0.04, and 0.66×10^{10} carriers/cm². Initial carrier distributions are thermal at a temperature of 36 K. When the probe pulse is short (200 fs), the closed system's optical absorption and emission properties depend sensitively on the mw phase. In particular, Fig. 6(a) shows that the mw driving field significantly alters the optical gain and absorption of the system; while Fig. 6(b) shows that in a range of mw phases there can be net gain for the probe pulse even though the population inversion condition

$$\frac{1}{2}(N_+ + N_-) < N_H$$

is not fulfilled. However, because the pulse spectrum is wide (about 10 meV), we cannot resolve the two lower subbands at this pulse width.

When the probe pulse is relatively long (1000 fs), the mw phase sensitivity of the system almost completely vanishes, as shown in Fig. 7(a). Furthermore, Fig. 7(a) demonstrates that there can be gain switching between the two subbands if the time difference between the initiation of the mw field and the arrival of the probe pulse is appropriate. For example, in Fig. 7(a) the peak of the probe pulse arrives about 1800 fs after the mw field

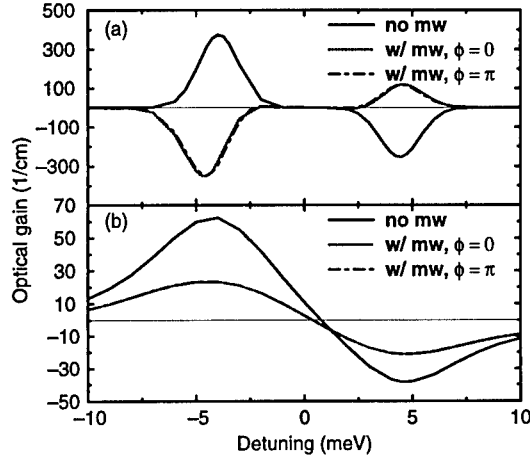


Figure 7. Optical gain with and without a mw driving field, for a long probe pulse (1000 fs), in (a) a closed system; (b) a current injection system. As shown, the optical absorption is not sensitive to the phase of the mw field. However, in (a), where there is no dissipation, there can be switch of gain peak between the two subbands. On the other hand, in (b) where dissipation is strong, there can not be switching of the gain peak.

is turned on. At this delay, there is optical gain at the spectral location of the H/– transition, even though there is no population inversion between the H and – subbands initially (with 0.30 and 0.66×10^{10} carriers/cm 2 , respectively).

2.3.2. Optical Pumping Scheme

We have investigated optical pumping for a closed double well of otherwise identical subband structure as before. To avoid inversion in the system, doping was used to populate the ground state doublet to 0.66 and 0.04×10^{10} carriers/cm 2 , which correspond to thermal carrier distributions at a temperature of 36 K. We use a pump-probe scheme. A pump pulse populates the upper electronic band “H” from the (heavy) hole band. Its intensity is such that, in the absence of phonon scattering, the final population in “H” is 0.574×10^{10} carriers/cm 2 . A (delayed) probe pulse couples the “H” band and the lower electronic subband doublet. Both pump and probe pulses have a Gaussian shape with a duration of 200 fs. In all our calculations, the probe-pump phase difference is zero. A cw mw driving field of constant amplitude resonantly couples the subband doublet.

Our results within the Boltzmann–Bloch equations, which account for electron-phonon scattering, are qualitatively consistent with what we presented in the last section for the case of a closed system. First we discuss the case of zero time delay between pump and probe. Fig. 8 shows the optical gain as a function of detuning of the probe pulse. Zero detuning again

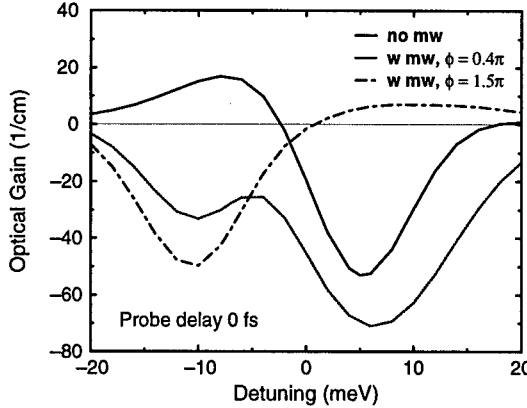


Figure 8. Optical gain with and without a mw driving field, for zero time delay between pump and probe. As shown, the optical absorption is sensitive to the phase of the mw field.

corresponds to resonance between “H” and the energy midpoint between the subband doublet. In the absence of the mw field, stimulated emission is stronger than absorption near the “H” to “+” transition (detuning ≈ -5 meV). This is because most of the electrons reside in the lower subband “-” due to the initial thermal population in the doublet. There are almost no carriers in the higher subband “+” and there is population inversion between subbands “H” and “+”. Hence, there is net emission when a probe pulse near that energy is used.

When a mw field is present, coherence (interband polarization $f_{+-}(\mathbf{k})$) between the doublet’s subbands “+” and “-” is established. This, combined with the probe light electric field, affects the high frequency interband polarization $f_{H+}(\mathbf{k})$ and $f_{H-}(\mathbf{k})$, which, in turn, influence the population in all three subbands. Thus it is possible that optical gain can be shifted to frequency regimes for which, in the absence of the mw field, no population inversion is present. Furthermore, the interband polarization $f_{+-}(\mathbf{k})$ is directly affected by the mw phase. Thus, by adjusting the latter, we can manipulate whether there is a net gain or absorption in a particular spectral regime. This is clearly illustrated in Figs. 8 and 9, where a shift in the mw phase by $\sim \pi$ (0.4π to 1.5π) leads to significant modifications in the gain spectrum and either leads to a suppression or an enhancement of net emission relative to the mw-free case. In Fig. 9, showing optical gain versus mw phase for a fixed detuning, we clearly demonstrate a strong mw-phase dependence of optical gain in a given spectral regime.

When the probe pulse is delayed by 100 fs relative to the pump pulse, the absorption and emission properties are qualitatively similar to the zero

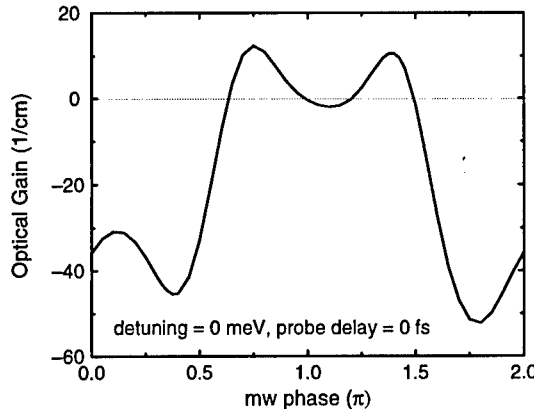


Figure 9. mw phase dependence of optical gain at a detuning of 0 meV.

delay case. Some quantitative differences arise. Results are shown in Fig. 10. Without mw field, overall emission is a little higher because now the pump pulse has more time to excite carriers into the upper subband before the probe pulse arrives. With the mw field on, spectral absorption and emission properties are again significantly different. Again the mw phase has a strong effect on whether absorption is suppressed or enhanced, as illustrated in Fig. 10. At longer time delays, absorption generally becomes larger because intersubband scattering mediated by phonons de-populates the upper subband “H” and increases the population in the lower subbands. Net emission disappears for time delay ≥ 200 fs because of this de-population of the “H” subband.

2.3.3. Current Injection Scheme

In a model of an open DW system, we prepare the electron population through current injection [10]. In order to maintain a certain steady-state subband population, tunneling times must be of the same order of magnitude as the electron interband relaxation time, which is about 400 fs. This leads to a reduced overall damping time to only about 200 fs. In the present case the tunneling times are 400 fs. This leads to a steady-state population of 0.30, 0.04, and 0.66×10^{10} carriers/cm² for subbands H, +, and -, respectively. Again a probe pulse is sent in and the change in subband population is used to determine the optical gain as a function of center frequency of the probe pulse. Because of the fast damping, the long pulse case changes significantly from that of the closed system, as illustrated in Fig. 7(b). It shows that there is no gain switching in the long probe pulse case anymore. Merely the heights of the peaks are altered compared to the

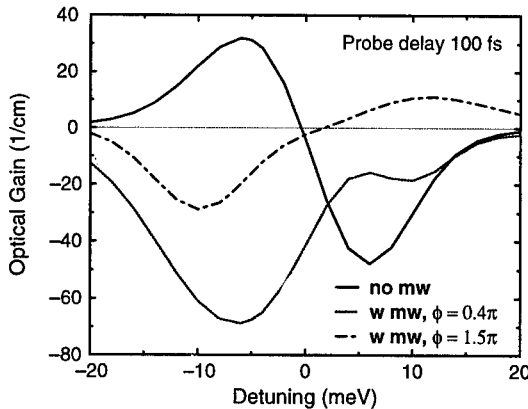


Figure 10. Intersubband optical gain with and without mw driving field, for time delay of 100 fs between probe and pump pulse.

mw-free case. Again, the regions of spectral absorption and gain are not sensitive to the mw phase.

For the short pulse case, shown in Fig. 11(a) and Fig. 11(b), the change of optical properties due to varying mw phase is still significant but less dramatic. The magnitude of net gain decreases significantly, too. However, as the total population in the upper subband is less than the average of the lower two subbands, the global population inversion condition is not satisfied. A more detailed study of the population distribution functions shows that there is no local population inversion either. Therefore, gain without local or global inversion persists in spite of the strong dissipation arising from tunneling and the electron-phonon interaction.

2.3.4. Discussion

In the case of a closed system without dissipation, a coherent mw driving field can have two types of effects. It creates a population transfer between the two subbands at the Rabi frequency, and it also generates a low frequency polarization. The time scale of these two effects is the inverse of the Rabi frequency and the inverse of the energy difference between the lower two levels. Depending on the duration of the probe pulse, one can experience either of these two effects, as we have demonstrated in the 200 fs and 1000 fs cases. In the presence of damping, Rabi oscillations are limited to a transient period. The steady state population difference becomes smaller than its initial value but maintains the same sign. Hence, no transfer of gain is possible for cw mw fields and long pulses (which can resolve the two subbands in the doublet). The effect of the mw field is reduced to

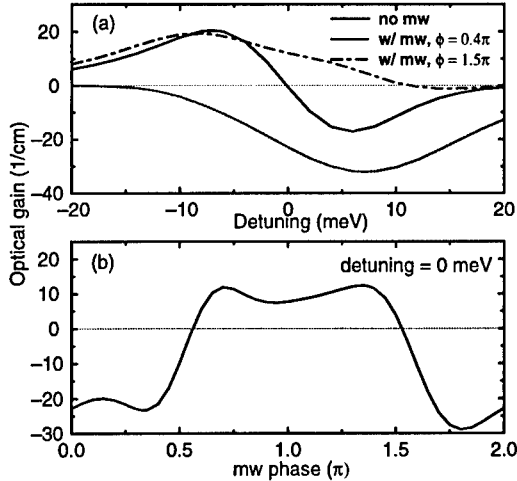


Figure 11. Optical gain with and without a mw driving field, for a short probe pulse (200 fs) in a current injected system. (a) shows the optical gain profile's dependence on mw and its phase, while (b) shows the mw phase dependence of optical gain at a certain detuning (0 meV). As shown, the optical absorption is still sensitive to the phase of the mw field.

a change of height of absorption and emission peaks (see Fig. 7(b)). On the other hand, the polarization still oscillates in the presence of damping and preserves its mw phase sensitivity, albeit with a frequency determined only by the subband splitting rather than the mw field intensity. Damping provided by phonon scattering and the openness of the system leads to profound changes in the carrier dynamics. However, in the short probe pulse case, since the low frequency polarization survives, the phase sensitivity of the optical properties of the structure also survives in spite of the strong dissipation.

2.4. COHERENT CONTROL OF PHONON EMISSION

Finally, we would like to report preliminary results regarding the coherent control of phonon emission. As is evident from Eq. (2), phonon emission rates are determined by electronic structure, electron-phonon coupling matrix elements, occupancy of states, and electron interband polarization. The former two may be engineered by structural design. The latter two depend on the (coherent) state of the system which can be manipulated externally. Here we will show that manipulation of the latter allows coherent control of the phonon-induced transfer between electron subbands. We use the scheme of Fig. 1(b) for three electronic subbands, with one ground state subband and a higher energy subband doublet. Such a scheme can most easily be realized in a semiconductor double well of unequal well depth

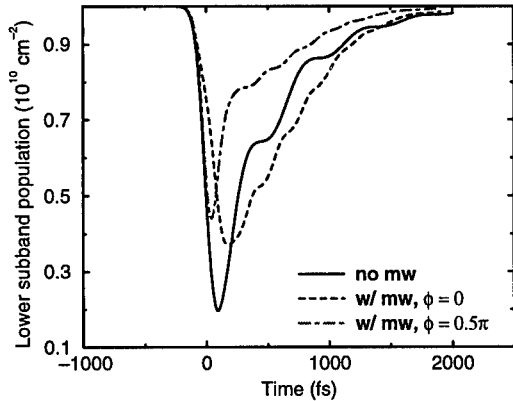


Figure 12. This is an illustration of how the intersubband carrier relaxation through phonon emission is modulated by a mw driving field.

and/or widths and can be fine-tuned by doping or external electric fields.

Here, the energy splitting between doublet and the lowest subband is 36 meV, close to the LO phonon energy in GaAs. The doublet splitting is 10 meV. For the present purpose, the ground state subband is populated by means of doping to 10^{10} carriers/cm² (at a temperature of 36 K). A 200 fs optical pump pulse is used to excite carriers into the upper two subbands. Subsequently, these carriers return to the lowest subband via phonon emission. The rate of return due to the electron-LO-phonon interaction is controlled by the intensity and phase of a mw field which manipulates the interband polarization $f_{+-}(\mathbf{k})$. For the present data we take into account only confined phonons [19]. Interface phonons and electron-electron scattering are neglected in this preliminary analysis. Phonon nonequilibrium may also be safely neglected here.

In Fig. 12 we monitor the carrier population of the lowest electron subband. Without mw driving of the subband doublet, represented by the solid line, we observe the expected population depletion when the optical pump pulse arrives, then the carrier population gradually returns to its initial value within about 2.5 ps due to carrier relaxation through phonon emission. On the other hand, when a mw field of 1.5 MW/cm² resonantly couples the subband doublet, the carrier relaxation (*i.e.*, the effective carrier-phonon emission) changes significantly as we vary the mw phase. This results from the participation of interband polarizations in the carrier relaxation process, as is evident from Eq. (2). Note that this phenomenon is distinctly different from previous experimental efforts to optically control phonon emission [7]. In these experiments the non-Markovian nature of

phonon emission which reveals itself on a time scale of a few 10 fs was probed with 15 fs pulses. Here we directly manipulate interband polarizations. Our pulse duration is more than an order of magnitude longer. Effects persist into the ps time regime. For future studies, however, we plan to incorporate non-Markovian phonon effects, as well as electron-electron scattering.

3. Summary and Conclusions

In summary, our theoretical studies confirm that a variety of coherent control phenomena can be studied in semiconductors and nanostructures. In particular, we have investigated control schemes based on semiconductor double wells which allow coherent control of THz emission, optical absorption and gain, as well as phonon-induced interband transitions. We have intentionally limited these investigations to simple nanostructures, such as semiconductor double wells, where we believe coherent control schemes to be most effective. Obviously, this work can be readily extended to more complicated subband (level) schemes. Both semiconductor growth and subpicosecond laser spectroscopy have matured to a degree where testing of these coherent control schemes is possible. Inevitably, if coherent control schemes are to be applied to semiconductor quantum wells or quantum dots, sources for suitable high-intensity light fields, such as mw fields, need to be developed. Moreover, coherent control is not limited to purely optical excitation but may be exercised in conjunction with other coupling mechanisms which may be built into the structure, such as phonons and coupling to continua (Fano resonances). It is hoped that coherent control and the quantum interference principle in general can be exploited to provide the basis for ultrafast optoelectronic devices of the future.

References

1. See for example, Sakurai, J.J. (1985) *Modern Quantum Mechanics*, Addison-Wesley, Redwood City.
2. For a review of recent developments on this issue in physical chemistry, see, for example, Gordon, R.J. (1997) Active control of the dynamics of atoms and molecules, *Annual Reviews of Physical Chemistry* **48**, 601–641.
3. Dupont, E., Corkum, P.B., Liu, H.C., Buchanan, M., and Wasilewsky, Z.R. (1995) Phase-Controlled Currents in Semiconductors, *Phys. Rev. Lett.* **74**, 3596–3599.
4. Hachè, A., Kostoulas, Y., Atanasov, R., Hughes, J.L.P., Sipe, J.E., and van Driel, H.M. (1997) Observation of Coherently Controlled Photocurrent in Unbiased, Bulk GaAs, *Phys. Rev. Lett.* **78**, 306–309.
5. Pötz, W. (1998) Coherent control of terahertz radiation from semiconductor nanostructures, *Appl. Phys. Lett.*, in press.
6. Faist, J., Capasso, F., Sirtori, C., West, K.W., and Pfeiffer, L.N. (1997) Controlling the sign of quantum interference by tunneling from quantum wells, *Nature* **390**, 589–591.

7. Wehner, M.U., Ulm, M.H., Chemla, D.S., and Wegener, M. (1998) Coherent Control of Electron-LO-Phonon Scattering in Bulk GaAs, *Phys. Rev. Lett.* **80**, 1992–1995.
8. Pötz, W. (1996) Microscopic theory of coherent carrier dynamics and phase breaking in semiconductors, *Phys. Rev. B* **54**, 5647–5664; Hohenester, U. and Pötz, W. (1997) Density matrix approach to free-carrier screening in non-equilibrium semiconductors, *Phys. Rev. B* **56**, 13177–13189.
9. Pötz, W. (1997) Manipulation of final state population in semiconductor heterostructures, *Appl. Phys. Lett.* **71**, 395–397.
10. Hu, X. and Pötz, W. (1998) Coherent control of optical gain from electronic intersubband transitions in semiconductors, *Appl. Phys. Lett.*, in press (1998).
11. Luo, M.S.C., Chuang, S.L., Planken, P.C.M., Brener, I., and Nuss, M.C. (1993) Coherent double-pulse control of quantum beats in a coupled quantum well, *Phys. Rev. B* **48**, 11043–11050; Brener, I., Planken, P.C.M., Nuss, M.C., Luo, M.S.C., Chuang, S.L., Pfeiffer, L., Leaird, D.E., and Weiner, A.M. (1994) Coherent control of terahertz emission and carrier populations in semiconductor heterostructures, *J. Opt. Soc. Am. B* **11**, 2457–2469.
12. Hu, X. and Pötz, W. (1998) Coherent control of interband transitions in semiconductor heterostructures, *SPIE Proceedings* **3277**, 36–43.
13. Pötz, W. (1996) Infrared light emission from semiconductor double wells, *Appl. Phys. Lett.* **68**, 2553–2555.
14. Leo, K., Shah, J., Göbel, E.O., Damen, T.C., Schmitt-Rink, S., Schäfer, W., and Köhler, K. (1991) Coherent Oscillations of a Wave Packet in a Semiconductor Double-Quantum-Well Structure, *Phys. Rev. Lett.* **66**, 201–204.
15. Kane, E.O. (1957) Band Structure of Indium Antimonide, *J. Phys. Chem. Solids* **1**, 249–261; Kane, E.O. (1966) The $k \cdot p$ Method, in R.K. Willardson and A.C. Beer (eds.), *Semiconductors and Semimetals*, Vol. 1, *Physics of III-V Compounds*, Academic Press, New York, pp. 75–100.
16. Dvorak, M.D., Schroeder, W.A., Andersen, D.R., Smirl, A.L., and Wherrett, B.S. (1994) Measurement of the Anisotropy of Two-Photon Absorption Coefficients in Zincblende Semiconductors, *IEEE Journal of Quantum Electronics* **30**, 256–268.
17. Pötz, W. (1997) Coherent Control of Light Absorption and Carrier Dynamics in Semiconductor Nanostructures, *Phys. Rev. Lett.* **79**, 3262–3265; Hu, X. and Pötz, W. (1997) Coherent control of intersubband transitions in semiconductor nanostructures, *Phys. Stat. Sol. (b)* **204**, 350–353.
18. Faist, J., Capasso, F., Sivco, D.L., Hutchinson, A.L., and Cho, A. Y. (1994) Quantum Cascade Laser, *Science* **264**, 553–556.
19. Ridley, B.K. (1989) Electron scattering by confined LO polar phonons in a quantum well, *Phys. Rev. B* **39**, 5282–5286; Ridley, B.K. (1991) Hot electrons in low-dimensional structures, *Rep. Prog. Phys.* **54**, 169–256.

Terahertz-Control of Charge-Carrier Wavepackets in Semiconductor Quantum Wells

S. Hughes and D. S. Citrin

*Department of Physics, Washington State University
Pullman, Washington 99164, USA
Email: shughes@wsu.edu*

With the advancement of free-electron lasers [FEL's] as well as THz solid-state emitters [1], THz physics and related technology is currently coming out of its infancy. Two-color techniques (optical and THz) applied to mesoscopic semiconductors have also been developed [2]. Consequently, the dynamics of charge carriers (electrons and holes) after excitation with short light pulses and terahertz fields in semiconductor heterostructures has been receiving an upsurge of attention recently. Besides being of fundamental interest, the investigation of interplaying THz and optical fields is also relevant in the operation of high-speed electronic and optoelectronic devices such as photodetectors, modulators, and switches. By application of strong THz fields, the effects of electron and hole transport in semiconductor devices can be considerable. The field perturbation is very intense but with a photon energy small compared to the bandgap energy. In the low density regime, in the presence of a broadband pulse, interfering electron-hole *relative motion* wave packets [WP's] are formed.

There are a number of field-induced physical mechanisms that may contribute to the optical response measured in quantum wells (QW's). In the linear regime, when a semiconductor is excited by an ultrashort optical pulse at near the bandgap, E_{gap} , electron-hole (e-h) pairs are created with excess energy since the pulse bandwidth may extend tens of meV above E_{gap} . By simultaneously applying a THz field, the carriers move in a highly complex manner depending on such effects as the electric field, excitonic binding energy, band structure, and the geometry. Initially when the optical pulse arrives, an instantaneous polarization is created for the photoexcited e-h pairs, and subsequently, the carriers undergo acceleration by the electric field for times shorter than the mean scattering times.

It is well established that when a strong DC field is polarized in the QW plane the Franz-Keldysh [3] effect takes place, i.e., induced absorption below and oscillatory behavior of the absorption above the bandgap occurs. Recently, for THz-frequency driving fields, the dynamical Franz-Keldysh effect (DFKE) has been theoretically

predicted [4] and experimentally verified [5]. When investigating the DFKE in the optical domain, experiments clearly demonstrated that in the THz regime, harmonic sidebands of the driving frequency were detected. With regard to superlattices, various effects including Zenner tunneling [6], collapse of the miniband [7], dynamic localization [8], and reflection of THz radiation [9] have been investigated. To characterize accurately and optimize the performance of the DFKE as well as to aid the development of related novel semiconductor devices, ultimately one has to understand the basic physical mechanisms. The investigation of interplaying THz and optical fields is also of general interest because it is connected to Coulomb many-body processes, such as excitonic effects, carrier transport phenomena, and electron correlations. As well as having a wide range of applications, these results are of fundamental interest as they provide a link between transport and optical phenomena.

The early observations of THz radiation from an oscillating WP in a semiconductor nanostructure, using an asymmetric double-quantum-well-structure, was reported in Ref. [10]. Such a structure can behave qualitatively like a three-level system by controlling the spacing between various electronic levels via the application of an electric field in the growth direction. Hence, when the system is excited with an ultrashort laser-pulse with a spectral width larger than the energy spacing between any two electronic levels, a nonstationary WP is created. Thereafter a number of schemes have been proposed for creating THz transients in QW's. Amongst the most popular methods include optical rectification and quantum beating between subbands (charge oscillations) [1]. Essentially these generated transients rely upon the application of a DC-bias field in the QW growth direction that drives the electrons and holes towards the interfaces of the QW. Consequently for a typical well-width of 80 \AA , peak dipole moments per e-h pair of the order $\sim 80 \text{ e\AA}$ (e is the electronic charge) can be achieved. The use of specially shaped optical pulses [11] and double-pulse control schemes [12] have also been studied. Ultimately, precise control over both the duration and the shape of the generated THz transients is desired [13].

In this work we introduce results based on the semiconductor-Bloch equations (SBE) [14] in the presence of both an intense THz field and a broadband (50 fs) optical probe pulse excited at the bandedge; this approach also allows us to analyze the creation and evolution of highly anisotropic e-h WP's, and, simultaneously, calculate the THz dynamics which are in qualitative agreement with recent experimental measurements [5]. In the following, we assume a two-band QW where each e-h state with relative wavenumber \mathbf{k} contributes to the total carrier density $N = 2A^{-1} \sum_{\mathbf{k}} f_{\mathbf{k}}^{e/h}$. Here, $f_{\mathbf{k}}^{e/h}$ is the electron or hole carrier distribution. The macroscopic polarization is $P = 2A^{-1} \sum_{\mathbf{k}} d_{cv} P_{\mathbf{k}}$, with d_{cv} the interband dipole matrix element. To obtain $P_{\mathbf{k}}$ we solve the SBE numerically, treating the influence of a THz field under optical excitation by an ultrashort optical pulse. The relevant SBE [8] for the *slowly-varying* polarization can be written ($\hbar = 1$),

$$\left(\frac{\partial}{\partial t} + \mathbf{F}_{\text{THz}}(t, \mathbf{r}) \cdot \nabla_{\mathbf{k}} \right) P_{\mathbf{k}} = -i\Delta_{\mathbf{k}} P_{\mathbf{k}} - i\Omega_{\mathbf{k}}(f_{\mathbf{k}}^e + f_{\mathbf{k}}^h - 1) + \left. \frac{\partial P_{\mathbf{k}}}{\partial t} \right|_{\text{cc}}, \quad (1)$$

with $\Delta_{\mathbf{k}} = E_{\mathbf{k}} - \omega_l - \sum_{\mathbf{q}} V_{\mathbf{k}-\mathbf{q}}(f_{\mathbf{q}}^e + f_{\mathbf{q}}^h)$ the renormalized energy dispersion for a parabolic two-band semiconductor with unrenormalized transition energy $E_{\mathbf{k}}$, $V_{\mathbf{q}}$ the Coulomb potential, and $\omega_l = E_{\text{gap}}$ the carrier frequency of the optical probe pulse assumed to be excited resonant with the bandedge. The generalized Rabi frequency is $\Omega_{\mathbf{k}} = d_{\text{cv}} \tilde{F}_{\text{Opt}}(t) + \sum_{\mathbf{q}} V_{\mathbf{k}-\mathbf{q}} P_{\mathbf{q}}$, with $\tilde{F}_{\text{Opt}}(t)$ the slowly-varying optical field polarized in the QW plane; $\mathbf{F}_{\text{THz}}(t, \mathbf{r})$ is the THz field that is also assumed to be polarized in the QW plane. In general, Coulomb correlations (cc) between the carriers must be taken into account; in this work we treat the dephasing of the optical polarization within the relaxation-time approximation, $\left. \frac{\partial P_{\mathbf{k}}}{\partial t} \right|_{\text{cc}} = -\gamma_o^p P_{\mathbf{k}}$ where γ_o^p is the total dephasing rate of the optical polarization.

For our theoretical approach the dynamics including the THz field can be treated exactly by introducing a moving coordinate frame $\tilde{t} = t, \tilde{\mathbf{k}} = \mathbf{k} + e \int^t \mathbf{F}_{\text{THz}}(t', \mathbf{r}) dt'$ [15]. In mathematical terms this numerical technique is called *method of characteristics* and has found a wide variety of applications in physics problems including solution of vector-Maxwell equations [16]. Thus our theoretical model arrives at the level of the modified, anisotropic two-dimensional SBE that fully incorporate the acceleration of the electrons and holes due to an applied field. To this end, we solve for the transformed polarization functions $\tilde{P}_{\mathbf{k}}$:

$$\frac{\partial \tilde{P}_{\mathbf{k}}}{\partial \tilde{t}} = \frac{\partial P_{\mathbf{k}}}{\partial t} \frac{\partial t}{\partial \tilde{t}} + \nabla_{\mathbf{k}} P_{\mathbf{k}} \cdot \frac{\partial \mathbf{k}}{\partial \tilde{t}}, \quad (2)$$

$$= \left[\frac{\partial}{\partial t} + \mathbf{F}_{\text{THz}} \cdot \nabla_{\mathbf{k}} \right] P_{\mathbf{k}}. \quad (3)$$

Such transformations are commonly employed for solving carrier transport equations and can be used for example in deriving the Chambers equation [17]. In the low density regime, the above relation allows us to write

$$\frac{\partial \tilde{P}_{\mathbf{k}}}{\partial t} = i\Delta_{\mathbf{k}(t)} \tilde{P}_{\mathbf{k}} + i\Omega_{\mathbf{k}(t)} - \gamma_o^p \tilde{P}_{\mathbf{k}}, \quad (4)$$

where \mathbf{k} is now a function of t . This apparent elimination of the THz-driving term may seem a little confusing at first so it warrants some discussion. Consider what happens to the transformed variables in the absence of exciton generation and scattering. The transform variable $\tilde{P}_{\mathbf{k}}$ is constant in time so that [with $\mathbf{F}_{\text{THz}}(t, \mathbf{r}) = \hat{\mathbf{n}}_x F_0 \cos(\omega_{\text{THz}} t)$] $P_{\mathbf{k}(t)} = P_{\mathbf{k} + \Lambda(t)}(t_0)$, with $\Delta t = t - t_0$, and $\Lambda(t) = \hat{\mathbf{n}}_x F_0 / \omega_{\text{THz}} \sin(\omega_{\text{THz}} \Delta t)$. Therefore, the original carriers propagate back and forth in \mathbf{k} -space by virtue of the acceleration theorem, i.e., each polarization component moves through \mathbf{k} -space with a rate proportional to the amplitude of the applied

electric field. It becomes clear that with the application of a THz field the carrier functions becomes anisotropic and one must solve the SBE on a two-dimensional grid (circular symmetry can no longer be exploited), where the two dimensions reflect the plane of the quantum well. Let us consider a simple example: After optical excitation of a WP, the maximum distance that the carriers can be accelerated in the low density regime, is $\delta k = F_0 e a_0 / \omega_{\text{THz}}$ (a_0^{-1}), which equals 1 inverse-Bohr-radius (InGaAs/GaAs) for $F_0 \approx 3 \text{ kV/cm}$. This value is still less than 5 % of the Brillouin-zone-to-zone-center range. In real space the polarization equation can be visualized as the exciton equation in an oscillating frame. Identical equations have been derived previously in Ref. [18] by choosing an appropriate gauge transformation. We make an immediate connection to this work [18] by noting that our detuning and excitonic Coloumb Hartree-Fock term can be written identically within the effective mass approximation:

$$\Delta_{\mathbf{k}} \rightarrow \frac{1}{2\mu} [\tilde{\mathbf{k}} - \mathbf{A}(t)]^2, \quad (5)$$

$$\sum_{\mathbf{q}} V_{\mathbf{k}-\mathbf{q}} P_{\mathbf{q}} \rightarrow \sum_{\tilde{\mathbf{q}}} V_{\mathbf{k}-\tilde{\mathbf{q}}} P_{\tilde{\mathbf{q}}}. \quad (6)$$

We will, however, not employ any time-averaging approximations of the kinetic energy since our pump fields have much smaller energies that results in a strong mixing of the different exciton states. It should be recognized that the relevant observables like the polarization or the current (\dot{P}) are given by the sum over all two-dimensional $P_{\mathbf{k}}$ states: $P = 2A^{-1} \sum_{\mathbf{k}} d_{cv} P_{\mathbf{k}} = 2/(2\pi)^2 \int d\tilde{k}_x \int d\tilde{k}_y d_{cv} \tilde{P}_{\tilde{k}_x, \tilde{k}_y}$.

The THz-induced intraband dipole moment can then be obtained from

$$\mathbf{P}_{\text{THz}}(t) = e \int d^2r P^*(\mathbf{r}, t) \mathbf{r} P(\mathbf{r}, t) = -e \sum_{\mathbf{k}} P_{\mathbf{k}}^* i \nabla_{\mathbf{k}} P_{\mathbf{k}}, \quad (7)$$

and subsequently for the THz electric field, assuming a point source (the actual spatial dependence will depend on the geometry) $\mathbf{F}_{\text{THz}}^G(t) = -(c^2 r)^{-1} \ddot{\mathbf{P}}_{\text{THz}}(t)$. Further, to depict the e-h WP dynamics, we calculate the polarization density (which in the low density limit corresponds to the quantum mechanical probability density of finding an electron and hole separated by \mathbf{r} at time t) from $|P(\mathbf{r}, t)|^2 = |\int d^2r P_{\mathbf{k}} \exp(-i\mathbf{k} \cdot \mathbf{r})|^2$.

For all following numerical calculations we choose parameters suitable for InGaAs/GaAs QW's: namely reduced mass, $\mu = 0.035 m_e$; $1s$ (2D) excitonic binding energy, $E_{1s} \approx 11 \text{ meV}$, $\gamma_o^p \approx 500 \text{ fs}$; and Bohr radius, $a_0 = 150 \text{ \AA}$. InGaAs/GaAs QW's are advantageous since with compressive strain one can increase the splitting of the heavy- and light-hole exciton. This leads to a particularly simple situation in which only the exciton series associated with a single valence conduction subband pair is expected. As mentioned above, we have in mind an experiment that employs both a strong THz field and an optical pulse simultaneously incident on the QW. For

the applied THz field we assume $\mathbf{F}_{\text{THz}}(t, \mathbf{r}) = \hat{\mathbf{n}}_x F_0 \cos \delta(t) = \hat{\mathbf{n}}_x F_0 \cos(2\pi\nu_{\text{THz}}t + \phi)$, with ϕ the phase of the driving field at $t = 0$ (center of the optical probe pulse), F_0 is the magnitude of the THz field (taken to be 3 kV/cm), $\hat{\mathbf{n}}_x$ is a unit vector in the QW plane, and $\nu_{\text{THz}} = 1$ THz. The optical field is taken to be a sech pulse with an input unrenormalized Rabi energy of 10^{-5} eV (irradiance $\sim 10^3$ Wcm $^{-2}$) and of 50 fs full-width half maximum irradiance (FWHM). In Fig. 1 we show a schematic of the double-field excitation scheme for studying harmonic generation.

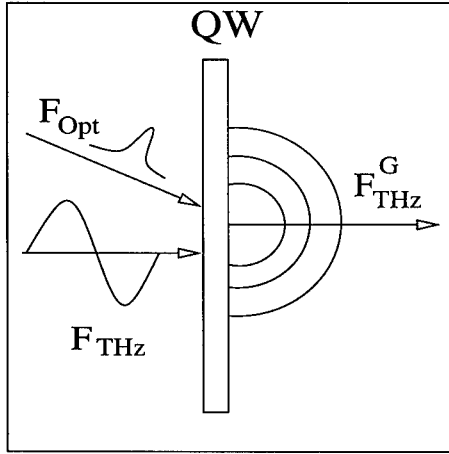


Figure 1. A schematic of the modelled experiment.

From an atomic viewpoint, the process of high-harmonic generation due to an intense atom-field interaction has received a great deal of attention in recent years [19], and coherent short-wavelength radiation well into the X-ray region has been demonstrated. Moreover, harmonically-generated X-ray transients as short as 100 attoseconds have been predicted [20]. The observed spectrum of harmonics is affected by both the single-atom emission and the ensuing collective behavior. Basically, the generation of high harmonics of a laser irradiating an ensemble of atoms can be viewed as follows: each atom emits radiation that propagates in the remaining atoms, ions and ionized electrons; consequently, they interfere, scatter, and may stimulate further harmonic emission. The theoretical problem of HHG has to be treated nonperturbatively in the atom-field interaction and is an intriguing problem. For Rydberg atoms [21], higher frequency harmonics are produced from continuum-state to bound-state transitions, in which electrons release the energy absorbed from the field during its excursion in the continuum. For intense fields, the ponderomotive energy of a detached electron can be larger than the bound states' energy. The harmonic generation in Rydberg atoms presents extensive plateaus [22]

(an extensive region of similar spectral intensity in frequency extending well above the fundamental excitonic binding energy). Below we demonstrate that harmonic generation for the QW is possible in the THz regime.

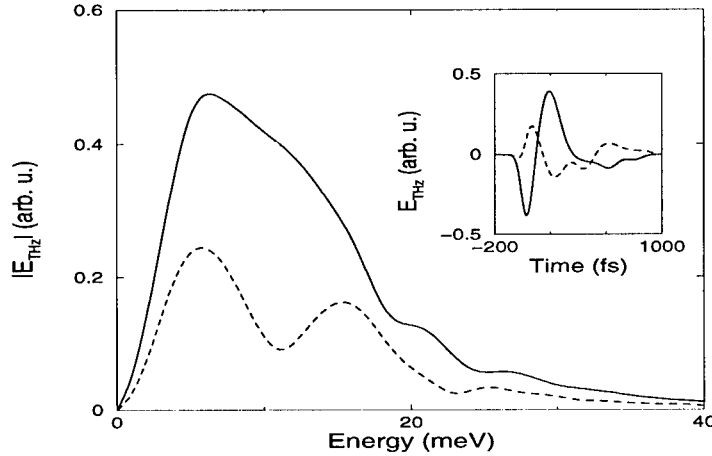


Figure 2. Magnitude of the emitted THz spectra with $\delta(t) = 2\pi\nu_{\text{THz}}t$ (solid line) and $\delta(t) = 2\pi\nu_{\text{THz}}t + \pi/2$ (dashed line). The inset depicts the temporal behavior of the emitted THz field with $\delta(t) = 2\pi\nu_{\text{THz}}t$ (solid line) and $2\pi\nu_{\text{THz}}t + \pi/2$ (dashed line). Note that an energy of 40 meV corresponds to a frequency of approximately 10 THz.

As an inset to Fig. 2 we show the emitted THz field versus t for the phases (at $t=0$, center of the optical pulse) of $\phi = 0$ (solid line) and $\pi/2$ (dashed line). Each transient is approximately 1 ps in duration which reflects the combined effect of WP spreading and dephasing (see Figs. 3 and 4 below). In the EM spectra (Fig. 2), a series of harmonics appear in the THz regime. Further, the sidebands are obviously dependent on the relative phase of the THz field (at $t = 0$), with respect to the arrival of the optical pulse. The phase ϕ can be controlled if both \mathbf{F}_{THz} and \mathbf{F}_{Opt} are derived from the same initial pulse using solid-state sources; although little phase control can be expected from FEL's. At $t = 0$, both free e-h pairs and excitons will be excited optimally from the crystal ground state, and the phase of $\mathbf{F}_{\text{THz}}(0)$ will determine the subsequent dynamics of the WP's internal motion. For $\phi = 0$, the THz field is a maximum at the center of the optical pulse and the carriers have minimum kinetic energy; at times before and after this instant, carriers can propagate through the continuum and harmonics of the driving field may be generated when carriers undergo Coulombic rescattering as they travel back towards the zero of the relative coordinate (which determines the optical properties). It is also noteworthy that the estimated peak dipole moments are 300 eÅ and 400 eÅ

per e-h pair for $\phi = 0$ and $\pi/2$, respectively. Moreover, our dipole moments are estimated to be substantially larger than those emitted in standard schemes for THz generation in QW's (charge oscillations and optical rectification); this stems from the fact that the wavefunctions can be displaced by much larger distances in the QW plane (see below) in comparison to a displacement in the growth direction. Terahertz driving fields have also recently been employed from the FEL to generate somewhat similar harmonic-generation from confined magnetoexcitons [2].

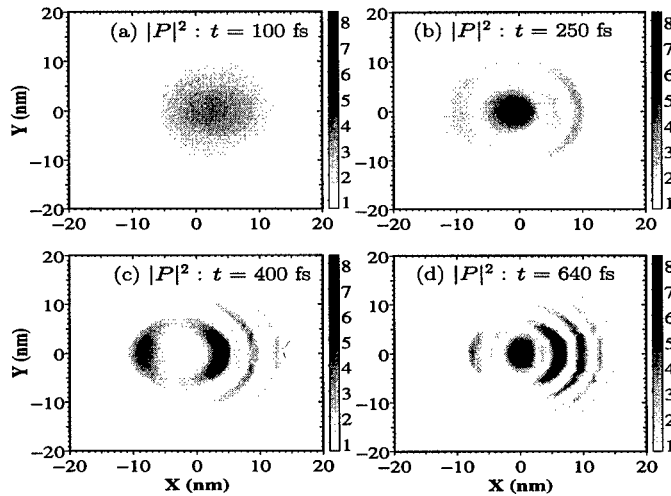


Figure 3: Wavepacket at several times (a: $t = 100$ fs, b: $t = 250$ fs, c: $t = 400$ fs, and d: $t = 640$ fs) for the polarization density with $\delta(t) = 2\pi\nu_{\text{THz}}t$. The units of the WP are scaled by 10^{-3} .

In Fig. 3 we show examples of the e-h WP (polarization density) at several snapshots in time corresponding to Fig. 2 ($\phi = 0$); as mentioned above, the driving field is linearly polarized in the X -direction which leads to the large asymmetry. Shortly after the optical pulse has arrived ($t = 100$ fs) the probability density is concentrated near the center (where there is a high probability of finding the electron and hole at the same relative position). Later ($t = 250$ fs), beating between the excitonic and free-carrier WP can be recognized. Because the WP is highly anisotropic, there is a net dipole moment which results in the THz transients shown in Fig. 2(a). At later times ($t = 400, 640$ fs), side lobes can be seen in the WP; these are formed by the combination of slow transverse spreading, the relatively fast field driven motion in the polarization direction, and the excitonic attraction (Coulombic rescattering). As can be seen, for reasonable driving fields of 3 kV/cm, the e-h WP's can easily be displaced by 20 nm—which is much greater than displacements that can be achieved in the growth direction. In Fig. 4 we also depict the WP dynamics

for $\phi = \pi/2$. Immediately one recognizes that a significant amount of the WP has already propagated to the negative X -direction (at $t = 100$ fs). At the later time of $t = 250$ fs the characteristic *sickle*-structure (due to beating) is obtained again, but the WP is much less pronounced at around 10 nm and has spread out more near the center than in Fig. 3. At later times, one sees spatial interference in the relative-coordinate space.

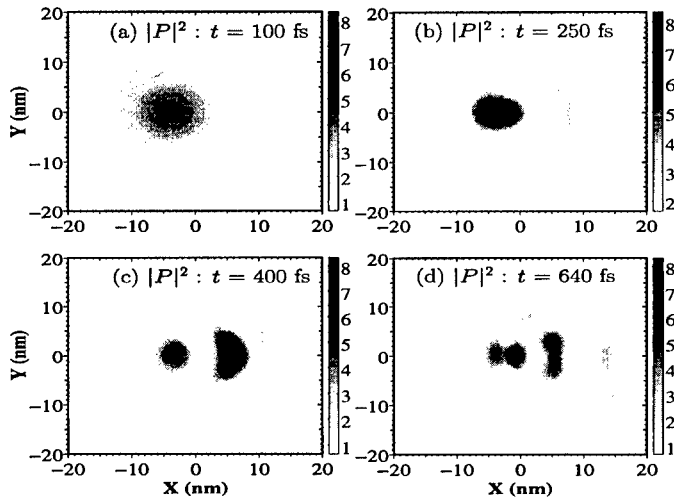


Figure 4: As in Fig. 3 but with $\delta(t) = 2\pi\nu_{\text{THz}}t + \pi/2$.

In conclusion, we have theoretically investigated the simultaneous exposure of an InGaAs QW to a broadband (50 fs) optical pulse — to excite both free e-h pairs and excitons from the crystal ground state — and a $F_0 = 3 \text{ kVcm}^{-1}$, $\nu_{\text{THz}} \sim 1 \text{ THz}$ driving field to enable a study of coherently-controlled charge carriers. The scenario produces beating, e-h relative motion WP's whose anisotropic structure manifests in unique spectral and time-dependent features in the THz regime of the electromagnetic spectrum. The technique can also be used to model the optical properties of the QW and obtain, for example, the phase-dependent dynamic Franz-Keldysh effect [23]. Our results are in agreement with recent experimental measurements. These initial studies have a wide range of applications including the investigation and application of interplaying THz (intraband) and optical (interband) carrier dynamics, polarization-sensitive, intraband low-frequency AC Stark effect [24], and the generation of upshifted THz transients (coherently controlled) whose peak dipole moments are estimated to be about an order of magnitude larger than standard schemes for THz generation in QW's. Additionally, beside being of interest on purely fundamental grounds, studies of THz generation and related phenomena have a host of

applications including FIR/time-domain spectroscopy, study and control of Rydberg atoms, T-ray imaging of optical materials, and mm-wave ultrahigh-speed photonics.

We thank Professor R. Zimmermann for stimulating discussions. This work was supported by the National Science Foundation by grant DMR9705403 and by the Office of Naval Research.

References

- [1] see, for example, S. L. Chuang, S. Schmitt-Rink, B. I. Greene, P. N. Saeta, and A. F. J. Levi, *Phys. Rev. Lett.* **68**, 102 (1992); P. C. M. Planken, M. C. Nuss, I. Brener, K. W. Goossen, M. S. C. Luo, S. L. Chuang, and L. Pfeiffer, *Phys. Rev. Lett.* **69**, 3800 (1992).
- [2] J. Kono, M. Y. Su, K. B. Nordstrom, J. Cerne, M. S. Sherwin, S. J. Allen, T. Inoshita, T. Noda, H. Sakaki, G. E. W. Bauer, M. Sundaram, and A. C. Gossard, *Phys. Rev. Lett.* **79**, 1758 (1997).
- [3] W. Franz, *Z. Naturforsch. Teil A* **13**, 484 (1958); L. V. Keldysh, *Sov. Phys. -JETP* **34**, 788 (1958).
- [4] A. P. Jauho and K. Johnsen, *Phys. Rev. Lett.* **24**, 4576 (1996).
- [5] K. B. Nordstrom, K. Johnsen, S. J. Allen, A. P. Jauho, B. Birnir, J. Kono, T. Noda, H. Akiyama, and H. Sakaki, *Phys. Stat. Sol. (b)* **204**, 52 (1997).
- [6] F. Bloch, *Z. Phys.* **52**, 555 (1929).
- [7] M. Holthaus, *Phys. Rev. Lett.* **69**, 351 (1992).
- [8] T. Meier, G. von Plessen, P. Thomas, and S. W. Koch, *Phys. Rev. Lett.* **73**, 902 (1994).
- [9] A. W. Ghosh, A. V. Kuznetsov, and J. W. Wilkins, *Phys. Rev. Lett.* **79**, 3494 (1997); J. Kono, M. Y. Su, K. B. Nordstrom, J. Cerne, M. S. Sherwin, S. J. Allen, T. Inoshita, T. Noda, H. Sakaki, G. E. W. Bauer, M. Sundaram, and A. C. Gossard, *Phys. Rev. Lett.* **79**, 1758 (1997).
- [10] H. G. Roskos, M. C. Nuss, J. Shah, K. Leo, D. A. B. Miller, A. M. Fox, S. Schmitt-Rink, and K. Köhler, *Phys. Rev. Lett.* **69**, 3800 (1992).
- [11] D. S. Citrin, *Optics Express*, **4**, 376 (1997); A. M. Weiner, *J. Opt. Soc. Am. B* **8**, 2480 (1994).

- [12] M.S.C. Luo, S. L. Chuang, P. C. M. Planken, I. Brener, and M. C. Nuss, Phys. Rev. B, **48**, 11043 (1993).
- [13] I. Brener, P. C. M. Planken, M. C. Nuss, M. S. C. Luo, S. -L. Chuang, L. Pfeiffer, D. E. Laird, and A. M. Weiner, J. Opt. Soc. Am. B **11**, 2457 (1994).
- [14] for a textbook discussion see, H. Haug and S.W. Koch, *Quantum Theory of the Optical and Electronic Properties of Semiconductors*, World Scientific, Singapore, 3rd ed., (1994), and references therein.
- [15] D. H. Dunlop and V. M. Kenkre, Phys. Rev. B. **34**, 3625 (1986); T. Meier G. von Plessen, P. Thomas, and S. W. Koch, Phys. Rev. B **51**, 14490 (1995).
- [16] J. A. Fleck, Jr., Phys. Rev. B **1**, 84 (1970); J. C. Eilbeck and R. K. Bullough, J. Phys. A **5**, 820 (1972).
- [17] for a review, see, for example, F. Rossi, P. Poli, and C. Jacoboni, Semicon. Sci. Technol. **7**, 1017 (1992).
- [18] R. Zimmermann, in *Nonlinear optics of semiconductor nanostructures*, Eds. F. Henneberger, S. Schmitt-Rink, and E. O. Göbel, Akademie-Verlag, Berlin, 51-74 (1993).
- [19] M. Protopapas, D. G. Lappas, P. L. Knight, **79**, 4550 (1997); G.G. Paulus, H. Walther, A. Lohr, W. Becker, and M. Kleber, Phys. Rev. Lett. **80**, 484 (1998); J. Zhou, J. Peatross, M. M. Murnane, H. C. Kapteyn, and I. P. Christov, Phys. Rev. Lett. **76**, 752 (1996).
- [20] I. P. Chrisov, M. M. Murnane, and H. C. Kapteyn, Phys. Rev. Lett. **78**, 1251 (1997).
- [21] J. L. Krause, K. J. Schafer, M. Ben-Nun, and K. R. Wilson, Phys. Rev. Lett. **79**, 4978 (1998).
- [22] P. Moreno, L. Plaja, and L. Roso, J. Opt. Soc. Am. B, **12**, 430 (1996).
- [23] S. Hughes and D. S. Citrin, submitted to Phys. Rev. Lett.
- [24] D. Fröhlich, S. Spitzer, B. Uebbing, and R. Zimmermann, Phys. Stat. Sol. (b) **173**, 83 (1992).

MICROCAVITY EXCITON-POLARITON

HUI CAO

*Department of Physics and Astronomy, Northwestern University
2145 Sheridan Road, Evanston, IL 60208-3112*

Abstract.

We have studied the exciton-photon coupling in a high-Q semiconductor microcavity. Strong coupling of quantum well exciton states to the cavity photon state results in the formation of exciton-polariton states. Coherent microcavity emission exhibits temporal oscillation due to the beating among exciton-polariton states. Our study indicates that a high-Q microcavity can strongly modify exciton's spontaneous emission process, leading to coherent coupling between excitons and photons.

1. Introduction

In the past few years there has been much interest and study of the coupled exciton-photon system in a quantum well (QW) embedded semiconductor microcavity [1, 2, 3, 4]. In the weak coupling regime, the radiation pattern and the decay rate of excitonic spontaneous emission can be drastically modified by a resonant microcavity [5]. In the strong coupling regime, new eigenstates of the system, i.e. the exciton-polariton states are formed [6]. The normal mode splitting and corresponding temporal oscillation of the emission have been observed in the absorption/emission spectra [7, 8, 9] and in the temporal measurement [10, 11, 12, 13].

Due to the in-plane momentum conservation, a QW exciton state with a well defined in-plane momentum $\hbar\mathbf{k}_{\parallel}$, couples to a single cavity photon mode with the same in-plane wavevector \mathbf{k}_{\parallel} [14]. In another word, for each \mathbf{k}_{\parallel} , there is only one QW exciton state and one cavity photon state coupled with each other. For $\mathbf{k}_{\parallel} = 0$, the Hamiltonian of the couple exciton-photon system can be written as:

$$H = \hbar\omega_c(a^\dagger a + \frac{1}{2}) + \hbar\omega_{ex}(b^\dagger b + \frac{1}{2}) + \hbar g(a^\dagger b + ab^\dagger), \quad (1)$$

where a (b) is the operator for the cavity photon (QW exciton), $\hbar\omega_c$ ($\hbar\omega_{ex}$) is the energy of the cavity photon (QW exciton), and g is the exciton-photon coupling constant. The first two terms represent the Hamiltonian of the uncoupled exciton and photon system, and the last term represents the exciton-photon coupling. In the weak coupling regime, the exciton-photon coupling term is very small and can be treated as a perturbation to the eigenstates of the uncoupled exciton-photon system. But in the strong coupling regime, the exciton-photon coupling is so strong that it can no longer be treated as a perturbation. Instead, the Heisenberg equations of motion for a and b are derived after introducing the damping terms Γ_c , and Γ_{ex} for the cavity photon and QW exciton [15]:

$$\frac{da}{dt} = -i\omega_c a + gb - \frac{\Gamma_c}{2}a + F_a \quad (2)$$

$$\frac{db}{dt} = -i\omega_{ex}b - ga - \frac{\Gamma_{ex}}{2}b + F_b \quad (3)$$

where F_a and F_b are the noise terms necessary to preserve the commutator. If we do not deal with the noise properties, we could neglect the noise terms. The solutions for above coupled equations are:

$$a(t) = \frac{(\omega_c - \omega_- - i\Gamma_c/2)a(0) + igb(0)}{\Delta} e^{-i\omega_+ t} + \frac{(-\omega_c + \omega_+ + i\Gamma_c/2)a(0) - igb(0)}{\Delta} e^{-i\omega_- t}, \quad (4)$$

$$b(t) = \frac{(\omega_{ex} - \omega_- - i\Gamma_{ex}/2)b(0) - igb(0)}{\Delta} e^{-i\omega_+ t} + \frac{(-\omega_{ex} + \omega_+ + i\Gamma_{ex}/2)b(0) + igb(0)}{\Delta} e^{-i\omega_- t}, \quad (5)$$

where $a(0)$ and $b(0)$ are the initial values of a and b at $t = 0$,

$$\omega_{\pm} = \frac{[\omega_{ex} + \omega_c - i(\Gamma_c + \Gamma_{ex})/2] \pm \sqrt{[\omega_c - \omega_{ex} - i(\Gamma_c - \Gamma_{ex}/2)]^2 + 4g^2}}{2}, \quad (6)$$

and

$$\Delta = \omega_+ - \omega_- = \sqrt{[\omega_c - \omega_{ex} - i(\Gamma_c - \Gamma_{ex})/2]^2 + 4g^2}. \quad (7)$$

This indicates that the strong coupling of the QW exciton state to the cavity photon state results in two new eigenstates with eigen-energies $\hbar\omega_{\pm}$. They are called microcavity exciton-polariton states. They are superposition states of the uncoupled exciton and photon states. The energy separation between the two exciton-polariton states Δ is called exciton-polariton mode splitting. It is the solid state analog to the vacuum Rabi splitting in the atom-cavity case.

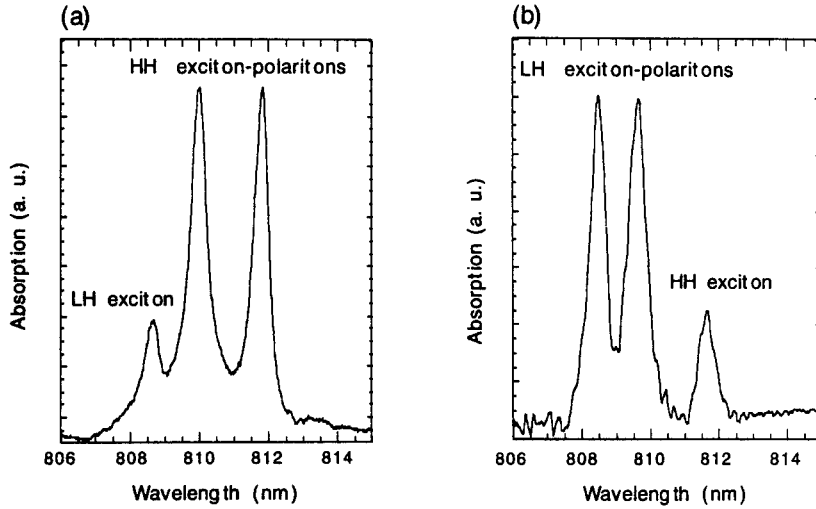


Figure 1. The measured absorption spectra when the cavity photon frequency is tuned to (a) HH exciton emission frequency, (b) LH exciton emission frequency.

2. Exciton-Polariton mode splitting and oscillation

Our microcavity sample grown by molecular beam epitaxy (MBE) consists of a 20 nm GaAs QW in the middle of a $\lambda/2$ DBR cavity. The top (bottom) mirror consists of 15.5 (30) pairs of $\text{Al}_{0.15}\text{Ga}_{0.85}\text{As}$ and AlAs layers. The top $\text{Al}_{0.3}\text{Ga}_{0.7}\text{As}$ spacer layer is tapered along one direction of the sample so that the cavity resonant photon frequency varies with sample position. The sample was cooled down to 4.2 K in a liquid Helium cryostat. The coupled exciton-polariton modes are probed in the absorption measurement. As compared to photoluminescence, absorption is a direct probe of the density of states since it is not affected by exciton population [16]. We have used both a white light source and a broad-band mode-locked Ti:Sapphire laser as the probe beam. The probe beam was focused by a lens to a 30 μm spot on the sample at normal incidence. The reflected beam was guided to a spectrometer. Near resonance, since the transmissivity T of the microcavity is much less than the reflectivity R ($T \ll R$), the absorption $A = 1 - R - T \simeq 1 - R$. By subtracting the spectrum of the reflected beam from the spectrum of the incident beam, we obtained the absorption spectrum.

Without cavity, the absorption spectrum of a GaAs quantum well consists of two peaks, due to the absorption of the QW heavy-hole (HH) exciton and QW light-hole (LH) exciton. In a cavity, when the cavity photon energy is tuned to be resonant with the QW HH exciton energy, we observed two HH exciton-polariton states resulted from the strong coupling of the QW HH exciton state to the cavity photon state, as shown in figure 1 (a).

The HH exciton-polariton splitting is about 4 meV. The exciton-polariton linewidth is about 1 meV. Similarly, as the cavity photon energy comes into resonance with the QW LH exciton energy, we observed two LH exciton-polariton states resulted from the strong coupling of the QW LH exciton state to the cavity photon state, as shown in figure 1 (b). The LH exciton polariton splitting is smaller than HH exciton-polariton splitting because the oscillator strength of LH exciton is smaller than that of HH-exciton.

We measured the absorption spectrum as we tuned the cavity photon frequency by shifting the excitation position on the sample. Figure 2 shows the energies of the exciton-polariton peaks as a function of the cavity bare photon energy. The exciton-polariton dispersion curves feature two anti-crossing due to the strong coupling of both QW HH exciton and LH exciton to the cavity photon. The solid lines in figure 2 are the theoretically fitted exciton-polariton dispersion curves using the the Hamiltonian:

$$H = \hbar\omega_c(a^\dagger a + \frac{1}{2}) + \hbar\omega_h(b_h^\dagger b_h + \frac{1}{2}) + \hbar\omega_l(b_l^\dagger b_l + \frac{1}{2}) + \hbar g_h(a^\dagger b_h + a b_h^\dagger) + \hbar g_l(a^\dagger b_l + a b_l^\dagger), \quad (8)$$

where b_h and b_l ($\hbar\omega_h$ and $\hbar\omega_l$) are the operators (energies) of the QW HH exciton and LH exciton, respectively, and g_h (g_l) is the coupling constant of the HH (LH) exciton to the cavity photon state. We calculated the eigen-energies of the system's normal modes by diagonalizing the matrix. After choosing appropriate values for the coupling constants $g_h \simeq 1.6$ meV and $g_l \simeq 1.3$ meV, the calculated exciton-polariton dispersion curves fit the experimental data well.

The temporal evolution of the microcavity emission was measured by a AC balanced homodyne detection system. 150 fs pulses from a mode-locked Ti:Sapphire laser were split by a beam splitter into two arms of a modified Mach-Zehnder interferometer. One beam was used as the local oscillator wave, the other was used to resonantly excite the microcavity sample at an incident angle of 2.5 degree. The reflected pulses and the microcavity emission into the reflection direction were combined with the local oscillator pulses at a second beam splitter. The two outputs from the second beam splitter were detected by two identical photodetectors, whose photocurrents were fed into a differential amplifier. The intensity noise of the local oscillator were reduced by 35 dB due to the common mode rejection of the balanced homodyne detection. To eliminate the instability of the interferometer, the optical path of the signal arm was modulated with Δl at a frequency ν_l by a mirror mounted on a PZT scanner. This optical path length modulation generates a sinusoidal signal in the differential amplifier output at a frequency $\nu_m = \nu_l \times \Delta l / \lambda$, where λ is the center wavelength of the optical pulses. Since this AC balanced homodyne detection scheme

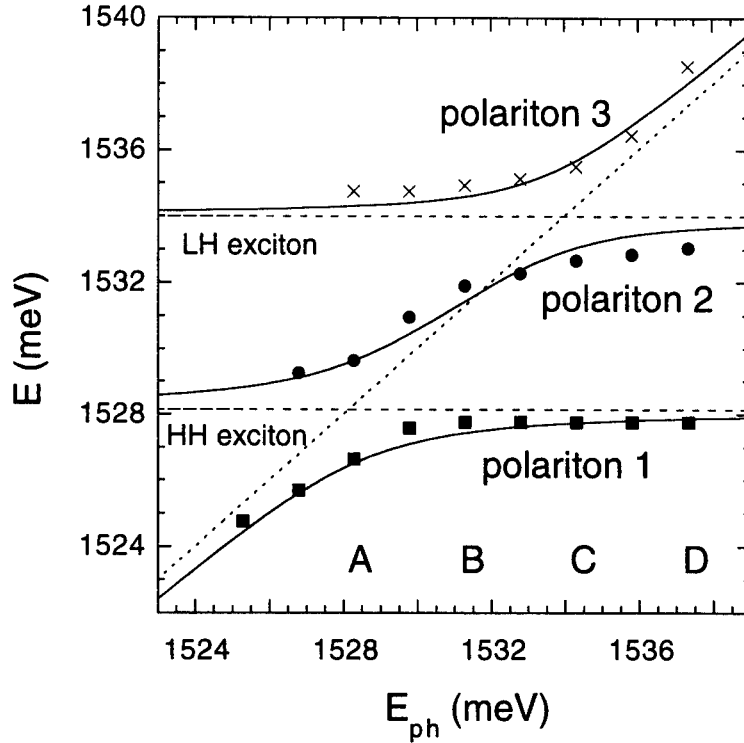


Figure 2. The exciton-polariton dispersion curves deduced from absorption measurement. The solid lines are the theoretically fitted exciton-polariton dispersion curves. The dashed (dotted) lines are the uncoupled exciton (photon) dispersion curves.

is insensitive to the long-term drift and short-term instability of the Mach-Zehnder interferometer, it gives ultra-high sensitivity [17]. The time delay τ of the local oscillator pulses can be varied by moving a corner mirror placed on a translational stage. The time evolution of the amplitude of the coherent emission from the microcavity was detected by measuring the sinusoidal output signal at frequency ν_m at different time delay τ by a narrow bandpass filter and an AC voltage meter.

The top trace in figure 3 (a) shows the microcavity emission as a function of the time delay τ at the HH resonance (position A in figure 2). The pump power was 0.5 mW. The spot size of the pump beam on the sample was about $30\mu\text{m}$ in diameter. The spectra of the pump pulses were centered at 814 nm (1526.26 meV) with a FWHM of 9 nm (17 meV). We observed a regular oscillation due to the beating between the two (upper and lower) HH exciton-polariton states. The contribution by the third LH exciton-polariton is negligible at this point. The first peak in the top trace of figure

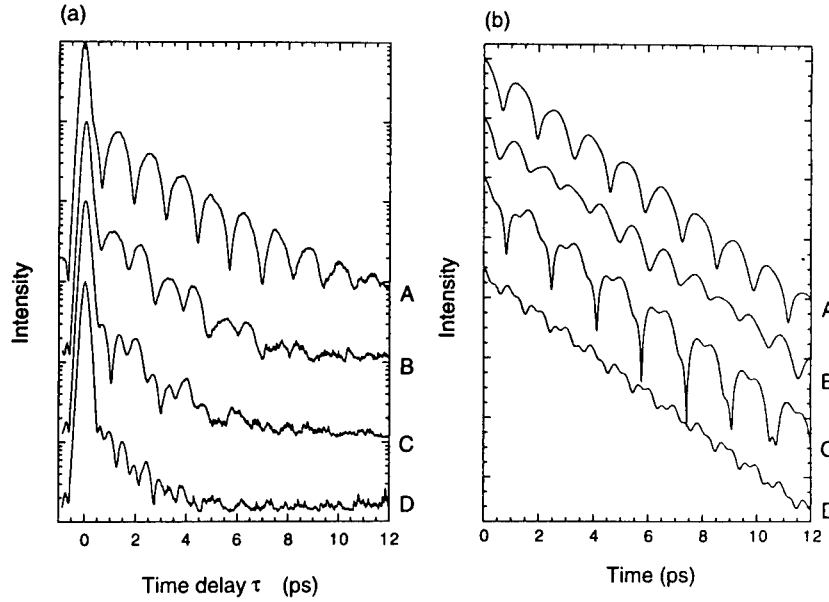


Figure 3. (a) The measured microcavity emission as a function of the time delay τ at positions A, B, C, D of the dispersion curves in figure 2. (b) The calculated time evolution of the microcavity emission at positions A, B, C, D.

3 (a) is the reflected pump pulse, which acts as the zero of the time marker. Nine subsequent oscillation cycles of the microcavity emission were observed due to the high sensitivity of our AC balanced homodyne detection system. After the pump pulse creates excitons in the QW, the excitons radiative recombine and emit photons into the cavity mode. Some of the photons escape from the cavity and gives the first emission peak which corresponds to the second peak in the top trace of figure 3 (a). The rest of the photons remain inside the cavity and create excitons again in the QW, leading to the valley following the first emission peak. Then the excitons emit photons again and results in the second emission peak. In this way, the microcavity system is oscillating back and forth between the QW exciton state and the cavity photon state. This oscillation is called exciton-polariton oscillation. The oscillation is damped due to the cavity loss and exciton scattering. The oscillation period was measured to be about 1.2 ps, which is in good agreement with the spectral splitting of about 2.1 nm (4.1 meV) between the two HH exciton-polariton states.

3. Collapse and revival of exciton-polariton oscillation

However, as we tuned the cavity photon energy away from the HH exciton energy by shifting the excitation position on the sample, the oscillation

became irregular, as shown in figure 3 (a).

To understand it, we have to take into account the beating among all three exciton-polariton states. The time evolution of the microcavity emission was calculated by solving the Heisenberg equation of motion for the cavity field amplitude $a(t)$, assuming the initial state is the bare photon state. As shown in figure 3 (b), our calculation result agrees well with the experimental data [figure 3 (a)]. It indicates that the irregular oscillation is caused by the beating among the three exciton-polariton modes. The magnitude of each polariton mode is determined by the projection coefficient of the initial state onto each polariton state, and also the spectral density of the pump pulse energy at each polariton energy. At HH exciton resonance (position A in figure 2), the magnitude of the LH exciton-like polariton (polariton 3 in figure 2) is much smaller than the magnitudes of the two HH exciton-like polaritons (polariton 1 and 2), and thus it can be neglected. Therefore the beating between polariton 1 and 2 gives a damped sinusoidal oscillation. However at the LH exciton resonance (position C in figure 2), the magnitude of HH exciton polariton (polariton 1) is not negligible although it is smaller than the magnitudes of the two LH exciton-polaritons (polariton 2 and 3), since the HH exciton-photon coupling coefficient g_h is larger than the LH exciton-photon coupling coefficient g_l , and also the center frequency of the pump pulse is near the HH exciton emission frequency. Therefore the beating of three polariton modes results in a non-sinusoidal oscillation.

We also measured the microcavity emission at fixed sample position as we tuned the pump wavelength. At HH exciton resonance (position A), as we increased the center frequency of the pump pulses, the magnitude of polariton 3 (the one with the highest energy) increased. Thus the microcavity emission showed a transition from two-mode beating to three-mode beating. Figure 4 (a) shows the measured microcavity emission at the HH exciton resonance when the center wavelengths of the pump pulses are 814 nm, 811 nm, and 808 nm, respectively. When the center wavelength of the pump pulses is 808 nm, we can clearly see the collapse and revival of the oscillation. This phenomenon can be well predicted by our model [see figure 4 (b)]. When the center frequency of the pump pulses is tuned toward LH exciton emission frequency, the magnitude of polariton 3 increases, and the magnitude of polariton 1 decreases. Eventually, the magnitude of polariton 3 is almost equal to that of polariton 1, and they are both smaller than the magnitude of polariton 2 (symmetric excitation of three polariton modes). The beating between the polaritons 1 and 2 produces an oscillation with a frequency $\omega_h = (E_2 - E_1)/\hbar$, while the beating between the polaritons 2 and 3 produces another oscillation with a slightly different frequency $\omega_l = (E_3 - E_2)/\hbar$, where E_1, E_2, E_3 are the energies of the three polari-

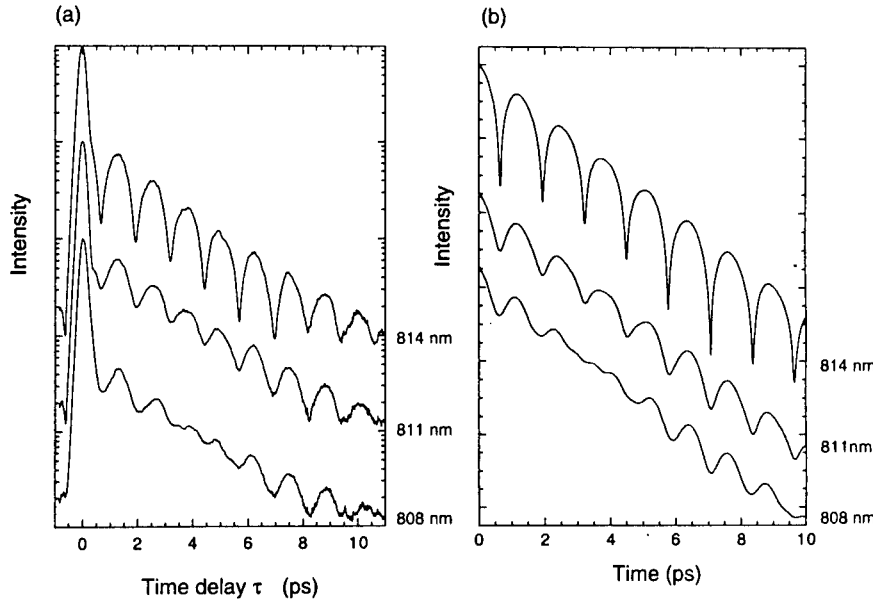


Figure 4. The microcavity emission as a function of the time delay τ at HH resonance when the center energies (wavelengths) of the pump pulses are 1526.26 meV (814 nm), 1531.91 meV (811 nm), and 1537.59 meV (808 nm). (a) shows the measurement results, (b) corresponds to the theoretical simulation.

ton states. Since these two oscillations have almost same amplitudes but slightly different periods, the beating between them results in a collapse of the oscillation at $t = \pi/(\omega_l - \omega_h) \simeq 3.5$ ps, and then a revival of the oscillation at $t = 2\pi/(\omega_l - \omega_h) \simeq 7.0$ ps. The experimental data shown in figure 4 (a) agrees well with such theoretical prediction.

4. Transition From Strong to Weak Coupling Regime

As the excitation intensity increases, rapid dephasing of excitons and bleaching of excitonic oscillator strength induces a transition from the strong coupling regime to the weak coupling regime [18, 19, 20, 21].

Figure 5 (a) shows the temporal evolution of the microcavity emission at various pump power. The cavity photon frequency was tuned close to the QW heavy-hole (HH) exciton emission frequency. Figure 5 (b) shows the simultaneous measurement of the reflection spectra of a probe beam. At low pump power, the reflection spectrum shows two HH exciton-polariton peaks, and the temporal evolution of the microcavity emission exhibits a damped oscillation. As the excitation intensity increases, in the frequency domain, the exciton-polariton peaks are broadened, and their mode splitting is slightly reduced. In the time domain, the microcavity emission peak

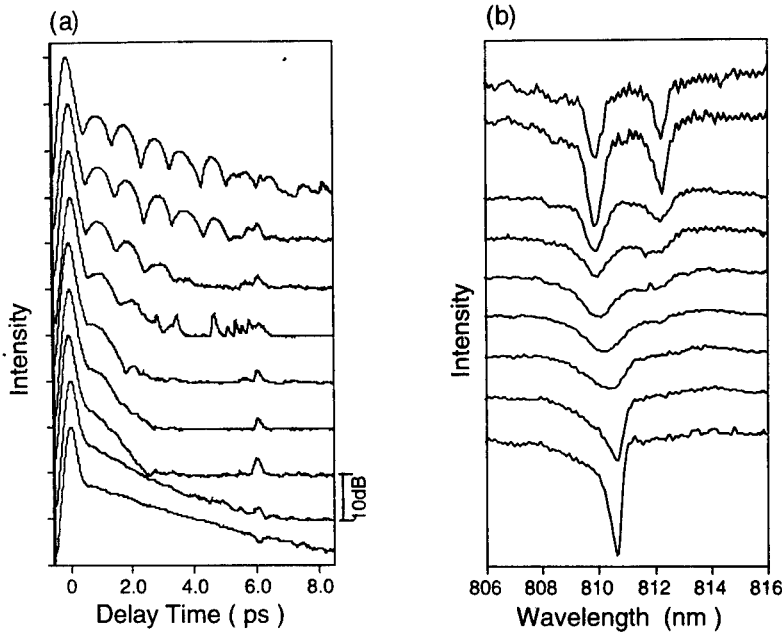


Figure 5. (a) The measured temporal evolution of the microcavity emission at different pump power. (b) Simultaneous measurement of the reflection spectra from the microcavity at different pump power.

intensity decays faster, but the exciton-polariton oscillation becomes slower. Eventually the two exciton-polariton peaks in the reflection spectra are replaced by a single cavity photon peak, indicating the transition from strong exciton-photon coupling to weak coupling. As the pump power increases further, the cavity photon peak becomes narrower. Meanwhile the temporal oscillation of the microcavity emission is replaced by an exponential decay. The decay rate decreases as the pump power increases.

To understand our experimental results, we have set up a simple model based on the Hamiltonian:

$$\begin{aligned}
 H = & \hbar\omega_c(a^\dagger a + \frac{1}{2}) + \hbar\omega_h(b^\dagger b + \frac{1}{2}) + \hbar g(a^\dagger b + a b^\dagger) \\
 & + \sum_k \hbar g_k(a^\dagger c_k + a c_k^\dagger) + \sum_l \hbar g_l(b^\dagger d_k + b d_k^\dagger),
 \end{aligned} \quad (9)$$

where a , and b ($\hbar\omega_c$, and $\hbar\omega_h$) are the operators (energies) of the cavity photon, and QW HH-exciton, respectively. g is the coupling constant between the HH-exciton and cavity photon. The fourth and fifth term in eq(1) represent the reservoir coupling of the cavity photon and HH exciton, respectively. We consider the resonant case $\omega_c = \omega_h$. Hence the light-hole (LH) exciton can be neglected since its emission frequency is far from the

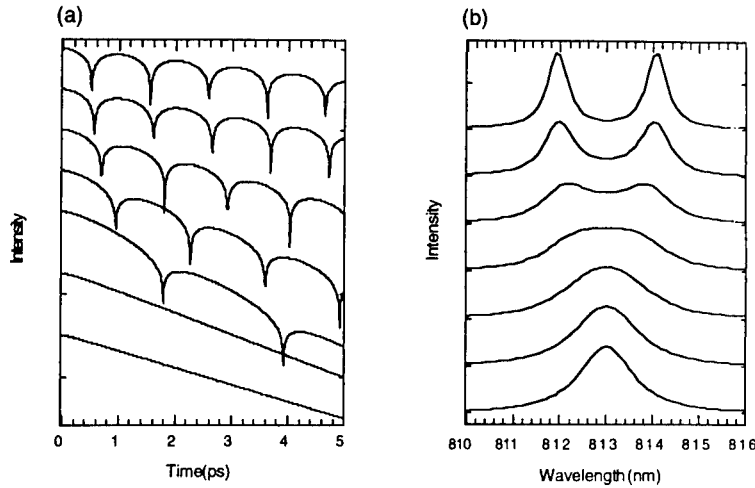


Figure 6. (a) Calculated temporal evolution of the microcavity emission at different Γ_h . (b) Calculated absorption spectra at different Γ_h . For the curves from the top to the bottom, Γ_h are 1, 2, 4, 6, 8, 10, and 12 meV, respectively.

cavity photon frequency. Heisenberg equations of motion for a and b are derived after eliminating the photon and exciton reservoir coordinates and introducing the damping terms Γ_c and Γ_h for the cavity photon and HH exciton, respectively. When $g < \Gamma_c/2$ or $\Gamma_h/2$, the system is in the weak coupling regime, and thus the exciton-photon coupling can be treated as a perturbation to the uncoupled exciton-photon system. On the other hand, when $g > \Gamma_c/2$ and $\Gamma_h/2$, the system is in the strong coupling regime where new eigenstates of the system, i.e. exciton-polariton states, are formed. At low excitation intensity where the exciton density is much lower than the Mott density, exciton-exciton interaction can be neglected since the average distance between excitons is much larger than the exciton Bohr radius. However as the exciton density increases, excitons scatter among each other and also with free carriers. The corresponding dephasing leads to an increase of Γ_h . Eventually when $\Gamma_h/2$ exceeds g , the system makes a transition from strong coupling to weak coupling. As the excitation density increases further, phase space filling and screening lead to a reduction of the excitonic oscillator strength, and thus a decrease of exciton-photon coupling constant g . In our simulation, we consider the excitation intensity regime where the reduction of g is negligible.

Figure 6 (b) shows the calculated absorption spectra as a function of Γ_h [15]. We set $g = 4.1$ meV, $\Gamma_c = 1$ meV, based on the experimental parameters of our samples. As Γ_h increases, the exciton-polariton peaks are broadened, because the linewidth of exciton-polariton peaks is proportional

to the sum of QW exciton linewidth (Γ_h) and cavity photon linewidth, i.e. $(\Gamma_c + \Gamma_h)/2$. The splitting Ω also decreases due to the increase of Γ_h according to

$$\Omega = \sqrt{4g^2 - \frac{(\Gamma_h - \Gamma_c)^2}{4}} \quad (10)$$

When $\Gamma_h/2$ approaches g , the two exciton-polariton peaks merge into a single broad peak, indicating the transition from strong coupling to weak coupling. As Γ_h increases further, the linewidth of this single peak decreases, eventually approaching the bare photon resonance linewidth Γ_c . This is because in the weak coupling regime, when $\Gamma_h \gg \Gamma_c$, the linewidth of the absorption peak is determined mostly by Γ_c . Therefore our simulation results are consistent with our experimental data.

The time evolution of the microcavity emission was calculated by solving the Heisenberg equation of motion for the cavity field amplitude $a(t)$, assuming the initial state is the bare photon state. As shown in figure 6 (a), when $\Gamma_h/2$ is smaller than g_h , the microcavity emission shows a temporal oscillation. This indicates that the microcavity system oscillates back and forth between QW exciton state and cavity photon state. As Γ_h increases, the oscillation decays faster, because the decay rate of exciton-polariton emission is proportional to $\Gamma_h + \Gamma_c$. The oscillation period, which is inversely proportional to the exciton-polariton mode splitting Ω , slightly increase due to the slight decrease in Ω at larger Γ_h . When $\Gamma_h/2$ approaches g , the temporal oscillation is replaced by an exponential decay. This change in the time domain is accompanied with the merge of the two exciton-polariton peaks into a single peak in the frequency domain. As Γ_h increases further, the decay rate of the microcavity emission starts decreasing, and eventually it approaches Γ_c in the weak coupling limit. The calculation results agree well with the experimental data.

5. Conclusion

We have studied the exciton-photon coupling in a high-Q semiconductor microcavity. Strong coupling of quantum well exciton states to the cavity photon state results in the formation of exciton-polariton states. Coherent microcavity emission exhibits temporal oscillation due to the beating among exciton-polariton states. Our study indicates that a high-Q microcavity can strongly modify exciton's spontaneous emission process, leading to coherent coupling between excitons and photons.

Acknowledgments: this work has been done in collaboration with Drs. Y. Yamamoto, G. Björk, J. M. Jacobson, S. Pau, S. Jiang, S. Machida, Y. Takiguchi, and R. Huang.

References

1. Y. Yamamoto, and R. E. Slusher, *Physics Today* **46**, 66 (June 1993).
2. R. E. Slusher, and C. Weisbuch, *Solid State Commun.* **92**, 149 (1994).
3. E. Burstein, and C. Weisbuch, eds. *Confined Electrons and Photons*, Plenum, New York (1995).
4. H. Yokoyama, and K. Ujihara, eds. *Spontaneous emission and laser oscillation in microcavities*, CRC, Boca Raton (1995).
5. Y. Yamamoto, G. Björk, K. Igeta, and Y. Horikoshi, in *Quantum Optics and Coherence V*, edited by H. H. Eberly, L. Mandel, and E. Wolf (Plenum, New York, 1990).
6. C. Weisbuch, M. Nishioka, A. Ishikawa, and Y. Arakawa, *Phys. Rev. Lett.* **69**, 3314 (1992).
7. R. Houdré, C. Weisbuch, R. P. Stanley, U. Oesterle, P. Pellandini, and M. Illegems, *Phys. Rev. Lett.* **73**, 2043 (1994).
8. T. A. Fisher, A. M. Afsar, D. M. Whittaker, M. S. Skolnick, J. S. Roberts, G. Hill, and M. A. Pate, *Phys. Rev. B* **51**, 2600 (1995).
9. T. R. Nelson, J. P. Prineas, G. Khitrova, H. M. Gibbs, J. D. Berger, E. K. Lindmark, J.-H. Shin, H.-E. Shin, Y.-H. Lee, P. Tayebati, *Appl. Phys. Lett.*, **69**, 3031 (1996).
10. T. B. Norris, J.-K. Rhee, C.-Y. Sung, Y. Arakawa, M. Nishioka, and C. Weisbuch, *Phys. Rev. B* **50**, 14663 (1994).
11. J. Jacobson, S. Pau, H. Cao, G. Björk, and Y. Yamamoto, *Phys. Rev. A* **51**, 2542 (1995).
12. H. Cao, J. Jacobson, G. Björk, S. Pau, and Y. Yamamoto, *Appl. Phys. Lett.* **66**, 1107 (1995).
13. H. Cao, S. Jiang, S. Machida, T. Takiguchi, and Y. Yamamoto, *Appl. Phys. Lett.* **71**, 1461 (1997).
14. R. Houdré, C. Weisbuch, R. P. Stanley, U. Oesterle, P. Pellandini, and M. Illegems, *Phys. Rev. Lett.* **73**, 2043 (1994).
15. S. Pau, G. Björk, J. Jacobson, H. Cao, and Y. Yamamoto, *Phys. Rev. B* **51**, 14437 (1995).
16. R. P. Stanley, R. Houdre, C. Weisbuch, U. Oesterle, M. Illegems, and Y. Arakawa, *Phys. Rev. B* **53**, 10995 (1996).
17. S. Jiang, S. Machida, Y. Takiguchi, H. Cao, and Y. Yamamoto, *Opt. Commun.* **145**, 91 (1998).
18. R. Houdre, J. L. Gibernon, P. Pellandini, R. P. Stanley, U. Oesterle, W. Weisbuch, J. O'Gorman, B. Roycroft, and M. Illegems, *Phys. Rev. B* **52**, 7810 (1997).
19. F. Jahnke, M. Kira, S. W. Koch, G. Khitrova, E. K. Lindmark, T. R. Nelson, D. V. Wick, J. D. Berger, O. Lyngnes, H. M. Gibbs, and K. Tai, *Phys. Rev. Lett.* **77**, 5257 (1996).
20. H. Cao, S. Pau, J. M. Jacobson, G. Björk, Y. Yamamoto, and A. Imamoğlu, *Phys. Rev. A* **55**, 4632 (1997).
21. X. Fan, H. Wang, H. Q. Hou, and B. E. Hammons, *Phys. Rev. B* **56**, 3233 (1997).

PART III: Coherent Phenomena and Related topics

COHERENT CONTROL OF QUANTUM LOCALIZATION

MARTIN HOLTHAUS

*Fachbereich Physik der Philipps-Universität
Renthof 6, D-35032 Marburg, Germany*

1. Atomic Landé Factors in High-Frequency Magnetic Fields

Twenty eight years ago, Haroche et al. [1] published measurements of Zeeman hyperfine spectra of Hydrogen and Rubidium atoms that were subjected to not only a static magnetic field B , but also to an additional *oscillating* magnetic field $B_1 \cos(\omega t)$. The latter was applied perpendicular to the static field; the oscillation frequency ω was small compared to the hyperfine separations, but large compared to the Lamor precession frequencies. These experiments demonstrated that the Landé factors g_F of the bare hyperfine levels F are drastically modified by the high-frequency magnetic field; they become

$$\bar{g}_F = g_F J_0 \left(\frac{g_F \mu_B B_1}{\hbar \omega} \right), \quad (1)$$

where μ_B is the Bohr magneton, and J_0 denotes the ordinary Bessel function of order zero.

Thus, varying the amplitude B_1 of the oscillating field allows one to control the Landé factors; they even vanish when $g_F \mu_B B_1 / (\hbar \omega)$ equals a zero of J_0 . This can be exploited, e.g., in alkali metals by cancelling \bar{g}_F simultaneously in two hyperfine levels that are coupled by a further weak resonant field. Then all allowed transitions between different hyperfine substates contribute to a single line, resulting in substantially increased intensity of that line [1].

This controllability of the Landé factors had originally been interpreted within the “dressed atom”-approach, where the oscillating field is regarded as a mode of the quantized electromagnetic radiation field [2]. A comparatively simple and straightforward picture emerges, however, if the field is treated *classically*, since then the Hamiltonian matrix $H(t)$ that describes a Zeeman-split hyperfine level in the presence of both magnetic fields is

periodic in time,

$$H(t) = H(t + T) \quad \text{with} \quad T = 2\pi/\omega. \quad (2)$$

Just as a spatially periodic potential in solid state physics gives rise to Bloch waves with quasimomenta $\hbar k$, such a T -periodic matrix possesses a complete set of Floquet states $|\psi_j(t)\rangle$ with quasienergies ε_j [3, 4],

$$|\psi_j(t)\rangle = |u_j(t)\rangle \exp(-i\varepsilon_j t/\hbar), \quad (3)$$

where the functions $|u_j(t)\rangle$ inherit the T -periodicity of the external drive, $|u_j(t)\rangle = |u_j(t+T)\rangle$. Inserting such a Floquet state into the time-dependent Schrödinger equation, one obtains the identity

$$[H(t) - i\hbar\partial_t] |u_j(t)\rangle = \varepsilon_j |u_j(t)\rangle, \quad (4)$$

which plays a conceptually decisive role: This is an eigenvalue equation for the quasienergies ε_j , just as the stationary Schrödinger equation $H|\psi\rangle = E|\psi\rangle$ is an eigenvalue equation for the energies E . Hence, for periodically time-dependent quantum systems the Floquet states take over the role of the stationary states. This insight allows one to immediately transfer a wealth of ideas, concepts, and computational strategies from time-independent quantum mechanics to the periodically time-dependent case [5, 6].

In particular, the “renormalization” of atomic Landé factors in crossed static and oscillating magnetic fields is explained by a simple generalization of degenerate-state perturbation theory. If one considers, e.g., a total angular momentum $F = 1$, orients the static field along the x -axis and the oscillating field along the z -axis, one obtains the Hamiltonian matrix

$$H(t) = g_1\mu_B B \frac{1}{\sqrt{2}} \begin{pmatrix} 0 & 1 & 0 \\ 1 & 0 & 1 \\ 0 & 1 & 0 \end{pmatrix} + g_1\mu_B B_1 \cos(\omega t) \begin{pmatrix} 1 & 0 & 0 \\ 0 & 0 & 0 \\ 0 & 0 & -1 \end{pmatrix}. \quad (5)$$

Without the static field, i.e., for $B = 0$, there are three obvious linearly independent solutions to the corresponding time-dependent Schrödinger equation:

$$\begin{aligned} |\psi_1(t)\rangle &= \begin{pmatrix} 1 \\ 0 \\ 0 \end{pmatrix} \exp\left(-i\frac{g_1\mu_B B_1}{\hbar\omega} \sin(\omega t)\right), \\ |\psi_2(t)\rangle &= \begin{pmatrix} 0 \\ 1 \\ 0 \end{pmatrix}, \\ |\psi_3(t)\rangle &= \begin{pmatrix} 0 \\ 0 \\ 1 \end{pmatrix} \exp\left(+i\frac{g_1\mu_B B_1}{\hbar\omega} \sin(\omega t)\right). \end{aligned} \quad (6)$$

All three wave functions are T -periodic (including $|\psi_2(t)\rangle$, of course!), so that they represent three Floquet functions $|u_j(t)\rangle = |\psi_j(t)\rangle$ with degenerate quasienergies $\varepsilon_j = 0$; $j = 1, 2, 3$. (Note that these are still not all the solutions to the eigenvalue problem (4): If $|u_j(t)\rangle$ is an eigenfunction, so is $|u_j(t)\rangle \exp(im\omega t)$, with arbitrary positive or negative integer m .)

Adding the static field then lifts the degeneracy. This process can be computed in the same manner as in analogous examples studied in time-independent quantum physics: One simply has to diagonalize the matrix of the perturbing operator $H^{(B)}$, i.e., of the term in eq. (5) that is proportional to B , in the subspace spanned by the degenerate eigenfunctions. For computing the matrix elements, one has to keep in mind that the eigenvalue problem (4) lives in an “extended Hilbert space” of T -periodic functions [7]; the scalar product in this space,

$$\langle\langle u|v\rangle\rangle = \frac{1}{T} \int_0^T dt \langle u(t)|v(t)\rangle, \quad (7)$$

is obtained from the usual scalar product $\langle \cdot | \cdot \rangle$ by time-averaging over one period. The desired matrix elements then are

$$\langle\langle u_j|H^{(B)}|u_k\rangle\rangle = g_1\mu_B B J_0\left(\frac{g_1\mu_B B_1}{\hbar\omega}\right) \cdot \frac{1}{\sqrt{2}} \delta_{j,k\pm 1}, \quad (8)$$

and diagonalizing the resulting 3×3 -matrix yields the quasienergies

$$\varepsilon_m = m \cdot g_1\mu_B B J_0\left(\frac{g_1\mu_B B_1}{\hbar\omega}\right) = m \cdot \bar{g}_1\mu_B B \quad (m = 0, \pm 1) \quad (9)$$

instead of the usual Zeeman energies $E_m = m \cdot g_1\mu_B B$. Thus, the response to the static field now looks as if the Landé factor were changed from g_1 to \bar{g}_1 , and there were no oscillating field. However, it should also be noted that not only do the quasienergies ε_m differ from the energies E_m , but also the Floquet functions become linear combinations of the energy eigenfunctions.

2. Control of Localization in ac-Driven Tight-Binding Lattices

The Hamiltonian (5) can be interpreted as representing three quantum states located at sites 1, 0, and -1 that are driven by an oscillating field and coupled by some nearest-neighbor interaction. A matrix of the same type describes the ground states in three adjacent semiconductor quantum wells that are exposed to a Terahertz electric field; the nearest-neighbor interaction then is provided by the tunneling effect. One might guess that the differences between the quasienergy levels now take over the role of the tunnel splittings [8], so that making the quasienergies coincide at the zeros

of J_0 should entail a “coherent destruction of tunneling”. This is, in fact, actually the case, at least if the driving frequency is sufficiently high [9, 10].

The possibility of coherently controlling the tunneling effect in periodically driven quantum systems shows up most clearly if one considers a one-dimensional tight-binding lattice

$$H_0 = -\frac{\Delta}{4} \sum_{\ell} (|\ell+1\rangle\langle\ell| + |\ell\rangle\langle\ell+1|) , \quad (10)$$

where the Dirac-ket $|\ell\rangle$ denotes a Wannier state that is centered at the ℓ -th lattice site. This system may be regarded as an idealized model for an electron in a semiconductor superlattice [11]; the interaction of neighboring sites (corresponding to the B -proportional term in the Hamiltonian matrix (5)) is furnished by the tunnel contact between adjacent superlattice wells. The lattice eigenfunctions are Bloch waves

$$|\chi_k\rangle = \sum_{\ell} \exp(ik\ell d)|\ell\rangle \quad (11)$$

with quasimomenta $\hbar k$ (d is the lattice constant); their dispersion relation

$$E(k) = -\frac{\Delta}{2} \cos(kd) \quad (12)$$

describes an energy band of width Δ .

When such a lattice is subjected to a static electric field F_0 , Wannier-Stark localization sets in [12], so that the eigenfunctions localize around the individual lattice sites and the energy band is destroyed. However, if one then applies an additional oscillating field $F_1 \cos(\omega t)$, such that the site-to-site energy difference eF_0d induced by the static field is precisely compensated by the energy of n photons,

$$eF_0d = n\hbar\omega \quad (n = 0, 1, 2, \dots) , \quad (13)$$

then band formation becomes possible again. Modeling the interaction with the two fields within the dipole approximation by

$$H_{\text{int}}(t) = e[F_0 + F_1 \cos(\omega t)]d \sum_{\ell} |\ell\rangle \ell \langle \ell| , \quad (14)$$

the system $H(t) = H_0 + H_{\text{int}}(t)$ admits the so-called Houston states [13, 14] (or “accelerated Bloch states”)

$$|\psi_k(t)\rangle = \sum_{\ell} |\ell\rangle \exp\left(iq_k(t)\ell d - \frac{i}{\hbar} \int_0^t d\tau E(q_k(\tau))\right) \quad (15)$$

with $q_k(t) = k - eF_0t/\hbar - eF_1/(\hbar\omega)\sin(\omega t)$. Provided the resonance condition (13) holds, the factors $\exp(iq_k(t)\ell d)$ are T -periodic, so that the Houston states can be brought into the Floquet-form (3):

$$\begin{aligned} |\psi_k(t)\rangle &= \sum_{\ell} |\ell\rangle \exp\left(iq_k(t)\ell d - \frac{i}{\hbar} \int_0^t d\tau E(q_k(\tau)) + \frac{i\varepsilon(k)t}{\hbar}\right) e^{-i\varepsilon(k)t/\hbar} \\ &\equiv |u_k(t)\rangle \exp(-i\varepsilon(k)t/\hbar); \end{aligned} \quad (16)$$

the quasienergy-quasimomentum dispersion relation becomes

$$\begin{aligned} \varepsilon(k) &= \frac{1}{T} \int_0^T d\tau E(q_k(\tau)) \quad \text{mod } \hbar\omega \\ &= (-1)^n J_n\left(\frac{eF_1 d}{\hbar\omega}\right) E(k) \quad \text{mod } \hbar\omega \end{aligned} \quad (17)$$

Such Floquet-Bloch states (16), which are simultaneously characterized by a quasienergy and a quasimomentum, and thus reflect both the temporal periodicity of the driving force and the spatial periodicity of the lattice, are useful, among others, for explaining the generation of high harmonics in the interaction of laser light with thin crystals [15]. For the single-band model considered here, the amplitude-dependent modification of the quasienergy band width described by eq. (17) can be considered, *mutatis mutandis*, as a direct generalization of the Landé factor renormalization (1).

Of particular interest now is the “collapse” of the quasienergy bands [16] at the zeros of the Bessel functions J_n , with n being given by eq. (13). Since the quasienergies $\varepsilon(k)$ determine, according to eq. (3), the phases which the individual components of an arbitrary Floquet wave packet acquire in the course of one driving period, all these phases are exactly equal at the collapse points, so that the packet can, on the average, neither move nor spread, but has to periodically reproduce itself. This is known as “dynamic localization” [17]. The importance of this phenomenon for Terahertz-driven semiconductor superlattices [18] rests in the fact that it persists even if the Coulomb interaction of the electron gas is taken into account [19, 20]; indeed, first experimental evidence for its occurrence has been reported recently [21].

However, the band collapse *must* have still further consequences, since the band width dictates the sensitivity of the Bloch states with respect to deviations from the exact lattice periodicity. If one adds to the tight-binding model (10) a single defect $\nu_0|\ell_0\rangle\langle\ell_0|$ describing a modification of the ℓ_0 -th on-site energy by an amount ν_0 , one gets an energy eigenstate that is exponentially localized around this defect. The localization length L then is determined by the ratio of the defect strength ν_0 and the band width Δ ,

such that the larger this ratio, the sharper the state is localized:

$$\left(\frac{L}{d}\right)^{-1} = -2 \ln \left(\sqrt{\frac{4\nu_0^2}{\Delta^2} + 1} - \left| \frac{2\nu_0}{\Delta} \right| \right). \quad (18)$$

This property survives when the system is driven by a high-frequency ac force (14) that obeys the resonance condition (13). If $\hbar\omega$ is at least comparable to Δ , one finds an exponentially localized Floquet state, with a localization length that now is determined by the ratio of the defect strength and the quasienergy band width; one merely has to replace Δ in eq. (18) by $\Delta J_n(eF_1d/(\hbar\omega))$. This result is crucial; it implies that the spatial extension of the defect state is controllable by adjusting the strength of the driving amplitude F_1 . In particular, by tuning $eF_1d/(\hbar\omega)$ to a zero of J_n one can confine the defect state to a single site [22, 23]. An example for this coherent control of the localization length is depicted in Fig. 1.

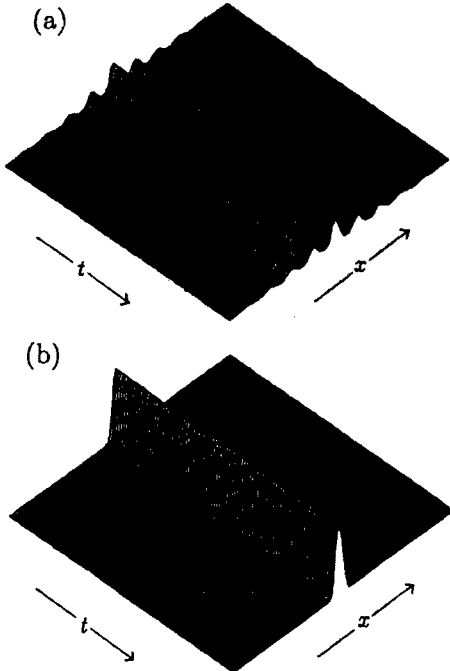


Figure 1. Localization of a defect state in a driven square-well lattice without static field F_0 ; the model parameters correspond to typical values for semiconductor superlattices (well width 100 Å, barrier width 50 Å, barrier height 0.3 eV; the effective particle mass is $0.067 m_e$, the defect is introduced by shortening one well by merely 0.5 Å). The interval in space x shown here corresponds to 10 lattice periods, the interval in time t is one driving period. The width $\Delta = 1.8$ meV of the lowest energy band is small compared to the photon energy $\hbar\omega = 5.0$ meV. The field strength F_1 is 3000 V/cm in (a) and 8016 V/cm in (b), corresponding to the first J_0 -band collapse.

The idea of utilizing the dependence of a quasienergy band width for manipulating the localization lengths of quantum states in disordered lattices can be pushed even further. If, instead of embodying merely a single defect, the one-dimensional lattice (10) is perturbed everywhere by adding site-diagonal disorder

$$H_{\text{random}} = \sum_{\ell} \nu_{\ell} |\ell\rangle\langle\ell|, \quad (19)$$

with random energies ν_{ℓ} varying between $-\nu_{\max}$ and $+\nu_{\max}$, then Anderson-localization of all states occurs [24, 25]; the typical localization length is proportional to the square of the ratio of the band width in the unperturbed lattice and the perturbation strength ν_{\max} ,

$$\frac{L}{d} \propto \left(\frac{\Delta}{\nu_{\max}} \right)^2 \quad (20)$$

Hence, one expects that it is feasible to coherently control the degree of Anderson localization by varying the strength of a resonant periodic force [26], in close analogy to the case of a single defect. One way to verify this conjecture by numerical means is to expand all the Floquet states of such a resonantly driven, randomly perturbed lattice $H_0 + H_{\text{int}}(t) + H_{\text{random}}$ with N sites in the Wannier basis,

$$|u_j(t)\rangle = \sum_{\ell=1}^N a_{\ell}^{(j)}(t) |\ell\rangle, \quad (21)$$

and to compute the averaged sum

$$P = \frac{1}{T} \int_0^T dt \frac{1}{N} \sum_{\ell,j=1}^N |a_{\ell}^{(j)}(t)|^4 \quad (22)$$

of the fourth powers of the expansion coefficients' absolute values. This so-called inverse participation ratio P is a useful measure for the degree of localization, since $P \rightarrow 1$, if all states are completely localized at individual sites, and $P \sim 1/N$, if all states are uniformly extended. If one considers P versus the dimensionless driving amplitude $z \equiv eF_1d/(\hbar\omega)$ for $n = 1, 2, 3, \dots$, then $P(0)$ will be comparatively large, since the static field gives rise to Wannier-Stark localization, even if there is no disorder. With increasing amplitude, $P(z)$ will first decrease, since the quasienergy band width in the corresponding unperturbed lattice grows according to eq. (17), so that the average localization length (20) increases. At a certain characteristic amplitude $z_{1/2}$ it reaches half the starting value, $P(z_{1/2}) = P(0)/2$.

If the Floquet states actually exhibit Anderson localization, so that $P(z_{1/2})$ can depend only on the ratio of quasienergy band width and disorder strength, there has to be a relation

$$\Delta J_n(z_{1/2}) = c_n \nu_{\max} \quad (23)$$

with dimensionless coefficients c_n of order unity. Figure 2 shows that this relation describes the numerical data very well [27], and thus confirms the basic idea: The ratio of quasienergy band width and disorder strength is the decisive parameter that determines the degree of Anderson localization in resonantly driven, randomly disordered tight-binding lattices. Whereas the disorder strength is a sample-specific property, the width of the quasienergy band is, in principle, at one's disposal. Changing the driving amplitude means changing this width, and thereby tuning the inverse participation ratio P .

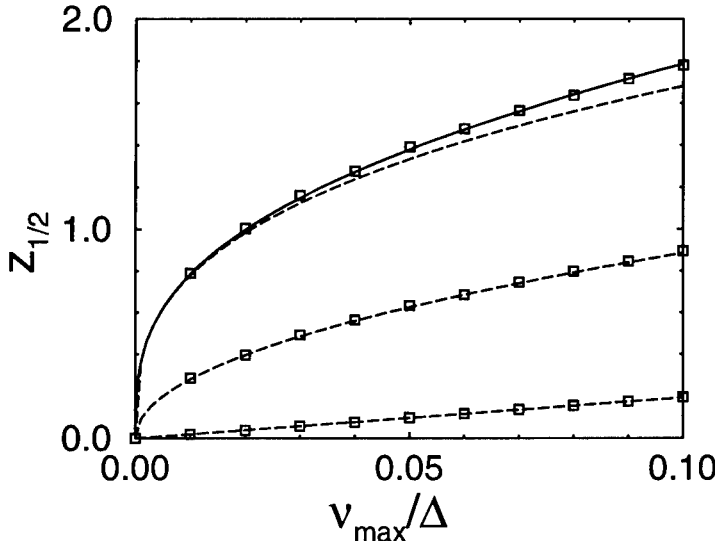


Figure 2. Characteristic amplitudes $z_{1/2}$ for resonantly driven tight-binding lattices (10) with random on-site disorder (19), versus the perturbation strength ν_{\max} . Boxes indicate numerically computed data for single-photon resonances ($n = 1$; lowest data set), two-photon resonances ($n = 2$), and three-photon resonances ($n = 3$); with $\hbar\omega = \Delta$ in all cases. The dashed lines are fits to the relations $z_{1/2} = 2(n! c_n \nu_{\max}/\Delta)^{1/n}$ found by approximating the Bessel function J_n in eq. (23) by its leading term. For $n = 3$ this approximation is not sufficient; here the full line is obtained from eq. (23) itself.

It is quite important that the connection between the degree of localization and the quasienergy band width is not restricted to the single-band model, where the quasienergy band (17) is obtained by simple averaging, but remains valid also in multiband systems, even though the individual quasienergy bands then become mixtures of the original energy bands [28]; a typical case is displayed in Fig. 3.

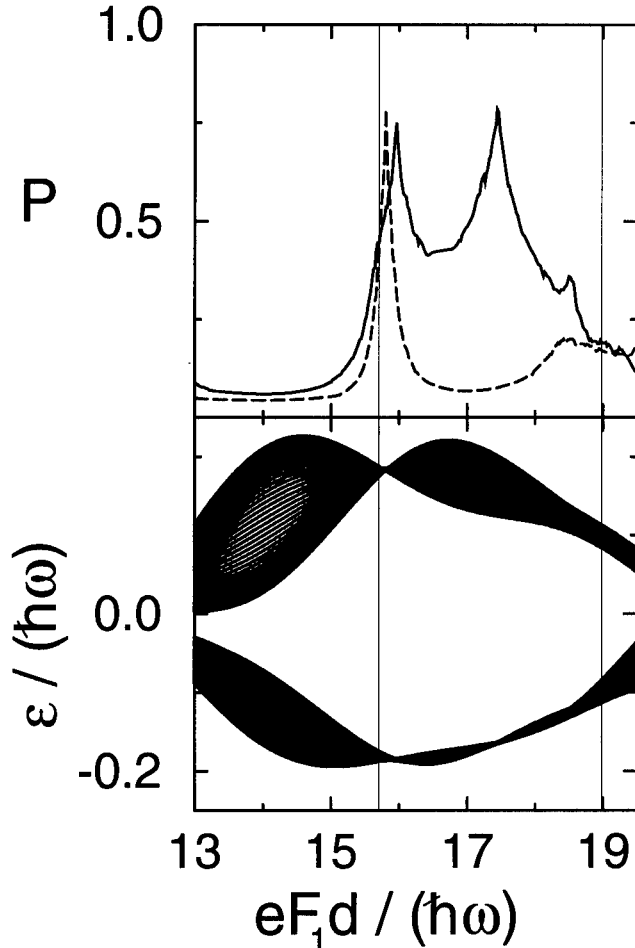


Figure 3. An example for the general connection between the degree P of localization and the quasienergy band structure. The top panel shows P for a randomly perturbed two-band model [28]; the lower panel shows the quasienergy bands for the corresponding ideal lattice. The dashed (full) line belongs to the upper (lower) band; even details in the behavior of P have their counterpart in the band structure.

In actual semiconductor superlattices a certain amount of disorder is unavoidable; one may even grow intentionally disordered samples [29]. Since such lattices consist of merely a limited number of quantum wells, 20 to 50, say, and supposing that the rather high coherence demands can be met, one might speculate that transport characteristics in the presence of a Terahertz field [21] tend to change in two opposite ways with temperature, depending on whether the typical localization length L is substantially longer or shorter than the sample size L_{sample} . In the first case, all states can be regarded as effectively extended, and phonon scattering would impede the flow of electrons, so that the conductivity should decrease with increasing

temperature. On the other hand, if $L \ll L_{\text{sample}}$, phonon scattering would help the electrons to hop from one site to another, so that the conductivity should increase with increasing temperature. The possibility of tuning L via the amplitude of the Terahertz field implies the possibility of switching from one case to the other, without exchanging the sample.

3. The Next Step: Controlling a Metal-Insulator Transition

Further exciting prospects emerge if one considers *quasiperiodic* lattices, such as the Harper model

$$H_{\text{Harper}} = H_0 + \nu_0 \sum_{\ell} \cos(2\pi\eta\ell + \delta) |\ell\rangle\langle\ell|, \quad (24)$$

where H_0 is again given by eq. (10), and the additional piece describes a periodic modulation of the on-site energies that is incommensurate with the lattice period if the number η is irrational. This model, which is well known from the theory of two-dimensional Bloch electrons in magnetic fields, exhibits a metal-insulator transition: For $\Delta > 2\nu_0$ all eigenstates are

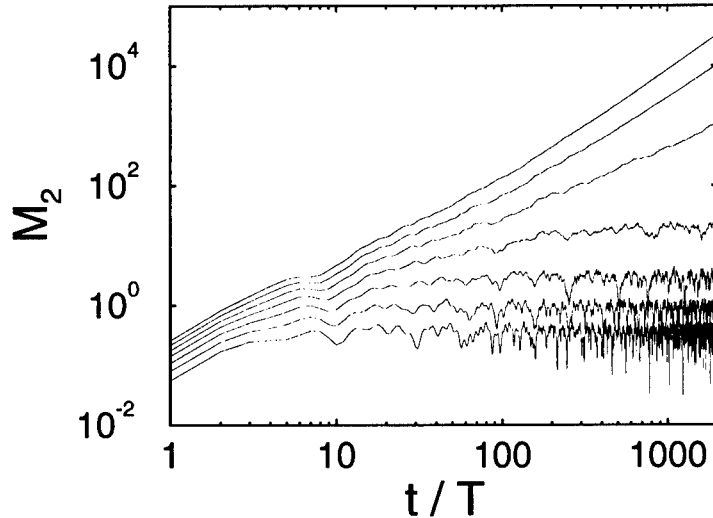


Figure 4. Second moments $M_2(t) = \sum_{\ell} \ell^2 |f_{\ell}(t)|^2$ as obtained from solutions $|\psi(t)\rangle = \sum_{\ell} f_{\ell}(t) |\ell\rangle$ to the Schrödinger equation for the Harper model (24) with forcing (14), for initially sharply localized packets $f_{\ell}(0) = \delta_{\ell,0}$. Parameters are $\Delta/(\hbar\omega) = 0.385$ and $\nu_0/(\hbar\omega) = 0.1$; the static field is set to zero. The driving amplitudes $z = eF_1d/(\hbar\omega)$ vary from 1.3 (upper line) to 1.9 (lower line), in steps of 0.1. As long as $\Delta J_0(z)$ remains larger than about $2\nu_0$, the system remains in the metallic phase. The wave packet then exhibits ballistic diffusion, i.e., $M_2(t)$ grows by two orders of magnitude when t increases by a factor of 10. When $\Delta J_0(z)$ exceeds $2\nu_0$ the system becomes an insulator, so that $M_2(t)$ stays bounded.

extended (with positive Δ and ν_0); for $\Delta < 2\nu_0$ all are localized [30]. Since — in precise analogy to the renormalization of Landé factors and to the coherent control of Anderson localization — the effective value of Δ can be manipulated by means of an external resonant periodic force, one can even switch from the metallic phase to the insulator phase, or the other way round, by varying the strength of that force. Figure 4 demonstrates how the transition manifests itself in the spreading of a wave packet that had originally been localized at an individual site. It has been suggested to look for this effect with ultracold atoms in far-detuned (and, hence, almost dissipation-free) driven optical lattices [31, 32]. Although it may be too early at the moment to speculate about the chances for harnessing this effect in, e.g., Terahertz-driven quasiperiodic semiconductor superlattices, the mere fact that one can coherently control a metal-insulator transition at least in principle appears noteworthy.

4. Conclusion

Whereas for atoms in crossed static and oscillating magnetic fields the modification of the Landé factors is itself of primary interest, the counterpart of this effect in ac-driven tight-binding lattices, the tunability of quasienergy band widths, brings about further phenomena if the lattice is not strictly periodic: One can coherently control the localization length of Floquet states tied to isolated defects, manipulate the degree of Anderson localization in randomly disordered lattices, and even switch between the metallic and the insulator regime of a quasiperiodic lattice by adjusting the strength of a coherent periodic driving force. For clarifying to what extent these effects can be exploited in real driven semiconductor devices, we need to understand precisely just how they are affected by a noisy environment and many-body interactions.

Acknowledgement

This work was supported by the Deutsche Forschungsgemeinschaft via the Schwerpunktprogramm *Zeitabhängige Phänomene und Methoden in Quantensystemen der Physik und Chemie*.

References

1. Haroche, S., Cohen-Tannoudji, C., Audoin, C. and Schermann, J.P. (1970) *Phys. Rev. Lett.* **24**, 861
2. Cohen-Tannoudji, C. (1994) *Atoms in Electromagnetic Fields*, p. 119. World Scientific, Singapore.
3. Shirley, J.H. (1965) *Phys. Rev.* **138**, B 979
4. Zel'dovich, Ya.B. (1967) *Sov. Phys. JETP* **24**, 1006

5. Breuer H.P. and Holthaus, M. (1989) *Z. Phys. D* **11**, 1
6. Breuer H.P. and Holthaus, M. (1991) *Ann. Phys. (N.Y.)* **211**, 249
7. Sambe, H. (1973) *Phys. Rev. A* **7**, 2203
8. Holthaus, M. (1992) *Phys. Rev. Lett.* **69**, 1596
9. Grossmann, F., Jung, P., Dittrich, T. and Hänggi, P. (1991) *Z. Phys. B* **84**, 315
10. Grifoni M. and Hänggi P. (1998) *Phys. Rep.* (in press)
11. Bastard, G. (1988) *Wave Mechanics Applied to Semiconductor Heterostructures*. Les Éditions de Physique, Les Ulis.
12. Fukuyama, H., Bari, R.A. and Fogedby, H.C. (1973) *Phys. Rev. B* **8**, 5579
13. W.V. Houston (1940) *Phys. Rev.* **57**, 184
14. J. Zak (1993) *Phys. Rev. Lett.* **71**, 2623
15. Faisal, F.H.M. and Kamiński, J.Z. (1996) *Phys. Rev. A* **54**, R1769
16. Holthaus, M. (1992) *Phys. Rev. Lett.* **69**, 351
17. Dunlap, D.H. and Kenkre, V.M. (1986) *Phys. Rev. B* **34**, 3625
18. Ignatov, A.A., Schomburg, E., Grenzer, J., Renk, K.F. and Dodin, E.P. (1995) *Z. Phys. B* **98**, 187
19. Meier, T., von Plessen, G., Thomas, P. and Koch, S.W. (1995) *Phys. Rev. B* **51**, 14490
20. Meier, T., Rossi, F., Thomas, P. and Koch, S.W. (1995) *Phys. Rev. Lett.* **75**, 2558
21. Keay, B.J., Zeuner, S., Allen Jr., S.J., Maranowski, K.D., Gossard, A.C., Bhattacharya, U. and Rodwell, M.J.W. (1995) *Phys. Rev. Lett.* **75**, 4102
22. Hone D.W. and Holthaus, M. (1993) *Phys. Rev. B* **48**, 15123
23. Holthaus, M. and Hone, D.W. (1996) *Phil. Mag. B* **74**, 105
24. Anderson, P.W. (1958) *Phys. Rev.* **109**, 1492
25. Thouless, D.J. (1974) *Phys. Rep.* **13**, 93
26. Holthaus, M., Ristow, G.H. and Hone, D.W. (1995) *Phys. Rev. Lett.* **75**, 3914
27. Holthaus, M., Ristow, G.H. and Hone, D.W. (1995) *Europhys. Lett.* **32**, 241
28. Dreese, K. and Holthaus, M. (1996) *J. Phys.: Condens. Matter* **8**, 1193
29. Mäder, K.A., Wang, L.-W. and Zunger, A. (1995) *Phys. Rev. Lett.* **74**, 2555
30. Sokoloff, J.B. (1985) *Phys. Rep.* **126**, 189
31. Dreese, K. and Holthaus, M. (1997) *Phys. Rev. Lett.* **78**, 2932
32. Dreese, K. and Holthaus, M. (1997) *Chem. Phys.* **217**, 201

TUNNELING OF LOW-ENERGETIC ELECTRONS IN THE PRESENCE OF INTENSE LASER FIELDS: THE FORMATION OF DYNAMICAL BARRIER STATES

..

MATHIAS WAGNER

Hitachi Cambridge Laboratory

Madingley Road, Cambridge, CB3 0HE, United Kingdom

Abstract. An analysis is presented on the stability of dynamical barrier states that exist underneath driven barriers against imperfections of the barrier or the driving potential that spoil the symmetry of the system. It is shown that asymmetric barriers as well as non-uniform driving amplitudes are not detrimental to observing these states. On the other hand, an asymmetry in the band profile to the left and right of the barrier exceeding a few photon quanta does seem to destroy the dynamical barrier states.

1. Introduction

The archetype of a quantum-mechanical state is that of a standing wave in a static square quantum well, and calculating its wave function using the time-independent Schrödinger equation is one of the very first textbook examples one encounters. Adding a periodic driving force to the quantum well introduces a new, enriched dynamics, which can be studied with the help of the Floquet formalism. And again, this dynamics is fairly well understood by now [1, 2, 3]. One of the more surprising recent results of driven systems is, however, that under certain circumstances *dynamical* quantum-mechanical states with highly unusual properties may be formed in the continuum spectrum that, in the limit of vanishing driving force, do *not* reduce to a “matching state” of the static system (as in a quantum well, for instance), but instead simply cease to exist without any apparent trace in the energy spectrum. These states are challenging in that they often seem to defy a simple explanation in terms of a “quasi-static” picture, which is so vital for our intuitive understanding.

One such example of a dynamically created state is that formed in a single barrier periodically driven by a uniform electric ac field $F_{ac} \cos \omega t$, where the time-averaging over the oscillating barrier potential leads to an effective double-barrier potential, in which “normal” resonances can build up [4]. In this paper I want to concentrate on a quite similar system where the barrier height is harmonically modulated as $V_b(t) = V_0 + V_{ac} \cos \omega t$, whilst either side of the barrier remain static [5, 6]. For such a system Kazanskii *et al.* predicted a huge variation in the transparency of the driven barrier for low-energetic electrons as a function of the driving amplitude V_{ac} . With low-energetic I mean in this context electrons incident on the barrier having kinetic energies of the order of or less than one photon quantum $\hbar\omega$. This variation in transparency with V_{ac} has been attributed to the creation of dynamical barrier states localised to the barrier region, which do not exist in the absence of the ac driving force. Similar results were found independently by Bagwell and Lake [7]. Both groups focused on the special case of a driven δ -function barrier.

In a recent work I have extended these studies to finite-width barriers [8, 9], thereby demonstrating that a δ -function barrier is actually the worst-case scenario as far as the relative ac driving strength is concerned before the dynamical barrier states become apparent in the transmission probability. This is very plausible considering that in our simple model the region of ac driving is restricted to the barrier only. Thus, the larger this region is, the better will be the coupling between the ac driving force and the electronic wave function. The aim of the present work is to furnish an analysis of the stability of these dynamical barrier states against some unavoidable imperfections in a potential experimental realisation, such as (I) non-square barriers, (II) non-uniform ac driving, and (III) differences in the conduction-band edges on either side of the barrier. The main results are that whilst the dynamical barrier states are very stable against (I) and (II), a conduction-band offset between the left- and right-hand side of more than a few photon quanta $\hbar\omega$ is highly detrimental.

2. Model

The model system I study is very simple, with a Hamiltonian of the form

$$H(z, t) = -\frac{\hbar^2}{2m} \frac{\partial^2}{\partial z^2} + V(z, t), \quad (1)$$

where the idealised barrier potential is given by

$$V(z, t) = \begin{cases} 0, & z < -d/2, \\ V_b^l + V_{ac}^l \cos \omega t, & -d/2 < z < 0, \\ V_b^r + V_{ac}^r \cos \omega t, & 0 < z < d/2, \\ V_r, & z > d/2. \end{cases} \quad (2)$$

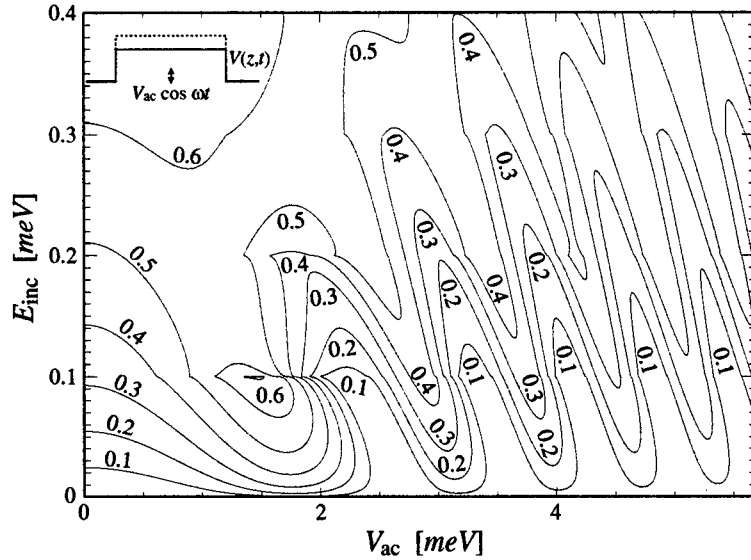


Figure 1. Contour plot of constant total transmission probability for a fully symmetric barrier (see inset), as a function of the kinetic energy of the incident electron and the driving amplitude V_{ac} . (Note that with $\hbar\omega = 0.1$ meV, the kinetic energy displayed ranges from 0 to $4\hbar\omega$).

A symmetric barrier is obtained for $V_r = 0$ and $V_b^l = V_b^r$, $V_{ac}^l = V_{ac}^r$. Based on this Hamiltonian, I calculate the Floquet scattering states relevant to transport which have the proper boundary conditions for incident and outgoing waves [10, 11]. From these states the time-averaged total transmission probability is then obtained by employing the standard formula $T = \sum_n T_n$, where n runs over all contributing (discrete) transport channels, and T_n are the corresponding partial transmission probabilities.

3. Results

In the following I will systematically vary the parameters of the barrier potential (2) to study the effect that asymmetries may have. For all of the subsequent calculations I have used $\hbar\omega = 0.1$ meV corresponding to 24 GHz, a barrier width of $d = 20$ nm, and an electronic mass $m = 0.067 m_0$, appropriate for GaAs. This is basically the same structural data as used in Refs. [8, 9]. For ease of reference, I have reproduced the transmission probability plot of the fully symmetric case in Fig. 1.

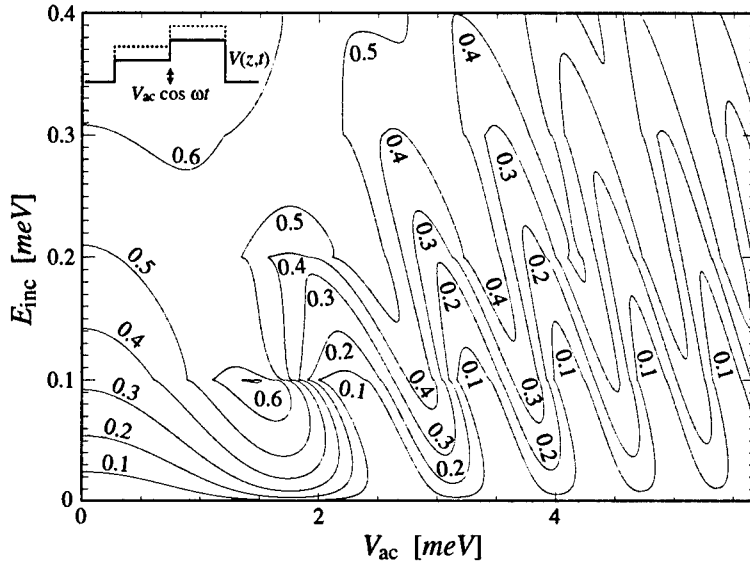


Figure 2. Contour plot of constant total transmission probability for an asymmetric static barrier (see inset), as a function of the kinetic energy of the incident electron and the driving amplitude V_{ac} .

3.1. ASYMMETRIC STATIC BARRIER

In the first study, I set $V_r = 0$ and $V_{ac}^l = V_{ac}^r \equiv V_{ac}$, which leaves me with an asymmetric static barrier driven by an ac potential which is uniform across the entire barrier. In the particular case of Fig. 2 I chose $V^l = 0.75$ meV and $V^r = 1.25$ meV — a choice which leaves the total area under the barrier unchanged compared to the symmetric case of Fig. 1.

Figure 2 shows a contour plot of constant total transmission probability through the driven barrier for incident electrons having kinetic energies ranging from 0 to $4 \hbar\omega$, as a function of the driving ac potential V_{ac} . The contour lines show more or less pronounced kinks at kinetic energies equalling a multiple of the photon quantum $\hbar\omega$, which can be easily understood as the effect of additional transport channels opening at these threshold energies. Secondly, the contour plot reveals a characteristic strong modulation of the transmission probability for electrons having kinetic energies less than one or two photon quanta. These valleys in the transmission probability are the fingerprint of dynamical barrier states that live under the barrier for certain driving conditions. They can be characterised by an almost perfect reflection of the incident electron. A more detailed analysis of these states in the symmetric case can be found in Refs. [8, 9].

A comparison of Fig. 2 with the symmetric case shown in Fig. 1 reveals

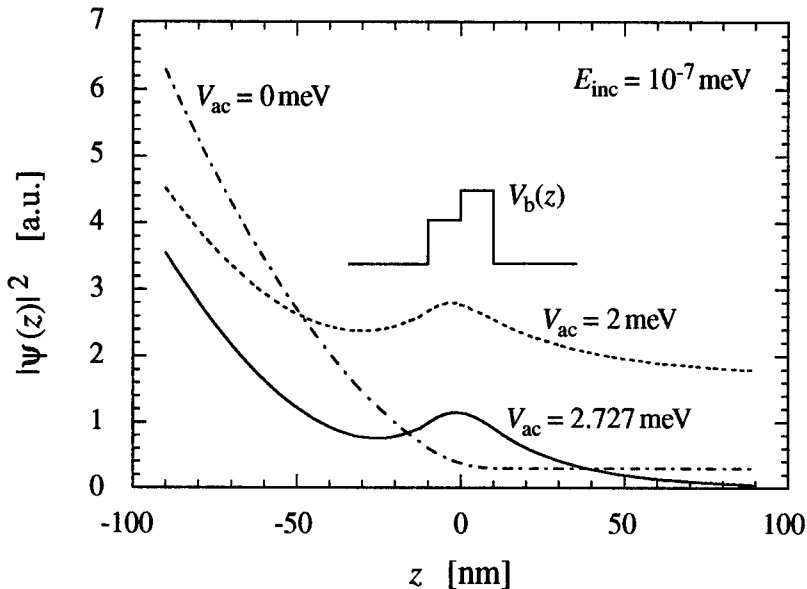


Figure 3. Time-averaged probability function $|\psi(z)|^2$ of the $l \rightarrow r$ scattering state for various driving amplitudes V_{ac} at almost zero incident energy. At $V_{ac} = 2.727$ meV the dynamical barrier state is seen as a pronounced local maximum in $|\psi(z)|^2$ in the barrier region.

that the valley structure (and in fact the entire plot) is virtually identical in both cases, suggesting that an asymmetric static barrier is not harmful to the development of dynamical barrier states underneath the barrier.

In Fig. 3 I have plotted the time-averaged squared wavefunction of the scattering state corresponding to an electron incident from the left at almost zero kinetic energy (10^{-7} meV). In the absence of any driving the wave function decays exponentially across the barrier, but for strong driving a local maximum is seen in the barrier region, which is caused by the dynamical barrier state. The localisation is optimal for $V_{ac} \approx 2.727$ meV, which according to Fig. 2 corresponds to a local minimum in the transmission probability. This change in transmission probability is also reflected in the huge variation of the value of $|\psi(z)|^2$ for $z \rightarrow \infty$ in the three cases shown in Fig. 3. The increase of $|\psi(z)|^2$ for negative z is simply due to the standing wave pattern generated by the interference of the incident and reflected wave, which completely mask the localisation of the dynamical barrier state on this side. A quantitative measure for the localisation length is the inverse of the k vector one photon quantum below the band edge, $\sqrt{\hbar/2m\omega}$, which is ≈ 75 nm in the present case.

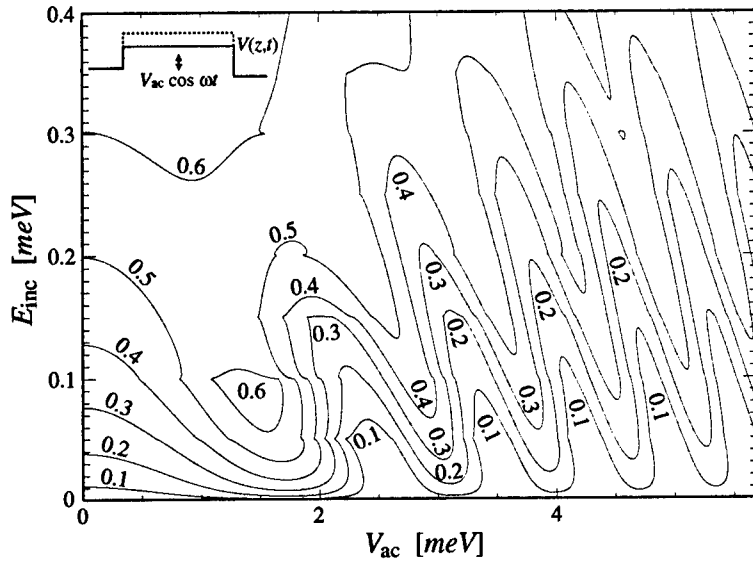


Figure 4. Contour plot of constant total transmission probability for a symmetric barrier with a band offset in the far contact of $V_r = -0.5 \hbar\omega$ (see inset).

3.2. ASYMMETRIC DRIVING

Asymmetric driving is realised by setting $V_r = 0$ and, say, $V_b^l = V_b^r = 1$ meV, whilst maintaining $V_{ac}^l \neq V_{ac}^r$. As in the case of an asymmetric static barrier with homogeneous driving discussed in the previous Subsection, one finds that qualitatively the dynamical barrier states are little if anything affected by the degree of asymmetry in the driving ac potential. (For this reason I do not present a Figure here.)

3.3. ASYMMETRIC CONDUCTION-BAND EDGE

To test for stability against imperfections in the symmetry between the left- and right-hand contact regions, I finally studied the case of a symmetric barrier ($V_b^l = V_b^r = 1$ meV) with symmetric driving ($V_{ac}^l = V_{ac}^r \equiv V_{ac}$), but different conduction-band edges on either side of the barrier, as schematically depicted in the inset of Fig. 4. For Fig. 4 the potential offset on the right-hand side was chosen to be $V_r = -0.5 \hbar\omega$, and already at such a small built-in potential difference an appreciable adverse effect on the dynamical barrier states can be noticed in the form of a somewhat reduced valley structure at the bottom of the Figure. When doubling the band offset to $V_r = -\hbar\omega$ as done for Fig. 5, the dynamical barrier states become even weaker and, eventually, for band offsets much larger than the photon energy $\hbar\omega$,

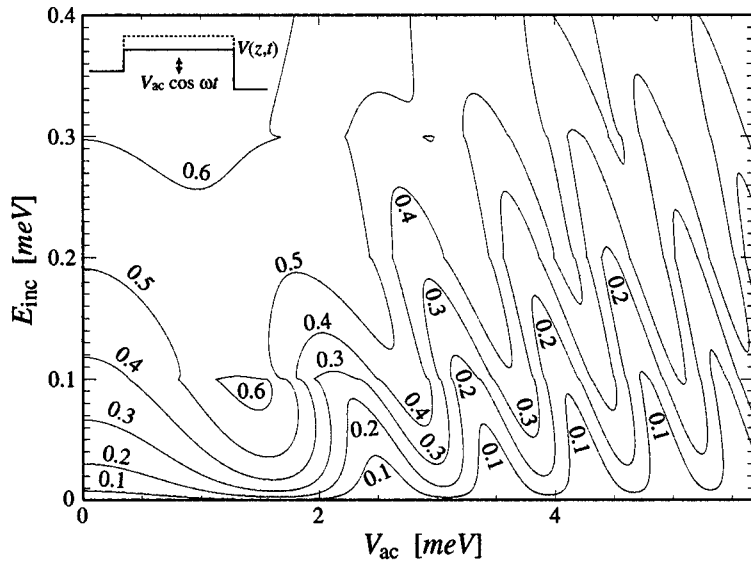


Figure 5. Contour plot of constant total transmission probability for a symmetric barrier with a band offset in the far contact of $V_r = -\hbar\omega$. Note the considerably reduced valley structure at the bottom of the Figure compared to Figs. 2 and 4.

they completely disappear.

This result suggests that ideally the static potential on either side of the barrier should be the same — and flat — for best observation of the dynamical barrier states. Of course, this is in practice not possible to achieve, at least in semiconductor heterostructures, and the question is what band bending one can tolerate. A reasonable criterium — which at the moment is only a conjecture, though, based on the localisation length of the dynamical barrier states — is that the potential must be flat over a distance larger than the inverse of the k vector at one photon quantum $\hbar\omega$ below the band edge, i.e., over a distance $d_f > \sqrt{\hbar/2\omega m}$. This criterium effectively serves as a lower cutoff for choosing the driving frequency. It goes without saying that the wave function must also be coherent over a similar distance, and that the electronic mass on either side of the barrier must be the same.

4. Conclusions

I have studied tunneling through a harmonically driven barrier for electrons having kinetic energies of the order of or less than the photon quantum $\hbar\omega$ associated with the driving. In this regime the tunneling electrons probe dynamical barrier states that form underneath the barrier for certain driving conditions, leading to large characteristic variations in the transmission

probability as a function of the driving amplitude.

The dynamical barrier states show a surprising resistance against a breaking of the symmetry of the structure. In particular, an asymmetric static barrier, or a driving amplitude which is not homogeneous across the barrier, does not seem to do any harm at all. On the other hand, lowering the static potential on one side of the structure only, whilst keeping the other side fixed, does have a strong effect on the dynamical barrier states, resulting in their complete destruction for band offsets between the left- and right-hand side potentials exceeding a few photon quanta.

This work has been supported by the EU via TMR contract FMRX-CT98-0180.

References

1. L. E. Reichl and W. A. Lin. Exact quantum model of field-induced resonance overlap. *Phys. Rev. A*, 33:3598, 1986.
2. H. P. Breuer and M. Holthaus. A semiclassical theory of quasi-energies and Floquet wave-functions. *Ann. Phys. (N. Y.)*, 211:249, 1991.
3. M. Wagner. Strongly driven quantum wells: An analytical solution to the time-dependent Schrödinger equation. *Phys. Rev. Lett.*, 76:4010, 1996.
4. I. Vorobeichik, R. Lefebvre, and N. Moiseyev. Field-induced barrier transparency. *Europhys. Lett.*, 41:111, 1998.
5. A. K. Kazanskii, V. N. Ostrovskii, and E. A. Solov'ev. Passage of low-energy particles through a nonstationary potential barrier and the quasi-energy spectrum. *Zh. Eksp. Teor. Fiz.*, 70:493, 1976. For a driven δ -function barrier. [Engl. transl. in: Sov. Phys. JETP **43**, 254 (1976)].
6. M. Büttiker and R. Landauer. Traversal time for tunneling. *Phys. Rev. Lett.*, 49:1739, 1982.
7. P. F. Bagwell and R. K. Lake. Resonances in transmission through an oscillating barrier. *Phys. Rev. B*, 46:15329, 1992.
8. M. Wagner. Can photon-assisted tunneling be observed in single barriers? *Phys. stat. sol. (b)*, 204:382, 1997.
9. M. Wagner. Erratum: Can photon-assisted tunneling be observed in single barriers? *Phys. stat. sol. (b)*, 207:307, 1998.
10. M. Wagner. Photon-assisted transmission through an oscillating quantum well: A transfer-matrix approach to coherent destruction of tunneling. *Phys. Rev. A*, 51:798, 1995.
11. M. Wagner. Quenching of resonant transmission through an oscillating quantum well. *Phys. Rev. B*, 49:16544, 1994.

HOPPING MECHANISM OF COHERENT PHOTOVOLTAIC EFFECT AND PHOTOINDUCED POLAR ANISOTROPY IN GLASS.

E.M. BASKIN, M.V. ENTIN.

*Institute of Semiconductor Physics, Siberian Branch
of Russian Academy of Science,
630090, Novosibirsk, Russia. E-mail: Entin@isp.nsc.ru*

Abstract. The appearance of DC in a glass acted by two intercoherent electromagnetic waves with the main and doubled frequency is studied. The light causes the transitions between the localized states. The interference of action of two coherent sources leads to the polar asymmetry of transitions. The asymmetric part of the transition probability is obtained in the third order of electric field. It depends on the phase shift between two waves.

The transitions inside pairs of close states produce a slow establishing static polarization of a glass. In the absence of transitions between different pairs, the polarization does not saturate, while the establishment current relaxes to zero.

In the stationary regime the DC is found, determined by a balance of phototransitions and intersite relaxation. The macroscopic current is studied having regards to geminate recombination.

1. Introduction

The new photoelectric effect has been studied during recent years, called coherent photovoltaic effect (CPVE) [1, 2, 3, 4, 5, 6, 7, 8]. We consider CPVE as a stationary current, caused by simultaneous action of two or more intercoherent light beams.

This current is possible in a medium with any symmetry, in particular in a homogeneous isotropic one. In the case of two light beams with the principal frequency ω and double frequency 2ω : $\mathbf{E}(t) = Re(\mathbf{E}_\omega e^{i\omega t} + \mathbf{E}_{2\omega} e^{2i\omega t})$ the current in the lowest order of the electric field $\mathbf{E}(t)$ is determined by

an expression

$$j_i = \frac{1}{2}(\alpha_{ijkl} E_{2\omega,j} E_{\omega,k}^* E_{\omega,l}^* + c.c.). \quad (1)$$

Unlike other photoelectric effects, the CPVE depends on the relative phase of fields. It is not proportional to the light intensity and vanishes for incoherent illumination.

In the macroscopic sample the current CPVE is usually inhomogeneous due to phase oscillations, caused by the difference of light beams velocities or their noncollinearity.

The different mechanisms of CPVE were studied earlier, impurity-band transitions [3, 7], intra- [2] and interband [6] transitions, and current, caused by quantum corrections to the conductivity [2].

The interest to the CPVE was heated by the circumstance that it hypothetically is responsible for the 2nd harmonic generation (SHG) in glass fibers [9]. The low value of glass conductivity leads to the electric fields $10^4 - 10^5 \text{ V/cm}$, sufficient to reduce the medium symmetry, which is necessary for SHG.

The scenarios of appearance of the second order permeability in glasses are carefully enough developed [9, 10, 11, 12]. The mechanism of current generation in glasses is much less clear.

In [7, 9] it was supposed, that CPVE in glasses is caused by the photoionization of impurity states. This mechanism needs the presence of relatively shallow filled impurity states with the depth less than 2 eV. In equilibrium such states, evidently will lead to the essential absorption of light in a glass. At the same time the fibers are remarkably transparent solid media. This returns us to the known question of N. Mott about the source of high transparency of oxide glasses.

The generally accepted explanation is that despite the large density of states in glass all of them are localized and the transition probabilities between them are suppressed due to tunnel factors. Nevertheless, just these transitions determine the photoelectric properties. Hence the change of properties of glasses is observable after very large expositions only.

Our purpose is the study of CPVE in glasses and in the disordered system of localized states (LS) generally. We shall consider a glass as a system of single level centers. The electron states of these centers are localized in the space and randomly and homogeneously distributed within the forbidden energy band. The large enough density of these states fixes the Fermi level in a forbidden band. The optical transitions are permitted between the states on the different sides from the Fermi energy.

The first part of the work considers the elementary act of transition. The transition probability is found in the tunnel Hamiltonian model. The electromagnetic field is taken into account in the shift of energy levels only.

Then we found the dynamic current of establishment of stationary polarization. The stationary current is limited by the geminate recombination, the probability of which is found in the third section. The resulting macroscopic current is determined by the photoexcitation together with the probability of surviving during electron relaxation.

2. Phenomenology of CPVE

The CPVE originates from the third order current response to the electric field

$$j_i(t) = \int_0^\infty dt_1 dt_2 dt_3 \alpha_{ijkl}(t_1, t_2, t_3) E_j(t - t_1) E_k(t - t_2) E_l(t - t_3). \quad (2)$$

Let the illumination to be stationary. This means that products of fields have translational invariance in time $E_i(t_1) \dots E_j(t_n) = E_i(t_1 + t_p) \dots E_j(t_n + t_p)$, where t_p is some period. In this case the response contains the stationary part. For the illumination by two light beams ω and 2ω (2) leads to (1).

Using the complex form of field, $E_{i,\omega} = \mathcal{E}_{i,\omega} \exp(i\varphi_{i,\omega})$, the formula (1) can be written as

$$j_i = (\alpha_{ijkl}^s \cos(\varphi_{j,2\omega} - \varphi_{k,\omega} - \varphi_{l,\omega}) + \alpha_{ijkl}^a \sin(\varphi_{j,2\omega} - \varphi_{k,\omega} - \varphi_{l,\omega})) \mathcal{E}_{j,2\omega} \mathcal{E}_{k,\omega} \mathcal{E}_{l,\omega}, \quad (3)$$

where $\hat{\alpha}^s = 1/2(\hat{\alpha} + \hat{\alpha}^*)$, $\hat{\alpha}^a = 1/2(\hat{\alpha} - \hat{\alpha}^*)$.

In an isotropic medium the tensor α_{ijkl} is determined by 4 real constants:

$$\mathbf{j} = \alpha_1^s \operatorname{Re}(\mathbf{E}_{2\omega}(\mathbf{E}_\omega^* \mathbf{E}_\omega^*)) + \alpha_2^s \operatorname{Re}(\mathbf{E}_\omega^*(\mathbf{E}_{2\omega} \mathbf{E}_\omega^*)) + \alpha_1^a \operatorname{Im}(\mathbf{E}_{2\omega}(\mathbf{E}_\omega^* \mathbf{E}_\omega^*)) + \alpha_2^a \operatorname{Im}(\mathbf{E}_\omega^*(\mathbf{E}_{2\omega} \mathbf{E}_\omega^*)). \quad (4)$$

The symmetrical constants α_i^s describe the current, caused by linearly polarized light and asymmetric components α_i^a correspond to the current caused by partially or fully circular polarized waves.

The CPVE needs the very high level of coherence of different beams. The phase fluctuations can cause the breaking of this coherence and vanishing of CPVE. We should emphasize that CPVE, determined by the relative phase of beams can exist even for incoherent light, if beams are mutually coherent. For example, two coaxial light beams ω and 2ω , reflected from a normally vibrating mirror are not coherent but mutually coherent.

This reflects more general situation. If the field is not absolutely coherent, the conditions of stationarity mean that the field is determined by a stationary random process and hence mean powers of field are time independent: $\langle E_i(t_1 + t_p) \dots E_j(t_n + t_p) \rangle = \langle E_i(t_1) \dots E_j(t_n) \rangle$ for any t_p .

The stationary current, determined by the third order correlator of electric field is

$$\begin{aligned} \langle j_i(t) \rangle &= \int \int \int_0^\infty dt_1 dt_2 dt_3 \alpha_{ijkl}(t_1, t_2, t_3) \times \\ &\lim_{t \rightarrow \infty} \frac{1}{t} \int_0^t dt' E_j(t' - t_1) E_k(t' - t_2) E_l(t' - t_3). \end{aligned} \quad (5)$$

Beyond the third order, the stationary current is possible if any correlator of fields is non-vanishing.

3. Transition probability.

We shall consider a glass as a system of LS, between which the tunnel transition occur induced by light or phonons (but not both in the same time). We neglect phonons in optical transitions while the thermal relaxation necessarily includes the emission or absorption of phonons.

Let us consider two states with energies ε_1 ε_2 and vector distance 1 between which the tunnel transition is possible with amplitude $T = T_0 \exp(-l/a)$, where a is a localization length (Figure 1). The difference of the localization lengths of states is neglected.

The system is illuminated by two linearly-polarized coherent light sources. The field amplitudes E_ω and $E_{2\omega}$ are real, the phases of different spatial components of field are the same. Hence it is convenient to introduce the relative phase $\varphi = 2\varphi_\omega - \varphi_{2\omega}$.

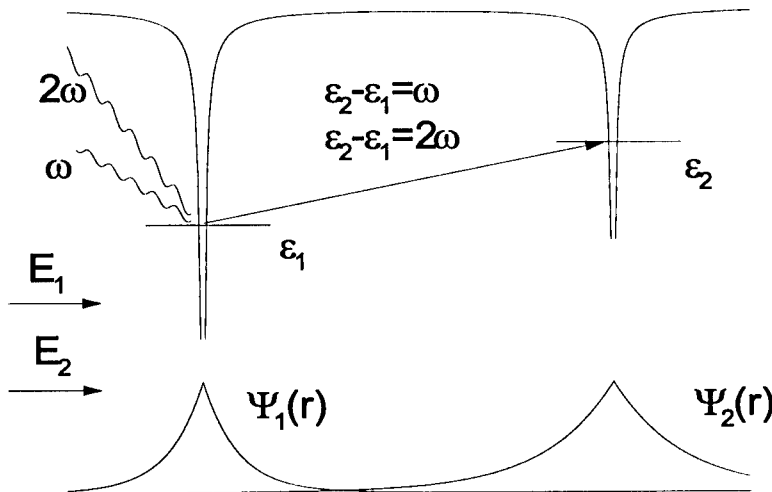


Figure 1. Phototransitions between localized states in glass caused by two beams with frequencies ω and 2ω

In general, the action of field leads to the alternating in time shift of energy levels

$$\pm \mathcal{U}(t) = 2(\mathcal{U}_\omega \cos \omega t + \mathcal{U}_{2\omega} \cos(2\omega t + \varphi)). \quad (6)$$

Here $\mathcal{U}_{\omega,2\omega} = 1/2(\mathbf{E}_{\omega,2\omega}\mathbf{l})$. Here and below we use atomic units $e = \hbar = m = 1$.

The system of equations for probability amplitudes for being in the first or in the second states is

$$\begin{aligned} i\dot{a}_1 &= (\varepsilon_1 + \mathcal{U})a_1 + Ta_2, \\ i\dot{a}_2 &= (\varepsilon_2 - \mathcal{U})a_2 + T^*a_1. \end{aligned} \quad (7)$$

The equations (7) are valid, if the inequalities $\{\omega, |\varepsilon_{12}|\} \ll (\varepsilon_1, \varepsilon_2)$ are fulfilled, where $\varepsilon_{12} = \varepsilon_1 - \varepsilon_2$.

The transition probability should be found in the first non-vanishing approximation, leading to the direct current. This current appears, if the transition probability becomes asymmetric relative to the coordinate inversion, which means the difference of the transition probabilities between the equivalent pairs of states distanced by 1 and -1 . The symmetry arguments demand that the expression for field should contain at least 3 fields (formula (4)).

The current is determined by the second order in field ω and first order in field 2ω . In accordance with the general theory of CPVE we should find the interference of transition amplitudes caused by \mathbf{E}_ω and $\mathbf{E}_{2\omega}$.

As a result the asymmetric part has form:

$$W_{12} = 2\pi |T|^2 / \omega^3 (\mathbf{E}_{2\omega}\mathbf{l})(\mathbf{E}_\omega\mathbf{l})^2 \cos \varphi [\delta(\varepsilon_{21} - 2\omega) + \delta(\varepsilon_{21} - \omega)]. \quad (8)$$

In (8) the processes of excitation of electrons are taken into account only. We should underline, that in the interference part of the transition probability the number of photons, taking part in transition, can not be separated. The first term in (8) corresponds to the interference of two-photon amplitude with participation of photons ω and one-photon amplitude with frequency 2ω , with resulting change of electron energy 2ω , the second one does to the one-photon amplitude with absorption of ω and mixed amplitude with absorption of quantum 2ω and emission ω .

It should be emphasized, that the CPVE is non-vanishing just because the states of system between which the transition occur have no definite parity. The situation is similar to the impurity-band transition when the finite state has definite translational momentum but not angular momentum (and has no definite parity).

In the present case the absence of parity is connected with the fact that the initial and final states have different localization centers.

4. The initial current.

First we shall find the current in the sample, which have been previously in equilibrium and then suddenly illuminated. In the initial stage of relaxation one can neglect for the relaxation of electrons. Hence photoproduction rate of the dipole momentum density $\dot{\mathbf{P}}$ is determined by the probability of asymmetric excitation (8), integrated with the vector $e(\mathbf{r}_i - \mathbf{r}_j)$ over all pairs of states. It is true if all relaxation processes have no time to pass of and the excited states have no time to saturate.

The final formula for the density of current in initial stage can be found averaging the formula (8). The result is

$$\mathbf{j}(0) = \frac{3\pi^2 a^7}{\omega^3} T_0^2 [\mathbf{E}_{2\omega} \mathbf{E}_\omega^2 + 2\mathbf{E}_\omega (\mathbf{E}_{2\omega} \mathbf{E}_\omega)] \cos \varphi \times \\ (\int_{\mu-2\omega}^{\mu} d\epsilon g(\epsilon) g(\epsilon + 2\omega) + \int_{\mu-\omega}^{\mu} d\epsilon g(\epsilon) g(\epsilon + \omega)). \quad (9)$$

μ is the equilibrial value of chemical potential, $g(\epsilon)$ is the density of states. The main contributions to the initial current results from close pairs with distance $l \sim 3a$ connected with random approaching of impurities.

5. The dynamic current.

First we shall neglect relaxation of electrons through the extrinsic states and consider the glass as a system of independent pairs of states. The kinetic equation for the number of exited pairs with the distance l can be written as

$$\dot{n}_l(t) = W_{12}(l) - n_l(t)/\tau(l), \quad (10)$$

where the recombination time is $\tau(l) = \tau_0 \exp(2l/a)$. The preexponential factor τ_0 depends on recombination mechanism. For radiative processes in optical range $\tau_0 \sim 10^{-8} s$. If the recombination is determined by one or many-phonon emission in nonadiabatic regime [14],

$$\tau_0 \sim \omega_D^{-1} \exp\left(\frac{\gamma|\epsilon_1 - \epsilon_2|}{\omega_D}\right). \quad (11)$$

Here ω_D is the Debye frequency, γ is the logarithm of dimensionless electron-phonon interaction constant. For $\epsilon_1 - \epsilon_2 \sim \omega$ with ω in the optical range the radiative relaxation prevails, while if the energy distance between states is small, the non-radiative relaxation becomes the main mechanism of relaxation. The dynamic current is determined by the radiative relaxation.

The solution of (10) with the initial condition $n_l(0) = 0$ is

$$n_l(t) = \tau(l) W_{12}(l) (1 - \exp(-t/\tau(l))). \quad (12)$$

The density of current is

$$\mathbf{j}(t) = \mathbf{j}(0)\tau_0 \int_{\tau_0}^{\infty} \frac{\log^6(\tau/\tau_0)}{\tau^2} d\tau \exp(-t/\tau). \quad (13)$$

In the limit $t \rightarrow \infty$ the current is not really stationary, but is slowly relaxing:

$$\mathbf{j}(t) = 1/6! \mathbf{j}(0)\tau_0 \frac{\log^6 t/\tau_0}{t}. \quad (14)$$

The relaxation is close to the power-like law $1/t^{1-\alpha}$, typical for dielectric response. The large power of logarithm is determined by the growth of the number of accessible states together with the growth of preexponent in optical transition with the distance l . The corresponding polarization does not establishing for infinitely long time: $\mathbf{P}(t) \sim \log^7 t/\tau_0$.

The model, we considered here, does not take into account the relaxation of electrons on the extrinsic states and the charge relaxation, caused by conductivity. These factors limit the decay of the current by the Maxwell time $(4\pi\sigma_{ef})^{-1}$. The stationary current, determined by the full relaxation of carriers, is considered below. Intermediate asymptotics will be discussed elsewhere.

6. The geminate recombination.

The relaxation of photoexcited electron and hole may be finished by the recombination on the same site (geminate recombination), or by the current through the external circuit. We shall find here the portion of electrons which don't subject the geminate recombination and achieve the external circuit. In analogy with the physics of photodetectors, this portion can be considered as "external quantum efficiency" of relaxation process. As the process can be separated on two phases, thermal relaxation and charge spreading off they leads to 2 independent multipliers, P_1 and P_2 .

We shall base on the theories of hopping transport [13] and geminate recombination [14].

The relaxation through the extrinsic states is determined by non-radiative processes. The probability of transition between two states ϵ_i and ϵ_j on the distance $\mathbf{r}_i - \mathbf{r}_j$ with many-phonon emission in nonadiabatic regime is

$$\omega_D \exp\left(-\frac{2|\mathbf{r}_i - \mathbf{r}_j|}{a} - \frac{\gamma|\epsilon_i - \epsilon_j|}{\omega_D}\right). \quad (15)$$

Below we neglect the dependence of density of states $g(\epsilon)$ on energy. In this case the relaxation process of photoexcited pair has two scenarios, in

dependence on the ratio of the energy of photoexcited electron $\epsilon \sim \omega$ and the characteristic energy,

$$\delta = \frac{\omega_D}{\gamma} \left(\frac{\Theta_0 \gamma}{\omega_D} \right)^{1/4}, \quad (16)$$

where $\Theta_0 = \beta/ga^3$, $\beta \approx 20$.

If $\epsilon \gg \delta$, an electron jumps to the site with lower-lying level for which the probability of hop is maximal, losing the small portion of energy δ in any hop with the typical length

$$\frac{a}{4} \left(\frac{\Theta_0 \gamma}{\omega_D} \right)^{1/4}. \quad (17)$$

The geminate recombination during each step has exponentially low probability. After achieving the energy δ , the relaxation continues according to the second scenario which corresponds to the small ratio ϵ/δ .

If $\epsilon \ll \delta$, an electron prefers to jump to the nearest neighbor with the energy below initial but does not take into account the difference of energy levels $|\epsilon_i - \epsilon_j|$. In this case the energy loss in a hop has the same order of magnitude as an initial energy. The length of subsequent jump grows exponentially with the number of jump.

If the mean squared distance between an electron and initial site after the first stage is larger than the distance between lower-lying states, the geminate recombination remains negligible. Otherwise in the second stage the probability to hop in any step to another empty state has the same order as the probability of geminate recombination on the initial site. This situation corresponds to the theory [14].

The last stage of relaxation is the motion in the energy band Δ , decisive for equilibrail conductivity. In our model of glass $\Delta = \Theta^{3/4} \Theta_0^{1/4}$, and the conductivity follows the known Mott law [13]: $\sigma_{ef} \sim \exp -(\Theta_0/\Theta)^{1/4}$ (here Θ is the temperature). In the energy band Δ both processes with excitation and absorption of phonons occur and an electron moves like thermalized one. So the number of steps, which are necessary to get to the band Δ , is determined by the ratio $\min\{\omega, \delta\}/\Delta$.

The resulting integral probability P_1 to survive before the stage of charge spreading depends on the temperature. If the temperature Θ is low enough, $\Theta \ll \chi \Theta_0$, and $\omega \gg \delta$

$$P_1 = \left(\frac{\Theta^2 \omega^4}{\Theta_0 \omega_D^5} \right)^{\alpha/8}. \quad (18)$$

Here

$$\chi = \left(\frac{\omega_D^5}{\omega^4 \Theta_0} \right)^{1/2} \ll 1,$$

temperature is measured in energetical units. The value $\alpha = 0.8 - 1.15$, according to calculations of [14].

If the temperature exceeds $\chi\Theta_0$, the geminate recombination is unimportant, and $P_1 = 1$.

Let us discuss the case of small ω/δ , where the value P_1 depends on the distance between the photoexcited electron and hole l . In this case the spatial dependence of exponent in (15) for typical distances between states is more strong than the energy dependence. As a result an electron prefers to hop to the nearest neighbor with the energy, which is lower, than in the previous state. More of that, firstly one can neglect the energetic exponents in the hopping probability.

In the limit of low density of states, $ga^3\omega \ll 1$ the sequence of visited states i is determined by conditions:

$$\epsilon_i > \epsilon_{i+1}, \quad |\mathbf{r}_i - \mathbf{r}_{i+1}| < r_i. \quad (19)$$

We chose the start site $\mathbf{r}_0 = 0$. The site $i + 1$ gives the minimal possible $|\mathbf{r}_i - \mathbf{r}_{i+1}|$ for fixed r_i and ϵ_i . These conditions determine the unique path and guarantee the optimization of probability in the case, when the probabilities of jumps are widely distributed.

The hops may continue infinitely if don't take into account the phonon absorption processes. If at some definite step the nearest neighbor is 0 site, the process stops, the geminate recombination occurs.

The result of sequence of hops depends on the distance between the initial and photoexcited sites. If they are closer than the mean distance between sites $(g\omega)^{-1/3}$, the probability to find next suitable site other than 0 has the order of $g\omega l^3 \ll 1$. The repetition of process leads to multiplication of probabilities and, hence, tends to zero. If $g\omega l^3 \gg 1$, the probability of each successive step, not returning to origin, is not small and the resulting probability of non-returning on the initial site goes to 1. Hence the threshold value of l , r_c should exist, separating runaway paths and returning paths. The threshold r_c has the order of the unique scale parameter with the dimension of length $(g\omega)^{-1/3}$.

The threshold r_c separates small sizes of photoexcited pair for which the geminate recombination dominates and the large sizes, for which the survival probability does not vanish. The integration over the pair size in the expression for current, hence, should be limited from below by the value r_c . Hence the pairs, important for photocurrent have mean distance between LS, $(g\omega)^{-1/3}$. For such pairs, the probability to survive is

$$\text{Min}\left\{1, \left(\frac{\Theta^3\Theta_0}{\omega^4}\right)^{\alpha/12}\right\}.$$

Integrating over l limited by r_c we find the exponentially small resulting quantum efficiency:

$$P_1 = 4/45 (r_c/a)^6 \text{Min} \left\{ 1, \left(\frac{\Theta^3 \Theta_0}{\omega^4} \right)^{\alpha/12} \right\} \exp(-2r_c/a). \quad (20)$$

7. Stationary current.

The last stage of relaxation can be considered as a charge spreading off. If two sites, where the thermalization finished are situated outside the path of best conductivity, the conductance between these sites will be short-circuited the charge and the charge hardly reach the external circuit.

If the distance between hole and electron after thermalization into the band Δ is larger than correlation length L_c , the medium may be considered as uniform from the point of view of spreading. Using value $L_c = a/4(\Theta_0/\Theta)^{1+\nu}$ (ν is a critical index [13]), we find, that $\Theta \gg \Theta_0 \chi^{1/(1+\nu)} \gg \Theta_0 \chi$. This means that random currents eW_{ij} are connected between the start point i and the point of relaxation finish j in the uniform medium. One can easily show that the part of mean current density due to optical transitions has form

$$\mathbf{j}_{opt} = 2e/V \sum_{i,j} (\mathbf{r}_j - \mathbf{r}_i) W_{ij}. \quad (21)$$

Here V is the system volume, the summing is done with respect to all states i, j , for which $\varepsilon_i < \mu$ and $\varepsilon_j > \mu$.

To prove this we cut the sample with cross section S and length L by a plane $x = const$. Then the current density across this section in x direction is determined by all transitions between LS from the right to the left of section:

$$j_{opt,x} = e/S \left[\sum_{x_i < x, x_j > x} W_{ij} - \sum_{x_i > x, x_j < x} W_{ij} \right].$$

So far as in large sample all possible configurations of resonant pairs are realized the sums in the formula does not depend on x and the current can be averaged with respect to x :

$$1/L \int dx j_{opt,x} = 2e/V \sum_{i,j} (x_j - x_i) W_{ij}$$

The repetition of that procedure for all components of current gives (21). During the thermal relaxation without recombination the mean vector distance between electron and hole does not change. As a result the number

j can be changed to the number of final state for excitation f . From this one can conclude that in the case $\Theta \gg \Theta_0 \chi^{1/(1+\nu)} \gg \Theta_0 \chi$, $P_2 = 1$.

Let us consider the case $\Theta_0 \chi^{1/(1+\nu)} \gg \Theta \gg \Theta_0 \chi$. In this case the distance between electron and hole is less than L_c . The resistivity R_{if} between the sites, where they are situated, has a exponentially wide distribution function. It is important, that just half of resistors are larger than the resistivity R_c of cell with size L_c . If R_{if} is less than R_c , the sites are short-circuited and quickly discharging, not contributing to the macroscopic current. Otherwise some part of the current say, $1/2$, flows through the infinite cluster with the less resistivity, than the quasi-insulating phase. As a result $P_2 \sim 1$ in that case too. Hence the stationary current is determined by expression

$$\mathbf{j}(\infty) = P_1 \mathbf{j}(0).$$

The value of P_1 is determined by formulae (18, 20). The stationary current has no exponential smallness in the case of large frequency of light $\omega \gg \delta$ and is exponentially small in the opposite case.

8. Discussion

In the present study we gave the answer on the question, how the steady current can be generated in the dielectric without the excitation of electrons into the delocalized states.

Let us estimate the CPVE in the case of undoped oxide glasses. The typical band gap has value 5-9 eV, so direct transitions of electrons from the middle of forbidden gap to the permitted band are impossible. The absorption coefficient changes from 10^{-2} cm^{-1} to 10^{-4} cm^{-1} . In the case of transitions from one local state to another the cross-section of light absorption has the order $\alpha a^2 \exp(-2l/a)$, where α is the constant of fine structure. The density of close pairs is $4\pi/3 g\hbar\omega l^3$. So the reasonable absorption coefficient $\sim 10^{-3} \text{ cm}^{-1}$ corresponds to the density of states $g \sim 2 \times 10^{19} \text{ cm}^{-3} \text{ eV}^{-1}$. The estimation for PVGE current according to (9) for $a = 0.2 \text{ nm}$, $T_0 = 10 \text{ eV}$ gives $j(0) [\text{A}/\text{cm}^2] \sim 2 \times 10^{-17} E_{2\omega} E_\omega^2 [\text{V}^3/\text{cm}^3]$.

The stationary value of current in the case should be decreased by the factor $P_1 \sim 10^{-6}$, according to (20). Using experimental data of [11],[12] for the field $E_\omega \sim 10^6 \text{ V/cm}$ $E_{2\omega} \sim 3 \times 10^5 \text{ V/cm}$ we find the stationary current $j \sim 10^{-5} \text{ A/cm}^2$. This value satisfactorily corresponds to the experimental data [11],[12].

The obtained value is comparable with the current, caused by impurity-band transitions [7]. The difference is that the current due to intersite transitions, unlike the impurity-band transitions, do not need the preliminary excitation of electrons to the local states with depths less than 2eV, which, in turn, can be caused by the interimpurity transitions only.

Acknowledgments

The work was partially supported by Russian Foundation for Basic Researches (Grants 97-02-18397, 96-02-19353) and Volkswagen-Stiftung (Gr. I/71162).

References

1. Shmelev, G.M., Nguen Xong Shon, Tsurkan, G.I. (1985) Photoinduced even acoustoelectrical effect, *Izv. Vuzov, Fizika* **28**, 84-87.
2. Baskin, E.M., Entin, M.V. (1988) The coherent photovoltaic effect, caused by the quantum corrections, *JETP Lett.* **48**, 601-603.
3. Entin, M.V. (1989) Theory of the coherent photovoltaic effect, *Sov. Phys. Semicond.* **23**, 664-667.
4. Zel'dovich, B.Ya., Chudinov, A.N. (1989) Interference of fields with frequencies ω and 2ω , *JETP Lett.* **50**, 439-441.
5. Baranova, N.B., Zel'dovich, B.Ya. (1991) Physical effects in optical fields with nonzero average cube, $\langle E^3 \rangle \neq 0$, *J. Opt. Soc. Am. B* **8**, 27-32.
6. Agafonov, V.L., Belinicher, V.I. (1992) The coherent photovoltaic effect on intraband and interband optical transitions *Sov. Phys.-Solid State* **34**, 2606-2610.
7. Sulimov, V.B. (1992) Theory of the coherent photovoltaic effect and method of nonequilibrium Green functions, *Sov. Phys. JETP* **74**, 932-947.
8. Atanasov, R., Hache, A., Hughes, J.L.P., van Driel, H.M., and Sipe J.E. (1996) Coherent control of photocurrent generation in bulk semiconductors, *Phys. Rev. Lett.* **76**, 1703-1706, and references therein.
9. Dianov, E.M., Kazansky, P.G. and Stepanov D.Yu. (1989) On the origin of photoinduced SHG in optical fibers, *Sov. J. Quantum Electron.* **16**, 887-888.
10. Balakirev, M.K., Smirnov, V.A. (1995) Observation of self-diffraction and refractive-index grating induced in a glass by mutually coherent optical fields E_ω and $E_{2\omega}$, *JETP Lett.* **61**, 544-548.
11. Balakirev, M.K., Vostrikova, L.J., Smirnov, V.A., and Entin, M.V. (1996) Relaxation of the optical density of glass modulated with bichromatic radiation, *JETP Lett.* **63**, 176-181.
12. Balakirev, M.K., Vostrikova, L.J., Smirnov, V.A. (1997) Photoelectric instability in oxide glass, *JETP Lett.* **66**, 809-815.
13. Shklovskii, B.I., Efros, A.L. (1984) *Electronic Properties of Doped Semiconductors* Springer-Verlag, Berlin, Heidelberg, New York, Tokyo.
14. Shklovskii, B.I., Fritzsch, H., Baranovskii, S.D. (1989) Electronic transport and recombination in amorphous semiconductors at low temperatures, *Phys. Rev. Lett.* **62**, 2989-2992.

HETERODYNING SCHEME EMPLOYING QUANTUM INTERFERENCE

J. B. KHURGIN,

Dept. of ECE, Johns Hopkins University Baltimore MD 21218

B. SAIF,

Swales Aerospace, 5050 Powder Mill Rd, Beltsville, MD 20705

B. SEERY,

NASA Goddard Space Flight Center, Seabrook MD 20705

We propose a fundamentally new method of heterodyne detection of FIR signals using quantum interference between one- and two-photon absorption. We suggest different implementations of the scheme using multiple QW detectors and evaluate its sensitivity.

Far-infrared range of electromagnetic radiation, extending roughly from 10 to 100 μm is of great interest for applications in the remote sensing, communications, and others. There are, however, formidable obstacles on the road to development of both sources and detectors of this radiation. While quantum-cascade lasers have been successful in operating at mid - IR, only incoherent emission has been achieved so far in injection-pumped intersubband schemes [1], and, so far, the most promising sources of THz radiation have been those obtained by beating two optical rays [2], [3].

As for the detection, the main problem is associated with large dark current and associated thermal noise in the detectors which significantly reduces detectivity of the system. It is well known, that the detectivity can be improved substantially in the coherent, or heterodyne schemes where the sensitivity can be pushed to its quantum limit, $h\nu\Delta\nu/\eta$ where $\Delta\nu$ is a signal bandwidth and η is quantum efficiency. This limit is achieved when shot (or generation-recombination) noise $\langle i_s \rangle^2$ produced by the local oscillator surpasses the shot noise due to the dark current and the Johnson noise. Heterodyne detection in the $10.6\mu m$ range, had been successfully implemented in Quantum Well Intersubband Detectors (QWIP's) [4],[5]

That is why a substantial effort had been directed towards development of the efficient local oscillators in the FIR range. But to this day, despite a substantial progress, no efficient and compact local oscillator technology had emerged, which, in our opinion, can be traced to the fact that the frequency of the FIR radiation is too low for the efficient emission of the radiation to take place that is, while the nonlinear polarization or current

at the frequency in the 1-10THz range is achievable, the extraction of power is difficult. Indeed, if the extraction of power is to be achieved by means of an antenna [3], the coupling efficiency is proportional to $\nu^{(4)}$. If, on the other hand one uses nonlinear optical means of power extraction, then, assuming perfect phasematching, the output efficiency is proportional to L/λ requiring for long FIR λ 's long propagation distances - which, given strong absorption of FIR in many materials is unrealistic.

It is therefore only natural to propose a different heterodyning scheme where local oscillator current (or polarization) is first generated intrinsically by mixing two local oscillators at near-IR frequencies $E(\nu_{L1})$ and $E(\nu_{L2})$ within the photodetector itself and is immediately mixed there with the FIR signal $E(\nu_{FIR})$ *without emitting FIR radiation*. Such approach of mixing three waves has been first implemented by Liu et al in [5] in a QWIP, where two CO_2 lasers with frequencies ν_{L1} and ν_{L2} have been used to produce a difference frequency photovoltage of about 40 GHz frequency, which subsequently have been mixed with an incoming microwave signal at $\nu_{\mu W} \sim 20\text{GHz}$ to produce an intermediate frequency GHz signal. The second mixing process essentially relied upon nonlinearity of the $I-V$ curve of the QWIP. The bandwidth of it is limited by the transit time of QWIP and, according to [5] cannot be extended beyond 100 GHz.

If one wants to extend the applicability of three-wave heterodyning to the THz domain, one should take advantage of faster nonlinearities, typically associated with bound, rather than with free charges and currents. From the nonlinear optical point of view this process is nothing but the third-order interference of one-photon absorption at ν_{L2} and two-photon absorption of ν_{L1} and ν_{FIR} resulting in a nonlinear photocurrent

$$J_{nonl}(\nu_{IF}) \sim \Im \left[\chi^{(3)}(\nu_{IF} = \nu_{L2} - \nu_{L1} - \nu_{FIR}) \right] \mathcal{E}(\nu_{L2})^* \mathcal{E}(\nu_{L1}) \mathcal{E}(\nu_{FIR}) \quad (1)$$

The fact that in multi-photon processes, the interference of different quantum-mechanical pathways results in a dependence of the medium response on the relative phases of the participating photons has been noticed as early as 1967 [6]. Experimentally, the effect of quantum-pathways interference was first demonstrated in Xe [[7]] photoionization experiments. with concept later extended to the photoionization of donor levels in semiconductors [8] and later to inter-band transitions in semiconductors. [9], [10]. We propose here to use this quantum interference process to generate a signal at intermediate frequency in the quantum well photoconductors or photodiodes and evaluate the potential performance of the proposed scheme.

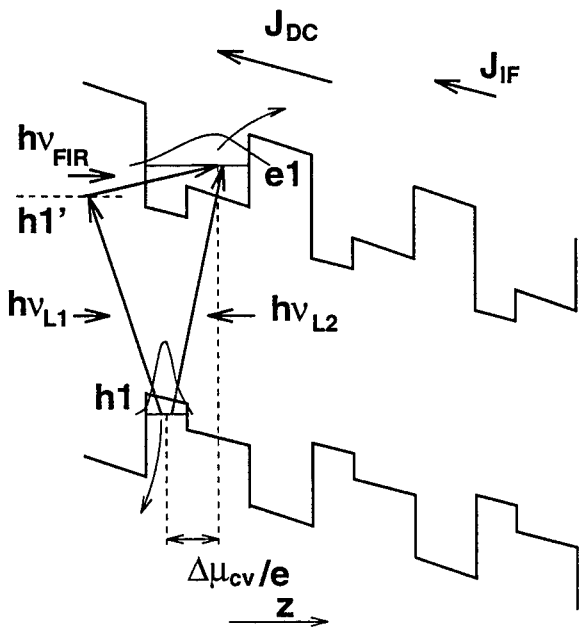


Figure 1: Quantum Interference Heterodyning Photodiode Scheme. h' is a virtual (dressed) level.

The first photodiode scheme is shown in Fig.1 and it consists of basically a "p-i-n" structure incorporating asymmetric QW's (although built-in asymmetry is not necessary since the wells are biased - our calculations have shown that one gains flexibility by using asymmetric QW's. The asymmetry results in a non-zero electric dipole matrix element

$$\Delta\mu_{cv} = -e \int (|\psi_{e1}(z)|^2 - |\psi_{h1}(z)|^2) dz \quad (2)$$

where $\psi_{e1}(z)$ and $\psi_{h1}(z)$ are the envelope wavefunctions of electron and heavy hole respectively. The transition energy between the two states is in resonance with the photon energy of the TE - polarized "local oscillator" $h\nu_{L2}$,

$$E_{e1}(k_{||} = 0) - E_{h1}(k_{||} = 0) \approx h\nu_{L2}, \quad (3)$$

where $k_{||}$ is the in-plane wavevector. The second TE - polarized "local oscillator" has a lower frequency ν_{L1} chosen in such a way that with the

TM - polarized signal at the FIR frequency ν_{FIR} the two-photon transition between the same states $e1$ and $h1$ is also nearly resonant

$$E_{e1}(\mathbf{k}_{||} = 0) - E_{h1}(\mathbf{k}_{||} = 0) \approx h\nu_{L1} + h\nu_{FIR} \quad (4)$$

One can evaluate the rate of the photo-excitation per well of an electron-hole pairs via single-photon excitation process

$$\begin{aligned} \frac{dN_{1p}}{dt}(z) &= \sum_{\mathbf{k}_{||}} \frac{\mu_{cv}^2 |\mathcal{E}_{L2}|^2}{2\hbar} \\ &\times \frac{\Gamma}{[E_{e1}(\mathbf{k}_{||}) - E_{h1}(\mathbf{k}_{||}) - h\nu_{L2}]^2 + \Gamma^2} = \alpha_{1p}(\nu_{L2}) \frac{I(\nu_{L2})(z)}{h\nu_{L2}} \end{aligned} \quad (5)$$

where Γ is a broadening, α_{1p} is the absorption coefficient per well, and $I(\nu_{L2})$ is a power-density. Integrating over the distance z and assuming the quantum efficiency η we obtain the familiar equation for the *DC* photo-current density.

$$J_{DC} = \eta e I(\nu_{L2}) / h\nu_{L2} \quad (6)$$

Let us now evaluate the rate of the photo-excitation per well of an electron-hole pairs via the interference of one- and two-photon processes

$$\begin{aligned} \frac{dN_{1p-2p}}{dt}(z) &= \sum_{\mathbf{k}_{||}} \frac{\mu_{cv}^2 \Delta\mu_{cv} \mathcal{E}_{L2} \mathcal{E}_{L1} \mathcal{E}_{FIR}}{4\hbar [E_{e1}(\mathbf{k}_{||}) - E_{h1}(\mathbf{k}_{||}) - h\nu_{L1}]} \\ &\times \frac{\Gamma \cos(2\pi\nu_{IF}t)}{[E_{e1}(\mathbf{k}_{||}) - E_{h1}(\mathbf{k}_{||}) - h\nu_{L2}]^2 + \Gamma^2} \\ &\approx \frac{1}{2} \alpha_{1p}(\nu_{L2}) \frac{\sqrt{I(\nu_{L2})I(\nu_{L1})}}{h\nu_{L2}} \times \frac{\Delta\mu_{cv} \mathcal{E}_{FIR}}{h\nu_{FIR}} \cos(2\pi\nu_{IF}t) \end{aligned} \quad (7)$$

Once again, integrating over the distance z we obtain the current density at the intermediate frequency

$$\begin{aligned} J(\nu_{IF}) &= \eta e \frac{\sqrt{I(\nu_{L1})I(\nu_{L2})I(\nu_{FIR})2\eta_{FIR}}}{h\nu_{L2}} \times \frac{\Delta\mu_{cv}}{h\nu_{FIR}} \\ &= J_{DC} \sqrt{\frac{I(\nu_{L1})}{I(\nu_{L2})}} \sqrt{I(\nu_{FIR})2\eta_{FIR}} \frac{\Delta\mu_{cv}}{h\nu_{FIR}} \end{aligned} \quad (8)$$

where $\eta_{FIR} = 377\Omega/n(\nu_{FIR})$ is the medium admittance at the FIR frequency.

We can now evaluate the signal-to-noise ratio of the proposed scheme under the assumption that $J_{DC} \gg J_{dark}$ to obtain.

$$\begin{aligned}
 \frac{S}{N} &= \frac{\langle J_{\nu_{IF}} A \rangle^2}{\langle 2eJ_{DC} A \Delta\nu \rangle} \\
 &= \frac{2\eta_{FIR} P(\nu_{L1}) \Delta\mu_{cv}^2}{A(h\nu_{FIR})^2} \frac{\nu_{FIR}}{\nu_{L1}} \frac{\eta P(\nu_{FIR})}{2h\nu_{FIR}\Delta\nu} \\
 &= \frac{P(\nu_{L1})}{P_{sat}} \frac{\nu_{FIR}}{\nu_{L1}} \frac{\eta P(\nu_{FIR})}{2h\nu_{FIR}\Delta\nu}
 \end{aligned} \tag{9}$$

where A is the detector area, and $P_{sat} = (h\nu_{FIR})^2 A / 2\eta_{FIR}\Delta\mu_{cv}^2$. For the minimum detectable signal one obtains

$$P(\nu_{FIR})_{min} = P(\nu_{FIR})_{QL} \frac{\nu_{L1}}{\nu_{FIR}} \frac{P_{sat}}{P(\nu_{L1})} \tag{10}$$

where $P(\nu_{FIR})_{QL} = 2h\nu_{FIR}\Delta\nu$ is the quantum limit of direct detection,

Let us assume that we are interested in the detection of radiation in the $100 \mu m$ range ($h\nu_{FIR} \sim 10 meV$). With quantum wells of about 200\AA the separation of the wavefunction of electron and a hole can be of the order of 150\AA , resulting in saturation intensities of $200 MW/cm^2$. Considering the smallest detector area to be of the order of λ^2 , we obtain the saturation power of the order of $10W$. Thus using a $1W$ semiconductor laser the minimum detectable power becomes about three orders of magnitude above the quantum limit. In any other type of detector, this performance can be approached only by cooling the detector below $4K$.

In order to better understand the physical origin of the effect discussed here, one can introduce the Rabi frequency of the detuned local oscillator field as $\Omega_{L1}^2 = 2\mu_{cv}^2 \eta_{L1} P(\nu_{L1}) / \hbar^2$ and re-write (10) as

$$P(\nu_{FIR})_{min} = \frac{\Omega_{L1}^2}{(2\pi\nu_{L1})^2} \times \frac{\eta_{FIR}\nu_{L1}\mu_{cv}^2}{\eta_{L1}\nu_{FIR}\Delta\mu_{cv}^2} \times P(\nu_{FIR})_{QL} \tag{11}$$

The first term in (11) indicates that a Rabi splitting and mixing occurs with a new dressed state $h1'$ having a fraction of the the upper state $e1$ mixed into it -

$$|h1'\rangle \approx |h1, N_{L1} + 1\rangle + \frac{\Omega_{L1}^2}{(2\pi\nu_{L1})^2} |e1, N_{L1}\rangle \tag{12}$$

where N_{L1} is the number of photons of frequency ν_{L1} . Due to non-zero $\Delta\mu_{cv}$, the transition from these state to the state $|e1, N_{L1}\rangle$ can take place and the heterodyning takes place by mixing the transition from the lower state with transition from the dressed state.

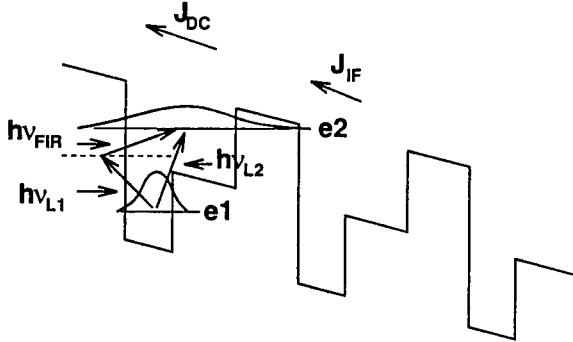


Figure 2: Intersubband Quantum Interference Heterodyning Scheme.

One can also consider a photoconductive scheme, using, for example intersubband transitions with confined [11] or unconfined [12] states. Such scheme is shown in Fig.2 and it holds two-fold advantage over the band-to-band photodiode described above: photoconductive gain and the lower requirement for the local oscillator power (which is proportional to its photon energy $h\nu_{L1}$). On the other hand, lowering $h\nu_{L1}$ would also result in the increase in dark current, so, for a given temperature and signal levels there must exist some optimal wavelength for the local oscillator.

It is important to establish the limits of the applicability of the scheme. The minimum FIR frequency is limited by the broadening of the transitions, i.e. realistically lies near 1THz. The maximum FIR frequency is determined by the decrease in output level in (8) with the increase in detuning, and it probably extends to the 10-30 THz, where conventional IR detectors can operate.

The schemes described above have a problem with large dark current. This problem can be circumvented by using the coherent photo-voltaic effect [9],[10],[13]). From the nonlinear optical point of view this process can be described by the presence of nonlinear conductivity resulting in a nonlinear photocurrent

$$J_{nonl}(\nu_{IF}) \sim \Im \left[\sigma^{(3)}(\nu_{if} = \nu_{L2} - \nu_{L1} - \nu_{FIR}) \right] \mathcal{E}(\nu_{L2})^* \mathcal{E}(\nu_{L1}) \mathcal{E}(\nu_{FIR}) \quad (13)$$

The proposed scheme consists simply of an unbiased bulk neutral semiconductor or a quantum well (single or multiple) with ohmic contacts. Since

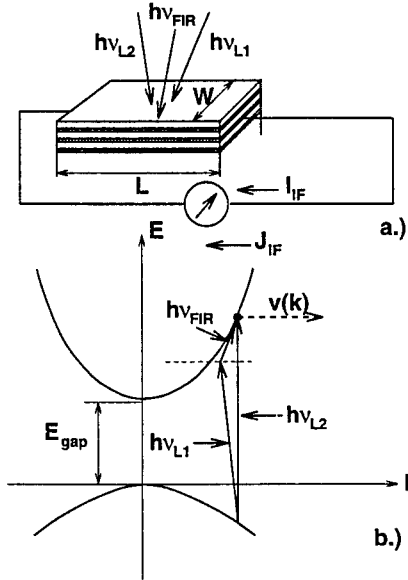


Figure 3: Heterodyning using coherent photovoltaic effect a.) Geometry
b.) Band Diagram

the excitation takes place above the band gap it is desirable to avoid the surface effects and it is a quantum well scheme that is considered here and shown in Fig.3. The two near-IR or visible local oscillators are both TE polarized and have above-the-gap photon energies ν_{L2} and ν_{L1} . We analyze this scheme following earlier for [9]. The carriers of a given in-plane wavevector \mathbf{k}_i can be generated by either a single-photon absorption

$$\frac{dN_{1p}(\mathbf{k})}{dt}(z) = \sum_{i=1,2} \frac{e^2 P_{cv}^2 |\mathcal{E}_{Li}|^2}{2\hbar m_0^2 \omega_{Li}^2} \frac{\Gamma}{[E_{e1}(\mathbf{k}) - E_{h1}(\mathbf{k}) - \hbar\omega_i]^2 + \Gamma^2} \quad (14)$$

where $E_{e1}(\mathbf{k})$ and $E_{h1}(\mathbf{k})$ is the energy of the state lowest conduction or heavy-hole band with the in-plane wave-vector \mathbf{k} , P_{cv} is the matrix element of the inter-band transition and Γ is a broadening, or by a combination of a single and two-photon absorption

$$\begin{aligned} \frac{dN_{1p-2p}(\mathbf{k})}{dt} &= \sum_{i=1,2; j \neq i} \frac{e^3 P_{cv}^2 \mathcal{E}_{Li} \mathcal{E}_{Lj} (\mathbf{k} \cdot \vec{\mathcal{E}}_{fir}) (\omega_{L1} \omega_{L2} \omega_{fir})^{-1}}{4m_0^2 m_r [E_{e1}(\mathbf{k}) - E_{h1}(\mathbf{k}) - \hbar\omega_j]} \\ &\times \frac{\Gamma \cos(2\pi\nu_{IF}t)}{[E_{e1}(\mathbf{k}) - E_{h1}(\mathbf{k}) - \hbar\omega_i]^2 + \Gamma^2} \end{aligned} \quad (15)$$

where m_r is the in-plane reduced effective mass. Performing the summation over the wavevectors we find out the density of the photo-carriers

$$N_{1p} = \sum_{i=1,2} \frac{m_r e^2 P_{cv}^2 \eta_{fir}}{E_{gap} m_0^2} \frac{I(\nu_{Li})}{\hbar \omega} \tau_r = \sum_{i=1,2} \alpha \frac{I(\nu_{Li})}{\hbar \omega_{Li}} \tau_r \quad (16)$$

where α is the absorption coefficient (per well), I_{Li} is local oscillator power density, and τ_r is recombination time. At the same time, there will be directional photocurrent density along the polarization direction of the FIR field, say x .

$$\begin{aligned} J_x(\nu_{IF}) &= -\frac{e\hbar}{m_r} \sum_{\mathbf{k}} k_x \frac{dN_{1p-2p}(\mathbf{k})}{dt} \tau_s \\ &= -\frac{e}{2} \alpha \sqrt{\frac{I(\nu_{L1})I(\nu_{L2})}{\hbar^2 \omega_{L1} \omega_{L2}}} \sqrt{2\eta_{fir} I(\nu_{FIR})} \frac{e}{m_r \omega_{fir}} \frac{\tau_s}{\sqrt{1 + \tau_s^2 \omega_{IF}^2}} \\ &\approx \frac{e}{4} N_{1p} \sqrt{2\eta_{fir} I(\nu_{FIR})} \frac{e}{m_r \omega_{fir}} \frac{\tau_s}{\tau_r} \end{aligned} \quad (17)$$

where $\eta_{fir} = 377\Omega/n(\nu_{FIR})$ is the medium impedance at the FIR frequency, τ_s is the momentum relaxation time, determined by combination of electron-electron and phonon scatterings and we assume $\omega_{IF} \ll \tau_s^{-1}$. We shall now determine the noise in the detector. There will be two sources of noise: a) thermalized photo-excited carriers giving the Johnson noise

$$\langle i_T^2 \rangle = \frac{4k_B T \Delta \nu}{R} = 4 \left[\frac{P(\nu_{L1})}{h\nu_{L1}} + \frac{P(\nu_{L2})}{h\nu_{L2}} \right] e^2 \Delta \nu \times \frac{\tau_s \tau_r}{\tau_t^2} \quad (18)$$

where $\tau_t = L\sqrt{m_r/k_B T}$ is a time that it would take a thermalized carrier to transit the length L of the detector in the absence of scattering. b) generation-thermalization noise associated with the ballistic photo-excited carriers. This noise arises because when the carrier is photo-excited by the above-the-gap radiation via the single photon absorption, it has a randomly directed ballistic velocity. Although the average current carried by all those carriers is obviously zero, their random generation and random thermalization in the band result in the noise

$$\langle i_B^2 \rangle = \left[\frac{P(\nu_{L1})}{h\nu_{L1}} + \frac{P(\nu_{L2})}{h\nu_{L2}} \right] e^2 \Delta \nu \frac{\tau_s^2}{\tau_b^2} \quad (19)$$

where $\tau_b = L\sqrt{m_r/k_B T_e}$ is a transit time of the average ballistic carrier, and $T_e = (h\nu_{L1}/2 + h\nu_{L2}/2 - E_{gap})/k_B$ is the average ballistic electron

temperature. The ratio of two types of noise is then can be written as

$$\frac{\langle i_T^2 \rangle}{\langle i_B^2 \rangle} = \frac{\tau_r T}{\tau_s T_e} \quad (20)$$

It is clear that in pure intrinsic semiconductors at room temperature $\tau_r \sim 10^{-10} s$, $\tau_s \sim 10^{-13} s$, $T \sim 300 K$, $T_e \sim 10^2 - 10^4 K$, the thermal noise dominates. On the other hand, if one can significantly reduce the recombination time using either low-temperature grown semiconductors [3] or heavily-doped material and cool the detector, the generation-thermalization noise will dominate. To calculate total current at ν_{IF} we sum over all the quantum wells to obtain and multiply by the width of the detector W to obtain, assuming that $P(\nu_{L1}) = P(\nu_{L2})$,

$$\frac{S}{N}|_B = \frac{(\alpha^{-1} J_x(\nu_{IF}) W)^2}{\langle i_B^2 \rangle} = \frac{1}{4} \frac{P(\nu_{FIR})}{2h\nu_{FIR}\Delta\nu} \frac{h\nu_{FIR}}{k_B T_e} \frac{P(\nu_{L1})}{A h\nu_{L1}} \frac{e^2 \eta_{fir}}{m_r \omega_{fir}^2} \quad (21)$$

where A is the detector area, for the case when generation-thermalization noise dominates, and

$$\frac{S}{N}|_T = \frac{(\alpha^{-1} J_x(\nu_{IF}) W)^2}{\langle i_B^2 \rangle} = \frac{1}{4} \frac{P(\nu_{FIR})}{2h\nu_{FIR}\Delta\nu} \frac{h\nu_{FIR}}{k_B T} \tau_s \tau_r \frac{P(\nu_{L1})}{A h\nu_{L1}} \frac{e^2 \eta_{fir}}{m_r \omega_{fir}^2} \quad (22)$$

for the case of the Johnson noise dominance. For the minimum detectable signal one obtains

$$P(\nu_{FIR})_{min} = P(\nu_{FIR})_{QL} \frac{P_{sat}}{P(\nu_{L1})} \quad (23)$$

where

$$P_{sat} = \begin{cases} \frac{4A h\nu_{L1} m_r \omega_{fir}^2}{e^2 \eta_{fir}} \frac{k_B T}{h\nu_{FIR}} \frac{\tau_r}{\tau_s} & -Johnson\ noise \\ \frac{4A h\nu_{L1} m_r \omega_{fir}^2}{e^2 \eta_{fir}} \frac{k_B T_e}{h\nu_{FIR}} & -generation-thermalization\ noise \end{cases} \quad (24)$$

Let us assume that we are interested in the detection of radiation in the $100 \mu m$ range ($h\nu_{FIR} \sim 10 meV$). Considering the smallest detector area to be of the order of λ^2 , temperature of $77 K$, and ratio of $\tau_r/\tau_s \sim 10$ for low temperature grown GaAs, we can see that the detectivity is limited by the Johnson noise and $P_{sat} \sim 10^4 W$. On the other hand cooling to $4 K$ would produce the detector limited by the generation-thermalization noise with $P_{sat} \sim 10^3 W$

With 1W semiconductor laser we may just achieve the detectivity three-to-four orders of magnitude worse than quantum limit. This is not bad considering the fact that the speed of the detector is limited by the momentum relaxation time, i.e. it is essentially sub-picosecond.

In conclusion, we have proposed two fundamentally new techniques for detection of FIR signals using quantum interference and estimated its sensitivity and limits in various implementations.

This work is supported by AFOSR and NASA

References

- [1] B. Xu, Q. Hu, and M.R. Melloch, *Appl. Phys. Lett.*, **71**, 440 (1997)
- [2] H. G. Roskos, M. C. Nuss, J. Shah, K. Leo, D. A. B. Miller, A. M. Fox, S. Schmitt-Rink and K. Kohler, *Phys. Rev. Lett.*, **68**, 2216 (1992)
- [3] S. Verghese, K. A. McIntosh and E. R. Brown *Appl. Phys. Lett.*, **71**, 2743 (1997)
- [4] H. C. Liu, G. E. Jenkins, E. R. Brown, K. A. McIntosh, K. B. Nichols, and M. J. Manfra, *IEEE Electron Device Lett.*, **16**, 253 (1995)
- [5] H. C. Liu, J. Li, E. R. Brown, K. A. McIntosh, K. B. Nichols, and M. J. Manfra, *Appl. Phys. Lett.*, **67**, 1594 (1997)
- [6] E. A. Manykin and A. M. Afanas'ev, *Sov. Phys. JETP* **25**, 828 (1967)
- [7] J. C. Miller, R. N. Compton, M. G. Payne, W. W. Garret *Phys. Rev. Lett.*, **45**, 114 (1980)
- [8] G. Kurizki, M. Shapiro, P. Brumer, *Phys. Rev. B*, **39**, 3435 (1989)
- [9] J. B. Khurgin, *J. Nonlinear Opt. Phys. Mater.*, **4**, 163 (1995)
- [10] R. Atanasov, A. Hache, J. L. P. Hughes, H. M. van Driel, and J. E. Sipe, *Phys. Rev. Lett.*, **76**, 1703 (1996)
- [11] J. B. Khurgin and S. Li, *Appl. Phys. Lett.*, **62**, 126 (1993) i
- [12] S. Li and J. B. Khurgin, *J. Appl. Phys.* **73**, 4367 (1993)
- [13] A. Hache, Y. Kostoulas, R. Atanasov, J. L. P. Hughes, J. E. Sipe, H. M. van Driel, *Phys. Rev. Lett.*, **78**, 306 (1997)

GENERATION OF WIDELY TUNABLE THz-WAVE USING NONLINEAR OPTICS

KODO KAWASE and HIROMASA ITO

Res. Inst. of Electrical Communication, Tohoku University,
2-1-1 Katahira, 980-8577, Japan

Abstract. We had recently demonstrated a room temperature operated widely tunable THz-wave generation (frequency : 0.9-2.1THz, wavelength : 140-310 μ m) introducing a Si prism coupler onto a LiNbO₃ crystal which was pumped by a Q-switched Nd:YAG laser. The process involved is an optical parametric oscillation (OPO) utilizing the polariton mode scattering of LiNbO₃. This tunable THz-wave source was applied to the problem of differential imaging. In a proof-of-concept experiment, we optically tagged objects embedded in a shade and measured the difference between transmittance at two wavelengths. The image of a tagged object was emphasized in comparison with that of an untagged objects. Differential THz imaging has not been reported previously, to our knowledge, mainly because of the lack of convenient tunable THz-wave sources. It seems possible to use dual-wavelength differential transmittance spectroscopy in the THz-wave region to monitor the gases in the industry.

1. Introduction

The development of coherent and tunable THz-wave radiation is one of the great interest, because of an abundance of excitations in molecular systems and condensed media, as well as the future ultra-high frequency communication studies which bridge the gap between the optical waves and microwaves. Soon after the invention of the laser, many pioneering works have been carried out on nonlinear optics, which includes the tunable submillimeter wave generation using nonlinear difference frequency mixing between two laser sources, though the conversion efficiency observed was poor[1,2]. Higher conversion efficiency was obtained by simultaneous Raman and parametric oscillation, utilizing the polariton mode scattering of LiNbO₃ [3-5]. However, these efforts ended in the mid 1970's, mainly due to the invention of molecular gas submillimeter lasers. During the past several years, THz-wave generation and detection have attracted much attention from both the fundamental and applied points of view. Most studies have utilized ultrabroad bandwidth characteristics of the mode-locked subpicosecond laser pulses with the sacrifice of their temporal coherence[6-9]. In contrast, we have demonstrated a coherent and widely tunable THz-wave generation by LiNbO₃ OPO, introducing a new coupling method for the THz-wave into the system to

drastically improve the efficiency [10-12]. Further, we have recently obtained more than one hundred times higher efficiency by cryogenic cooling[13]. In this paper, characteristics of this THz-wave source are reviewed as well as reporting the result of differential imaging.

2. Principle of operation

This scheme is based on an optical parametric oscillation (OPO) utilizing the lowest A_1 -symmetry polariton mode of LiNbO_3 and the contribution of both second and third order nonlinearities[5]. The stimulated radiation results from a parametric process to create a photon at THz frequency (ω_T) and a near infrared photon (ω_i ; idler), where the input pump photon of frequency ω_p with the energy conservation of $\omega_p = \omega_T + \omega_i$. In this parametric process, coherent excitation of the polariton mode is essential, where the momentum of the interacting waves are conserved noncollinearly ($\mathbf{k}_p = \mathbf{k}_T + \mathbf{k}_i$) as shown in the inset of Fig. (1). Wide tunability is obtained by slightly changing the angle ϕ between the pump and the idler. At the same time the angle δ of the generated THz-wave inside the crystal changes. In order to get the oscillation, the feedback at the idler wavelength ($\sim 1.07\mu\text{m}$) is necessary as shown in Fig. (1). Although the interaction between waves occurred by the stimulated oscillation, most of the generated THz-wave is absorbed or totally reflected inside the crystal due to the material's large absorption coefficient and its large refractive index (5.2 at the THz range). We have recently reported the uni-directional THz-wave radiation using a prism coupling method as shown in Fig. (1). The phase matching angle δ changes inside the crystal, though the radiation angle θ inside the prism is almost constant due to the ultra low dispersion characteristics of Si at THz range, as well as the relation between the refraction at the interface and phase matching relation. Therefore the direction of emitted THz-wave outside the prism is almost fixed for the entire tuning range.

The experimental setup is shown in Fig. (1). A 5mm-thick LiNbO_3 z-plate was cut to a dimension of $70(x) \times 10(y) \times 5(z)$ (mm^3). Two end-surfaces in the x-plane were cut parallel, polished and anti-reflection (AR) coated for operation at $1.07\mu\text{m}$. The y-surface was also polished flat in order to minimize the coupling gap between the prism base and the crystal surface. High resistivity Si ($\rho > 1000\Omega \cdot \text{cm}$, $\alpha \equiv 0.6\text{cm}^{-1}$) was chosen for fabricating the prism. The Si-prism was prepared with a length of 10mm along the base, and a prism angle of 39deg. so that the THz-wave would emerge normal to the prism exit surface. The prism base was slightly pressed with an adjustable spring against the LiNbO_3 crystal to maximize the coupling efficiency. The crystal with the prism was placed inside the cavity which was resonated at an idler wave using two high-reflection mirrors, M1 and M2. Both mirrors were half-area coated, so that only the idler wave could resonate and the pump beam propagate through the uncoated area without scattering or reflection. The pump source used was a Q-switched Nd:YAG laser whose electric field was along the z-axis of the LiNbO_3 crystal. The pump power, pulse width, and repetition rate were 13mJ/pulse, 10nsec, 16.7Hz, respectively. The

pump beam entered the x-surface of the crystal and traversed the LiNbO_3 crystal in proximity to the y-surface.

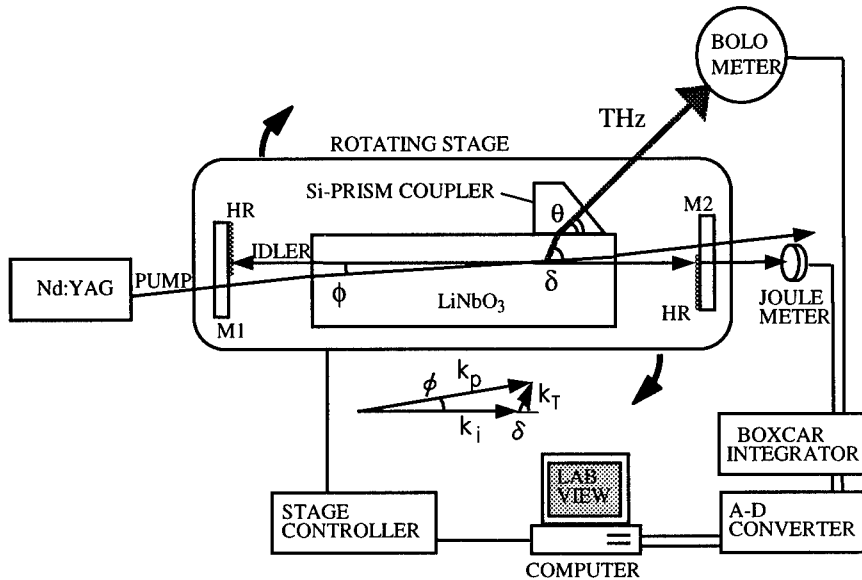


Figure 1. Experimental cavity arrangement for the THz-wave radiation utilizing a Si-prism coupler on the LiNbO_3 crystal.

3. Characteristics of THz-wave Generation

By varying the incident angle of the pump beam from 1 to 2 deg., the angle ϕ between the pump and idler inside the crystal was changed from approximately 0.5 to 1 deg. as shown in Fig. (2). As the phase matching angle was tuned, the idler and the THz wavelengths varied from $1.068\text{-}1.072\mu\text{m}$ and $310\text{-}140\mu\text{m}$, respectively. The angle δ between the idler and THz-wave inside the crystal changed from 64.9 to 65.8 deg. The observed THz-wave beam was directed to $\theta \approx 51\text{deg.}$, and had an approximately Gaussian cross section with an e^{-2} power radius of 5mm at the distance of 50cm away from the prism. An aperture was placed at this position as a spatial filter, and a 4.2K Si-bolometer was placed behind the aperture to detect the transmitted THz-wave. The measured direction angle θ agreed with the theoretical value.

The signal wavelength and its linewidth were measured by a scanning Fabry-Perot etalon consisting of two metal mesh plates. Fig. (3) shows an example of the measurement. The displacement of one of the metal mesh plates corresponds directly to a half of the wavelength. The free spectral range (FSR) of the etalon was about 83GHz, and the linewidth was measured to be $\geq 15\text{GHz}$. It is expected that the linewidth will be dramatically narrowed by introducing the quasi-phase-matching method using a domain inverted structure[14]. The polarization characteristics of the

THz-wave was analyzed by a wire grid polarizer, and it was linearly polarized along the z-axis of the crystal.

The signal output from the Si prism coupler was measured to be about 3mW with a pump power of 14mJ/pulse. This is almost three orders more efficient than the angled surface coupling. The input-output characteristics are shown in Fig. (4). We further investigated the cryogenic characteristics of THz output. With the same experimental setup as shown in Fig. (1), the LiNbO₃ crystal was placed inside a cooling dewar which can cool the crystal down to liquid N₂ temperature. We achieved 125 times higher THz output at 78K, compared to that obtained at room temperature, and the threshold pump power decreased 32%. These results were due to the increase of the gain coefficient as well as the decrease of the absorption coefficient of the THz wave in the crystal, and a small change of these coefficients leads to a hundred time enhancement of the THz output.

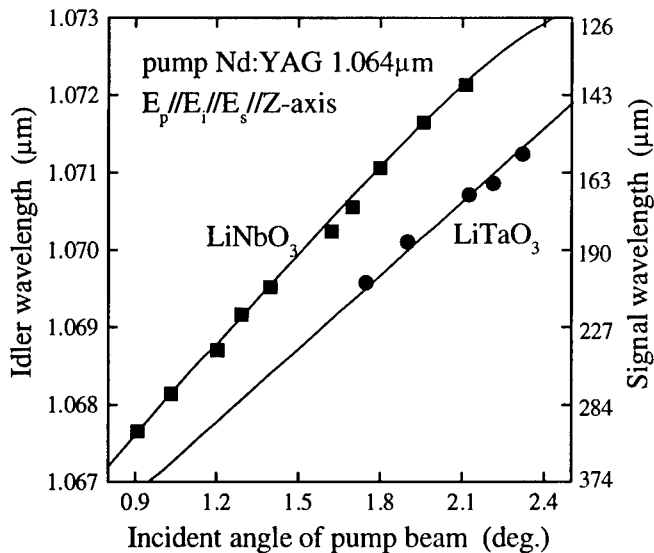


Figure 2. The tuning characteristic between the incident angle of the pump to the x-surface of the crystal normal and THz wavelength. Solid curve indicates the calculated tuning curve.

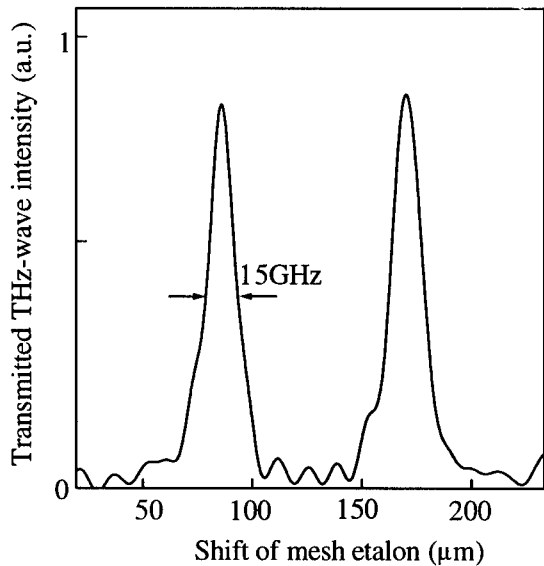


Figure 3. Example of the wavelength and linewidth measurement using the scanning Fabry-Perot etalon consisting of metal mesh plates.

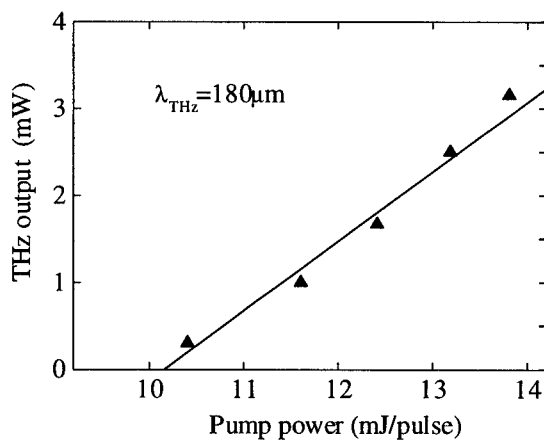


Figure 4. The input-output characteristic of the oscillator.

4. Differential Imaging

In Fig. (5), the THz-wave was focused with a TPX lens ($f=30\text{mm}$) on the imaging target, and the transmitted intensity was measured by a Si-bolometer. The imaging target was scanned by a x-z stage up to $20\times20\text{mm}$. The rotating stage, x-z stage, and data acquisition were controlled by a Labview system. The spatial resolution of our imaging system was measured as almost $500\mu\text{m}$ by imaging an Al-grid deposited on a GaAs wafer. We then demonstrated that differential imaging between two wavelengths emphasized the image of a tagged object with an absorption coefficient dependent on wavelength. In Fig. (6), the transmittance spectra for a metal mesh (Ni, $65\mu\text{m}$ grid) and for copy paper are shown. The wavelength dependence of transmittance is large for the metal mesh, and less for the copy paper. We cut out "L" shapes from the metal mesh and the copy paper, and hide them in an envelope. Their images were measured with one wavelength ($\lambda=180\mu\text{m}$) as shown in Fig. (7a), and both "L" shapes were clearly imaged. On the other hand, the differential image between two wavelength ($\lambda=180\mu\text{m}$, and $220\mu\text{m}$) was obtained as shown in Fig. (7b), and only the left "L" (metal mesh) was emphasized. Next, we had demonstrated that the difference in thickness of the shades can be eliminated by differential imaging. In Fig. (8a), both "L" shapes were cut out from the metal mesh. The left "L" was covered by two sheets of papers though the right "L" was covered by one sheet of paper. The difference in thickness of the paper is obviously shown in Fig. (8a) using one wavelength ($\lambda=180\mu\text{m}$). On the other hand, the difference was clearly eliminated by differential imaging using two wavelengths ($\lambda=180\mu\text{m}$, and $220\mu\text{m}$) as shown in Fig. (8b). These results mean that the image of a tagged object embedded in an inhomogeneous medium can be extracted by this method.

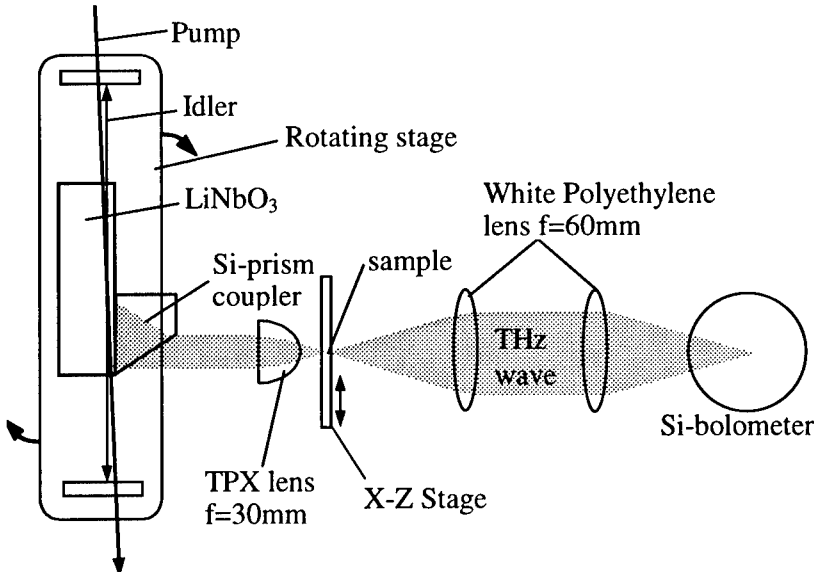


Figure 5. Experimental setup for differential THz imaging.

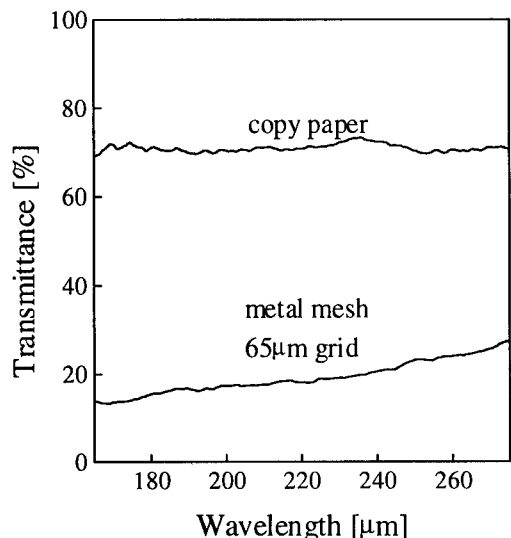


Figure 6. The transmittance spectra for a metal mesh (Ni, 65 μ m grid) and for copy paper. The wavelength dependence of transmittance is large for the metal mesh, and less for the copy paper.



Figure 7. (a) THz imaging of metal mesh (left L) and copy paper (right L) with one wavelength ($\lambda=180\mu\text{m}$). (b) Differential THz imaging between two wavelengths ($\lambda=180\mu\text{m}$, and $220\mu\text{m}$).

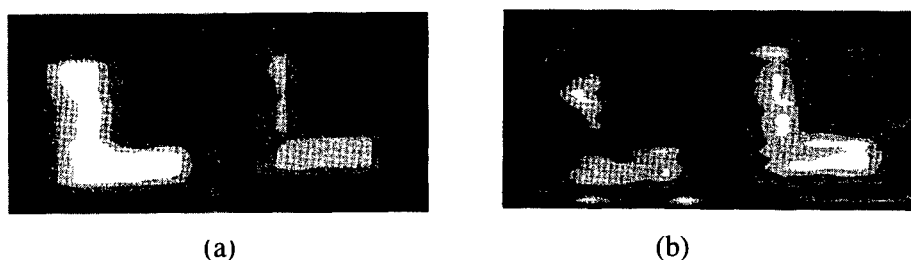


Figure 8. Both "L" shapes were cut out from the metal mesh. The left "L" was covered by two sheets of papers though the right "L" was covered by one sheet of paper. (a) THz imaging using one wavelength ($\lambda=180\mu\text{m}$). (b) Differential imaging between two wavelengths ($\lambda=180\mu\text{m}$, and $220\mu\text{m}$).

5. Conclusion

We have demonstrated efficient THz-wave generation from LiNbO₃ OPO using a Si-prism coupler. Measurements on its radiation characteristics and cryogenic cooling have been accomplished, proving this method to be suitable for various application fields. These include spectroscopy, THz imaging, gas monitoring, biological applications, and so forth. For tunable THz-wave applications, the simplicity of the wave source is an essential requirement since cumbersome systems do not encourage new experimental thoughts and ideas. Compared with the available sources, the present parametric method has significant advantages in compactness, tunability, and ease of handling.

The author is greatly indebted to C. Takyu for his excellent coating on the crystal surfaces and mirrors, and T. Shoji for his excellent polishing of nonlinear crystals. This work was partly supported by the Research Foundation for Opt-science and Technology.

References

1. Zernike, Jr., and P. R. Berman, Phys. Rev. Lett. **15**, 999 (1965).
2. R. Morris and Y. R. Shen, Phys. Rev. A **15**, 1143 (1977).
3. J. M. Yarborough, S. S. Sussman, H. E. Puthoff, R. H. Pantell, and B. C. Johnson, Appl. Phys. Lett. **15**, 102 (1969).
4. B. C. Johnson, H. E. Puthoff, J. SooHoo, and S. S. Sussman, Appl. Phys. Lett. **18**, 181 (1971).
5. M. A. Piestrup, R. N. Fleming and R. H. Pantell, Appl. Phys. Lett. **26**, 418 (1975).
6. P. R. Smith, D. H. Auston, and M. C. Nuss, IEEE J. Quantum Electron. **24**, 255 (1988).
7. M. van Exter and D. Grischkowsky, IEEE Trans. Microwave Theory Tech. **38**, 1684 (1990).
8. M. C. Nuss and J. Orenstein, in *Millimeter-Wave Spectroscopy of Solids*, G. Gruener, Ed. ' Heidelberg, Germany: Springer-Verlag (1997).
9. D. M. Mittleman, R. H. Jacobsen, and M. C. Nuss, IEEE J. Selected Topics in Quantum Electron. **2**, 679 (1996).
10. K. Kawase, M. Sato, T. Taniuchi, and H. Ito, Appl. Phys. Lett. **68**, 2483 (1996).
11. K. Kawase M. Sato, T. Taniuchi, and H. Ito, Int. J. Infrared Millimeter Waves **17**, 1839 (1996).
12. K. Kawase, K. Nakamura, M. Sato, T. Taniuchi, and H. Ito, Appl. Phys. Lett. **71**, 753 (1997).
13. J. Shikata, K. Kawase, T. Taniuchi, and H. Ito, to be submitted to Appl. Phys. Lett.
14. K. Kawase and H. Ito, Nonlinear Optics **7**, 225 (1994).
15. K. Kawase and N. Hiromoto, Applied Optics **37**, 1862 (1998).

Addresses of Participants

Thierry Amand
Laboratoire de Physique de la Matiere Condensee, CNRS-UMR 5830
Institut National des Sciences Appliquees
Departement de Genie Physique
Complexe Scientifique de Rangueil
31077 Toulouse cedex 4, FRANCE
Tel.:+33 (0)5 61 55 96 34
Fax.:+33 (0)5 62 17 18 50
e-mail: amand@insa-tlse.fr

M. K. Balakirev
Institute of Semiconductor Physics
Russian Academy of Sciences
Siberian Branch
Prosp. Lavrentyeva, 13
Novosibirsk, 630090
RUSSIA
E-mail:Balak@isp.nsc.ru

Rudolf H Binder
Optic Sci Ctr
Univ of Arizona
Tucson AZ 85721
Phone (520) 621-2892
Fax (520) 621-6778
Email binder@argonaut.opt-sci.arizona.edu

Paul W Brumer
Dept of Chem
Univ of Toronto
Toronto ON M5S 3H6 Canada
Phone 416 975 3569
Email pbrumer@tikva.chem.utoronto.ca

Hui Cao, Ph.D.
Assistant Professor
Dept. of Physics & Astronomy, Northwestern University
2145 Sheridan Road, Evanston, IL 60208
Tel: (847) 467-5452 Fax: (847) 491-9982
Email: h-cao@nwu.edu

Dimitrios Charalambidis
University of Crete, Physics Department
and
FO.R.T.H.-I.E.S.L.
P.O. Box 1527, 711 10 Heraklio, Crete, Greece

Tel.: +30-81-391464
Fax: +30-81-391318
e-mail: chara@iesl.forth.gr

Shun Lien Chuang
Dept of Elec & Comp Engr
UIUC
1406 W Green St
Urbana IL 61801
Phone (217) 333-3359
Fax 217 333 5701
Email s-chuang@uiuc.edu

David Scott Citrin
Dept of Phys
Washington State Univ
Pullman WA 99164-2814
Phone (509) 335-3698
Fax (509) 335-7816
Email citrin@wsu.edu

P. B. Corkum,
Steacie Institute for Molecular Sciences
National Research Council of Canada
Ottawa, Ontario, Canada K1A 0R6.
e-mail: paul.corkum@nrc.ca

Supriyo Datta
Sch of Elec Engr
Purdue Univ
West Lafayette IN 47907-1285
Phone (317) 494-3511
Fax 317 494 6440
Email DATTA@ECN.PURDUE.EDU

Daniel Elliott
1285 Elec Engr
Purdue Univ
West Lafayette IN 47907
Phone (765) 494-3442
Fax (765) 494-6951
Email ELLIOTTD@ECN.PURDUE.EDU

Matvey Vul'fovich Entin Institute of Semiconductor Physics
Siberian Branch
Russian Academy of Sciences
Novosibirsk 630090, Russia.
Fax:007-383-2-332-771,

e-mail: entin@isp.nsc.ru

Robert J Gordon
Dept of Chem MC 111
Univ of Illinois
845 W Taylor St
Chicago, IL 60607-7061
Phone (312) 996-3280
Fax (312) 996-0431
Email rjgordon@uic.edu

Martin Holthaus
Universitaet Marburg
FB Physik
D-35032 Marburg
fx: 01106421284511

Xuedong Hu
432 S Clinton #B2
Oak Park, IL 60302
Phone (312) 996-3407
Fax (312) 996-9016
Email xuh@uic.edu

Misha Ivanov
Femtosecond Program,
Steacie Institute for Molecular Sciences
NRC of Canada, 100 Sussex Drive, room 2069,
Ottawa, Ontario K1A 0R6, Canada
phone: (613)-993-9973
NEW (!!) fax: (613)-991-3437
e-mail: ivanov@ned1.sims.nrc.ca,
misha.ivanov@nrc.ca

Kodo Kawase
Applied Physics
Tohoku Gakuin University
Katahira
Sendai 980-77
Japan
kawase@tjxx.tohoku-gakuin.ac.jp

Peter Kocevar
Inst. Theoretische Physik
Universitaet Graz
Universitaetsplatz 5
A-8010 Graz
Austria

Tilmann Kuhn
Inst. f. Theor. Physik
Universitaet Muenster
D-48149 Muenster
Germany
kuhnti@nwz.uni-muenster.de

Jacob B. Khurgin
Department of Electrical and Computer Engineering
Johns Hopkins University
Baltimore MD 21218
(410) 516 7518
(410) 516 8380
Fax (410) 516 5566
jbk@doomsday.ece.jhu.edu

P P Lambropoulos
Max-Planck Inst for Quantenoptik
Hans-Kopfermann Str 1
D-85748 Garching, Germany
Email labro@mpq.mpg.de
Homepage www.mpq.mpg.de

Falk Loeser
Institut fuer Angewandte Photophysik
Technische Universitaet Dresden
D-01062 Dresden
Ph: +49-351-463-4389, Fax: +49-351-463-7065

Dmitri E. Nikonov
Assistant Research Engineer
Department of Electrical and Computer Engineering
University of California
Santa Barbara, CA 93106-9560
phone (805) 893-7682
fax (805) 893-3262
dmitri@quantum.ece.ucsb.edu

Ted Norris
Center for Ultrafast Optical Science
University of Michigan
2200 Bonisteel Blvd.
Ann Arbor, MI 48109-2099
734-764-9269
tnorris@eecs.umich.edu

Wolfgang Porod
Dept of Elec Engr

Univ of Notre Dame
Notre Dame IN 46556
Phone (219) 631-6376
Fax 219 631 4393
Email wolfgang.porod@nd.edu

Herschel A Rabitz
Dept of Chem
Princeton Univ
129 Frick Lab
Princeton NJ 08544-1009
Phone (609) 258-3917
Fax (609) 258-6746
Email hrabitz@chembax.princeton.edu

F. Rossi
Univ. di Modena
Dipartimento di Fisica
I-41100 Modena
FX: 0113959367488

Marlan O Scully
Phys Dept
Texas A&M Univ
College Station TX 77843-4242
Phone (409) 862-2333
Fax 409 845 2590

Tamar Seideman
National Research Council of Canada
100 Sussex Drive
Ottawa, Ontario K1A 0R6
(613) 990-0945
(613) 947-2838
tamar.seideman@nrc.ca

John Edward Sipe
Dept of Phys
Univ of Toronto
Toronto ON M5S 1A7 Canada
Phone 416 978 4517
Fax 416 978 2537
Email sipe@physics.utoronto.ca

Arthur L Smirl
Photonics Lab
Univ of Iowa
100 IATL

Iowa City IA 52242-1000
Phone (319) 335-4580

Henry M van Driel
Dept of Phys
Univ of Toronto
Huron and Russell
Toronto ON M5S 1A1 Canada
Phone (416) 978 4200
Fax 416 978-5848
Email vandriel@physics.utoronto.ca

Mathias Wagner
Cavendish Lab
Hitachi Cambridge Lab
Madingley Rd
Cambridge C83 0HE
England
Phone 865 272338
Fax 865 272400

A. M. Weiner
School of Elec Engr
Purdue Univ
1285 Elec Engr Bldg
West Lafayette IN 47907-1285
Phone (765) 494-5574
Fax (765) 494-6951
Email amw@ecn.purdue.edu

Coherent Control in Atoms, Molecules, and Semiconductors

Proceedings of an International Workshop
held in Chicago, USA, 19-22 May 1998

Walter Pötz and W. Andreas Schroeder (Eds.)

This volume contains the Proceedings of the International Workshop on Coherent Control of Carrier Dynamics in Semiconductors, held in May 1998 at the University of Illinois at Chicago. Coherent control of charge carrier dynamics has evolved into an interdisciplinary topic involving atomic and molecular physics, condensed matter physics, quantum optics, laser spectroscopy, and the physics of electronic devices. This is reflected by the contributions contained in this volume which, to our knowledge, is the first of its kind on the issue of coherent control. Containing both review articles and latest results in the field in atomic, molecular, and semiconductor physics, it addresses experts and novices to the field alike. All articles have been reviewed and emphasis has been given to clarity and a detailed list of references.

This volume will be of interest to research workers, engineers, students and postgraduates.

Coherent Control in
Atoms, Molecules, and Semiconductors

Walter Pötz and
W. Andreas Schroeder (Eds.)



KLUWER ACADEMIC PUBLISHERS